Dissertation zur Erlangung des Doktorgrades der Fakultät für Chemie und Pharmazie der Ludwig-Maximilians-Universität München

DNA Origami Biosensors with Single-Molecule FRET Readout: Particle Size Characterization, Vesicle Detection and Cargo Transfer

Ece Büber

aus

Bergama, Türkiye

2023

Erklärung

Diese Dissertation wurde im Sinne von § 7 der Promotionsordnung vom 28. November 2011 von Herrn Prof. Dr. Philip Tinnefeld betreut.

Eidesstattliche Versicherung

Diese Dissertation wurde eigenständig und ohne unerlaubte Hilfe erarbeitet.

München, 13.11.2023

Ece Büber

Dissertation eingereicht am: 13.11.2023

1. Gutachter: Prof. Dr. Philip Tinnefeld

2. Gutachter: Prof. Dr. Alena Khmelinskaia

Mündliche Prüfung am: 12.12.2023

Abstract

Harnessing the precision of DNA origami and the sensitivity of single-molecule Fluorescence Energy Transfer (sm-FRET), this dissertation aims to make a contribution to enhance the capabilities of current biosensing technologies. The research explores two main projects: DNA origami curvature sensors and DNA origami vesicle sensors.

In the first project, a novel non-destructive method for single-particle size characterization and curvature sensing in biosystems was introduced. Utilizing flexible DNA origami structures that can adapt to a range of curvatures, and using sm-FRET as the transduction mechanism, this approach enables precise quantification of particle size and curvature. The sensors, consisting of segmented DNA origami structures linked together via flexible DNA linkers and incorporating a strategically placed FRET pair, demonstrated the ability to conform to the shape of nanoparticles. The activity of the sensors was validated on various particle types, including model DNA origami templates, silica particles and lipid vesicles, proving its adaptability and precision. The results, measuring particle sizes from 50 nm to 300 nm and bending angles from 50° to 180°, demonstrated the versatility and accuracy of the sensors. Importantly, the modularity of the DNA origami technique, which allows for customization to specific applications, further enhanced the practicality of the sensors in real-world applications ranging from accurate nanoparticle characterization to opening new avenues in nanotechnology research.

The second project explored the transformative potential of DNA origami vesicle sensors in biosensing and molecular cargo transport. Through the design of DNA origami structures capable of detecting the presence of a vesicle and performing triggered cargo transport, this research potentially contributes to the field of therapeutic and diagnostic innovations. Designed as rectangular DNA origami nanostructures, the sensors employed ATTO647N-labeled ssDNA protrusions and cholesterol anchors to detect lipid vesicles by sm-FRET readout. The hydrophobic nature of the ATTO647N fluorophore ensured strong anchoring to lipid vesicles, inducing stretching of the ssDNA strand which resulted in distinct FRET contrasts. As a significant step towards therapeutic applications, the capabilities of the sensors were explored in a proof-of-concept

molecular cargo transport system using a strand displacement mechanism to facilitate the transfer of ATTO647N-labeled cargo to surrounding lipid vesicles. Our results confirm the potential of this versatile system as a biosensor tailored for real-time detection of lipid vesicles and as a promising molecular cargo transport mechanism.

These projects collectively exemplify how the specificity and adaptability of DNA origami, when coupled with sm-FRET, contribute to the evolving landscape of biosensors. By advancing these interdisciplinary techniques, this work aims to expand the scope and utility of biosensors across various disciplines, including material science, molecular diagnostics and medical treatment.

List of Abbreviations

bp: Base Pair

BSA: Bovine Serum Albumin

DLS: Dynamic Light Scattering

DNA: Deoxyribonucleic Acid

DOPC: 1,2-dioleoyl-sn-glycero-3-phosphocholine

DOPE 1,2-dioleoyl-sn-glycero-3-phosphoethanolamine

dsDNA: double-stranded DNA

EDTA: Ethylenediaminetetraacetic acid

FLIM: Fluorescence Lifetime Imaging

FRET: Fluorescence Resonance Energy Transfer

GUV: Giant Unilamellar Vesicle

LUV: Large Unilamellar Vesicle

PAINT: Point Accumulation in Nanoscale Topography

PBS: Phosphate-Buffered Saline

ROXS: Reducing and Oxidizing System

TEM: Transmission Electron Microscopy

TIRF: Total Internal Reflection Fluorescence

sm-FRET: Single Molecule Fluorescence Resonance Energy Transfer

ssDNA: single-stranded DNA

SUV: Small Unilamellar Vesicle

“I was taught that the way of progress was neither swift nor easy.”

Marie Skłodowska Curie

1. Introduction

As our perception of the complexity of the world continues to deepen, the advent of biosensors has revolutionized our ability to explore and exploit the wonders of life. Biosensors are analytical devices combining a biological recognition element with a transducer that can generate a quantifiable signal from a biological input. Traditional laboratory assays often involve separation and identification processes, such as Gas Chromatography-Mass Spectrometry (GC/MS) for analysis of chemical mixtures, or purification steps followed by Nuclear Magnetic Resonance (NMR) spectroscopy for structure determination, which can be time-consuming and require specialized and expensive equipment. Biosensors, on the other hand, provide a simpler, faster, and often less expensive method for specific analyte detection with high sensitivity and accuracy by providing real-time results without the need for isolation or complex identification steps that can be easily interpreted by the user.[1] Thanks to advances in technology, versatile biosensors can now be made small enough to fit in wearable devices, moving from labs to everyday use. Moreover, this technology promotes collaboration across fields like biology, chemistry and engineering, leading to innovative solutions in a wide range of application areas including diagnostics, environmental monitoring, biophysics and materials science.

While there is a large pool of materials that are suitable for biosensing applications, meeting specific requirements for sensitivity, selectivity, responsiveness, stability, biocompatibility and cost-effectiveness can be challenging. Therefore, it is essential to investigate materials that meet these diverse biosensing specifications while simplifying the manufacturing process.[2] In this regard, nanotechnology has been playing a transformative role in enhancing the capabilities of biosensors. The nanoscale properties of materials such as nanoparticles, quantum dots and carbon nanotubes provide a high surface-to-volume ratio compared to bulk materials, resulting in enhanced reactivity, different optical behaviors and altered mechanical and electrical properties. These features lead to increased sensitivity, specificity and the ability to miniaturize sensors for point-of-care testing.[3] Gold nanoparticles in biosensors, for example, change their surface plasmon resonance upon interaction with certain biomolecules, resulting in a

visible color change. This property makes it possible to detect biological targets, such as viral proteins in rapid HIV tests, with high specificity and sensitivity.[4, 5] Furthermore, features like multiplexing allow for simultaneous detection of multiple targets.

In the rapidly growing worlds of biosensing and nanotechnology, DNA nanotechnology has emerged as a transformative platform with remarkable capabilities to create nanoscale structures with exceptional precision and versatility. In the early 80s, Ned Seeman's ground-breaking research[6] established the foundations of DNA nanotechnology, which demonstrated the extraordinary potential of using DNA as a programmable molecular building block. Paul Rothemund later pioneered the concept of DNA origami[7-9], a method in which a long, single-stranded DNA molecule is folded into desired shapes by means of shorter "staple" strands. The biosensing field quickly recognized the great application potential of Rothemund's DNA origami innovation. Leveraging this technique, scientists can now precisely design and modify DNA structures for specific applications. This precision is due to the specific interactions between the DNA base pairs, ensuring accurate detection of the target with minimal interference from other substances. The modularity of the technique enables versatile and adaptable DNA nanostructures, which can incorporate different components such as biorecognition elements, fluorescent markers and nanoparticles, and can be reconfigured to meet different needs, from biomarker identification to cargo transport regulation.[10-13] Consequently, these diverse properties enable the fabrication of customized, adaptable DNA origami biosensors[14-18] with unique detection and transduction properties that have attracted considerable attention from the research community.

Incorporating Single-Molecule Fluorescence Resonance Energy Transfer (sm-FRET)[19, 20] into biosensors as an optical transduction mechanism provides a unique understanding of biomolecular interactions and the ability to detect rapid changes at the molecular level. FRET is a non-radiative process through which energy is transferred from an excited donor fluorophore to an acceptor fluorophore, which is in close proximity, typically within 1 nm to 10 nm. The efficiency of this energy transfer is strongly dependent on the distance between the donor and acceptor molecules, as well as the spectral overlap between the donor emission and the acceptor absorption.[21] This characteristic makes

FRET a great transduction mechanism for biosensors, as it can precisely detect biomolecules.[22, 23] The fluorescence of the acceptor molecule is only elicited when the donor and acceptor fluorophores are closely positioned. This means that any environmental changes impacting the distance between these molecules will influence the fluorescence, facilitating the detection of even minor changes, like the presence of a specific biomolecule. This phenomenon has been widely utilized as a powerful tool in biological and chemical studies, allowing researchers to investigate molecular interactions, distances and dynamics with high spatial and temporal resolution. Additionally, since FRET does not produce harmful radiation, it is a safer alternative to other sensing methods that rely on radioactive or ionizing radiation.[24]

The accuracy of FRET measurements could be further improved by combining FRET with DNA origami to optimize the precise positioning of donor and acceptor fluorophores. Taking this approach to the single-molecule level provides an even greater level of precision. Observing individual molecules, instead of averages from many, gives a clearer picture of heterogeneous molecular behaviors and interactions. When combined with FRET and the precise placement capabilities of DNA origami, sm-FRET biosensors are able to detect these individual molecular events, which brings a level of detail and accuracy that is transformative for understanding complex biological processes and interactions at the most fundamental level.[25]

Based on the strong foundation of Ned Seeman's and Paul Rothemund's groundbreaking works, this thesis aims to contribute to the constantly evolving worlds of DNA nanotechnology and biosensing, bringing us closer to a future where molecular interactions can be resolved with precision and utilized in broad range applications, from medical diagnostics to pharmaceutical science. The results of an extensive research centered around two main projects are presented here: DNA origami curvature sensors and DNA origami vesicle sensors. Each of these projects is an example of combining DNA nanotechnology and single-molecule fluorescence sensing enabling applications in particle characterization, cargo transport and beyond.

The first project, DNA origami curvature sensors (Section 3), introduces a non-destructive method for single-particle size characterization and curvature sensing in biosystems. This novel approach challenges the limits of DNA origami by designing dynamic

structures capable of detecting a range of curvatures, instead of possessing an on/off behavior. Accurate nanoparticle size measurement is essential across industries, influencing their physical and chemical properties and ultimately the safety, efficiency, and functionality of their applications. For instance, in the biomedical field, the size of a nanoparticle can determine its biological fate, affecting its circulation time in the blood, its uptake by cells and its distribution in the body.[26-28] Current methods, like dynamic light scattering (DLS), transmission electron microscopy (TEM) and scanning electron microscopy (SEM), face challenges such as sample preparation, instrument limitations and particle interactions which can influence the accuracy of the measurements. Addressing this need, the DNA origami curvature sensors project dives into a novel solution. The DNA origami curvature sensors adapt to particle shape, with size differences detected through shifts in FRET efficiency at the single-molecule level, covering a range of 50 nm to 300 nm. The DNA origami curvature sensors do not only measure particle size, they are also capable of sensing curvature. This method could revolutionize our understanding of biological phenomena and precision medicine, as it can profile soft dynamic systems such as cell membrane curvature in disease and exosome-based liquid biopsies for early-stage tumors. The sensors can be attached to cells, providing a promising tool for studying local membrane curvatures. In this regard, this thesis contributes to the field by combining rational DNA origami designs with single-molecule approaches to tackle some of the most challenging biosensing applications.

In the second project, DNA origami vesicle sensors (Section 4), we aimed to address the critical role of lipid vesicles in cellular processes and their emerging role in nanomedicine, as evident by their use in pioneering COVID-19 vaccine formulations. The main focus here is to challenge the applicability of DNA origami into more complex avenues by designing structures that are able to not only sense the presence of a vesicle but potentially perform triggered cargo delivery into the vesicles that they are attached to. This precision in detection and manipulation of lipid vesicles is vital for therapeutic and diagnostic innovations and intersects seamlessly with the intricate web of molecular interactions which require high specificity. Biosensors that utilize these specific affinity interactions allow for real-time cellular monitoring. However, effective application within the complex environment of lipid vesicles remains challenging. Motivated by this, our study combined the precision of DNA origami with the sensitivity of sm-FRET to achieve real-time lipid

vesicle detection and to explore molecular transport methodologies. Exploiting the hydrophobic interactions between lipid vesicles and a labeled DNA probe precisely placed on a DNA origami structure, this sensor displays a significant FRET signal contrast in the absence and presence of lipid vesicles, signifying a strong affinity-based interaction. Utilization of these affinity specific interactions provides opportunities for precise vesicle detection and potential delivery mechanisms, making the sensor a promising candidate to be used as a triggered cargo transfer and drug delivery system.

Following this general introduction, this dissertation begins with a foundational theoretical background section that explores the essentials of biosensors, DNA nanotechnology and fluorescence with a particular focus on sm-FRET. Subsequently, the thesis is partitioned into two main sections, each dedicated to one of the two core projects forming this work. These sections begin with the highlights of the individual motivations and literature review that guided our focus toward these research topics. This is followed by an overview of the publications that have emerged from these projects. The dissertation is completed in a conclusion and outlook section, summarizing key findings and suggesting future directions for research in these areas. Lastly, the appendices provide additional information, including a detailed materials and methods section of the experiments as well as supplementary information of the related publications.

The work demonstrates the strong potential of DNA nanotechnology to shape the future of biosensing and molecular diagnostics.

2. Theoretical Background

2.1. Biosensors: Bridging Biology with Technology

In a world where the unseen can change everything, biosensors have emerged as a critical bridge between the invisible molecular world and our perceivable surroundings, converting subtle biochemical interactions into clear, identifiable signals. Biosensors, at the intersection of biology, chemistry and electronics, trace their roots back to the early 20th century. One of the most notable milestones in the history of biosensors was in the 1960s, when Leland C. Clark Jr. introduced the concept of the enzyme electrode, which became the precursor to the first glucose biosensor.[29] His innovation shaped the management of diabetes, and since then, biosensors have expanded into numerous fields, from medical diagnostics to environmental monitoring.

A biosensor refers to a specialized device or system integrating biological elements, such as enzymes, antibodies, or living cells, with a transducer to detect and measure specific biological substances or processes.[1] The signal generated by the interaction of the biological element and analyte is converted into a measurable electrical or optical output by the transducer (Figure 1). Biosensors are designed to provide rapid, accurate and selective detection of target molecules or biological events with a high sensitivity. The advantages of real-time monitoring, portability and the potential for miniaturization, make biosensors valuable tools in various fields, including scientific research, medicine, environmental monitoring, food safety and biotechnology.

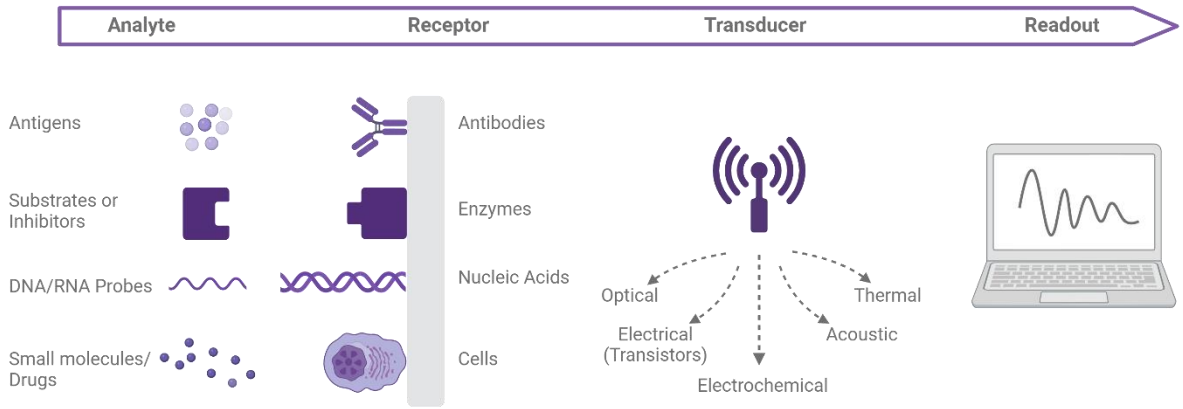

Figure 1. Schematic diagram of a typical biosensor setup illustrating the key components, including the receptor, transducer and readout. Various types of receptors and transducers are depicted, showcasing the versatility of biosensors in detecting different analytes and enabling diverse applications.

Among the numerous types of biosensors, from electrochemical to thermal, optical biosensors offer a unique perspective into the world of molecular interactions.[30] In particular, fluorescence biosensors can detect specific biological processes through the use of molecules that absorb and emit light at different wavelengths. As these fluorescent entities bind to their target molecules, their emission properties change. This change results in signals that correlate with the concentration or activity of the analyte being studied. Because of their rapid response, high sensitivity, specificity and versatility in probe design, fluorescence biosensors are used in a wide range of applications ranging from diagnostics to environmental monitoring.[31] Fluorescence-based biosensors are primarily based on three methods: fluorescence quenching[32], fluorescence enhancement[15] and fluorescence resonance energy transfer (FRET)[33]. Among these, FRET-based optical biosensors have recently gained prominence in cellular studies due to their superior sensitivity to conformational changes.[34-38]

With numerous technological advancements, biosensors have evolved significantly, and the integration of nanomaterials presents an innovative pathway towards enhanced, cost-effective and portable devices. In particular, nano-engineering of DNA stands out as a particularly promising way to improve biosensor capabilities.[39, 40] Merging DNA nanotechnology with FRET-based biosensors enhances detection potential of

biosensors. The distance dependency of FRET makes it essential to control the placement of dyes, a requirement that is fully addressed by the programmable nature of DNA. This confluence of technologies allows for unparalleled precision, specificity and modularity in biosensor design and functionality. Precision provides accurate and reliable measurements through the ability to fine-tune and control sensor response. The specificity is based on the precise base pair interactions in the DNA, which ensures that the sensor detects only the intended target molecules with minimal interference from other substances. By allowing the incorporation of different functional modules such as biorecognition elements, fluorescent markers or nanoparticles, modularity enables the creation of versatile DNA nanostructures with increased complexity and controllability. These structures can be reconfigured in a controllable manner using nucleic acid strands, environmental stimuli and enzymatic treatments.[11, 41-44] Additionally, by exchanging DNA recognition elements, the same biosensor can be used for the detection of one biomarker to another[13] or can provide regulated cargo transport.[12] The modular nature of the system further allows different components to be modified independently. For example, the transduction mechanisms can be modified without changing the recognition mechanism. Similarly, biocompatibility and durability of the structures can be optimized without affecting the functionality. Taken together, due to their addressability, DNA nanostructures can precisely identify and attach to target molecules, while fluorescence provides a highly sensitive detection of molecular interactions. This collaboration is a notable step forward in the transition from traditional biosensors to more sophisticated tools, and highlights the evolving sophistication of molecular detection.

For a better understanding of DNA nanotechnology-enabled fluorescence biosensors, it is important to provide a basic background of each building block: DNA nanotechnology and fluorescence. Starting from the fundamental principles, the following sections will explain the basic principles of these two concepts and will establish a complete picture of how they apply to the projects of this dissertation.

2.2. Deciphering DNA: From Molecular Design to Nanotechnology

2.2.1. The Structure of the DNA Molecule

DNA is one of the most basic building blocks of life, carrying genetic information and instructions for the functioning, reproduction and development of all living organisms. The most common DNA structure found in nature is B-DNA, in which two long strands rotate around each another to form a right-handed double helix (Figure 2a) of approximately 10.5 base pairs in turn, resulting in a total turnover length of 3.4 nm. The DNA strand is made up of polynucleotides, which are composed of the repeating monomeric units of a phosphate group, a pentose sugar (2-deoxyribose), and a nucleobase (Figure 2b). The four nucleobases of a DNA molecule are adenine (A), thymine (T), cytosine (C) and guanine (G). Each of these nucleobases pairs in a DNA double helix in a way where G is paired with C via three hydrogen bonds and A is paired with T via two hydrogen bonds (Figure 2c). This specific pairing, known as Watson-Crick base pairing[45], is fundamental to the structure and function of DNA, allowing it to store genetic information and serve as a template for replication and transcription.

The right-handedness of DNA molecule is favored due to the specific arrangement of the nucleotides and the stacking interactions.[46] When viewed along the axis of helix, right-handedness refers to the clockwise direction, and it ensures the integrity and stability of DNA structure. According to the carbon atoms in the sugar molecules, each strand has distinct 5' and 3' ends where 5' end has a phosphate group attached to the 5' carbon of the sugar and 3' end is associated with a hydroxyl group attached to the 3' carbon (Figure 2b).[47] The strands of the double-helix run in opposite directions, *i.e.* the structure is anti-parallel.[47] This means that 5' end of one strand pairs with the 3' of the complementary strand and vice versa. From this asymmetrical arrangement, major and minor grooves arise along the double helix with major groove being wider in B-DNA structure (Figure 2a).[48] These grooves are important as they provide binding sites to proteins and other molecules.

One of the key features of DNA that has enabled its various applications is its excellent mechanical rigidity against bending.[49] Being a natural polymer, DNA is typically modeled

by worm-like chain (WLC) model which describes mechanical behavior of DNA as intermediate between a rigid rod and a random coil, accounting for both local stiffness and long-range flexibility with the inclusion of the persistence length.[50-53] The persistence length represents the characteristic length scale over which DNA maintains its stiffness before bending. Single-stranded DNA (ssDNA) behaves more like a flexible polymer, and the Freely Jointed Chain (FJC) model[52] which describes DNA as a series of connected flexible segments where each segment can rotate freely around the bond connecting it to the next segment becomes more applicable.

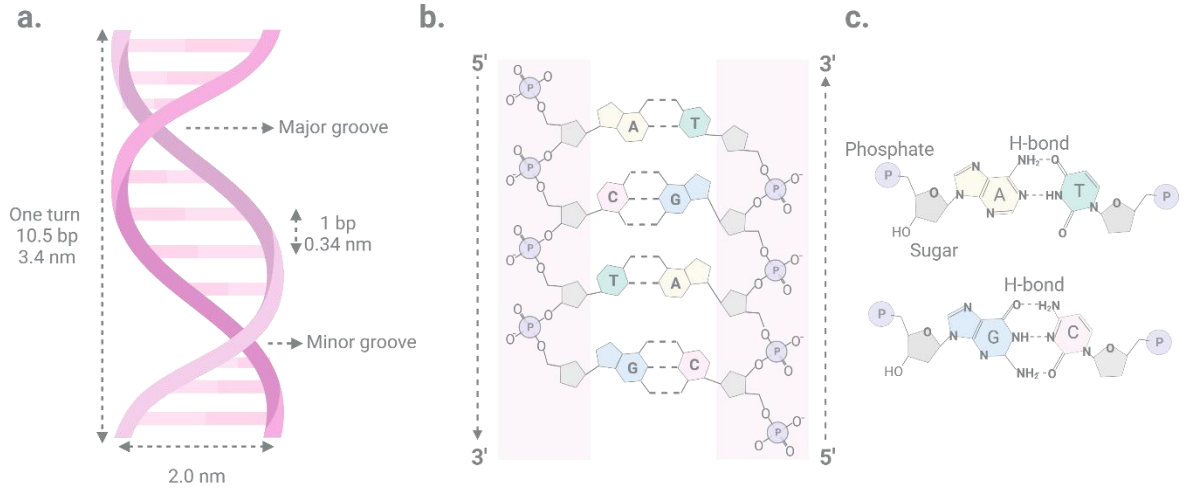

Figure 2. DNA molecule overview. (a) The double helix structure of the DNA molecule is depicted, highlighting the dimensions, major and minor grooves and the concept of turnovers. (b) The binding interactions between the bases (adenine (A), thymine (T), cytosine (C) and guanine (G)) and sugar-phosphate backbone are illustrated. The 3' and 5' ends of the DNA strands are indicated. (c) Detailed chemical structures and bonding arrangements of the bases are presented, showcasing their unique characteristics and bonding patterns.

2.2.2. DNA Nanotechnology: DNA as an Engineering Tool

Beyond the role it plays in biological systems, DNA has also become a versatile tool in engineering. By exploiting the remarkable self-assembly and programmability of DNA to create complex nanostructures and functional devices, researchers have pioneered a new concept known as DNA nanotechnology. As he raised the conceptual foundation of DNA nanotechnology in the early 1980s, it is essential to acknowledge Ned Seeman. The

development of immobile nucleic acid junctions by specifically designing DNA strand sequences to remove the symmetry of the assembled molecule[6] turned DNA into a scaffold for the precise placement of functional components at the nanoscale, paving the way for the realization of sophisticated nanostructures.

Building on these fundamentals, in 2006, the innovative work of Paul Rothemund[7] demonstrated how DNA can be folded into complex two- and three- dimensional shapes on the nanoscale, creating the concept of DNA origami.[9] Just as traditional paper origami transforms a two-dimensional sheet of paper into different three-dimensional shapes, DNA origami uses a long DNA scaffold to fold into pre-designed three-dimensional nanostructures by exploiting the programmability and specificity of DNA base pairing (Figure 3a). A bottom-up self-assembly technique, DNA origami relies on the folding of a long single-stranded DNA (scaffold, typically a viral DNA of ~7000 nucleotides) with the help of a set of short DNA strands (staples). The staples are designed to have complementary sequences to specific regions of the scaffold. When the strands are mixed, sequentially heated and cooled, the multiple binding domains of the staples facilitate the assembly of the scaffold into a designed shape through crossover base pairing (Figure 3b). Since its invention, DNA origami has continued to evolve, allowing the synthesis of virtually any arbitrary shape from 1D to 3D structures with custom asymmetry, cavities,[54, 55] or curvatures,[56-58] enabling advanced applications such as hierarchical or crisscross assembly,[59-62] single-stranded origami,[63, 64] and dynamic structures.[14, 65-68] Following the development of DNA origami, tools have been created to assist in the design and visualization of the DNA origami nanostructures. One example is CaDNAno[69], a software that provides an easy-to-use interface for creating arbitrary two- or three-dimensional DNA nanostructures by visualizing the placement of DNA strands and their interactions. It has greatly simplified the design process and made it more accessible for researchers to create complex and functional DNA nanostructures for a wide variety of applications.

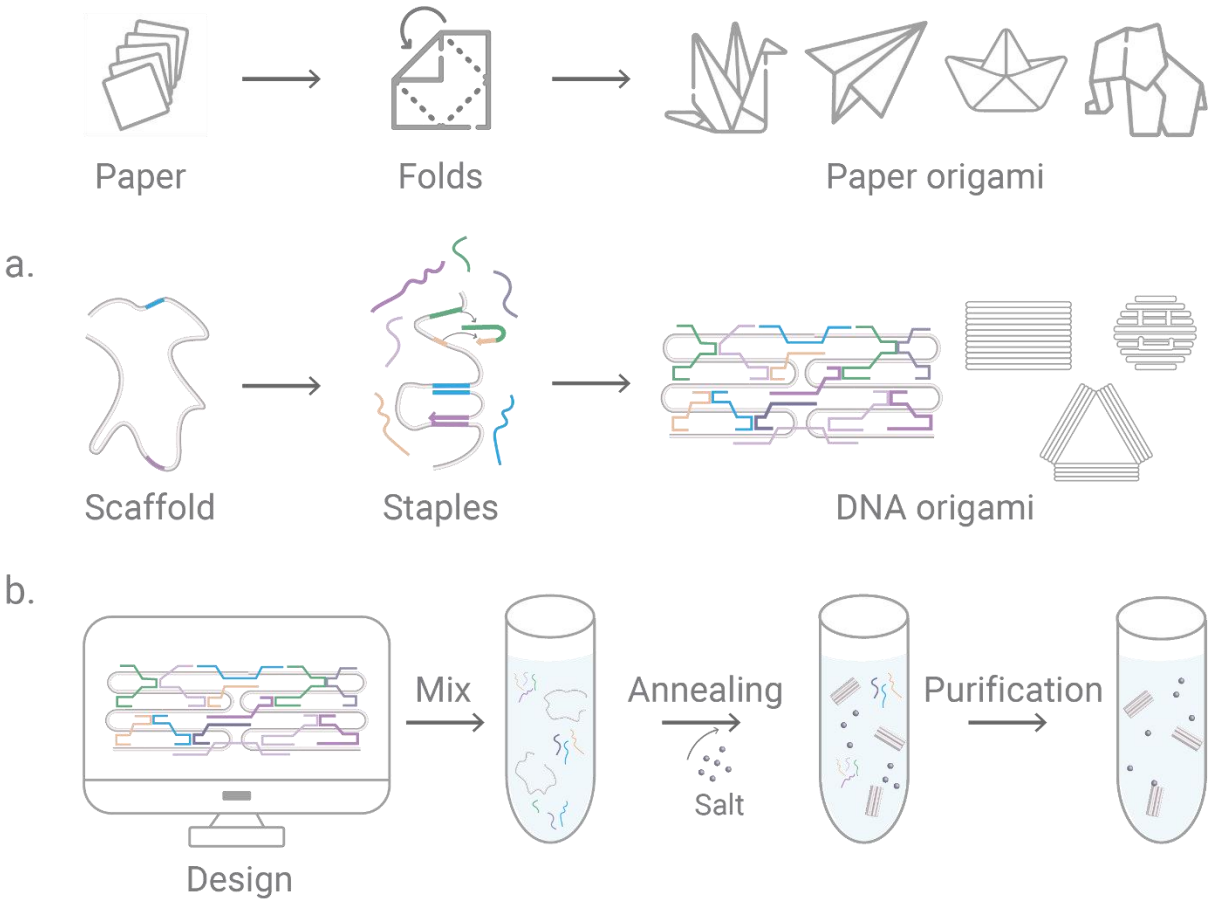

Figure 3. (a) Schematic representation of DNA origami folding. Starting with a long, single-stranded DNA scaffold, short staple strands are added to guide the folding into a specific shape. Through a series of carefully controlled thermal cycles, the DNA is coaxed into a desired structure. (b) Stages of DNA origami preparation: Design of scaffold and staple strands using computational tools – Mixing of scaffold and staples in proper stoichiometry – Controlled thermal annealing to facilitate folding – Purification and verification of the final structure.

The technology further enables the integration of functional components, such as nanoparticles, biological ligands, or fluorescent dyes with perfect addressability and precision, leading to the development of novel tools for sensing, drug delivery, computing, and more. Altogether, DNA is a powerful nanoscale engineering tool[70-74] with exciting prospects for scientific research and technological innovation due to its programmability, modularity and biocompatibility.

2.3. Light as a Tool: Fluorescence, FRET and Single-Molecule Techniques

Light is an essential part of the way we perceive the world. It consists of visible electromagnetic radiation and can be understood as a collection of photons, which display both wave and particle characteristics, known as the wave-particle duality. From the wave perspective, light is an electromagnetic wave with oscillating electric and magnetic fields perpendicular to its direction of propagation. These oscillations determine its properties like wavelength, frequency and amplitude.

When light interacts with an object, its behavior depends on the interaction with the atoms or molecules of that object. Some materials absorb specific wavelengths of light, giving rise to color perception. Others transmit light, allowing it to pass without much absorption or reflection. The interaction can also cause refraction, where light changes its direction as it moves between media due to speed changes. Diffraction is another outcome, where light waves bend or spread when encountering obstacles or narrow openings. This phenomenon leads to interference patterns and enables light to propagate around obstacles.

When discussing the basic concept of light, the fundamental equations to mention are:

The wave equation:

$$c = \lambda . \nu \tag{1}$$

which relates the speed of light (c) to its wavelength (λ) and frequency (ν). It states that the speed of light is equal to the product of its wavelength and frequency.

Planck's equation:

$$E = h . \nu \tag{2}$$

formulated by Max Planck, this formula describes the energy (E) of a photon in relation to its frequency (ν). It states that the energy of a photon is directly proportional to its frequency with the proportionality constant being Planck's constant (h).

These equations are critical to the understanding of the nature of light, its propagation, and the quantization of energy. They provide a foundation for various principles and

phenomena in optics, such as the wave-particle duality of light and the interaction of light with matter.

2.3.1. Fluorescence

Understanding light and its properties is the foundation for the exploration of the fascinating phenomenon of luminescence. When a material absorbs light, the energy of the photons is transferred to the electrons, as well as the vibrational and rotational states of the molecules, in the material. This energy excites the electrons to higher energy levels, called the excited states. The energetically unstable nature of these excited states causes the electrons to rapidly return to the lower energy states, resulting in release of excess energy in the form of either heat dissipation or light emission. The latter occurs when the material has specific energy levels within its electronic structure that allow the electrons to transition from the excited states back to the ground state through a process called radiative decay. The emitted light has a longer wavelength and lower energy than the absorbed light, resulting in a characteristic Stokes-shift[75] in color.

Luminescence refers to the emission of light from a substance when it is in an electronically excited state. This phenomenon can be categorized into two main types based on the nature of the excited state: fluorescence and phosphorescence. In fluorescence, the excited state is typically a singlet state, where the electron in the excited orbital is paired with the electron in the ground-state orbital. In this case, the return of the electron to the ground state is allowed by spin, resulting in the rapid emission of a photon. The emission rate constants of fluorescence are around 10^8 per second (10^8 s^{-1}) for fluorescent dyes, leading to a typical fluorescence lifetime of approximately 1-10 nanoseconds (10 ns, $10x10^{-9}$ s). In contrast, phosphorescence involves an excited triplet state with an unpaired electron, leading to a spin-forbidden return to the ground state. Being a much slower process, phosphorescence lifetimes range from microseconds to seconds or even longer.[76]

Overall, fluorescence exhibits fast emission rates and short lifetimes, making it a valuable tool for various applications, including fluorescence spectroscopy, imaging and biochemical assays.

2.3.2. Jablonski Diagram and Characteristics of Fluorescence Emission

The interactions that take place between light absorption and emission are commonly depicted using the Jablonski diagram (Figure 4a).[77] It is a graphical representation that illustrates the electronic energy levels and various transitions involved in luminescent processes. Professor Alexander Jablonski, considered the pioneer of fluorescence spectroscopy, is honored with the eponymous Jablonski diagrams[77] due to his significant contributions, which included the elucidation of concentration depolarization and the introduction of the term "anisotropy" to characterize the polarized emission from solutions.

The diagram incorporates two important principles: Kasha's rule and the Franck-Condon principle. Kasha's rule[78] states that upon absorption of light, the excited molecule rapidly undergoes vibrational relaxation within the same excited electronic state, reaching the lowest vibrational level of that state. As a result, the excited molecule is considered to be in a vibrationally relaxed state before any subsequent emission occurs. This relaxation occurs on an ultrafast timescale, typically within picoseconds (10^{-12} seconds). Additionally, since only one state is expected to produce emission, the emission wavelength is not affected by the excitation wavelength.

The Franck-Condon principle[79, 80] (Figure 4b) refers to the probability of electronic transitions during absorption and emission processes. It states that electronic transitions between energy levels occur so rapidly compared to nuclear motions that the nuclei remain fixed during the electronic transition. This principle implies that the geometry of the molecule does not significantly change during electronic transitions, resulting in vertical transitions on the Jablonski diagram.

A typical Jablonski diagram is shown in Figure 4a. The vertical axis represents the energy levels. The ground electronic state (S_0), where the electrons normally reside, is located at the bottom, while the excited electronic states are positioned higher up. These excited states can include singlet states (S_1, S_2, etc.) and triplet states (T_1, T_2, etc.). Each electronic

energy level of the fluorophores can possess various vibrational energy levels, represented as 0, 1, 2 and so forth.

Upon absorption of a photon, several possible processes can occur. Usually, the molecule gets excited to an electronically excited state, typically to a singlet state (S_1). From this excited state, with a few exceptions, the molecule can undergo internal conversion (represented by vertical dashed lines in Figure 4a), a rapid process where the excess energy is dissipated through non-radiative pathways such as vibrations or interactions with the surroundings. Following Kasha's rule, this internal conversion brings the molecule to the lowest vibrational level of the excited singlet state.

Following the internal conversion, the molecule has two possible paths. The first path is fluorescence, where the molecule undergoes a radiative decay from the excited singlet state (S_1) to the ground state. During this transition, the molecule emits a photon with lower energy compared to the absorbed photon. The difference in energy (or wavelength) between the absorbed and emitted photons is called the Stokes shift (Figure 4c). This shift occurs due to various relaxation processes, such as vibrational relaxation and energy dissipation during internal conversion. Kasha's rule is relevant here as it explains the rapid relaxation of the molecule to the lowest vibrational level of the excited state, allowing for efficient fluorescence emission. It is typically observed that the emitted photon has lower energy (longer wavelength) than the absorbed photon, resulting in a red-shifted emission.

In the second path, the molecule can undergo intersystem crossing, a process in which it transitions from the excited singlet state to an excited triplet state (T_1). This transition involves a change in the spin state of the electron. From the excited triplet state, the molecule can undergo a slower radiative decay back to the ground state, resulting in phosphorescent emission. Phosphorescence is characterized by its longer emission timescales, ranging from microseconds to seconds or even longer. The Franck-Condon principle comes into play here, as it suggests that electronic transitions occur much faster than nuclear movements. Hence, the positions of the atomic nuclei essentially remain unchanged during these electronic transitions.

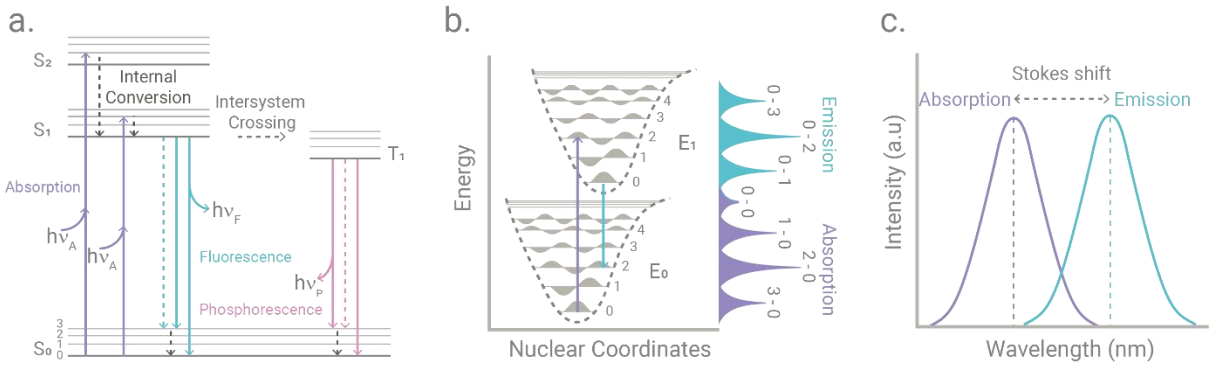

Figure 4. Schematic illustrations representing key concepts in spectroscopy. (a) Jablonski diagram illustrating energy levels and transitions involved in electronic spectroscopy. (b) Franck-Condon principle visualized through overlapping vibrational energy levels of the excited and ground states. (c) Absorption-emission spectrum showcasing the Stokes shift, depicting the energy difference between the absorbed and emitted photons.

Fluorophore lifetime (τ) and quantum efficiency (Q) are important parameters that can be calculated based on the Jablonski diagram. The lifetime of an excited state is the average time it takes for the molecule to return to the ground state through radiative or non-radiative processes. In the Jablonski diagram, the lifetime can be estimated by considering the rates of the different relaxation pathways (k). For example, if fluorescence is the dominant relaxation pathway, the lifetime can be calculated by considering the rate of radiative decay from the excited state to the ground state:

$$\tau = \frac{1}{k_{rad}} \tag{3}$$

where k_{rad} is the rate constant for radiative decay from the excited state to the ground state. Alternatively, if non-radiative processes dominate, the lifetime can be estimated by considering the rates of non-radiative transitions with the formula:

$$\tau = \frac{1}{k_{rad}+k_{nr}} \tag{4}$$

where k_{nr} is the rate constant for non-radiative transitions.

Quantum efficiency (Q) represents the efficiency with which an excited molecule undergoes radiative decay compared to non-radiative processes. It is expressed as the ratio of the number of photons emitted through radiative decay to the total number of absorbed photons. The quantum efficiency can be calculated using the formula:

$$Q = \frac{k_{rad}}{k_{rad}+k_{nr}} \quad (5)$$

A higher value of Q indicates a higher efficiency of radiative decay, while a lower value suggests a higher predominance of non-radiative processes.

2.3.3. Fluorescence Resonance Energy Transfer

Fluorescence Resonance Energy Transfer (FRET) is a spectroscopic technique for investigating molecular interactions and distances at the nanoscale. FRET is named "resonance energy transfer" because it relies on the resonant interaction between donor and acceptor fluorophores, facilitating energy transfer. FRET was first described in the 1940s by Theodor Förster, who outlined the theoretical principles of non-radiative energy transfer between nearby molecules. Therefore, FRET is also often referred to as Förster resonance energy transfer in recognition of his pioneering work.

In contrast to radiative transfer, FRET involves non-radiative energy exchange between fluorophores with closely matched energy levels (Figure 5a). This transfer mechanism is similar to coupled oscillators, where energy is transferred through dipole-dipole interactions. The principle underlying FRET is also based on dipole-dipole interactions; if the absorption spectrum of the acceptor overlaps with the emission spectrum of the donor, the excited donor transfers energy to the acceptor in close proximity, leading to fluorescence emission at a longer wavelength (Figure 5b). Because FRET is sensitive to molecular proximity, it is often referred to as a "spectroscopic ruler"[81] and is used to study molecular interactions, spatial arrangements and conformational changes of molecules such as proteins and nucleic acids.

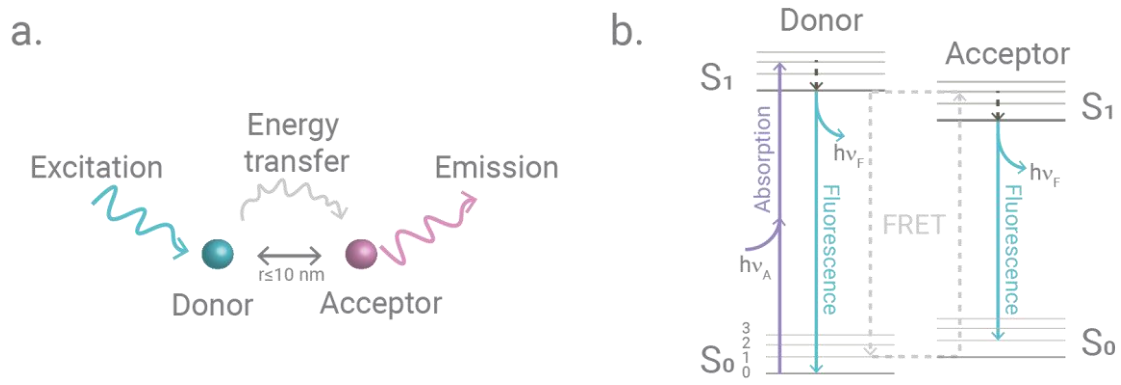

Figure 5. Energy transfer between a donor and an acceptor molecule. The scheme (a) illustrates the process of energy transfer from the excited state of the donor molecule (cyan) to the acceptor molecule (magenta) through FRET. (b) Jablonski diagram showcasing the energy levels and transitions involved in FRET, depicting the excitation and relaxation processes of a donor molecule and an acceptor molecule.

2.3.3.1. Understanding the Calculations and Parameters of FRET

To understand FRET more quantitatively, it is essential to consider the Förster theory.[82, 83] This theory describes the energy transfer efficiency **(E)** between the donor and acceptor fluorophores. The rate of energy transfer from a donor to an acceptor $\mathbf{k_T(r)}$ is given by

$$k_T(r) = \frac{1}{\tau_D}\left(\frac{R_0^6}{r^6}\right) \tag{6}$$

where τ_D is the decay time of the donor in the absence of acceptor, R_0 is the Förster distance and **r** is the donor-to acceptor distance. Förster distance signifies the distance at which the energy transfer efficiency is 50% and is typically in the range of 2 to 6 nm.

The efficiency of energy transfer is influenced by several factors, including the quantum yield of the donor **(Q_D)**, the spectral overlap integral between the donor emission spectrum and the acceptor absorption spectrum **($J(\lambda)$)**, the relative orientation of their transition dipoles **(κ^2)** and the distance **(r)** between them. Equation 7 expresses the relation of the energy transfer rate **(k_T)** to these parameters as a function of distance **(r)**.

$$k_T(r) = \frac{Q_D K^2}{\tau_D r^6}\left(\frac{9000(ln10)}{128\pi^5 N n^4}\right)\int_0^\infty F_D(\lambda)\,\varepsilon_A(\lambda)\lambda^4 d\lambda \tag{7}$$

In this equation, Q_D represents the quantum yield of the donor in the absence of the acceptor, n denotes the refractive index of the medium (typically assumed to be 1.4 for biomolecules in aqueous solution), N is Avogadro's number, τ_D stands for the lifetime of the donor in the absence of the acceptor, $F_D(\lambda)$ represents the corrected fluorescence intensity of the donor in the wavelength range λ to $\lambda+\Delta\lambda$, $\varepsilon_A(\lambda)$ is the extinction coefficient of the acceptor at λ (typically given in units of M^{-1} cm^{-1}) and κ^2 is a factor describing the relative orientation of the transition dipoles of the donor and acceptor.

The overlap integral $J(\lambda)$ measures the spectral overlap between the emission of the donor and the absorption of the acceptor. With isoenergetic energy transfer, where the donated and accepted energies match, a higher $J(\lambda)$ indicates a greater probability of successful energy transfer (Figure 6a). Therefore, a significant overlap between the donor emission and the acceptor absorption spectra increases the probability of effective energy transfer. The spectral overlap integral $J(\lambda)$ is described by the formula:

$$J(\lambda) = \int_0^\infty F_D(\lambda)\varepsilon_A(\lambda)\lambda^4 d\lambda \quad (8)$$

If equation 7 is written in terms of the Förster distance knowing that at that distance $k_T(r) = \tau_D^{-1}$ from the equation 6, Förster distance can be calculated from with the following formula:

$$R_0 = 0.211(\kappa^2 n^{-4} Q_D J(\lambda)^{1/6} \text{ in Å} \quad (9)$$

The orientation factor (κ^2) accounts for the relative orientation of the donor and acceptor transition dipoles in FRET (Figure 6b). Experimental determination of the precise κ^2 value is challenging due to molecular complexity, but theoretical models can provide estimates. It can be mathematically expressed in terms of the angles (θ) between the donor and acceptor transition dipole moments. The orientation factor is described by the formulas:

$$\kappa^2 = (cos\theta_T - 3cos\theta_D cos\theta_A)^2 \quad (10)$$

$$\kappa^2 = (sin\theta_D sin\theta_A cos\Phi - 2cos\theta_D cos\theta_A)^2 \quad (11)$$

where θ_T represents the angle between the emission transition dipole of the donor and the transition absorption dipole of the acceptor. θ_D and θ_A are the angles between these dipoles and the vector that connects the donor and the acceptor. Additionally, Φ denotes the angle between the planes defined by these dipoles. The orientation factor ranges

from 0 to 4π, representing all possible orientations. A value of 1 indicates perfect alignment, maximizing energy transfer, while a value of 0 represents perpendicular orientation, inhibiting energy transfer. In the calculations to determine R_0, the value of κ^2 is generally assumed to be 2/3. This assumption considers that donor and acceptor undergo rapid rotational diffusion prior to energy transfer, ensuring a random orientation distribution between them.

The efficiency of energy transfer (E) corresponds to the proportion of absorbed photons by the donor that undergo successful transfer to the acceptor. This fraction can be determined by the following expression:

$$E = \frac{k_T(r)}{\tau_D^{-1} + k_T(r)} \tag{12}$$

representing the ratio of the transfer rate to the total decay rate of the donor in the presence of the acceptor. By recalling the relationship $k_T(r) = \tau_D^{-1}(R_0/r)^6$, one can conveniently rearrange equation 12 to obtain:

$$E = \frac{R_0^6}{R_0^6 + r^6} \tag{13}$$

Equation 13 once again shows that transfer efficiency is highly dependent on the distance between the donor and acceptor when it is near R_0 (Figure 6c). As the distance decreases below R_0, the efficiency rapidly increases to 1.0 and the donor emission becomes unobservable. In contrast, the efficiency quickly drops to zero if the distance exceeds R_0. Reliable distance measurements are feasible within a range of $r = 0.5R_0$ to $r = 2R_0$. Outside this range, FRET is not practical for distance measurements.

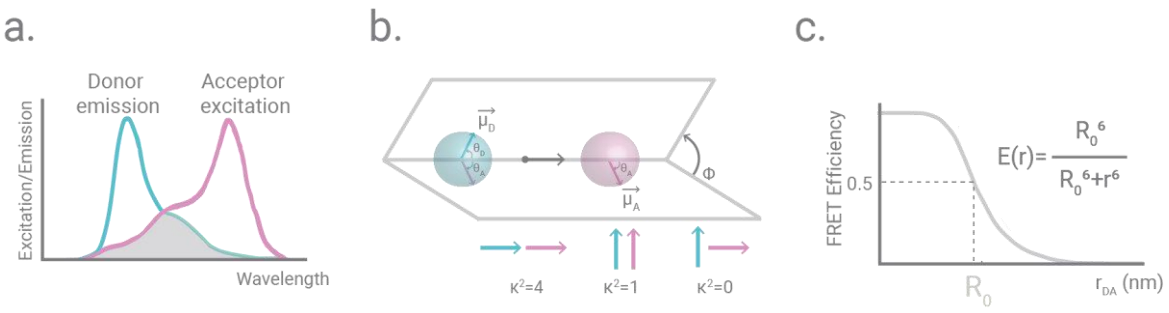

Figure 6. Components of FRET analysis. (a) Spectral overlap: Illustrates the overlap between the donor emission and acceptor excitation spectra, indicating efficient energy transfer. (b) κ^2

dependence on donor emission and acceptor excitation dipole orientations. Different orientations result in varying κ^2 values, affecting the efficiency of energy transfer in FRET. (c) FRET efficiency vs distance plot: The graph presents the FRET efficiency as a function of distance between the donor and acceptor molecules. The Förster radius, $\mathbf{R_0}$, is highlighted as the distance where FRET efficiency drops to 50% of its maximum value.

The transfer efficiency is commonly evaluated by comparing the relative fluorescence intensity of the donor in the absence $(\mathbf{F_D})$ and presence $(\mathbf{F_{DA}})$ of the acceptor.

$$E = 1 - \frac{F_{DA}}{F_D} \tag{14}$$

It can also be deducted from the lifetimes of the fluorophores as in the following:

$$E = 1 - \frac{\tau_{DA}}{\tau_D} \tag{15}$$

FRET has been an essential spectroscopy technique in detecting molecular interactions and dynamics with remarkable sensitivity. However, to further explore the complexity of these interactions and to bypass ensemble averaging, which can mask the behaviors of individual molecules, the scientific community began to move toward single-molecule techniques. These techniques allow researchers to analyze heterogeneities and transient states that would otherwise remain hidden in bulk measurements, providing an extraordinary view of molecular behavior. Exploiting the power of FRET at the single-molecule level allows for more detailed observation of individual molecular interactions, revealing subtleties and nuances that are often lost in ensemble studies.

2.3.4. Single-Molecule Fluorescence

Single-molecule detection (SMD) is a sophisticated and highly sensitive technique that allows for the observation and analysis of individual molecules providing insight into their behavior, characteristics and interactions.[84-86] Since it provides high sensitivity and a bright signal against a dark background, fluorescence is a primary method of choice for SMD.

Single-molecule measurements overcome the limitations of ensemble-averaging measurements, where bulk methods observe the average or collective behavior and

mask unique characteristics. Instead, single-molecule measurements allow the study of individual molecules and uncovering variations known as molecular heterogeneities. These heterogeneities can take the form of static heterogeneities, such as different intrinsic molecular states (for example, various protein folding states), or dynamic heterogeneities, like transitions between different states (e.g., alternate chemical reaction pathways).[87, 88] Operating at the highest level of analytical sensitivity, single-molecule measurements can detect rare and hidden events otherwise averaged in bulk measurements.[86]

One of the requirements of single-molecule fluorescence (SMF) is the careful selection of a suitable fluorophore that is bright, non-toxic, and possesses desirable photophysical properties such as high photostability.[89] Different applications require various fluorophores and labeling techniques, and choices must be aligned with the demands of the specific experiment. It is critical to ensure that the labeling strategy is both specific and efficient, and that the labeled molecule remains functional.

Furthermore, SMF techniques require careful control over the concentration of the molecules being studied.[90] This is essential to reduce the probability of having multiple molecules within the observation volume, which would lead to ensemble effects rather than single-molecule behavior. The concentration must be low enough to achieve single-molecule sensitivity but not so low that the molecules of interest are rarely encountered. This often requires a sensitive balance that depends on the particular system and the detection method being used.

The experimental setup for SMF often requires advanced instrumentation, including highly sensitive detectors, specialized optics and controlled environmental chambers to minimize background noise and interference. Both confocal microscopy and widefield microscopy techniques are commonly used, each of which has its own specific application.[91] In confocal microscopy (Figure 7a), a laser is used to excite a single point in the sample, and a spatial pinhole is placed at the confocal plane in the detector path to eliminate out-of-focus signal. This ensures that only the light from the focused plane reaches the detector, allowing for the creation of high-resolution, three-dimensional images. By scanning through different planes, a 3D image can be reconstructed. The confocal setup is particularly useful in reducing background noise, making it an attractive

choice for single-molecule studies. In widefield microscopy (Figure 7b), the entire specimen is uniformly illuminated, and the emitted fluorescence is captured simultaneously across the field of view. Although this method is simpler and often faster than confocal microscopy, it can result in more background noise since out-of-focus light is also detected. Within widefield microscopy, total internal reflection fluorescence microscopy (TIRFM) is a specialized technique that uses the phenomenon of total internal reflection to create an evanescent field. When the incident light is above the critical angle at the interface between two media with different refractive indices (e.g., glass and water), an evanescent field is created that decays exponentially with distance from the interface. This wave can excite fluorophores within approximately 200 nm of the interface, allowing for highly selective imaging of molecules at surfaces. TIRFM provides excellent signal-to-noise ratios and is particularly useful for studying processes that occur near the surface. This approach enables more selective imaging of the sample and is great for studying surface-bound or near-surface molecules, but its applicability is limited to "quasi-two-dimensional samples". Objective-based TIRF and prism-based TIRF are techniques used in microscopy to selectively illuminate molecules near a surface (Figure 7c). In objective-based TIRF, the critical angle for total internal reflection is achieved using the objective lens of the microscope, creating an evanescent field that illuminates only a shallow region near the interface. Prism-based TIRF creates the same effect by directing laser light through a prism on top of the cover glass. Together, these techniques enable a wide range of applications in single-molecule studies, with the choice of method depending on the specific nature of the sample and the research questions being investigated.

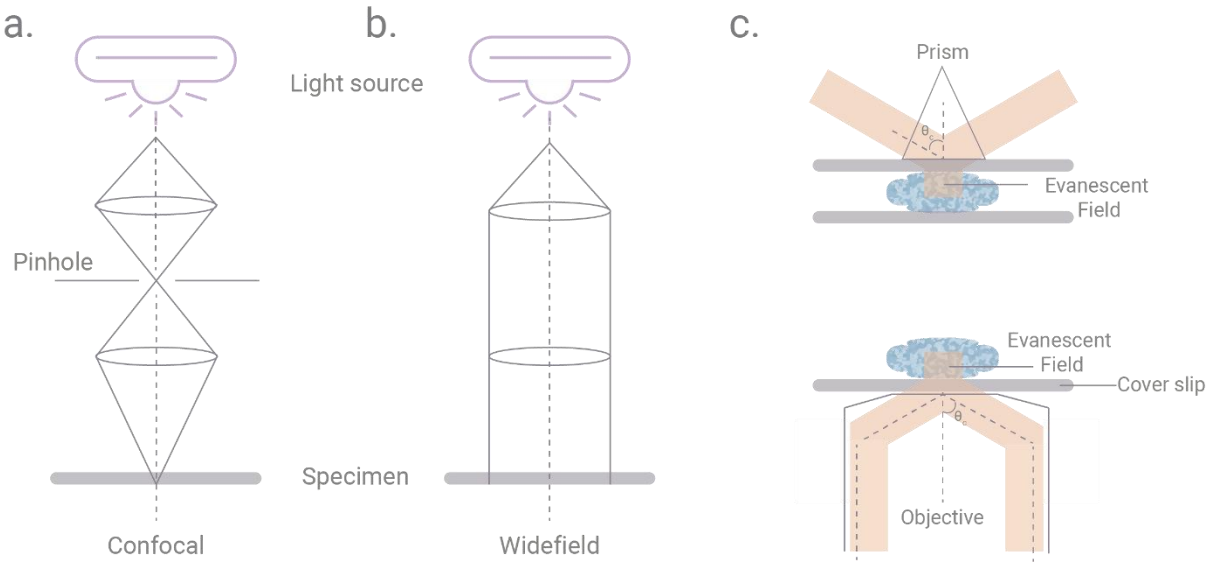

Figure 7. Comparative schematic representations of various microscopy techniques for single molecule fluorescence detection. (a) Confocal Microscope: Depicts the use of pinhole apertures to eliminate out-of-focus light, achieving greater resolution and contrast. (b) Widefield Microscope: Illustrates the basic optical system, where a large area of the sample is uniformly illuminated, capturing the entire field of view at once. (c) Prism Total Internal Reflection Fluorescence (TIRF) Microscopy (top) and Objective TIRF Microscopy (bottom): Showcases the specific configurations for illuminating a sample at a critical angle, enabling selective illumination of a thin region adjacent to the interface, and thus improving the imaging of surface events.

Single-molecule fluorescence techniques can provide detailed information about a fluorophore and its surrounding environment by analyzing its position, brightness, emission wavelength and other photophysical properties. Since these properties are sensitive to many biological, physical and chemical parameters, fluorescence-based single-molecule techniques are increasingly finding their ways into different fields of research. Besides their predominant use in biophysical research, these methods are also being adapted to study chemical reactions at a single-molecule level, providing valuable insights into the mechanical understanding of chemical reactions and the exploration of alternative reaction pathways. Through single molecule detection techniques, we are approaching the dream, first described by Richard Feynman in 1963 as; "everything the living things do can be understood in terms of jiggling and wiggling of atoms".

2.3.5. Lipid Vesicles: A Brief Introduction

Lipids are organic compounds that are insoluble in water but soluble in organic solvents, and they play critical roles in the integrity and functionality of living cells. One of the most significant arrangements of lipids in cell biology is the lipid bilayer, which forms the basic structure of cell membranes. It provides a dynamic matrix that shapes the cell and contributes to its selective permeability, enabling compartmentalization within the biological systems. In the complex world of cellular biology, lipid vesicles emerge as essential biomimetic systems, modeling the fundamental structure of cellular membranes. As a tool for understanding membrane dynamics, lipid-lipid and lipid-protein interactions, these self-assembled spherical structures consist of lipid bilayers encapsulating an aqueous compartment.

Vesicles naturally arise during secretion (exocytosis), material uptake (endocytosis) and the movement of substances within the plasma membrane.[92] When vesicles are released from the cell, they are termed extracellular vesicles (EVs). EVs can be categorized into three main types based on their size and biogenesis: exosomes (30-150 nm) originating from the endosomal system, microvesicles or ectosomes (100-1000 nm) formed by direct budding from the plasma membrane and apoptotic bodies (50-5000 nm) released during programmed cell death (Figure 8a).[93, 94] Conversely, vesicles can be prepared artificially, where they are termed liposomes.[95] Liposomes are commonly classified based on their layering (Figure 8a). Those with a single phospholipid bilayer are termed unilamellar vesicles, while those with multiple layers are called multilamellar vesicles (Figure 8b). Their size is another distinguishing feature: Small unilamellar vesicles (SUVs) measure just several tens of nanometers across, while large unilamellar vesicles (LUVs) are about a hundred nanometers wide. Giant unilamellar vesicles (GUVs), on the other hand, are significantly bigger, being 10 to 1000 times larger than SUVs and LUVs (Figure 8b).[96]

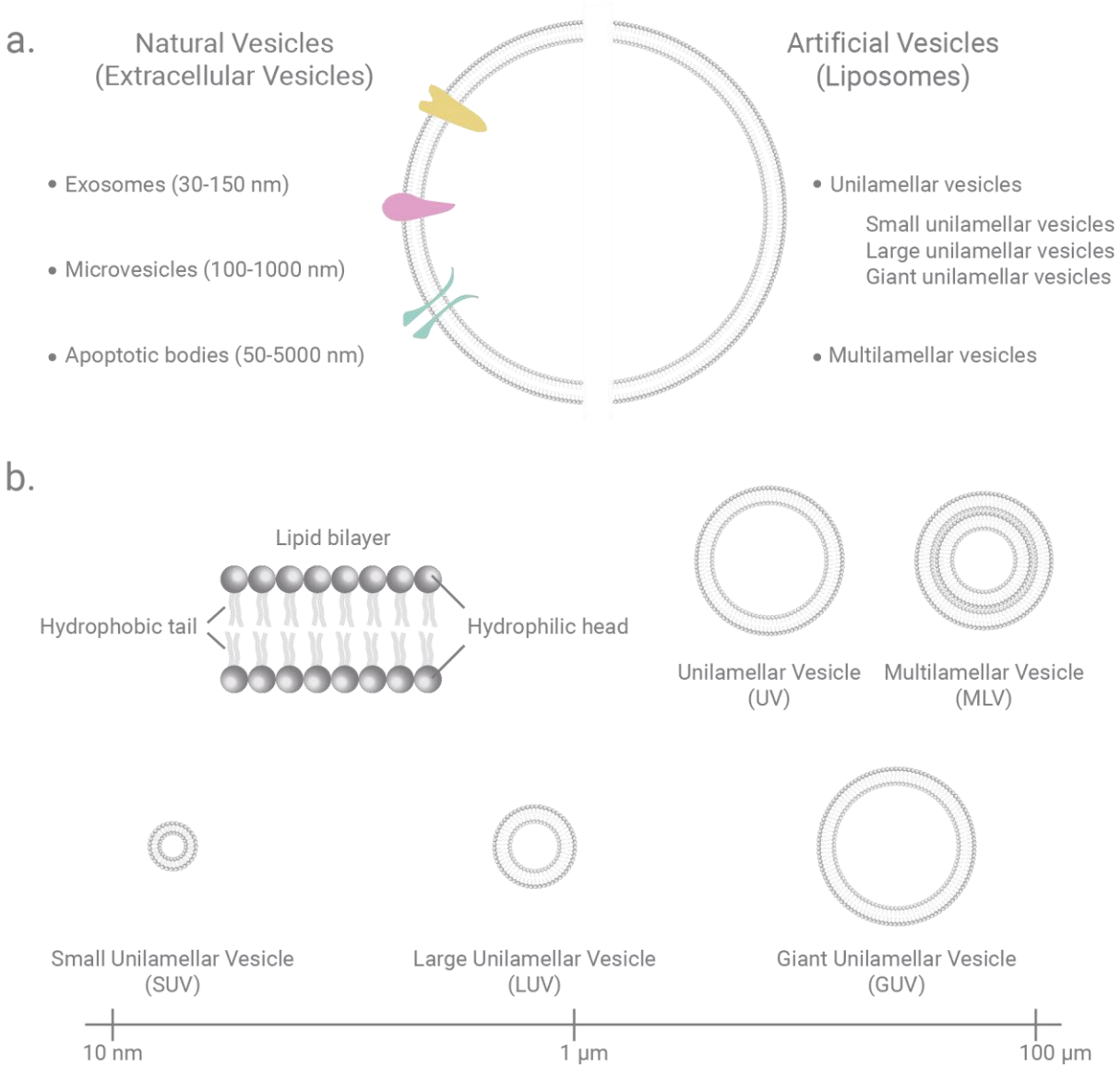

Figure 8. Classification of lipid vesicles. (a) The two primary categories of lipid vesicles: natural vesicles, derived from biological membranes and artificial vesicles, synthesized for research and therapeutic purposes. (b) (Top) Details of the molecular structure of a lipid bilayer, highlighting the hydrophilic heads facing the aqueous environment and the hydrophobic tails oriented inward. Accompanying this illustration is a schematic categorization of vesicles based on layering; unilamellar vesicles with a single lipid bilayer and multilamellar vesicles composed of multiple concentric lipid bilayers. (Bottom) Classification of vesicles according to size: small unilamellar vesicles (SUVs), large unilamellar vesicles (LUVs) and giant unilamellar vesicles (GUVs), each with distinct diameter ranges.

Lipid vesicles have long been recognized for their role as models for cell membrane research. Lipid vesicles serve as biomimetic systems that mimic the biophysical properties of cellular membranes, facilitating in-depth studies of cellular interactions and functions.[97] The foundational importance of vesicles in cellular function was highlighted when the 2013 Nobel Prize in Physiology or Medicine was awarded to James E. Rothman, Randy W. Schekman and Thomas C. Südhof for unveiling the molecular principles of vesicular trafficking, an essential system to the regulation of key intracellular transport pathways.[98-103]

After establishing a fundamental understanding of biosensors, DNA nanotechnology, the principles of fluorescence techniques and lipid vesicles, the next focus is on their application in the two main projects of this dissertation. In the following sections, these projects will be discussed, both of which involve the sophisticated integration of DNA origami structures with sm-FRET readout.

3. DNA Origami Curvature Sensors

3.1. Motivation

In the world of molecular and cellular interactions, size matters. Within the scope of particles, especially at the nanoscale, the size has a profound impact on various aspects of material science, medicine, pharmacology and biology. For example, in the case of lipidic nanocarriers such as liposomes, the dimensions of the nanocarrier can determine its efficacy and stability in drug delivery.[104] However, accurate characterization of such particles is quite challenging, especially in dynamic environments like cellular membranes. The drawbacks and limitations of traditional techniques, such as dynamic light scattering (DLS) and electron microscopy, highlight the need for innovative approaches.

In this study, we showcased the potential of our DNA origami curvature sensors for the size determination of nanoparticles. These self-assembled nanodevices adapt to the shape of the particles to which they bind, and this change is quantified as a sm-FRET readout. Their adaptable and modular design has been effectively applied to various platforms, including DNA origami templates with diverse geometries, solid silica particles and large unilamellar vesicles (LUVs). Using a variety of interaction chemistries, from DNA hybridization to cholesterol insertion into lipid membranes[105-109], we observed consistent FRET value trends as expected. A significant feature of these sensors is their ability to adjust their dynamic range based on modifications, such as the position of the anchoring moieties or the FRET pair.

3.1.1. Particle Characterization

Particle size is a comprehensive and essential parameter for many applications. Certain physical and chemical properties, as well as the purity of the particles can be evaluated using particle size distribution. The rate of reactions, packing density, solubility and success of drug delivery are a few examples of some critical properties that are

influenced by particle size. Many diverging industries require particle size analysis techniques in order to characterize the materials, and eventually to manufacture high quality, safe, pure and cost-effective products. All these factors make reliable and precise size measurement of particles a crucial step towards different purposes. Particle size analysis techniques diverge in terms of their working principles, quantification, or type and amount of the sample required.[110, 111] Some of the typical particle size analysis techniques include dynamic light scattering (DLS), laser diffraction and direct imaging techniques such as transmission or scanning electron microscopy (TEM or SEM). DLS struggles with particle heterogeneity since it gauges the intensity of scattered light which is greatly influenced by larger particles. In a sample with a mixture of small and large particles, DLS may overemphasize the presence of the larger particles, potentially giving misleading information about the average particle size in the sample.[112, 113] On the other hand, EM requires extensive sample preparation that can potentially alter the natural state of the particles.[114] Both DLS and EM have limitations for biological applications. In biological systems, the complexity and diversity of samples can interfere with the accuracy and reliability of these techniques. The diverse nature of biological samples can disrupt the accuracy of these techniques. For DLS, biological macromolecules can affect light scattering, and in EM, they may hinder clear imaging.[114] Additionally, optical methods, when assessing sub-micrometer structures, encounter resolution constraints due to the inherent limits of light. This barrier can obscure finer details in biological processes, impeding progress in fields like nanomedicine.

The curvature, or the particle size, is also an important parameter for lipidic nanoparticles. The use of lipidic nanocarriers especially in clinical applications is increasing together with the realization of the profits of such materials. One of the most utilized examples of such lipidic nanocarriers are the liposomes, which are small, spherical, artificial lipid vesicles. Because of their size, biocompatibility, targetability and amphiphilic character, liposomes are promising drug delivery systems.[95] Since the particle size distribution of such lipidic nanocarriers can have a drastic influence on the bulk properties, stability and performance of the end product, determination of the average diameter and the size distribution are fundamental quality control assays for such products.[104] Additionally, lipid vesicles are utilized as simple model membranes presenting the lipid bilayer as the principle component of cell membranes.[97] This makes lipid vesicles as ideal structures

to investigate existing biosystems as well as the emergence, evolution and functioning of cells.

Given the profound influence of particle size across diverse fields, from material science and chemistry to pharmaceuticals and biology, it is essential to prioritize the development of systems that can measure particle size with precision and reliability.

3.1.2. Curvature Sensing for Cellular Membranes

As the boundary of the cell, the cell membrane is the compartment where sensing and cellular response are first elicited. Much of our understanding of membrane biology comes from observing cellular membrane processes, where membrane curvature plays an indisputable role. As a very dynamic system, the cell membrane often undergoes conformational changes leading to drastic changes in the local membrane curvature. Sensing the changes in the local curvature of membranes can help us to understand the mechanisms of the cell membrane remodeling in intra- and extracellular processes.[115-119] These membrane curvatures appear and disappear dynamically, and their locations are very difficult to predict. Also, the size of these curvatures is usually below the diffraction limit of visible light, making it a real challenge to resolve their values using live-cell imaging.[120] In order to get insights into the membrane curvature, several *in vitro* systems and simulations have been implemented for precise sensing of curvature at relevant scales. In one of the most common model systems, tubular structures from optically visible giant unilamellar vesicles (GUVs, 5-50 µm in diameter) are formed via micromanipulation with a pipette. In curvature sensitive protein studies, these structures are used to adjust membrane tension and tubular diameter.[121, 122] Fluorescence techniques are also employed to quantify the binding of curvature sensitive proteins to vesicle surfaces. The DNA origami method has proven to be an extremely versatile engineering tool especially when combined to model membranes.[107, 123-128] The unique advantages of DNA origami technique, allow us to make modular designs where different functions can be optimized separately. The ability of being membrane-active with modifications on the DNA origami nanodevices makes it, for example, possible to analyze lipid vesicles or sense cellular membrane curvature. Taking into account recent studies

proving that model lipid membranes can be tightly wrapped around DNA origami nanostructures to generate stable membrane curvatures, such type of synthetic nanodevices can be used to work on the membrane curvature properties.[129] Indeed, Franquelim *et al.* developed and studied a set of curved DNA origami coats that mimic the shape of membrane-scaffolding proteins (e.g. BAR domains); revealing how curved DNA origami can controllably deform and tubulate membranes dependent on curvature, membrane affinity and surface density.[124] In another study, Xu *et al.* developed a system to prompt membrane fusion by providing SNARE protein organizations on DNA structures as supporting platforms.[130] Inspired by dynamin proteins, Grome *et al.* developed a spiral DNA origami that can induce membrane tubulation.[131, 132] All-in-all, whereas model systems enable tight control membrane curvature and composition, *in vivo* systems, on the other hand, lack facile solutions for controlling and localizing membrane curvature events. Moreover, the current membrane curvature sensors typically test only the binding of a membrane to a geometrically matching entity[133] or require incorporation of membrane binding proteins.[118, 134] Given the challenges for gauging the mechanisms of membrane shape and function, there is an apparent need for developing a simple way to sense and measure membrane curvature, and therefore engineering a minimal membrane sensing system.

3.2. Overview of the Associated Publication

DNA Origami Curvature Sensors for Nanoparticle and Vesicle Size Determination with Single-Molecule FRET Readout

Ece Büber, Tim Schröder, Michael Scheckenbach, Mihir Dass, Henri G. Franquelim and Philip Tinnefeld,

published in

ACS Nano, 17 (3), (2023) 3088.

DOI: 10.1021/acsnano.2c11981

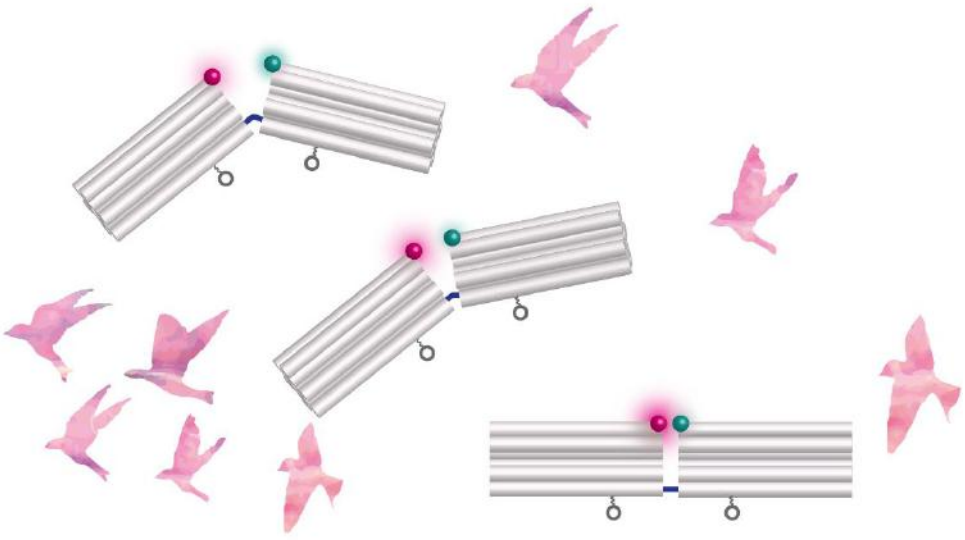

In our published work "DNA Origami Curvature Sensors for Nanoparticle and Vesicle Size Determination with Single-Molecule FRET Readout", we discussed the importance of particle size analysis in various industries and highlighted the limitations of existing techniques such as laser diffraction, DLS and electron microscopy in accurately measuring particle size, especially at the nanoscale. We proposed an alternative approach using DNA origami curvature sensors that can adapt to the shape of particles and report on their size through changes in FRET on the level of single molecules (Figure 9).

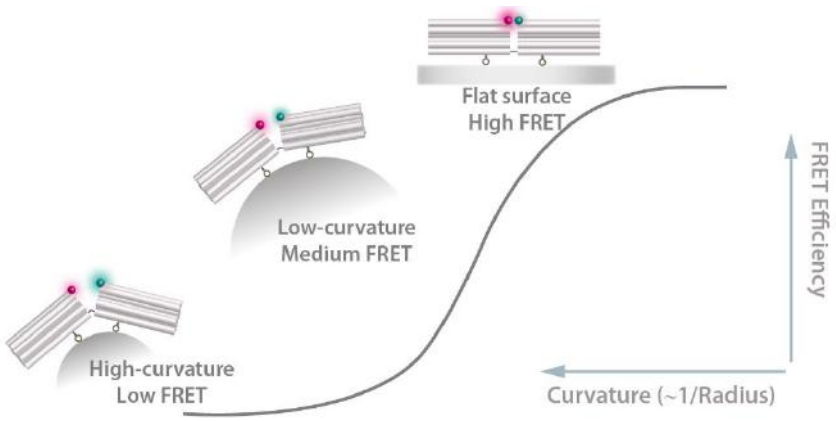

Figure 9. The working principle of the DNA origami curvature sensors.

The curvature sensors were designed as segmented DNA origami structures with two rigid blocks connected by DNA linkers. The linkers were designed as mainly double-stranded DNA to ensure the maintenance of the rigidity of the blocks. They were strategically positioned near the edges to minimize twisting motions. Furthermore, a one-nucleotide gap was introduced in the middle of the linkers, serving as a well-defined hinge point. A FRET pair, consisting of a donor (Cy3B) and an acceptor (ATTO647N) dye, was positioned at the interior edges of the blocks. The working principle of the curvature sensors was based on their ability to adapt to the shape of particles. When the particles bound to the sensors, the structure of the sensors bent to accommodate the surface curvature of the particles. This bending resulted in a change in the distance between the fluorescent donor and acceptor dyes located on the two separate blocks of the sensors. As a result, the efficiency of FRET between the dyes was altered. It is important to note

that an important role in adjusting the dynamic range of the curvatures studied was played by individual anchors placed at different marked distances from the hinge (6 nm, 13 nm and 20 nm distances from the hinge). By measuring this change in FRET efficiency, the sensors provided a quantitative indication of the particle size or local surface curvature.

In order to validate the concept, the curvature sensors were tested initially on model DNA origami templates, which was followed by tests on silica particles and eventually on lipid vesicles. For the DNA origami templates, the sensors successfully adapted to different bending angles and showed distinct FRET efficiencies. The same trend was observed when testing the sensors on BAR domain mimicking DNA origami nanostructures, published by Franquelim *et al.*[124], which had intrinsic curvature. When the sensors were applied to silica particles of different sizes, the resulting FRET efficiencies were correlated with the size of the particles, demonstrating the ability to distinguish between different size populations. By changing the position of the FRET pair, the dynamic range and sensitivity of the sensor could be adjusted. Finally, the curvature sensors were successfully employed on lipid vesicles, which served as models for biological membranes. The sensors attached to the vesicles via biotin or cholesterol anchors and exhibited FRET efficiencies corresponding to the size of the vesicles. The results showed that the curvature sensors did not deform the soft vesicles and could accurately sense their curvature.

Overall, the DNA origami curvature sensors proved to be a reliable and adaptable approach for measuring particle size and curvature. The use of FRET allowed for sensitive and quantitative detection, and the modularity of the DNA origami technique allowed for customization of the sensors to specific applications. We suggest that these sensors could be further applied to study membrane remodeling in cellular processes and provide insights into the biophysics of membranes.

In conclusion, our publication introduced an alternative approach to particle size analysis utilizing DNA origami curvature sensors. These sensors demonstrated the remarkable ability to conform to the shape of particles and precisely measure their size by detecting changes in FRET. Through extensive experimental testing, we validated the efficiency of these sensors on model DNA origami templates, silica particles and lipid vesicles. The

tunability of the sensors allowed us to customize their dynamic range and sensitivity, making them adaptable for diverse applications. We believe that, with further adjustments this study will contribute to the accurate characterization of nanoparticles and will open up new possibilities for the study of membrane dynamics.

ACS NANO

www.acsnano.org

ARTICLE

DNA Origami Curvature Sensors for Nanoparticle and Vesicle Size Determination with Single-Molecule FRET Readout

Ece Büber, Tim Schröder, Michael Scheckenbach, Mihir Dass, Henri G. Franquelim,* and Philip Tinnefeld*

Cite This: *ACS Nano* 2023, 17, 3088−3097

Read Online

ACCESS | Metrics & More | Article Recommendations | Supporting Information

ABSTRACT: **Particle size is an important characteristic of materials with a direct effect on their physicochemical features. Besides nanoparticles, particle size and surface curvature are particularly important in the world of lipids and cellular membranes as the cell membrane undergoes conformational changes in many biological processes which leads to diverging local curvature values. On account of that, it is important to develop cost-effective, rapid and sufficiently precise systems that can measure the surface curvature on the nanoscale that can be translated to size for spherical particles. As an alternative approach for particle characterization, we present flexible DNA nanodevices that can adapt to the curvature of the structure they are bound to. The curvature sensors use Fluorescence Resonance Energy Transfer (FRET) as the transduction mechanism on the single-molecule level. The curvature sensors consist of segmented DNA origami structures connected via flexible DNA linkers incorporating a FRET pair. The activity of the sensors was first demonstrated with defined binding to different DNA origami geometries used as templates. Then the DNA origami curvature sensors were applied to measure spherical silica beads having different size, and subsequently on lipid vesicles. With the designed sensors, we could reliably distinguish different sized nanoparticles within a size range of 50−300 nm as well as the bending angle range of 50−180°. This study helps with the development of more advanced modular-curvature sensing devices that are capable of determining the sizes of nanoparticles and biological complexes.**

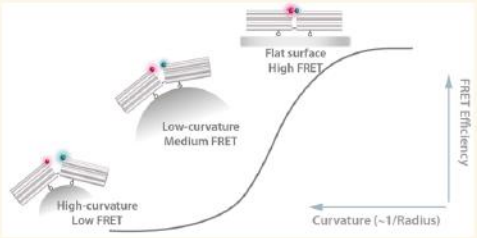

KEYWORDS: *Particle size, DNA origami, single-molecule FRET, curvature sensor, lipid vesicles*

Particle size is a comprehensive and essential parameter for many applications. Many diverse industries require particle size analysis techniques in order to characterize the materials, and eventually to manufacture high quality, safe, pure and cost-effective products. These factors make reliable and precise size measurement of nanoparticles a crucial step for nanomaterials. Particle size analysis techniques vary in terms of their working principles, quantification, or type and amount of the sample required. Some of the classical particle size analysis techniques include dynamic light scattering (DLS), laser diffraction and direct imaging techniques such as optical imaging, transmission or scanning electron microscopy (TEM or SEM). While laser diffraction method suffers from low sensitivity and resolution, DLS is an ensemble method with the similar problem of low resolution. It further has the disadvantage of being highly affected by the presence of large aggregates due to scattering intensities.[1−3] Electron microscopy techniques have the drawback of providing static snapshots as well as carrying the analysis in vacuum.[2] Moreover, conventional electron microscopy variants, such as TEM or SEM, may require additional staining, chemical fixation, or dehydration of the samples,[4] which can be a problem for biological and more fragile samples where accurate sizing requires preservation of the native hydrated state. In these cases, cryogenic EM (cryo-EM) would be a viable, albeit demanding, alternative in which a close-to-native state of the specimens can be preserved by embedding the samples in vitreous ice.[5] This EM variant, however, is typically carried out

Received: December 1, 2022
Accepted: January 31, 2023
Published: February 3, 2023

https://doi.org/10.1021/acsnano.2c11981
ACS Nano 2023, 17, 3088−3097

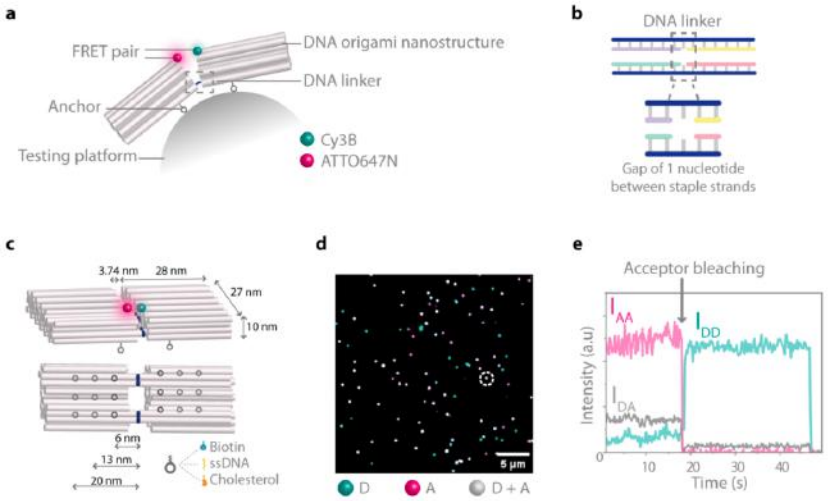

Figure 1. System definition of the curvature sensor. (a) Segmented DNA origami blocks functionalized with anchoring moieties attached to the testing platform. The FRET pair, Cy3B (donor)−ATTO647N (acceptor), is positioned at the interior edges of the blocks. (b) A schematic showing the DNA linkers between the two blocks of the curvature sensor. The DNA linkers have a gap of one nucleotide between the staple strands (c) The side and bottom views of the curvature sensor with the dimensions. The bottom view shows the alternative positions of the anchoring moieties with the distances of 6 nm, 13 nm and 20 nm to the hinge. Biotin or cholesterol moieties, or ssDNA binding sites were utilized depending on the nanostructure to be tested. (d) A superimposed TIRF image with donor dye (D) in cyan and acceptor (A) in magenta. Gray spots indicate sensor incorporating both donor and acceptor dyes. (e) An exemplary single-molecule FRET (smFRET) transient. The fluorescence intensity over time is shown for the donor excitation−donor emission I_{DD} channel (cyan), the donor excitation−acceptor emission I_{DA} channel (gray) and the acceptor excitation−acceptor emission I_{AA} channel (magenta). From the I_{DD} and the I_{DA} channels, mean FRET efficiencies are determined.

on expensive 300 kV transmission electron microscopes, and suffers from low signal-to-noise ratio.[6] It is therefore important to measure the particle size on the nanoscale by developing cost-effective, rapid, biocompatible and sufficiently precise systems, as optical techniques on submicrometer structures suffer from resolution limitations.

For spherical particles, molecular biosensors could report on particle size by measuring the curvature of the particle. Living cells, for example, measure the curvature of vesicles as well as the local curvatures of membranes, as curvature is related to function and/or assembly of molecular complexes. To this end, bacteria and eukaryotic cells contain geometry-sensing tools in their cytosol. BAR proteins, for example, recognize membrane features such as concave or convex, deep or shallow.[7] The principle is that different BAR proteins bind to specific structural features as has recently been emulated with artificial DNA origami systems.[8] To measure the size of spherical particles or local curvatures of membranes or surfaces, however, a pool of geometry-recognizing sensors would be required in combination with a transduction mechanism that reports binding of the sensors to the structure of interest.

Here, we propose an alternative approach for measuring the size of spherical particles or local surface curvature. We present DNA origami curvature sensors. These self-assembled nanodevices adapt to the shape of the particles they bind to. This adaptation is then transduced optically by a change in Fluorescence Resonance Energy Transfer (FRET), visualized on the level of single molecules.

In the DNA origami technique, a long (7000−8000 nucleotides (nt)) single-stranded DNA (ssDNA) (scaffold strand) is folded into a desired shape by hybridizing with hundreds of short (~15−50 nt) ssDNA oligonucleotides (staple strands) in a programmable way.[9−16] For DNA origami curvature sensors, we explore specific advantages of the DNA origami technique to create nanostructures with design features like well-defined rigid structures,[17−20] and flexible ones with hinges or joints.[21−27] Additionally, the modularity of the technique allows the attachment of different functional units including anchoring groups at specific sites[28−30] or incorporation of fluorescent dyes for signal transduction.[31−35]

To demonstrate the concept of a shape-adaptable DNA origami system, we used flat and curved DNA origamis as model templates (Figure S1) to which the sensors can be specifically attached through hybridization of single-stranded DNA sequences. In this way, the DNA sensors adapted to the geometry of the model templates, giving a specific readout that exploits the high distance sensitivity of FRET together with single-molecule detection. Therefore, the two sides of the segmented DNA origami structures were equipped with a Cy3B as the donor and an ATTO647N as the acceptor. As the distance between the FRET pair changes with curvature, we provide a ratiometric FRET ruler to quantitatively measure the interaction of different curvatures. Next, we extended the approach to silica particles (Figure S1) in a size range of 50−300 nm and membrane vesicles (Figure S1) employing different binding chemistries such as NeutrAvidin/biotin and cholesterol/lipid interactions. By changing the location of the

https://doi.org/10.1021/acsnano.2c11981
ACS Nano 2023, 17, 3088−3097

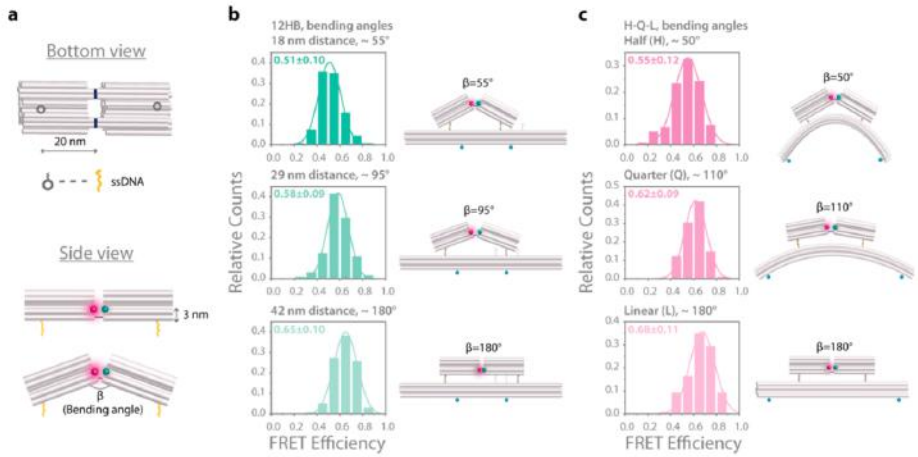

Figure 2. Curvature sensor on alternative DNA origami nanostructures. (a) The bottom and side views of the curvature sensor showing the position of the ssDNA binding site extensions as well as the fluorophores. FRET efficiency distributions of the curvature sensor on (b) 12HB nanostructures with ~55°, 95° and 180° bending angles and (c) on Half, Quarter and Linear DNA origami nanostructures with the illustrations of the sensor on those structures. The error refers to the standard deviation (SD). Number of molecules is 134 for ~55°, 128 for ~95° and 142 for ~180° bending angles on 12HBs and 120 for Half, 115 for Quarter and 136 for Linear DNA nanostructures.

FRET pair on the DNA origami curvature sensors, we showed that it is possible to tune the dynamic range of the sensor as well as the signal direction. The approach holds great promise for measuring curvature also on living cells that is currently difficult to assess by structures that probe binding geometries[8,36] or by polarization imaging.[37,38]

RESULTS AND DISCUSSION

Design and the Working Principle of the Curvature Sensor. The curvature sensor is a segmented DNA origami nanostructure consisting of two three-dimensional blocks that were connected via four DNA linkers arranged within one plane (Figure 1a). The linkers are mainly double-stranded to maintain the stiffness of the blocks and they were placed close to the edges to minimize torsional flexibility. In the middle of the DNA connectors, a gap of one nucleotide was left by the staple strands. This provides a clearly defined hinge between the stiff blocks with minimal flexural modulus as single-stranded DNA has a negligible persistence length compared to double-stranded DNA (Figures 1b and S2).

Each block has the dimensions of ~28 nm × 27 nm × 10 nm (L × W × H) and the gap between the blocks has the length of ~3.7 nm resulting in a total origami length of ~60 nm (Figure 1c). The structure displays additional modification sites. For signal transduction, a FRET pair, Cy3B as the donor and ATTO647N as the acceptor dye, was positioned at the interior edges of the two blocks. As the structure bends, the distance between the dyes changes leading to a different FRET efficiency. For the attachment of our sensor to the structures to be analyzed, anchoring moieties were incorporated. Depending on the surface chemistry of the nanostructures to be investigated, biotin or cholesterol moieties, or single-stranded DNA (ssDNA) binding sites were utilized for specific binding (Figure 1c). On each block, there are three possible anchor positions placed with the same distance to the hinge (anchors one under the other in Figure 1c). The anchors on the two blocks were positioned on different helices to prevent their face-to-face interaction that could induce unwanted closing interactions, e.g., for cholesterols.[30] Individual anchors could be placed at different marked distances from the hinge (6 nm, 13 nm and 20 nm distances to the hinge are indicated in Figure 1c), in order to adjust the dynamic range of curvatures that can be studied. Alternatively, the position of the dyes was also changed (e.g., 3 nm or 10 nm height above the hinge) to further adjust the dynamic readout range of the sensor (Appendix A, Supporting Information).

We used total internal reflection fluorescence microscopy (TIRF) to image single DNA origami curvature sensors and deduced the underlying curvature values from smFRET output. smFRET experiments were carried out on a commercial fluorescence microscope (Nanoimager S, ONI Ltd., UK), with green−red alternating laser excitation (ALEX) (see Supporting Information for details on sample preparation and imaging).[39−41] From TIRF videos, we extracted fluorescence intensity transients of individual fluorescent spots using iSMS software that is based on Matlab.[42] Figure 1d presents a superimposed false-color image with donor dye emission in cyan, acceptor dye emission in magenta and an overlay of the two resulting in gray. To ensure that identified fluorescent spots represented individual DNA origami structures, we investigated the fluorescent transients with respect to their photobleaching behavior and only considered those with single-step photobleaching for further analysis. In the exemplary transient in Figure 1e (representing the circled spot in Figure 1d), the acceptor emission after donor excitation (I_{DA}, gray) was initially high and dropped after ~18 s when photobleaching occurred. Instantaneously, the donor emission (I_{DD}, cyan), which was initially low, increased as the donor excitation energy was no longer transferred to the acceptor. Acceptor emission after acceptor excitation (I_{AA}, magenta) was also monitored to evaluate photophysical processes related to acceptor intensity fluctuations and to increase the fraction of

https://doi.org/10.1021/acsnano.2c11981
ACS Nano 2023, 17, 3088−3097

molecules with acceptor bleaching first. The FRET efficiency for each sensor was quantified from the intensity information on data channels I_{DD} (donor excitation-donor emission) and I_{DA} (donor excitation−acceptor emission) for each molecule over the whole period of the energy transfer as

$$\text{FRET efficiency} = \frac{I_{DA}}{\gamma \times I_{DD} + I_{DA}}$$

The γ correction factor accounts for the different quantum yields of the dyes and the wavelength dependent detection efficiencies of the detector. The I_{DA} is corrected for direct acceptor excitation at the donor excitation wavelength and leakage of donor emission into the acceptor emission channel. The corrected I_{DA} is calculated as

$$I_{DA} = I_{DA,raw} - D_{leakage} \times I_{DD} - A_{direct} \times I_{AA}$$

where $I_{DA,\,raw}$ is the total intensity measured in the acceptor emission channel, I_{AA} is the direct acceptor excitation. The $D_{leakage}$ accounts for the amount of leakage of the donor emission into the acceptor emission channel upon donor excitation.

At least 100 molecules were analyzed per sample in the same way to have sufficient statistical accuracy and the FRET efficiencies were presented in histograms together with Gaussian fits where applicable.

Sensor on DNA Nanostructures. Taking advantage of the uniformity and handiness of DNA nanostructures, we started by investigating the curvature sensors against various DNA origami templates. Here, the attachment of the sensors to the origami templates was achieved with the help of complementary single-stranded DNA extension modifications, following a zipper conformation for tighter binding.[43]

To enable a larger range of bending angles (from ~50° to 180°), we placed the ssDNA extensions on the curvature sensors at the 20 nm positions from the hinge. As the testing platforms included only two binding sites, we used one anchor per block on the curvature sensors (Figure 2a). In order to be sensitive in the related bending angle range, the FRET pair was placed at a 3 nm height from the hinge (based on expected calculations described in Appendix A, Supporting Information, see Figure S-A2).

As the first testing platform, we chose a 12-helix bundle (12HB) DNA origami nanostructure.[44] Three 12HBs were prepared with DNA extensions acting as binding sites for the curvature sensors separated by 18 nm, 29 nm and 42 nm, respectively. These placements force the curvature sensor to adapt different conformations with corresponding bending angles of 55°, 95° and 180° (see the schemes in Figure 2b). After the immobilization of 12HBs on functionalized glass coverslips, the curvature sensors with complementary DNA extensions were incubated on them until an optimum surface coverage was achieved (see Supporting Information, Section 1.1 and Section 1.4.2 for the details of sample preparation).

smFRET analysis revealed that the sensors successfully bound to the 12HB nanostructures and showed mean FRET efficiencies of 0.51 ± 0.10 (standard deviation of the mean, SD) for 55°, 0.58 ± 0.09 for 95° and 0.65 ± 0.10 for 180° bending angles (Figure 2b). These homogeneous populations exhibiting clear shifts with respect to each other clearly proved that the curvature sensors report on the properties of the structure they are binding to.

All-in-all, the experimental FRET efficiencies for the bent curvature sensors were similar to the expected FRET values shown in Figure S-A2. However, the value of the flat sensor for the bending angle of 180° was substantially lower than the expected FRET efficiency of 0.9. We assume that the conformational freedom including torsional and bending motions increased the average distance between donor and acceptor. Torsions might be likely in this construct as the attachment occurred only by one binding strand on each side. Further control experiments using flat curvature sensors also indicated noticeable reduced FRET efficiencies induced by photophysical effects such as dye−dye interactions, as the conformational flexibility does not prevent touching of dyes in this conformation. Details on these experiments and indications for direct dye−dye interactions are discussed in the Supporting Information (Appendix B).

In addition to the 12HB templates, the curvature sensor was subsequently tested against BAR (Bin/Amphiphysin/Rvs) domain mimicking DNA origami nanostructures, previously designed and published by Franquelim et al.[8] These include one linear (Linear) and two curved (Half and Quarter) DNA origami nanostructures with different curvature values. Utilizing those nanostructures allowed us to test the curvature sensor on intrinsically curved and stiff platforms. The curvature angle of the Half (131°) and Quarter (73°) DNA nanostructures corresponded to the bending angles of ~50° and ~110° on the curvature sensor, respectively. The ssDNA binding sites were positioned on these nanostructures at suitable distances for the attachment of the curvature sensors via DNA hybridization with the anchors of complementary sequence at 20 nm distance to the hinge. As the binding platform became more linear, the shorter distance between the dyes on the sensor prompted higher FRET values. According to the smFRET data, the sensor once again met the expectations and showed alterations toward higher FRET efficiencies from Half- to Linear DNA nanostructures with the data of 0.55 ± 0.12 for Half, 0.62 ± 0.09 for Quarter and 0.68 ± 0.11 for Linear nanostructures (Figure 2c). An equitable lower FRET contrast issue as in the case of 12HB with 180° bending angle was also observed with the Linear DNA nanostructure. With the data supporting each other, it can be deduced that due to certain conformational distortions, the curvature sensor cannot be attached in a perfectly flat conformation. Also, in consequence of dyes getting closer to each other, their interactions induce lower mean FRET efficiencies due to photophysical effects.[45]

In summary, our experimental data (with Förster Radius, R_0 = 7.1) fit very well with the theoretical predictions (expecting R_0 = 6.7[46]), with the small disparities putatively arising from possible spectral and orientation deviations (Figure S3-a). Considering the experimental FRET efficiency values between ~0.4 and 0.6, the curvature sensor successfully distinguished the small differences in the most sensitive FRET range around 0.5.

We further questioned whether the width of the FRET efficiency distributions could be affected from the presence of curvature sensors binding to the testing platforms with only one of the blocks. Since leaving the other block free to move would affect the FRET distributions, we aimed to prove the complete binding of the curvature sensors to the testing platforms with both of the blocks. In this direction, a control experiment was performed with the curvature sensors modified with ssDNA anchors only on one of the blocks. The sensors

https://doi.org/10.1021/acsnano.2c11981
ACS Nano 2023, 17, 3088−3097

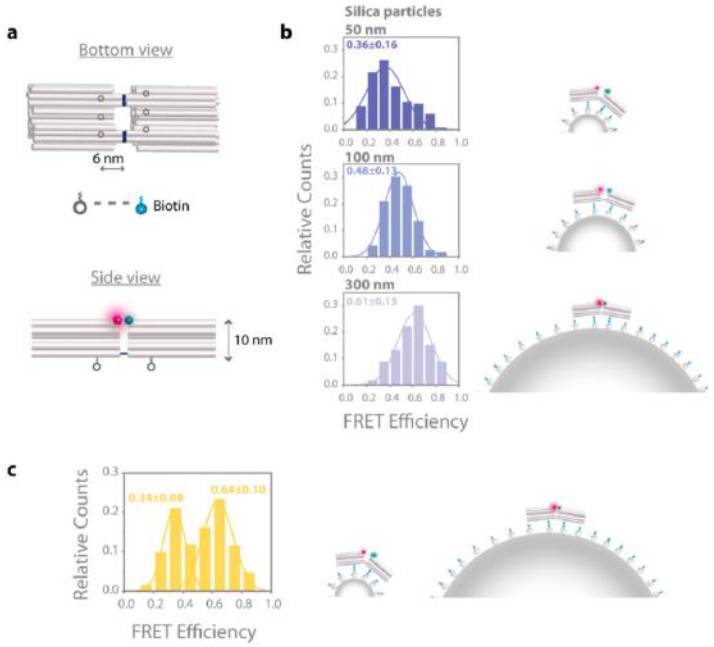

Figure 3. Curvature sensor on silica particles. (a) The bottom and side views of the curvature sensor showing the positions of the biotin anchors as well as the fluorophores. (b) FRET efficiency distributions for the curvature sensor on silica particles of 50 nm, 100 nm and 300 nm (from top to bottom) with the illustrations of the sensor on the particles of corresponding sizes. (c) FRET efficiency distributions of the curvature sensor on a surface covered by a mixture of 50 nm and 300 nm silica particles. The error refers to the standard deviation (SD). Number of molecules is 134 for 50 nm, 119 for 100 nm, 113 for 300 nm and 253 for the mixture of 50 nm and 300 nm silica particles.

were anchored on Half, Quarter and Linear DNA nanostructures via DNA hybridization at the binding sites. As the freely moving block without any anchor could adapt different conformations due to bending and rotation of the two DNA origamis with respect to each other, we obtained fairly broad FRET histograms (Figure S4) which are clearly different from the previous data where both of the blocks were equipped with ssDNA anchors (Figure 2c). This control experiment confirmed the complete binding of the vast majority of the curvature sensors with the anchors on both of the blocks. Still, a small fraction of the sensors binding to the testing platforms with only one block could be counted as a factor to broaden the FRET distributions. Especially if the binding site distances might slightly differ due to certain twists or flexibilities of the testing platforms, one of the blocks of the curvature sensor might be incapable of binding resulting in deviations from the expected FRET efficiencies. A similar scenario might occur in case the sensor or the testing platforms are missing some of the binding sites due to the fact that they are not incorporated or that they are not addressable all the time.[47]

Sensor on Silica Nanoparticles. Next, we used the DNA origami curvature sensors to study silica nanoparticles with different mean diameters. Despite displaying a size distribution, silica nanoparticles are fairly homogeneous. As part of the increasing complexity of systems studied with the curvature sensors, silica particles do not exhibit binding sites at defined positions but distributed over the surface. Modification of silica particles with biotinylated BSA allowed us to immobilize them on glass coverslips as well as to provide a specific binding chemistry for curvature sensors having biotin anchors.

First, silica particles modified with biotinylated BSA were immobilized on a passivated and functionalized glass coverslip. When the immobilized particles were further covered with NeutrAvidin, the curvature sensors could be anchored on them via biotin anchor (Supporting Information, Section 1.2 and Section 1.4.3 for the details of sample preparation). As the anchoring strategy might lead to off-target binding to the Neutravidin coated glass coverslips in addition to the functionalized silica particles, we estimated the amount needed to cover the glass coverslips with a dilution experiment. The sensor was tested on glass coverslips covered with 100 nm silica particles of 1/100, 1/20 and 1/10 dilution. Accordingly, we observed that silica particles of 1/10 dilution were required to have a sufficiently covered surface where off-target binding to the glass surface is minimized (Figure S5). Due to presence of multiple binding sites on silica particles, three biotin anchors on each block at 6 nm distance to the hinge were utilized on the sensors in order to increase the binding probability (Figure 3a).

We performed smFRET measurements on the curvature sensor with three different sizes of silica particles (50 nm, 100 nm and 300 nm). The range of these silica particles corresponded to a relatively narrow bending angle range (100−170°). In order to increase the sensitivity of the

https://doi.org/10.1021/acsnano.2c11981
ACS Nano 2023, 17, 3088−3097

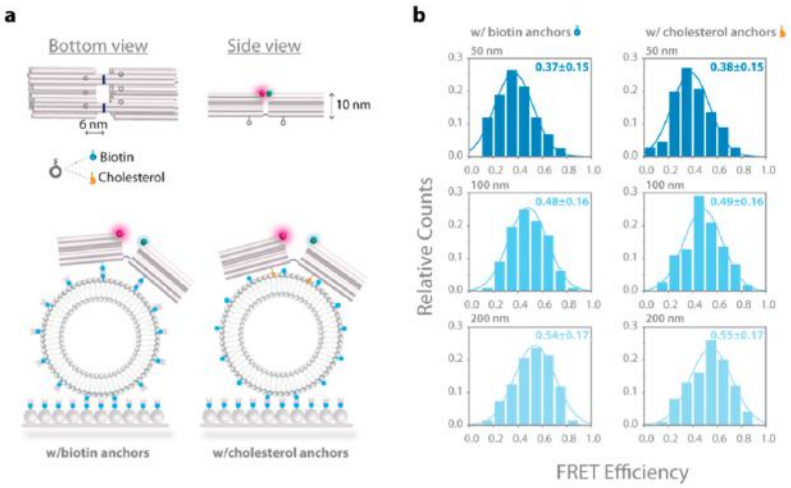

Figure 4. Curvature sensor on lipid vesicles. (a) The bottom and side views of the curvature sensor showing the position of the anchors (biotin or cholesterol) as well as the fluorophores together with the sketches of the sensor on biotinylated lipid vesicles anchored via biotin or cholesterol anchors. (b) FRET efficiency distributions of the curvature sensor on lipid vesicles of 50 nm, 100 nm and 200 nm (from top to bottom) anchored via biotin and cholesterol anchors. The error refers to the standard deviation (SD). Number of molecules is 117 for 50 nm, 112 for 100 nm and 136 for 200 nm lipid vesicles that were tested with biotin anchors and 111 for 50 nm, 110 for 100 nm and 100 for 200 nm lipid vesicles tested with cholesterol anchors.

curvature sensor in this range, we shifted the FRET pair from its initial position of 3 nm height to 10 nm (Figure 3a and Figure S-A2).

From the Gaussian fits of the smFRET histograms, we obtained mean FRET efficiencies of 0.36 ± 0.16 for 50 nm, 0.48 ± 0.13 for 100 nm and 0.61 ± 0.15 for 300 nm silica particles (Figure 3b). These distributions with apparent shifts with respect to each other further corroborated the reliability of the curvature sensor to sense different degrees of curvature. The data also proves that any possible off-target binding to the passivated glass coverslips is minimized as we have well-defined and separated distributions on silica particles of different sizes. On the contrary, the sensor gives a very broad distribution when it binds to the NeutrAvidin functionalized glass coverslips as shown in the distribution in Figure S5-a. Additionally, the sensor was tested on a surface covered with a mixture of 50 nm and 300 nm silica particles. The results displayed two distinguishable fits with defined mean FRET efficiencies, which were matching with the individual silica particles (Figure 3c). This clearly demonstrates the ability of the curvature sensor to resolve two significantly distinct size populations of nanoparticles. Compared to the results obtained with the sensors against DNA nanostructures, broader FRET distributions were observed with silica particles, which is reflected in the increased standard deviations. We analyzed the size of the silica particles by TEM measurements (see Supporting Information, Section 2.1 for the details of TEM characterization) and noticed overall substantial heterogeneity that was, however, less pronounced for the size distributions of larger silica particles. It is visible in the TEM images that the silica particles become more monodisperse and more spherical as their size gets bigger (Figure S6).

To demonstrate the tunability of the sensor, we next reversed the working principle of the curvature sensor by changing the position of the FRET pair. For that, the dyes were placed close to the height of the hinge but moved apart horizontally to a distance of ~7.5 nm (see sketch in Figure S7). The idea of this design was that the dyes would come closer as the structure bends. We tested this approach on silica particles of 100 nm and 300 nm as well as on a functionalized glass coverslip. The sensor showed the highest mean FRET efficiency value of 0.56 ± 0.14 and a lower FRET efficiency of 0.48 ± 0.11 on the curved surfaces of 100 nm and 300 nm silica particles, respectively. The lowest value of 0.27 ± 0.10 on the functionalized glass coverslip (Figure S7) underlines our model of how the curvature sensor works and shows how it can be tuned in a FRET-ON or FRET-OFF configuration.

Sensor on Lipid Vesicles. Finally, we applied our curvature sensor to lipid vesicles. Along with their use in targeting, drug delivery and encapsulation of biomolecules, lipid vesicles are utilized as simplified models of biological membranes and are therefore of superior interest as targets of curvature sensors. By virtue of their similarity to cellular membranes, lipid vesicles are perfect models to gain insight into existing biosystems, or the functioning, emergence and evolution of cells.[48] In contrast to the structures studied before, lipid vesicles are very soft, posing the challenge that curvature sensors have to adapt to the shape of the vesicles and should not influence their shape.

In order to make the sensors reliably work with lipid vesicles, we had to change the buffer conditions since the amount of Mg^{2+} ions present in our typical buffers enhanced the interaction probability between the vesicles, which could lead to changes in their size distributions due to vesicle fusion.[49−51] On the other hand, presence of positively charged ions is

https://doi.org/10.1021/acsnano.2c11981
ACS Nano 2023, 17, 3088−3097

crucial for the stability of DNA origami nanostructures.[13,52,53] After screening different salt concentrations, we found 650 mM NaCl in the buffer as optimal for both vesicle and DNA origami stability. As lipid vesicle models, large unilameller vesicles (LUVs) were used. LUVs composed of 99% DOPC (1,2-dioleoyl-*sn*-glycero-3-phosphocholine) and 1% Biotinyl-cap-PE (1,2-dioleoyl-*sn*-glycero-3-hosphoethanolamine-*N*-(cap-biotinyl)), were obtained from rehydration of a lipid film, followed by extrusion of the lipid vesicle suspension.[54−56] The curvature sensors were tested on LUVs of different sizes; that were produced by extrusion through membrane filters with 50 nm, 100 nm and 200 nm pore diameters. In the extrusion process, vesicles smaller than the pore size of the filter can pass so that the polydispersity of the vesicle mixture increases with larger pore sizes of membranes.[55,57,58] The extruded vesicles were characterized by DLS measurements (see Supporting Information, Section 2.2 for the details) yielding mean number-normalized diameters of 69.48 ± 3.43 (SD of the mean) nm for vesicles extruded with the 50 nm size filters and 92.16 ± 4.28 nm for vesicles extruded with the 100 nm size filters. For vesicles extruded using a larger 200 nm size filter, however, we did not obtain a reasonable mean number-normalized diameter likely because of the increased polydispersity (Figure S8).

After diluting the number of liposomal particles to ~100 pM, the biotin-labeled lipid vesicles were attached to functionalized glass coverslips and further covered with NeutrAvidin. The curvature sensors then attached to the vesicles via biotin anchors (Figure 4a). The detailed protocols for the preparation of lipid vesicles and the surfaces are provided in Supporting Information, Section 1.3 and Section 1.4.4. Figure 4b shows the FRET distributions with mean FRET efficiencies of 0.37 ± 0.15, 0.48 ± 0.16 and 0.54 ± 0.17 for vesicle suspensions extruded using 50 nm, 100 nm and 200 nm filters, respectively. As supported by the relatively higher standard deviations, our foresight of polydispersity for vesicles was confirmed with the obtained broader distributions compared to the previous experiments with the rigid and more uniform testing platforms. However, recalling the mean FRET efficiencies of 0.36 ± 0.16 for 50 nm and 0.48 ± 0.13 for 100 nm silica particles, both results for silica particles and lipid vesicles are in good agreement. In addition, the distribution of 200 nm lipid vesicles showed a shift toward higher mean FRET efficiency still being smaller than the mean FRET efficiency of 300 nm silica particles.

We rationalized the experimental results for the spherical structures (silica particles and lipid vesicles) by comparing to the expected values. Figure S3-b shows the FRET efficiency values vs measured particle diameters of silica particles (obtained from the TEM data) and vesicles (obtained from the DLS data). Experimental estimations for lower and upper limits for the curvature sensor are also possible from the calibration curves that we provide in Figure S3-b. The fit shows that FRET efficiency drops below 10% for particles smaller than 36 nm making the analysis of smFRET traces unreliable which is consistent with the theoretical calculations for the lower limit. In addition, the fit starts to flatten for particles larger than 300 nm indicating the upper limit of the sensor. For the spherical structures the deviations to the calculations are more pronounced than for the DNA origami model templates which is likely related to the heterogeneities of particles and vesicles as also indicated by the broader FRET distributions. In addition, for high FRET the photophysical dye−dye interactions again prevent the occurrence of very high FRET values.

Finally, we tested anchoring the sensor onto lipid vesicles via cholesterol moieties which is a more common and compatible anchoring strategy and does not require chemical modification of the lipid membrane investigated.[59,60] FRET distributions obtained after cholesterol binding to lipid vesicles were very similar to the distributions obtained with biotin anchors (Figure 4b). The identical results of two different anchoring strategies with the fact that cholesterol cannot bind to the NeutrAvidin coated glass surface further support our statements for the minimized off-target binding. All these results confirmed the robustness as well as the reproducibility of curvature sensor experiments. The values obtained for the vesicles matching the values of solid nanoparticles indicate that the DNA origami fully adapt to the shape of the underlying structure and do not impose a measurable deformation even on soft nanostructures such as vesicles.

CONCLUSION

Nanoparticles are typically characterized by DLS, electron microscopy and other spectroscopic and imaging methods. Single-particle methods can be advantageous to directly reveal and characterize particle heterogeneities often critical for particle applications. Using DNA origami nanotechnology, we created here a set of adaptable curvature sensors displaying two rigid arms, a floppy hinge and distinct binding positions at a defined distance to the hinge. In combination with single-molecule FRET readout, this strategy enables a fundamentally different approach to curvature sensing. We demonstrated our sensing devices on DNA origami templates with different geometries, solid silica particles and large unilamellar vesicles. Different interaction chemistries were employed including DNA hybridization, biotin-NeutrAvidin and cholesterol insertion into lipid membranes, and the sensor stability was tested at different salt concentrations of, e.g., NaCl and $MgCl_2$. In all cases, the expected tendency of FRET-values was observed. Besides adapting the attachment chemistry, the modular design of the DNA origami curvature sensor enabled adaptation of the dynamic range by simple measures such as the position of the attachment chemistry and the position of the FRET pair. Depending on the FRET pair position, the response of the sensor could even be reversed. Besides measuring the size of nanoparticles, our controllable nano-devices could in future be used for studying cell membrane remodeling in intra- and extracellular processes, among other biological applications. The possibility to observe dynamic membrane changes could, e.g., be demonstrated by osmotic swelling of vesicles and visualizing the swelling with the membrane curvature sensors. Similarly, sensors that bind from the inside to the membrane of endocytic vesicles could yield further insight into the fate of internalized vesicles. Curvatures on cell membranes could also be correlated with the accumulation of protein complexes and receptors opening another window into the biophysics of membranes.

MATERIALS AND METHODS

Design, Production and Characterization of the DNA Origami Nanostructures. The curvature sensors were designed using caDNAno (version 2.2.0),[12] and the initial 3D models were predicted using CanDo.[13,61] The design utilizes the p7560 scaffold derived from M13mp18 bacteriophage and includes labeled positions for attaching fluorophores and anchoring moieties. Folding of all the

https://doi.org/10.1021/acsnano.2c11981
ACS Nano 2023, 17, 3088−3097

DNA origami structures was performed in a one-pot reaction mix of the scaffold DNA and unmodified/modified oligonucleotides, which was then subjected to a multistep thermocycler protocol. Purification of the folded curvature sensors was performed by gel electrophoresis. Besides the curvature sensors, all the DNA origami nanostructures that were used as model templates were prepared as explained in the Supporting Information. Further details of the DNA-origami structures, sample preparation and purification can be found in Supporting Information, Section 1.1. The correct folding of the DNA origami nanostructures was characterized with transmission electron microscopy (TEM) (Figure S9). The details of TEM characterization are in Supporting Information, Section 2.1.

Surface Preparation. For surface preparation, 150 μL SecureSeal Hybridization Chambers (Grace Bio-Laboratories) were glued on cleaned glass coverslips and the surfaces were passivated with biotinylated-BSA (1.0 mg/mL) and functionalized with NeutrAvidin (1.0 mg/mL, Thermo Fisher Scientific Inc.) for further modifications. The details of the preparation of different surfaces which are flat, with DNA origami nanostructures, with silica particles and with lipid vesicles can be found in Supporting Information, Section 1.4.

Imaging and Data Analysis. For the fluorescence measurements on the DNA origami nanostructures, with silica particles and on a flat surface, the buffer was exchanged to the FRET buffer containing a reducing and oxidizing system (ROXS)[62,63] as well as oxygen scavenging agents in order to increase the photostability of the fluorophores. In particular, we used trolox/troloxquinone as the reducing and oxidizing system in a 10 mM Tris−HCl, 1 mM EDTA buffer with 1% (wt/v) D-(+)-glucose (Sigma-Aldrich, USA), 165 units/mL glucose oxidase (G2133, Sigma-Aldrich, USA), 2170 units/mL catalase (C3155, Sigma-Aldrich, USA), 1 mM Trolox (~12% was aged under UV light) and 12.5 mM $MgCl_2$. LUV buffer containing 5 mM Tris−HCl, 1 mM EDTA, 0.5 mM Trolox and 650 mM NaCl, pH 7.0, was used for the smFRET measurements with lipid vesicles.

The smFRET measurements of the curvature sensor were performed on a commercial fluorescence microscope, Nanoimager S (ONI Ltd., UK), with TIRF illumination. The light program was set to alternating laser excitation of red (~20 mW) and green (~15 mW) lasers. For each sample, ~10−20 videos were acquired in a large field of view (50 μm × 80 μm) with 100 ms exposure time with a length of 500 frames. For the smFRET data analysis, the iSMS software that is based on Matlab[42] was used. Intensity time traces of individual immobilized molecules were extracted from each of the movies. These single-molecule transients were analyzed and the individual transients showing FRET were picked for the intensity based mean FRET efficiency calculation. Further details of the imaging and data analysis can be found in Supporting Information, Section 3.

ASSOCIATED CONTENT

Supporting Information

The Supporting Information is available free of charge at https://pubs.acs.org/doi/10.1021/acsnano.2c11981.

Materials and methods, details of DNA origami nanostructures, sample preparation, characterization techniques, imaging and data analysis, list of buffers, list of DNA oligonucleotides, theoretical calculations, experiments on flat conformation (PDF)

AUTHOR INFORMATION

Corresponding Authors

Henri G. Franquelim − *Max Planck Institute of Biochemistry, 82152 Martinsried, Germany; Interfaculty Centre for Bioactive Matter, Leipzig University, 04109 Leipzig, Germany;* orcid.org/0000-0001-6229-4276; Email: henri.franquelim@uni-leipzig.de

Philip Tinnefeld − *Department of Chemistry and Center for NanoScience, Ludwig-Maximilians-University, 81377 Munich, Germany;* orcid.org/0000-0003-4290-7770; Email: philip.tinnefeld@cup.lmu.de

Authors

Ece Büber − *Department of Chemistry and Center for NanoScience, Ludwig-Maximilians-University, 81377 Munich, Germany;* orcid.org/0000-0001-7495-4059

Tim Schröder − *Department of Chemistry and Center for NanoScience, Ludwig-Maximilians-University, 81377 Munich, Germany*

Michael Scheckenbach − *Department of Chemistry and Center for NanoScience, Ludwig-Maximilians-University, 81377 Munich, Germany*

Mihir Dass − *Faculty of Physics and Center for NanoScience, Ludwig-Maximilians-University, 80539 Munich, Germany*

Complete contact information is available at: https://pubs.acs.org/10.1021/acsnano.2c11981

Notes

The authors declare no competing financial interest.

ACKNOWLEDGMENTS

This work was funded by the Deutsche Forschungsgemeinschaft (DFG, German Research Foundation) − Project-ID 201269156 − SFB 1032 (A13) and the Bavarian Ministry of Science and the Arts through the ONE MUNICH Project "Munich Multiscale Biofabrication". The authors thank Tim Liedl/Joachim Rädler (Ludwig-Maximilians-University, Faculty of Physics, Munich, Germany) for providing access to their facilities, especially to the transmission electron microscope. H.G.F. thanks Petra Schwille (MPI Biochemistry, Martinsried, Germany), the Max Planck Society, as well as the financial support by the DFG (project-ID 111166240 − SFB 863 (B10)) and the STARK project 46SKD023X (Federal Ministry for Economic Affairs and Energy (BMWi) and Saxon State Ministry of Science and Art (SMWK)). E.B. thanks Renukka Yaadav, Lorena Manzanares, and Viktorija Glembockytė for the fruitful discussions and Alan Szalai for his help with software.

REFERENCES

(1) Berne, B. J.; Pecora, R.*Dynamic Light Scattering*; Dover Publications: 2000; p 376.

(2) Merkus, H. G.*Particle Size Measurements*, 1 ed.; Springer: Dordrecht, 2009; p XII, 534.

(3) Stetefeld, J.; McKenna, S. A.; Patel, T. R. Dynamic light scattering: a practical guide and applications in biomedical sciences. *Biophysical Reviews* **2016**, *8* (4), 409−427.

(4) Castón, J. R.Conventional Electron Microscopy, Cryo-Electron Microscopy and Cryo-Electron Tomography of Viruses. In *Structure and Physics of Viruses: An Integrated Textbook*; Mateu, M. G., Ed., Springer Netherlands: Dordrecht, 2013; pp 79−115.

(5) Doerr, A. Cryo-electron tomography. *Nat. Methods* **2017**, *14* (1), 34.

(6) Skiniotis, G.; Southworth, D. R. Single-particle cryo-electron microscopy of macromolecular complexes. *Microscopy (Oxf)* **2016**, *65* (1), 9−22.

(7) Antonny, B. Mechanisms of Membrane Curvature Sensing. *Annu. Rev. Biochem.* **2011**, *80* (1), 101−123.

(8) Franquelim, H. G.; Khmelinskaia, A.; Sobczak, J.-P.; Dietz, H.; Schwille, P.Membrane sculpting by curved DNA origami scaffolds. *Nat. Commun.***2018**, *9* (1). DOI: 10.1038/s41467-018-03198-9.

(9) Seeman, N. C.; Belcher, A. M. Emulating biology: Building nanostructures from the bottom up. *Proc. Natl. Acad. Sci. U. S. A.* **2002**, *99* (suppl_2), 6451−6455.

(10) Rothemund, P. W. K. Folding DNA to create nanoscale shapes and patterns. *Nature* **2006**, *440* (7082), 297−302.
(11) Douglas, S. M.; Dietz, H.; Liedl, T.; Högberg, B.; Graf, F.; Shih, W. M. Self-assembly of DNA into nanoscale three-dimensional shapes. *Nature* **2009**, *459* (7245), 414−418.
(12) Douglas, S. M.; Marblestone, A. H.; Teerapittayanon, S.; Vazquez, A.; Church, G. M.; Shih, W. M. Rapid prototyping of 3D DNA-origami shapes with caDNAno. *Nucleic Acids Res.* **2009**, *37* (15), 5001−5006.
(13) Castro, C. E.; Kilchherr, F.; Kim, D.-N.; Shiao, E. L.; Wauer, T.; Wortmann, P.; Bathe, M.; Dietz, H. A primer to scaffolded DNA origami. *Nat. Methods* **2011**, *8* (3), 221−229.
(14) Wang, P.; Meyer, T. A.; Pan, V.; Dutta, P. K.; Ke, Y. The Beauty and Utility of DNA Origami. *Chem.* **2017**, *2* (3), 359−382.
(15) Wagenbauer, K. F.; Engelhardt, F. A. S.; Stahl, E.; Hechtl, V. K.; Stömmer, P.; Seebacher, F.; Meregalli, L.; Ketterer, P.; Gerling, T.; Dietz, H. How We Make DNA Origami. *ChemBioChem.* **2017**, *18* (19), 1873−1885.
(16) Dey, S.; Fan, C.; Gothelf, K. V.; Li, J.; Lin, C.; Liu, L.; Liu, N.; Nijenhuis, M. A. D.; Saccà, B.; Simmel, F. C.; Yan, H.; Zhan, P., DNA origami. *Nat. Rev. Method. Primers***2021**, *1* (1). DOI: 10.1038/s43586-020-00009-8.
(17) Dietz, H.; Douglas, S. M.; Shih, W. M. Folding DNA into Twisted and Curved Nanoscale Shapes. *Science* **2009**, *325* (5941), 725−730.
(18) Acuna, G. P.; Moller, F. M.; Holzmeister, P.; Beater, S.; Lalkens, B.; Tinnefeld, P. Fluorescence Enhancement at Docking Sites of DNA-Directed Self-Assembled Nanoantennas. *Science* **2012**, *338* (6106), 506−510.
(19) Nickels, P. C.; Wünsch, B.; Holzmeister, P.; Bae, W.; Kneer, L. M.; Grohmann, D.; Tinnefeld, P.; Liedl, T. Molecular force spectroscopy with a DNA origami−based nanoscopic force clamp. *Science* **2016**, *354* (6310), 305−307.
(20) Sigl, C.; Willner, E. M.; Engelen, W.; Kretzmann, J. A.; Sachenbacher, K.; Liedl, A.; Kolbe, F.; Wilsch, F.; Aghvami, S. A.; Protzer, U.; Hagan, M. F.; Fraden, S.; Dietz, H. Programmable icosahedral shell system for virus trapping. *Nat. Mater.* **2021**, *20*, 1281.
(21) Andersen, E. S.; Dong, M.; Nielsen, M. M.; Jahn, K.; Subramani, R.; Mamdouh, W.; Golas, M. M.; Sander, B.; Stark, H.; Oliveira, C. L. P.; Pedersen, J. S.; Birkedal, V.; Besenbacher, F.; Gothelf, K. V.; Kjems, J. Self-assembly of a nanoscale DNA box with a controllable lid. *Nature* **2009**, *459* (7243), 73−76.
(22) Liedl, T.; Högberg, B.; Tytell, J.; Ingber, D. E.; Shih, W. M. Self-assembly of three-dimensional prestressed tensegrity structures from DNA. *Nat. Nanotechnol.* **2010**, *5* (7), 520−524.
(23) Zhou, L.; Marras, A. E.; Su, H.-J.; Castro, C. E. DNA Origami Compliant Nanostructures with Tunable Mechanical Properties. *ACS Nano* **2014**, *8* (1), 27−34.
(24) Marras, A. E.; Zhou, L.; Su, H.-J.; Castro, C. E. Programmable motion of DNA origami mechanisms. *Proc. Natl. Acad. Sci. U. S. A.* **2015**, *112* (3), 713−718.
(25) Funke, J. J.; Dietz, H. Placing molecules with Bohr radius resolution using DNA origami. *Nat. Nanotechnol.* **2016**, *11* (1), 47−52.
(26) Shi, Z.; Castro, C. E.; Arya, G. Conformational Dynamics of Mechanically Compliant DNA Nanostructures from Coarse-Grained Molecular Dynamics Simulations. *ACS Nano* **2017**, *11* (5), 4617−4630.
(27) Lee, C.; Lee, J. Y.; Kim, D.-N.Polymorphic design of DNA origami structures through mechanical control of modular components. *Nat. Commun.***2017**, *8* (1). DOI: 10.1038/s41467-017-02127-6.
(28) Czogalla, A.; Petrov, E. P.; Kauert, D. J.; Uzunova, V.; Zhang, Y.; Seidel, R.; Schwille, P. Switchable domain partitioning and diffusion of DNA origami rods on membranes. *Faraday Discuss.* **2013**, *161*, 31−43.
(29) Burns, J. R.; Göpfrich, K.; Wood, J. W.; Thacker, V. V.; Stulz, E.; Keyser, U. F.; Howorka, S. Lipid-Bilayer-Spanning DNA Nanopores with a Bifunctional Porphyrin Anchor. *Angew. Chem.* **2013**, *125* (46), 12291−12294.
(30) List, J.; Weber, M.; Simmel, F. C. Hydrophobic Actuation of a DNA Origami Bilayer Structure. *Angew. Chem., Int. Ed.* **2014**, *53* (16), 4236−4239.
(31) Zanacchi, F. C.; Manzo, C.; Alvarez, A. S.; Derr, N. D.; Garcia-Parajo, M. F.; Lakadamyali, M. A DNA origami platform for quantifying protein copy number in super-resolution. *Nat. Methods* **2017**, *14* (8), 789−792.
(32) Domljanovic, I.; Carstens, A.; Okholm, A.; Kjems, J.; Nielsen, C. T.; Heegaard, N. H. H.; Astakhova, K., Complexes of DNA with fluorescent dyes are effective reagents for detection of autoimmune antibodies. *Sci. Rep.***2017**, *7* (1). DOI: 10.1038/s41598-017-02214-0.
(33) Trofymchuk, K.; Glembockyte, V.; Grabenhorst, L.; Steiner, F.; Vietz, C.; Close, C.; Pfeiffer, M.; Richter, L.; Schütte, M. L.; Selbach, F.; Yaadav, R.; Zähringer, J.; Wei, Q.; Ozcan, A.; Lalkens, B.; Acuna, G. P.; Tinnefeld, P., Addressable nanoantennas with cleared hotspots for single-molecule detection on a portable smartphone microscope. *Nat. Commun.***2021**, *12* (1). DOI: 10.1038/s41467-021-21238-9.
(34) Ochmann, S. E.; Joshi, H.; Büber, E.; Franquelim, H. G.; Stegemann, P.; Saccà, B.; Keyser, U. F.; Aksimentiev, A.; Tinnefeld, P. DNA Origami Voltage Sensors for Transmembrane Potentials with Single-Molecule Sensitivity. *Nano Lett.* **2021**, *21*, 8634.
(35) Pfeiffer, M.; Trofymchuk, K.; Ranallo, S.; Ricci, F.; Steiner, F.; Cole, F.; Glembockyte, V.; Tinnefeld, P. Single antibody detection in a DNA origami nanoantenna. *iScience* **2021**, *24* (9), 103072.
(36) Bassereau, P.; Jin, R.; Baumgart, T.; Deserno, M.; Dimova, R.; Frolov, V. A.; Bashkirov, P. V.; Grubmüller, H.; Jahn, R.; Risselada, H. J.; Johannes, L.; Kozlov, M. M.; Lipowsky, R.; Pucadyil, T. J.; Zeno, W. F.; Stachowiak, J. C.; Stamou, D.; Breuer, A.; Lauritsen, L.; Simon, C.; Sykes, C.; Voth, G. A.; Weikl, T. R. The 2018 biomembrane curvature and remodeling roadmap. *J. Phys. D: Appl. Phys.* **2018**, *51* (34), 343001.
(37) Kabbani, A. M.; Kelly, C. V. The Detection of Nanoscale Membrane Bending with Polarized Localization Microscopy. *Biophys. J.* **2017**, *113* (8), 1782−1794.
(38) De Martino, S.; Zhang, W.; Klausen, L.; Lou, H.-Y.; Li, X.; Alfonso, F. S.; Cavalli, S.; Netti, P. A.; Santoro, F.; Cui, B. Dynamic Manipulation of Cell Membrane Curvature by Light-Driven Reshaping of Azopolymer. *Nano Lett.* **2020**, *20* (1), 577−584.
(39) Kapanidis, A. N.; Laurence, T. A.; Lee, N. K.; Margeat, E.; Kong, X.; Weiss, S. Alternating-Laser Excitation of Single Molecules. *Acc. Chem. Res.* **2005**, *38* (7), 523−533.
(40) Lee, N. K.; Kapanidis, A. N.; Wang, Y.; Michalet, X.; Mukhopadhyay, J.; Ebright, R. H.; Weiss, S. Accurate FRET Measurements within Single Diffusing Biomolecules Using Alternating-Laser Excitation. *Biophys. J.* **2005**, *88* (4), 2939−2953.
(41) Margeat, E.; Kapanidis, A. N.; Tinnefeld, P.; Wang, Y.; Mukhopadhyay, J.; Ebright, R. H.; Weiss, S. Direct Observation of Abortive Initiation and Promoter Escape within Single Immobilized Transcription Complexes. *Biophys. J.* **2006**, *90* (4), 1419−1431.
(42) Preus, S.; Noer, S. L.; Hildebrandt, L. L.; Gudnason, D.; Birkedal, V. iSMS: single-molecule FRET microscopy software. *Nat. Methods* **2015**, *12* (7), 593−594.
(43) Vietz, C.; Lalkens, B.; Acuna, G. P.; Tinnefeld, P. Functionalizing large nanoparticles for small gaps in dimer nanoantennas. *New J. Phys.* **2016**, *18*, 045012.
(44) Derr, N. D.; Goodman, B. S.; Jungmann, R.; Leschziner, A. E.; Shih, W. M.; Reck-Peterson, S. L. Tug-of-War in Motor Protein Ensembles Revealed with a Programmable DNA Origami Scaffold. *Science* **2012**, *338* (6107), 662−665.
(45) Schröder, T.; Scheible, M. B.; Steiner, F.; Vogelsang, J.; Tinnefeld, P. Interchromophoric Interactions Determine the Maximum Brightness Density in DNA Origami Structures. *Nano Lett.* **2019**, *19* (2), 1275−1281.
(46) Bartnik, K.; Barth, A.; Pilo-Pais, M.; Crevenna, A. H.; Liedl, T.; Lamb, D. C. A DNA Origami Platform for Single-Pair Förster Resonance Energy Transfer Investigation of DNA−DNA Interactions and Ligation. *J. Am. Chem. Soc.* **2020**, *142* (2), 815−825.
(47) Strauss, M. T.; Schueder, F.; Haas, D.; Nickels, P. C.; Jungmann, R.Quantifying absolute addressability in DNA origami

with molecular resolution. *Nat. Commun.***2018**, *9* (1). DOI: 10.1038/s41467-018-04031-z.
(48) Danaei, M.; Dehghankhold, M.; Ataei, S.; Hasanzadeh Davarani, F.; Javanmard, R.; Dokhani, A.; Khorasani, S.; Mozafari, M. Impact of Particle Size and Polydispersity Index on the Clinical Applications of Lipidic Nanocarrier Systems. *Pharmaceutics* **2018**, *10* (2), 57.
(49) Schultz, Z. D.; Pazos, I. M.; McNeil-Watson, F. K.; Lewis, E. N.; Levin, I. W. Magnesium-Induced Lipid Bilayer Microdomain Reorganizations: Implications for Membrane Fusion. *J. Phys. Chem. B* **2009**, *113* (29), 9932−9941.
(50) Brasnett, C.; Longstaff, G.; Compton, L.; Seddon, A.Effects of Cations on the Behaviour of Lipid Cubic Phases. *Sci. Rep.***2017**, *7* (1). DOI: 10.1038/s41598-017-08438-4.
(51) Le, C. T. M.; Houri, A.; Balage, N.; Smith, B. J.; Mechler, A., Interaction of Small Ionic Species With Phospholipid Membranes: The Role of Metal Coordination. *Front. Mater.***2019**, *5*. DOI: 10.3389/fmats.2018.00080.
(52) Wang, D.; Da, Z.; Zhang, B.; Isbell, M. A.; Dong, Y.; Zhou, X.; Liu, H.; Heng, J. Y. Y.; Yang, Z. Stability study of tubular DNA origami in the presence of protein crystallisation buffer. *RSC Adv.* **2015**, *5* (72), 58734−58737.
(53) Kielar, C.; Xin, Y.; Shen, B.; Kostiainen, M. A.; Grundmeier, G.; Linko, V.; Keller, A. On the Stability of DNA Origami Nanostructures in Low-Magnesium Buffers. *Angew. Chem., Int. Ed.* **2018**, *57* (30), 9470−9474.
(54) Olson, F.; Hunt, C. A.; Szoka, F. C.; Vail, W. J.; Papahadjopoulos, D. Preparation of liposomes of defined size distribution by extrusion through polycarbonate membranes. *Biochimica et Biophysica Acta (BBA) - Biomembranes* **1979**, *557* (1), 9−23.
(55) Mayer, L. D.; Hope, M. J.; Cullis, P. R. Vesicles of variable sizes produced by a rapid extrusion procedure. *Biochimica et Biophysica Acta (BBA) - Biomembranes* **1986**, *858* (1), 161−168.
(56) Ong, S.; Chitneni, M.; Lee, K.; Ming, L.; Yuen, K. Evaluation of Extrusion Technique for Nanosizing Liposomes. *Pharmaceutics* **2016**, *8* (4), 36.
(57) Jousma, H.; Talsma, H.; Spies, F.; Joosten, J. G. H.; Junginger, H. E.; Crommelin, D. J. A. Characterization of liposomes. The influence of extrusion of multilamellar vesicles through polycarbonate membranes on particle size, particle size distribution and number of bilayers. *Int. J. Pharm.* **1987**, *35* (3), 263−274.
(58) Hunter, D. G.; Frisken, B. J. Effect of Extrusion Pressure and Lipid Properties on the Size and Polydispersity of Lipid Vesicles. *Biophys. J.* **1998**, *74* (6), 2996−3002.
(59) Khmelinskaia, A.; Franquelim, H. G.; Petrov, E. P.; Schwille, P. Effect of anchor positioning on binding and diffusion of elongated 3D DNA nanostructures on lipid membranes. *J. Phys. D: Appl. Phys.* **2016**, *49* (19), 194001.
(60) Khmelinskaia, A.; Mücksch, J.; Petrov, E. P.; Franquelim, H. G.; Schwille, P. Control of Membrane Binding and Diffusion of Cholesteryl-Modified DNA Origami Nanostructures by DNA Spacers. *Langmuir* **2018**, *34* (49), 14921−14931.
(61) Kim, D.-N.; Kilchherr, F.; Dietz, H.; Bathe, M. Quantitative prediction of 3D solution shape and flexibility of nucleic acid nanostructures. *Nucleic Acids Res.* **2012**, *40* (7), 2862−2868.
(62) Vogelsang, J.; Kasper, R.; Steinhauer, C.; Person, B.; Heilemann, M.; Sauer, M.; Tinnefeld, P. A Reducing and Oxidizing System Minimizes Photobleaching and Blinking of Fluorescent Dyes. *Angew. Chem., Int. Ed.* **2008**, *47* (29), 5465−5469.
(63) Cordes, T.; Vogelsang, J.; Tinnefeld, P. On the Mechanism of Trolox as Antiblinking and Antibleaching Reagent. *J. Am. Chem. Soc.* **2009**, *131* (14), 5018−5019.

https://doi.org/10.1021/acsnano.2c11981
ACS Nano 2023, 17, 3088−3097

3.3. Further Studies on DNA Origami Curvature Sensors

3.3.1. Dynamic Curvature Sensing on Lipid Vesicles

In our subsequent experiments, our first goal was to elevate the adaptability of the DNA origami curvature sensors. Our approach was to make the system dynamic, that is, to report real-time changes in the curvature of the particles being tested. In this direction, we chose to work with LUVs, and planned to dynamically change their shape by manipulating the osmotic pressure of their external solution.[135] This manipulation was achieved through the introduction of different agents: salts, sucrose and Polyethylene glycol (PEG).[136-140] Theoretically, by adjusting the osmotic balance, we expected the vesicles to either shrink or expand. Such changes would be detected by shifts in our sm-FRET measurements.

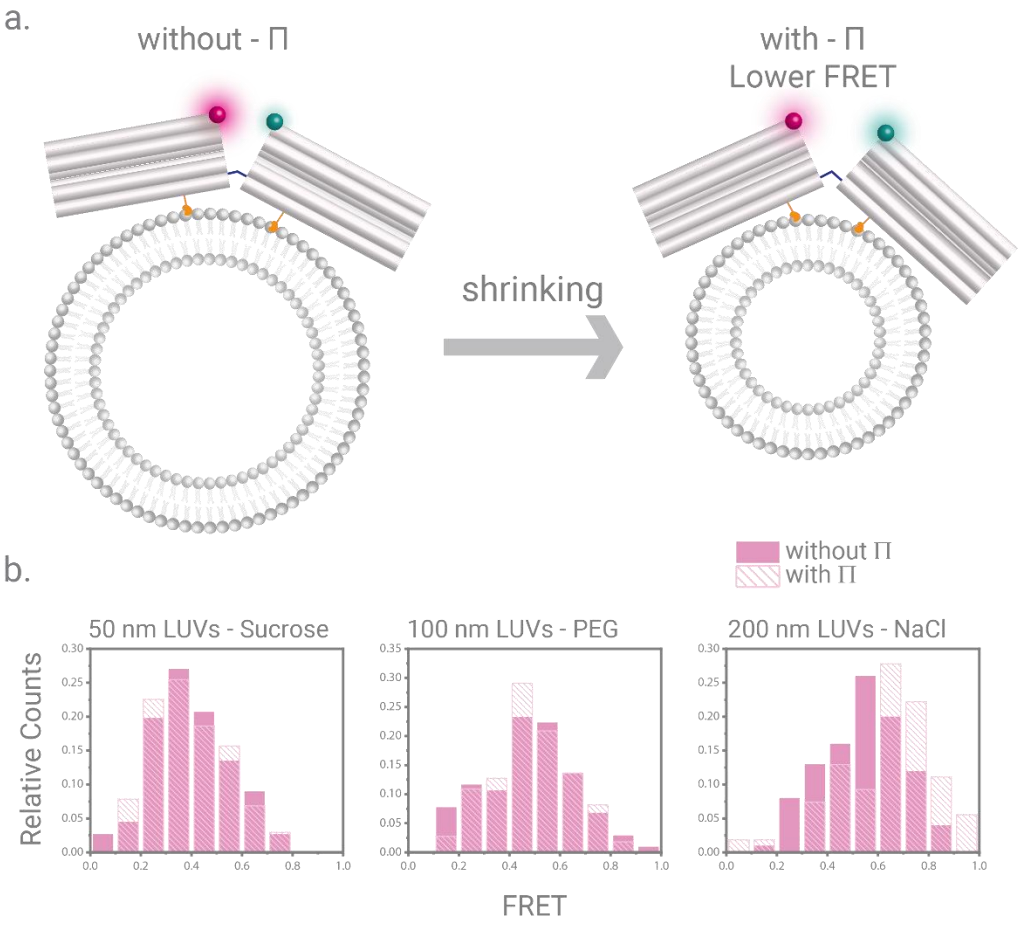

Figure 10. Overview of dynamic curvature sensing on lipid vesicles. (a) Schematic illustration of increased osmotic pressure effects on lipid vesicles. When the osmolarity of the outer environment of lipid vesicles is increased, the vesicles release their water content, leading to shrinkage. This results in reduced curvature and higher FRET signals from the curvature sensors. (b) FRET histograms of curvature sensors on 50 nm, 100 nm and 200 nm lipid vesicles under osmotic pressure manipulation. The histograms display the distributions with osmotic pressure (dashed lines) and without osmotic pressure (filled areas) for three different agents: sucrose, PEG and NaCl (from left to right). While sucrose and PEG do not significantly impact the sizes of lipid vesicles, NaCl exhibits an unexpected effect, suggesting its direct interaction with the DNA origami curvature sensors rather than altering vesicle size.

The results, however, were mixed. Although increasing the salt concentration of the external buffer resulted in a change in FRET readings, the change was counterintuitive. We increased the osmolarity of the external buffer, which should have caused the LUVs to release water and shrink (Figure 10a). This should have resulted in higher curvature and lower FRET efficiencies reported by the curvature sensors. However, instead of reduced FRET efficiencies due to the vesicles shrinking, we observed an increase in the FRET efficiency (Figure 10b, the last histogram). This result suggested an alternative influence at play, possibly indicating that the salt changes interacted directly with the DNA origami curvature sensors, affecting their conformation.[141-145] It is likely that the high salt concentration would bring the two blocks of curvature sensors closer together, resulting in a decreased distance between the FRET pair and ultimately increased FRET efficiency.

On the other hand, the addition of sucrose and PEG, both designed to tweak the osmotic pressure, did not result in noticeable changes in the FRET readout (Figure 10b, the first two histograms). This lack of change led us to reevaluate the experimental conditions, especially given the nature of the vesicles we were working with. LUVs posed unique challenges. LUVs have a better ability to cope with external perturbations, compared to Giant Unilamellar Vesicles (GUVs) which respond to external perturbations by undergoing changes in their shape and membrane properties.[96] Therefore, GUVs offer a more comprehensive model for studying the mechanical, thermodynamic, electrical and rheological properties of lipid bilayers in response to external factors, while LUVs are limited in their ability to provide such insights.[146, 147] Together with this, their modification with biotin-moieties made LUVs even less amenable to size modifications via osmotic shocks.[148] Moreover, their immobilization on modified glass coverslips added another layer of complexity. It should not be overlooked that their natural behavior under osmotic

changes may be limited by the possible surface effects such as strong adhesion via biotin-streptavidin interactions, electrostatic interactions, or van der Waals forces.

In order to overcome these difficulties, we moved to a different environment. The sensors and LUVs were mixed and tested in a solution, eliminating the potential surface effects. Yet, this solutions-based approach came with a new set of challenges. The high flexibility of our DNA origami curvature sensors turned out to be a problem here. In solution, the majority of the sensors adopted a bent conformation limiting their accessibility. This prevented LUVs from binding to the sensors, ultimately leading to an unbound sensor population. The freely diffusing sensors in the solution showed a broad range of FRET values, which made it quite difficult for us to interpret and analyze them.

To sum up, our trials to develop a dynamic system using DNA origami curvature sensors, while initially promising, encountered a series of unanticipated challenges. While our understanding has grown, optimizing the system for dynamic measurements requires further refined investigation.

3.3.2. Testing DNA Origami Curvature Sensors on Cellular Membranes

As a bridge to biological applications, we focused on the application of DNA origami curvature sensors to understand cellular membrane remodeling events. Our approach was to place our sensors on the cell membrane and use fluorescence lifetime imaging (FLIM) to detect differences in the curvature of the membrane.

We chose HeLa cells[149] as our model system because they are a widely recognized and used cell line in research due to their robustness and ease of culture.[150, 151] The curvature sensors were anchored to the surface fixed HeLa cells via cholesterol anchors (Figure 11a). However, the attachment of our nanostructures to the complex environment of a cell was not straightforward. Initial attempts suffered from significant background in the images, likely caused by non-specific interactions and autofluorescence of the cells. A BSA passivation strategy effectively decreased the background problem.

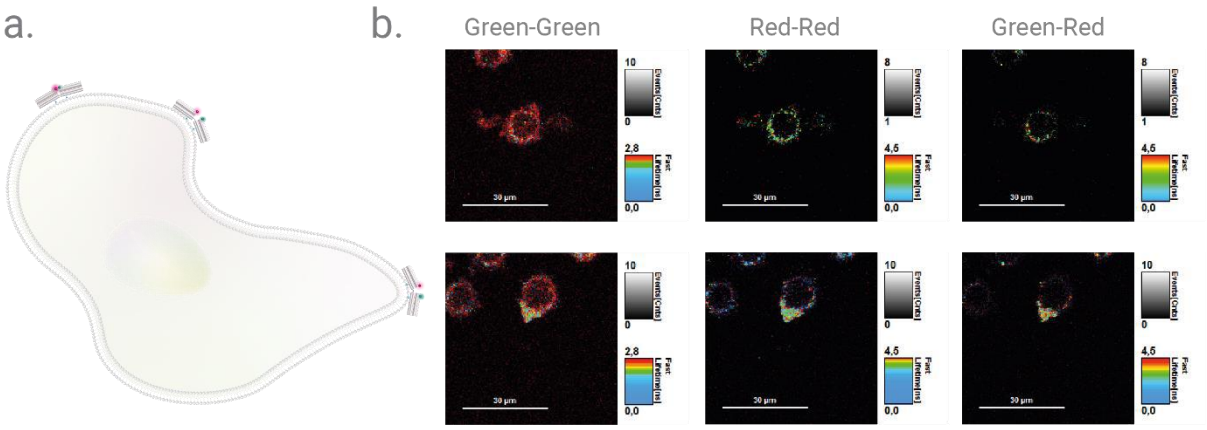

Figure 11. Overview of curvature sensing on cells. (a) Schematic representation of curvature sensors anchored on cells. (b) FLIM images of curvature sensors on surface-fixed HeLa cells showing successful anchoring of the sensors on the cellular membranes. The images consist of three channels: (i) Green excitation and green detection, (ii) Red excitation and red detection, and (iii) Green excitation and red detection (FRET).

While our initial results were promising (Figure 11b), showing the applicability of the sensor attachment on cells, there was an inherent limitation. Due to the relatively large curvature of many cellular structures, our nanoscale sensors often appeared to lie flat on these structures, which could mask real differences in curvature. However, our sensors may show noticeable fluorescence lifetime variations in areas of pronounced curvature. HeLa cells provided a starting point, setting the stage for future applications.

We also believe that our DNA origami curvature sensors might be ideal for studying structures like neuron cells and exosomes. Neuron cells have unique shapes and intricate structures with distinct parts which might possess a wide range of curvatures. On the other hand, exosomes[152-155] are small membrane-bound vesicles, often ranging from 30 to 150 nanometers in size. They are secreted by almost all cell types and play crucial roles in cell-to-cell communication by carrying a mix of proteins, lipids and genetic material. These vesicles provide insights into the health and state of their cells of origin and are even seen as potential markers for various diseases like cancer. Given their size and biological significance, they align well with the capabilities of our sensors, potentially letting us understand more about their biology.

To sum up, we made foundational progress in integrating our curvature sensors with cellular structures. Further research is required to build on our current knowledge of these

systems to further explore the promising potential of DNA origami curvature sensors in cell biology.

4. DNA Origami Vesicle Sensors

4.1. Motivation

Cellular processes involve a sophisticated network of molecular interactions where precision and specificity are paramount. Every cellular signal transduction, transport mechanism and biochemical pathway relies on these specific affinity interactions. In order to understand and exploit these processes, biosensors have been developed to detect and measure molecular interactions.

DNA origami technique, with its ability to create nanostructures tailored to specific molecular affinities, provides a promising basis for the design of such biosensors. However, effective use of this technique remains a challenge, especially in the complex environment of lipid vesicles. As previously mentioned in prior sections, lipid vesicles are essential for many cellular functions. By their very nature, they function through a series of specific affinity interactions. Therefore, the development of biosensors that can accurately read and manipulate lipid vesicles through their affinity interactions could greatly improve our knowledge and use of these cellular entities.

The importance of affinity interactions is further highlighted by the emphasis on precise molecular transport in modern medical applications. By designing delivery systems with specific molecular affinities, therapeutics can be transported to their targets with greater efficiency and with fewer side effects.

With this in mind, our work is motivated by the desire to provide a technology for the detection of lipid vesicles, the enhancement of molecular sensing capabilities, and the contribution of innovative delivery systems. In this work, we engineered a biosensor harnessing the principles of sm-FRET for precise lipid vesicle detection. The system centers on a hydrophobic ATTO647N modified single-stranded DNA (ssDNA) leash, protruding from a rectangular DNA origami which undergoes conformational changes in response to lipid vesicle presence, resulting in distinctive FRET signals. The strategic placement of cholesterol anchors further modulates this interaction, affecting the observed FRET populations. Beyond its role as a vesicle sensor, our system offers potential as a cargo transport tool at the nanoscale.

4.1.1. Lipid Vesicle Detection for Enhanced Therapeutics

Accurate identification, analysis and manipulation of lipid vesicles is essential to unraveling the intricacies of cellular dynamics, improving targeted drug delivery and pushing the boundaries of nanomedicine. With this in mind, our research aimed to contribute to the methods of lipid vesicle detection and ensure that their potential is exploited for improved therapeutic outcomes.

In the world of lipid vesicles, EVs, in particular exosomes, have gone beyond basic functionalities. They carry a variety of components, such as nucleic acids, proteins and metabolites that reflect their cell of origin. Additionally, their involvement in cell-to-cell communication has led to increased interest in their therapeutic applications, particularly as disease biomarkers in oncology.[155-158] Unlike liposomes, exosomes efficiently enter cells and can transport functional contents with little immune response. Therapeutically, they hold great promise as they are shown to be safe; repeated injections of exosomes from mesenchymal and epithelial cells in mice have not induced toxicity.[154] In recent years, artificial exosomes have been emerging based on nanobiotechnology to overcome the limitations of natural exosomes.[159-161]

Furthermore, as natural nanoscale carriers, exosomes have the ability to encapsulate and transport bioactive compounds. Their unique structure allows for targeted drug delivery to specific cellular or tissue sites, enhancing therapeutic efficacy.[155, 162, 163] As a result, this specificity not only enhances the pharmacological effects but also minimizes off-target transports, potentially reducing side effects. One of the most studied systems utilizing exosomes as delivery vehicles to transmit exogenous RNAs (small interfering RNA (siRNA) and MicroRNA (miRNA)) to target tissues or cells *in vivo*, regulating gene expression and inhibiting tumor development. Exosomes can modify tumor growth because of some proteins and RNAs which they deliver to the tumor cell.[164, 165] Valadi *et al.* and Skog *et al.* reported the two pioneering studies in which exosomes were used for gene delivery demonstrating the transport of native mRNAs and microRNAs expressed in the exosome-producing cells to other cells in culture.[166, 167] A following study by Alvarez *et al.* revealed the potential of exosomes in delivering siRNA to mouse brain cells, suggesting therapeutic avenues for Alzheimer's disease.[168] Furthermore, exosomes

have been investigated and identified as promising carriers for macromolecular proteins.[169-171]

With the advancement of the field, a newer generation of lipid-based carriers, known as lipid nanoparticles (LNPs), such as liposomes, solid lipid nanoparticles (SLNs) and nanostructured lipid carriers (NLCs), has emerged. These LNPs are designed to optimize the delivery of compounds, especially nucleic acids such as mRNA.[172, 173] Since the first clinical approval of Doxil[174-177] in 1995, they have gained considerable attention in the field of therapeutics and have achieved a great clinical success. At the same time, as evident by the approval of two RNA therapies and mRNA COVID-19 vaccines[178-183], LNPs have shown tremendous potential for the delivery of nucleic acid drugs.[184] As we move from lipid vesicles to the sophisticated world of LNPs, the emphasis on accurate vesicle detection becomes even more critical to ensure the efficacy and safety of next-generation therapeutics.[185]

4.1.2. Cargo Transport and Drug Delivery

At the heart of numerous biological and therapeutic processes lies molecular cargo transport and drug delivery. In essence, molecular cargo transport refers to the movement of molecular entities, such as proteins, nucleic acids and other biomolecules, from one location to another within a biological system or laboratory setting. Drug delivery, a specialized form of this transport, involved the introduction and distribution of therapeutic agents to targeted sites within an organism to achieve a desired therapeutic outcome.

The significance of efficient and targeted cargo transport and drug delivery is evident in various therapeutic settings.[186] For example, a drug administered systematically may not reach the intended site of action in optimal concentrations, leading to reduced efficacy or even undesirable side effects. By controlling the delivery of therapeutic molecules, scientists can maximize therapeutic benefits and minimize potential harms.

This is where the necessity for biosensors comes into play. Biosensors are invaluable tools for monitoring and regulating both cargo transport and drug delivery. With real-time

detection, biosensors can provide insights into the quality, quantity and condition of drugs being transported. They can be indicators of potential contaminants, degradation, or deviations, ensuring both safety and efficiency.

By using DNA origami, researchers can design drug delivery systems that are both precise in targeting and robust in delivery, bridging the gap between molecular biology and therapeutic application. Nanotechnologists aim to mimic living cells using artificial systems. Initial efforts have produced artificial molecular motors and transporters, with some integrated into molecular robotics.[68, 187-189] Recent advances in the field of DNA nanotechnology have opened up new possibilities for cargo transport and drug delivery.[190-192] These DNA-based structures can act as carriers, encapsulating and protecting cargo which can be a drug molecule or another therapeutic agent.[193] Given the programmable nature of DNA, these carriers can be tailored to release their cargo at specific targets, enhancing the specificity and efficiency of drug delivery.

Using DNA nanotechnology, progress has been made in the development of nanoscale devices for cargo transport. For example, molecular walkers have recently been shown to move over long distances on DNA origami tracks. Seeman and his team created the first molecular assembly line using DNA. A molecular walker was designed to systematically gather nanoparticles from various stations, resulting in the formation of small nanoparticle assemblies.[194] One of the pioneering works in this direction was done by Douglas *et al.*, in which an autonomous DNA nanorobot was developed that can transport molecular payloads to cells, respond to cell surface inputs, and reconfigure its structure for payload delivery, showing potential for targeted cell therapy.[187] Later on, a chemically responsive DNA polyhedron was designed, integrating a DNA icosahedron with a module that allows the nanocapsule to open in the presence of cdGMP, enabling controlled release of fluorescent dextran cargo.[195] In another work, Kopperger *et al.* focused on the diffusive transport of DNA cargo strands bound to a supramolecular DNA origami structure via an extended tether arm. Their results suggested that diffusive motion on a molecular tether is a highly efficient mechanism for fast transfer of cargoes over long distances.[196]

Recently, the remarkable self-assembly capabilities of DNA offer opportunities for designing diverse programmable formations and broader assemblies leading to

improved molecular transport systems[197-199] or systems tailored for cellular interventions, such as cancer treatment[200, 201] and enzyme replacement therapies.[202] As an example, biomolecular complexes can form robust assemblies and simultaneously exchange their subunit, ensuring both stability and adaptability. Drawing inspiration from these natural phenomena, Brown *et al.* developed a DNA origami receptor exploiting multivalent interactions to form stable complexes capable of rapid unit exchange, demonstrating applicability to various molecular cargo.[203] In another work, a DNA origami nanocapsule was developed that can be loaded with cargo and opened or closed by changing the pH of the surrounding solution.[204]

In conclusion, the synergy between biosensors and DNA nanotechnology holds promise for pioneering advancements in cargo transport and drug delivery. Through the course of this study, we aimed to establish a multifunctional system with potential applications in both diagnostics and therapeutics.

4.2. Overview of the Associated Publication

DNA Origami Vesicle Sensors with Triggered Cargo Transfer

Ece Büber, Renukka Yaadav, Tim Schröder, Henri G. Franquelim and Philip Tinnefeld,

preprint in

bioRxiv 2023.11.03.565475

DOI: https://doi.org/10.1101/2023.11.03.565475

In our submitted work titled "DNA Origami Vesicle Sensors with Triggered Cargo Transfer," we explored the transformative potential of nanoscale systems that respond to molecular signals, focusing on biosensing and cargo transfer. This work focused on the interface between DNA origami and lipid vesicles, which are one of the fundamental entities involved in cellular processes. Combining DNA origami precision with sm-FRET sensitivity, we developed a biosensor tailored for real-time lipid vesicle detection, highlighting its promise for molecular cargo transport.

The vesicle sensors were designed based on a rectangular DNA origami nanostructure with dimensions of 70 x 100 nm. This system consisted of an ATTO647N labeled 12 nt ssDNA protrusion, a donor dye ATTO542 and cholesterol anchors. It capitalized on the affinity interactions between ATTO647N fluorophore and lipid vesicles with sm-FRET readout. The role of this specific fluorophore was the basis of the sensor; its unique hydrophobic properties enabled the fluorophore to anchor firmly to lipid vesicles.[205, 206] Essentially, the conformation of the ssDNA leash changes depending on the absence or presence of lipid vesicles at its vicinity. In the absence of lipid vesicles, the leash adopts a coiled conformation and shows increased FRET due to the shorter distance between the donor and acceptor dye. On the other hand, in the presence of vesicles, the ATTO647N fluorophore anchors to the lipid vesicles, stretching the leash and increasing the dye distance, thereby decreasing FRET (Figure 12).

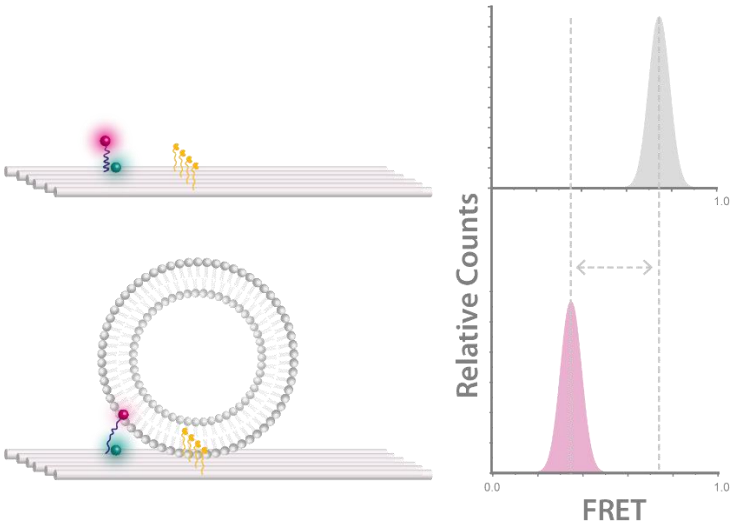

Figure 12. The working principle of the DNA origami vesicle sensors.

We aimed to validate our approach by testing FRET efficiencies in various scenarios. Initially, we used sensors with cholesterol anchors at a 15 nm distance from the probe position, which was chosen strategically to ensure optimal interactions with the anchored lipid vesicles. The sensor behavior both in the absence and presence of 100 nm DOPC LUVs was observed. Notably, there was a significant shift in the FRET efficiency value upon vesicle introduction, indicating effective binding and that the hydrophobic ATTO647N was successfully anchoring to the vesicle membrane. To further validate the principle, we replaced the ATTO647N fluorophore with AlexaF647, a fluorophore known for its minimal vesicle interaction due to its hydrophilic nature.[207] When we tested this control probe in the absence and presence of the lipid vesicles in the same way, the FRET values remained unchanged. This consistent result for the AlexaF647 probe further emphasized the unique affinity interactions between the ATTO647N probe and lipid vesicles.

The research expanded to examine the role of cholesterol anchor positioning on vesicle anchoring. In addition to 15 nm cholesterol distance, we further tested sensors with cholesterol anchors positioned at 5 nm and 30 nm distances from the probe. Our sm-FRET studies revealed that the 30 nm spacing showed no significant FRET differences between the absence and presence of lipid vesicles, confirming that the ATTO647N probe can only anchor into the lipid bilayer if the vesicle is sufficiently close. Interestingly, the 5 nm variant showed broad FRET distributions regardless of vesicle presence, likely due to the interactions of the ATTO647N probe with the nearby cholesterol anchors, further supporting the strong hydrophobic interactions that the sensor based on. Additionally, the 5 nm configuration showed no FRET differences when tested with the control AlexaF647 system.

We were further interested in the affinity of the sensor for different sizes of lipid vesicles. In this direction, besides 100 nm lipid vesicles, we tested the sensors with 50 nm and 200 nm DOPC vesicles. Along with the model distance of 15 nm cholesterols, we further utilized sensors crafted with cholesterol anchors placed at 20 nm distance from the probe. The 15 nm configuration showed consistent behavior across different vesicle sizes, while the 20 nm variant showed a discernable interaction with the larger 200 nm DOPC vesicles. These results emphasize the importance of precision in the design of

probes for vesicle interactions, as customization to specific sizes can improve their performance and expand their use in diverse application fields.

Finally, we explored the potential of our system as a molecular cargo transport tool. To achieve this, we planned a strand displacement system in which the sensor design was slightly altered and a 17 nt ssDNA strand labeled with ATTO647N was used as the cargo. A 17 nt protrusion was initiated from the probe position on the DNA origami and the 17 nt ATTO647N probe was attached to this protrusion, preserving a 5 nt toehold at the forefront. The cargo transport system involved a 17 nt cholesterol-modified displacer strand, which has a stronger affinity for the ATTO647N probe. Upon interaction, this displacer strand binds to the probe at the toehold segment, leading to its displacement from the origami structure. As we noted higher FRET values without vesicles and a decrease upon vesicle introduction, we further anticipated witnessing a loss of the FRET signal but a persisting red emission after the displacement of the ATTO647N probe. Observations showed that when vesicles were present, the FRET value dropped, consistent with the working principle of the sensor. The introduction of a cholesterol-labeled displacer strand led to the disappearance of the FRET signal but maintained a mobile red emission, indicating the successful relocation of the probe to the surrounding lipid vesicles. Further experiments with a Tween20 buffer, which disrupts vesicles, supported these findings showing the specificity of the vesicle-probe interaction. All in all, the results demonstrate the potential of the vesicle sensor as a cargo transport system, highlighting its versatility in molecular interactions.

Altogether, focusing on lipid vesicle detection, we developed a DNA origami-based biosensor with sm-FRET readout with potential applications in cargo transport. Because they mainly relied on molecular interactions, the hydrophobic ATTO647N fluorophore and strategic placement of cholesterol anchors were key to the success of the vesicle sensors. Together with the sensing characteristics, the design and the working principle of the sensor allowed it to be used as a cargo transport system. We believe, our simple sensor design has a great potential in the rapidly growing field of nanotechnology, providing a new perspective on nanoscale research.

DNA Origami Vesicle Sensors with Triggered Cargo Transfer

Ece Büber[a], Renukka Yaadav[a], Tim Schröder[a], Henri G. Franquelim[b,], and Philip Tinnefeld[a,*]*

[a]Department of Chemistry and Center for NanoScience, Ludwig-Maximilians-University, Butenandtstraße 5−13, 81377, Munich, Germany

[b]Interfaculty Centre for Bioactive Matter, Leipzig University, % Deutscher Platz 5 (BBZ), 04109 Leipzig, Germany

Correspondence to henri.franquelim@uni-leipzig.de or philip.tinnefeld@cup.lmu.de

KEYWORDS

Affinity interactions, DNA origami, lipid vesicles, cargo transfer, single-molecule FRET

ABSTRACT

Interacting with living systems typically involves the ability to address lipid membranes of cellular systems. The first step of interaction of a nanorobot with a cell will thus be the detection of binding to a lipid membrane. Leveraging the programmable nature of DNA origami, we engineered a biosensor harnessing single-molecule Fluorescence Resonance Energy Transfer (smFRET) as transduction mechanism for precise lipid vesicle detection. The system hinges on a hydrophobic ATTO647N modified single-stranded DNA (ssDNA) leash, protruding from a rectangular DNA origami. In a vesicle-free environment, the ssDNA adopts a coiled stance, ensuring high FRET efficiency. However, upon lipid vesicle binding to cholesterol anchors on the DNA origami, the hydrophobic ATTO647N induces the ssDNA to stretch towards the lipid bilayer, leading to reduced FRET efficiency. The strategic placement of cholesterol anchors further modulates this interaction, affecting the observed FRET populations. Beyond its role as a vesicle sensor, we show targeted cargo transport of the acceptor dye unit to the vesicle. The cargo transport is initiated by vesicle bound DNA and a strand displacement reaction. Our interaction platform opens pathways for innovative interaction such as biosensing and molecular transport with complex biosystems.

INTRODUCTION

In the rapidly advancing field of nanotechnology, the development of dynamic systems that respond to specific molecular signals is a major goal. These systems, capable of translating molecular behavior into practical applications, have the potential to reshape areas such as biosensing, targeted therapeutics, and precise engineering at the nanoscale. Central to these advancements is the DNA origami technique[1-7], which offers a reliable and customizable framework for designing nanoscale interactions by having stoichiometric and positional control over the DNA structure and attached functional elements. DNA origami, utilizing the innate programmability of DNA sequences, enables the design and realization of intricate nanostructures with exceptional precision. This unique capability has fostered innovations across nanotechnology, particularly in biosensing.[8-11] With the ability to design custom sensors tailored for specific molecular targets, DNA origami emerges as a powerful tool to address the challenges posed by complex biological systems.[12-19]

Among the challenges, membrane systems and especially lipid vesicles stand out. These membranous sacs play pivotal roles in diverse cellular functions, from molecular transport and signaling to compartmentalization.[20, 21] Therefore, detecting and characterizing lipid vesicles is of great importance. Sensors based on DNA origami can offer a subtle understanding of how lipid vesicles behave, with the potential to probe, detect, and even manipulate their activities.[22-27] Bridging the innovative capabilities of DNA origami to the intricate world of lipid vesicles can provide deeper insights into vesicular behaviors and potentially unlock new therapeutic opportunities.[28-31]

DNA origami has uses beyond just detection. As modern medicine and technology advance, the need for precise and controlled cargo transportation at the nanoscale becomes increasingly evident. From targeted drug delivery to the transfer of specific molecular agents, the ability to move and release cargo with specificity could reshape therapeutic strategies. The concept of molecular constructs for precise cargo transport is now an achievable reality in scientific research. This advancement holds significant implications for healthcare, diagnostics, and materials science. In one of the pioneering works, Douglas et al. developed a DNA nanorobot that delivers payloads to cells and changes its structure to release them, showing promise for targeted cell therapy. [32] Thubagere et al. created a self-powered DNA robot with three functional domains that can move across a DNA origami sheet and sort two types of molecular cargoes to their respective destinations using a simple algorithm.[33] In a more recent work involving lipid vesicles, Baumann et al. created a DNA mesh around lipid vesicles for drug delivery, releasing the dye calcein upon triggering. This method increased cytotoxicity in HEK293T cells and holds potential for targeted chemotherapy delivery.[34] In our research, we have developed a multifunctional system that is not only capable of sensing the presence of a vesicle, but also has the potential to deliver cargo directly to the vesicles it is attached to. By leveraging the capabilities of DNA origami, integrating the precision of single-molecule FRET (smFRET), and utilizing specific binding interactions, we have created innovative biosensing and molecular transport systems with dual functionality.

Combining this foundation with our previous experience with DNA origami nanosensors for lipid vesicle characterization[27], herein we introduce a DNA origami biosensor tailored for lipid vesicle detection. This system utilizes an ATTO647N labeled single-stranded DNA protrusion, a donor dye ATTO542, and cholesterol anchors. It capitalizes on smFRET and the affinity interactions of ATTO647N, allowing for real-time vesicle sensing and the potential for molecular

cargo transport. In our system, ATTO647N serves a dual role: not only is it the acceptor dye in the FRET process, but its hydrophobic nature also drives its interaction with lipid bilayers. Our research highlights how this system could change the way we detect and handle these lipid vesicles, setting the stage for innovative uses in biosensing and transporting molecules.

RESULTS

The vesicle sensor is crafted from a rectangular DNA origami nanostructure[2, 35] with the dimensions of 70 x 100 nm. It features a 12 nucleotide (nt) long single-stranded DNA (ssDNA) leash, modified with a ATTO647N fluorophore which serves as the main probe for vesicle sensing (Figure 1a). This probe, due to its hydrophobic and cationic properties, anchors itself in phospholipid vesicles, a behavior noted in prior studies.[36-38] Moreover, the sensor is equipped with an internally labelled ATTO542 fluorophore, serving as a donor for the fluorescence resonance energy transfer (FRET) (Figure 1a and Figure S1). We postulate that the relative position of the acceptor probe will change based on the presence or absence of lipid vesicles (Figure 1b). Specifically, without the vesicles, the ssDNA probe is more likely to coil up, leading to increased FRET. Conversely, with vesicles present, the leash will stretch out and anchor into the vesicles, increasing the gap between the FRET pair and resulting in decreased FRET. For the purpose of anchoring the sensor to modified glass coverslips, biotin attachments are located at the four corners of this DNA origami structure (Figure 1a and Figure S1). Additionally, the sensor comes with four cholesterol-based anchors that are placed parallel to each other in order to facilitate the capture of lipid vesicles (Figure 1a and Figure S1).[39, 40] These can be adjusted to various distances from the primary sensing probe in order to more efficiently capture and sense vesicles of different sizes.

To visualize individual vesicle sensors, we employed smFRET using total internal reflection fluorescence microscopy (TIRF) on a commercial fluorescence microscope (Nanoimager S, ONI Ltd., UK) with green-red alternating laser excitation (ALEX).[41, 42] Intensity transients of single spots were extracted from TIRF videos via the iSMS software based on Matlab.[43] In Figure 1c, a false-color image displays donor dye emission in cyan, acceptor in magenta, and their overlay in gray. We verified the fluorescence as originating from single vesicle sensors by observing single-step photobleaching patterns. For instance, in Figure 1c, the acceptor dye photobleaches around 11 seconds, leading to an increased, unquenched donor fluorescence (I_{DD}), while the FRET signal (I_{DA}) drops to zero. This synchronized response confirms the presence of a single DNA origami structure exhibiting FRET. We further tracked acceptor emission following its excitation (I_{AA}) to study associated photophysical behaviors and prioritize initial acceptor bleaching events. From the intensity data of both the I_{DD} and I_{DA} channels during energy transfer, the FRET efficiency of individual sensors were quantified as

$$FRET\ Efficiency = \frac{I_{DA}}{\gamma * I_{DD} + I_{DA}}$$

Here, the I_{DA} is corrected to account for the direct excitation of the acceptor at the donor excitation wavelength and for any donor emission leakage into the acceptor emission channel. The γ correction factor compensates for the different quantum yields of the dyes and wavelength-dependent efficiencies of the detection (see SI for detailed materials and methods). For each sample, we then analyzed a minimum of 100 molecules and represented the FRET efficiencies in histograms, complemented with Gaussian fits where relevant.

To validate our design, we contrasted the FRET efficiencies of the sensor both in the absence and presence of lipid vesicles. For this experiment, considering the highest possible overlap with

the leash length and 100 nm lipid vesicles, we used the sensors with cholesterol anchors placed at 15 nm distance from the probe position. After immobilizing the sensors on BSA-Biotin-NeutrAvidin-treated glass coverslips, smFRET measurements were performed. In the absence of vesicles, the mean FRET value was 0.83 ± 0.03 (standard deviation of the mean, SD). Upon introducing 1 nM of 100 nm DOPC vesicles with a 1-hour incubation, the mean FRET value shifted to 0.61 ± 0.06 (Figure 1d). This shift confirms the effective binding of lipid vesicle to our sensors and suggests the penetration of hydrophobic ATTO647N into the vesicle membrane. A remaining fraction with a mean FRET of 0.81 ± 0.03 likely represents either sensors devoid of vesicles or those where the probe fails to engage with the vesicles.

To further substantiate the role of affinity interactions in the sensor mechanism, the hydrophobic ATTO647N fluorophore was substituted with AlexaF647 on the ssDNA probe. Previous research has demonstrated that AlexaF647 exhibits minimal interaction with lipid vesicles due to its hydrophilic nature.[36] When analogous experiments were conducted without and with lipid vesicles for the sensors equipped with AlexaF647, the mean FRET values remained consistent at 0.78 ± 0.02 (Figure 1e). The notably homogenous and narrow distributions for the AlexaF647 probe further underscore the assertion that the distinct behavior of the sensor arises from the hydrophobic affinity interactions between the ATTO647N probe and lipid vesicles.

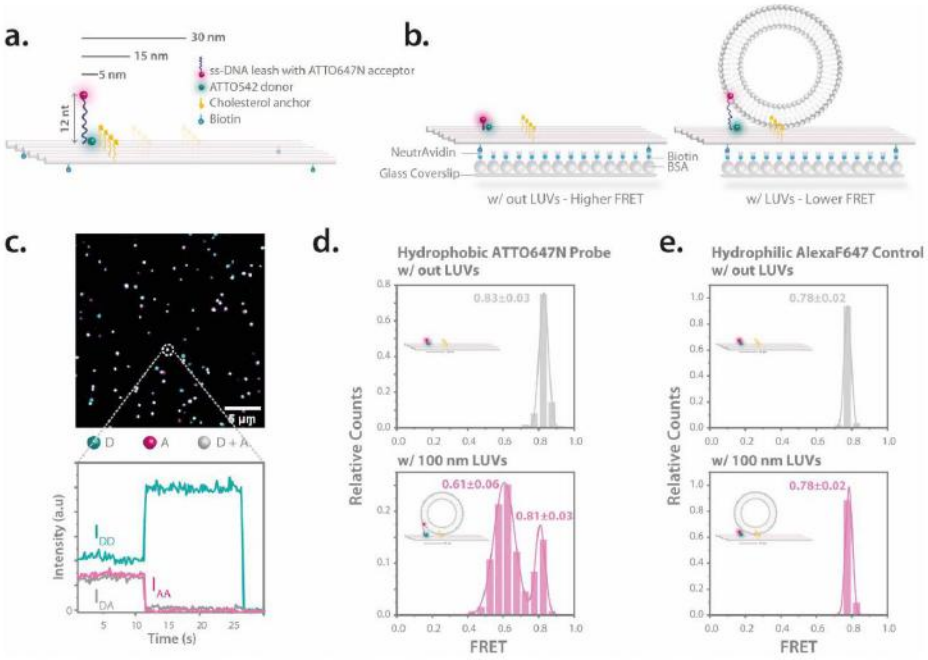

Figure 1. Concept and validation of the vesicle sensor. **(a)** A rectangular DNA origami base equipped with a sensing unit consisting of a ssDNA leash labeled with an ATTO647N acceptor and an ATTO542 donor positioned on the DNA origami base. Cholesterol anchors, strategically placed at various distances for vesicle capture, and biotin moieties for surface attachment are also featured. **(b)** These sensors have the capability to bind to BSA-Biotin-NeutrAvidin-treated glass coverslips using biotin moieties. Without lipid vesicles (left), the ssDNA sensing probe adopts a coiled configuration, positioning it closer to the donor dye, resulting in higher FRET. When lipid vesicles are present (right), the sensing probe elongates to permeate the lipid bilayer, driven by the hydrophobic nature of the ATTO647N fluorophore. Due to the increased distance between the probe and the donor dye, a decreased FRET is observed. **(c)** The image at the top presents a superimposed TIRF image with the donor dye (D) shown in cyan, and the acceptor (A) in magenta.

Gray spots denote sensors that incorporate both the donor and acceptor dyes. An exemplary single-molecule FRET (smFRET) trace at the bottom illustrates the fluorescence intensity over a period, detailing the donor excitation–donor emission (I_{DD}) channel (cyan), the donor excitation–acceptor emission (I_{DA}) channel (gray), and the acceptor excitation–acceptor emission (I_{AA}) channel (magenta). Mean FRET efficiencies are calculated from the I_{DD} and I_{DA} channels. **(d)** FRET efficiency distributions for vesicle sensors in scenarios both without (top) and with (bottom) lipid vesicles. Distributions are shown for the hydrophobic sensing probe with ATTO647N and **(e)** the hydrophilic control probe with AlexaF647. Accompanying illustrations in the plots suggest potential conformations of the probe. The error refers to the standard deviation (SD).

Building on our observations, we investigated the influence of the distance of the FRET probe to the cholesterol anchors. In addition to sensors with cholesterol anchors at 15 nm distance, we assembled vesicle sensors with cholesterol moieties positioned at 5 nm, and 30 nm distance from the probe. Each sensor was subjected to smFRET studies both with and without lipid vesicles.

For the sensor with the cholesterol anchors at a 30 nm distance from the leash, the smFRET results (Figure 2a) reported mean FRET values of 0.81 ± 0.04 and 0.81 ± 0.03 for scenarios without and with vesicles, respectively. The data suggests that, even when vesicles of 100 nm average diameter are present, the probe remains in its coiled state because the vesicles are too distant to be reached by the ATTO647N anchor. This design confirms that the FRET contrast arises solely when the ATTO647N probe anchors into the lipid bilayer—an event only possible when the vesicle is close enough to allow the probe to stretch toward it.

In the sensor variant with 15 nm cholesterols, as already presented in Figure 1d, a clear FRET shift occurred based on vesicle presence, underlining the effect of proximity (Figure 2b). However,

the results took a captivating turn when cholesterol anchors were only 5 nm from the probe. Independent of lipid vesicle presence, these sensors exhibited wider FRET distributions with comparable mean values (0.75 ± 0.07 without vesicles and 0.71 ± 0.09 with vesicles, Figure 2c), yet distinct from the other tested distances. This observation can likely be attributed to the strong hydrophobic interactions that allow the ATTO647N probe to already interact with closely positioned cholesterol anchors. Consequently, given the distinctive and reliable FRET shift observed with the 15 nm spacing, we chose to utilize sensors with cholesterol moieties at this distance for the remainder of our study. Additionally, a noteworthy observation was that, upon testing the 5 nm cholesterol configuration with a control system featuring AlexaF647, there was no apparent difference in FRET distributions (Figure S2).

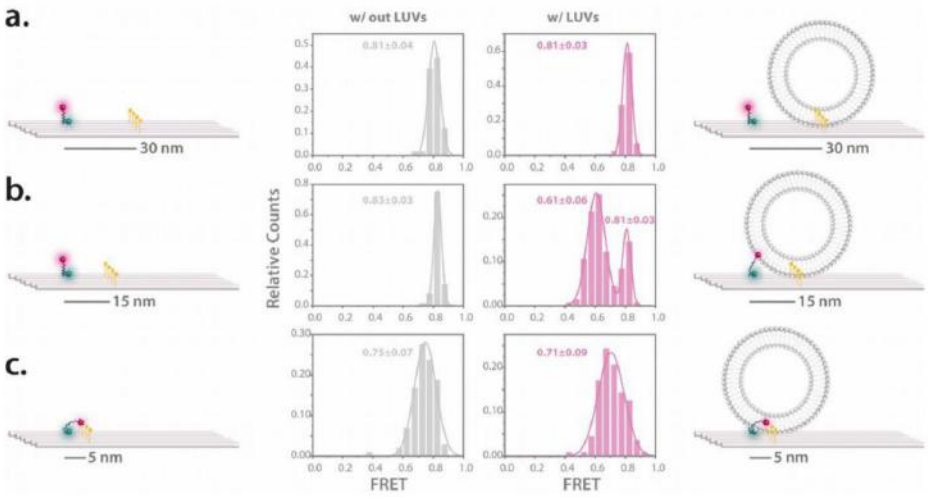

Figure 2. Influence of the cholesterol anchoring distances on the sensor both in the absence and presence of lipid vesicles. The distributions of FRET efficiency for the vesicle sensors, both without and with lipid vesicles, is depicted for **(a)** 30 nm, **(b)** 15 nm, and **(c)** 5 nm cholesterol-FRET probe distances. Illustrations accompanying the data highlight the positions of the cholesterol anchors and potential movement patterns of the sensing probe. The error refers to the standard deviation (SD).

In our pursuit to understand the sensor's response to varying lipid vesicle sizes, we further examined its behavior with 50 nm, and 200 nm DOPC vesicles using the 15 nm cholesterol as well as a 20 nm cholesterol configuration (Figure S3-a). Notably, while the 15 nm cholesterol-based sensor exhibited minimal variation across vesicle sizes (Figure S3), the 20 nm variant revealed a discernable peak in its interaction with the 200 nm DOPC vesicles, as illustrated in Figure S3-c. This indicates that the positioning of cholesterol in relation to the probe can influence the affinity of the sensor towards differently sized vesicles. Such findings underscore the importance of meticulous design and adaptation in probe creation for vesicle interactions, holding the potential to augment their relevance across diverse scientific and medical arenas.[44-46] Tailoring probes to align with specific vesicle dimensions can optimize their performance and extend their versatility in multiple disciplines.

Building upon the insights from our prior experiments and recognizing the transformative potential of cargo transport systems in molecular and nanoscale research, we delved deeper into an intricate investigation employing the ATTO647N probe within a strand displacement system. The design approach was systematic. A 17 nt single-stranded DNA was protruding from the probe position on the DNA origami and a 17 nt ATTO647N probe was attached to this protrusion,

preserving a 5 nt toehold at the forefront (Figure 3a). The cargo transport system involved a 17 nt cholesterol-modified displacer strand, which has a stronger affinity for the ATTO647N probe. Upon interaction, this displacer strand binds to the probe at the toehold segment, leading to its displacement from the origami structure. More precisely, as we noted higher FRET values without vesicles and a decrease upon vesicle introduction, we further anticipated witnessing a loss of the FRET signal but a persisting colocalization of green and red emission after the displacement of the ATTO647N probe. Due to the reason that a single cholesterol can diffuse in and out of lipid vesicles[47, 48], the transferred probe can subsequently relocate to surrounding lipid vesicles. Initial smFRET imaging without lipid vesicles revealed a mean FRET value of 0.39 ± 0.04. Presence of lipid vesicles reduced this value to 0.23 ± 0.06, corroborating the consistent working principle of the sensor (Figure 3b and Figure 3c, left and middle panels). The experiment took an intriguing turn when the 17 nt cholesterol-labeled displacer strand was introduced. The FRET signal immediately vanished, yet a red emission persisted (Figure 3b and Figure 3c, right panel). This red emission provided compelling evidence of the probe being successfully detached from the origami and transported to neighbouring lipid vesicles. Another captivating observation was the discrepancy in expected colocalization ratios after the introduction of the displacer strand in the presence of lipid vesicles. Prior to cargo translocation, the system exhibited a high degree of colocalization, as evidenced in Figure 3d, left and middle panels. However, upon introduction of the displacer strand, instead of the anticipated colocalized spots, numerous red-only spots emerged (Figure 3d, right panel). We theorize that this could be attributed to free lipid vesicles adhering to the surface, paired with the mobility of the cholesterol strand across vesicles[47], causing a transport of the probe from one vesicle to another. This phenomenon may result in diminished colocalization but a surge in red spots. Furthermore, the evident motion in these red spots post-displacement hints

at their dynamic diffusion in and across lipid vesicles. Supporting these observations, when lipid vesicles in the system were deliberately ruptured using a 0.05% Tween20 buffer[49], almost all red signals disappeared, reaffirming the specific vesicle-probe interaction (Figure S4-d). A separate evaluation of the impact of Tween20 on the system showed it only disrupts lipid vesicles and thereby resets the sensor to its original state without vesicle (see Figure S5). To fortify our hypothesis, a control test without vesicles was carried out. Upon introducing the cholesterol-labeled displacer strand, a near-complete disappearance of the red signal was evident which highlights the effectiveness of the strand in displacing the probe (Figure S6). In the absence of lipid vesicles, the displacement process was considerably slower, taking almost an hour for the red signal to fade, whereas in the presence of the vesicles, the red signal faded in just tens of seconds. Supposedly, the cholesterol displacer strand first binds to the lipid vesicles and gets upconcentrated. This upconcentration close to the probe results in increased transfer kinetics. Collectively, these results vividly demonstrate the potential of the vesicle sensor as a robust cargo transport system, emphasizing its versatility and specificity in molecular interactions.

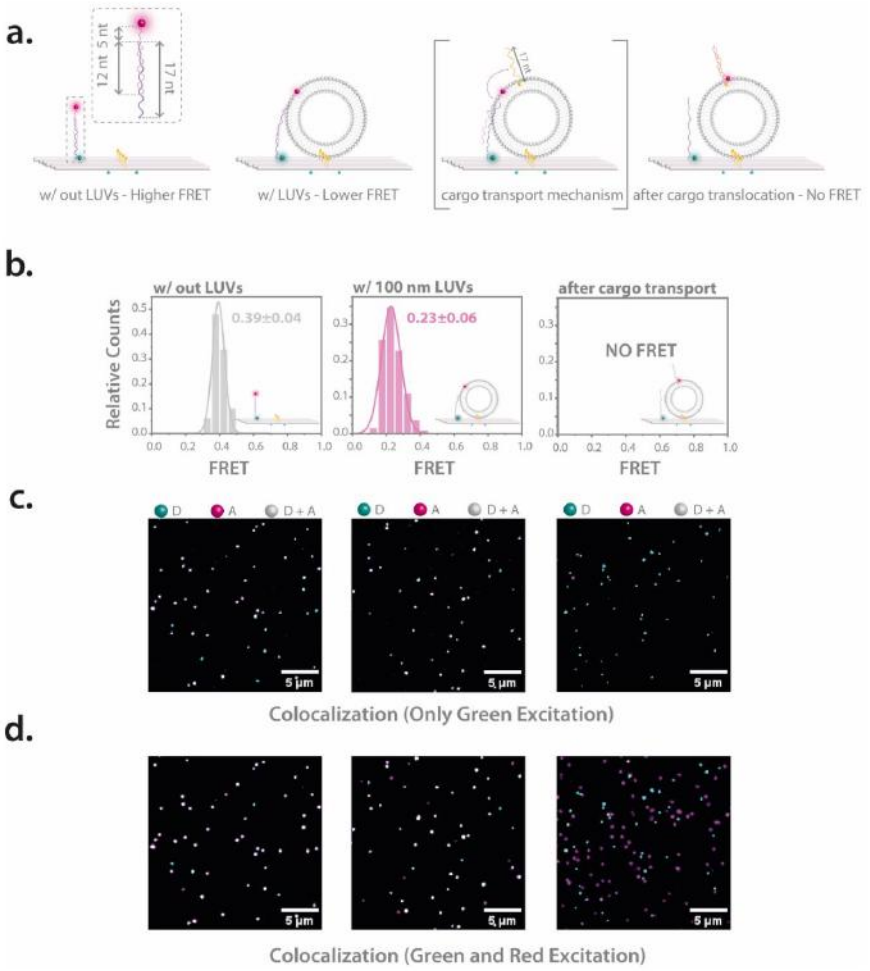

Figure 3. Investigation of cargo translocation to the lipid vesicles. **(a)** Schematic illustrations detailing the cargo transport system. A 17 nt strand protrudes from the DNA origami base, binding to a complementary 17 nt strand labeled with ATTO647N, leaving a 5 nt toehold exposed. The system initially exhibits higher FRET levels in the absence of lipid vesicles. Upon interaction with lipid vesicles, the ATTO647N-labeled strand anchors into the lipid bilayer, leading to reduced

FRET. After cargo translocation by strand displacement, the system shows no FRET due to increased separation between the FRET pair. **(b)** FRET histograms displaying the FRET characteristics of the system under different conditions: without lipid vesicles (left), with lipid vesicles (middle), and post-cargo translocation (right), where no FRET is observed. **(c)** Superimposed TIRF images after green-only excitation. The system without vesicles (left) and with vesicles (middle) show clear FRET, evidenced by colocalization. After cargo translocation (right), only green spots are observed, indicating the loss of FRET and absence of colocalization. **(d)** Superimposed TIRF images after both green and red excitation. In the absence (left) and presence (middle) of lipid vesicles, high degree of colocalization is observed. Following cargo translocation (right), the colocalization is lost, coinciding with the absence of FRET. However, numerous red spots remain distributed wherever lipid vesicles are present.

CONCLUSION

Understanding the interactions between vesicles and probes is not just of biophysical interest—it is a pathway to improving applications in medicine, diagnostics, and molecular biology. Built on the principles of affinity interactions, in this research, we have successfully developed a biosensor predicated on the flexibility and programmability of DNA origami structures. The vesicle sensor utilizes single-molecule Fluorescence Resonance Energy Transfer (smFRET) for the precise detection of lipid vesicles. Central to the effectiveness of the sensor is the hydrophobic ATTO647N dye-modified DNA leash, whose conformational shifts in the presence or absence of lipid vesicles facilitate distinguishable FRET signals. This observed versatility in response is further augmented by the strategic positioning of cholesterol anchors, underscoring the pivotal role of precise molecular design in dictating vesicle-sensor interactions. Moreover, the dynamic

behavior of the sensor, as evidenced by the FRET shift upon vesicle interaction and the subsequent engagement of the hydrophobic probe with the vesicle membrane, showcases its potential as a robust mechanism for targeted cargo transport at the nanoscale. The ability to modulate this transport and sensor response based on the proximity of cholesterol anchors provides insights into tailoring DNA origami systems for specific applications, offering a promising avenue for enhanced molecular specificity and efficiency. Our findings on the different affinities of hydrophobic and hydrophilic dyes to lipid vesicles further amplify the importance of selecting appropriate probes for specific biosensing endeavors. Such insights inform future design considerations, optimizing probe interactions for targeted applications. Furthermore, the study of the vesicle sensor within a strand displacement system illuminated the potential of DNA origami structures in molecular transport. Our design adds a physical dimension to conditional cargo transport that first requires the sensing of the vesicle depending on whether it can bridge from binding to the sensing unit followed by cargo transfer through strand displacement which is a different dimension compared to delivery upon molecular logics such as a logic and gate in the presence of two chemical receptors.[32]

In essence, our work has carved a significant stride in the domain of DNA origami-based biosensing. The interplay of FRET signals, hydrophobic dyes, and vesicle presence paints a picture of a sensor system that is not only versatile but is also specific, providing paths for real-world applications. As we advance into an era increasingly reliant on nanotechnology and molecular precision, tools such as the vesicle sensor developed in this study will play an indispensable role. Their versatility, as highlighted in both biosensing and molecular transport, provides a testament to the transformative potential of DNA origami in shaping the future of nanoscale research.

ASSOCIATED CONTENT

The Supporting Information is available. List of buffers, list of DNA oligonucleotides, materials and methods, and the details of DNA origami nanostructures, sample preparation, characterization techniques, imaging and data analysis.

AUTHOR INFORMATION

Corresponding Authors

Philip Tinnefeld – Department of Chemistry and Center for NanoScience (CeNS), Ludwig-Maximilians-University, 81377 Munich, Germany

Email: philip.tinnefeld@cup.lmu.de

Henri G. Franquelim – Interfaculty Centre for Bioactive Matter, Leipzig University, % Deutscher Platz 5 (BBZ), 04109 Leipzig, Germany

Email: henri.franquelim@uni-leipzig.de

Authors

Ece Büber – Department of Chemistry and Center for NanoScience (CeNS), Ludwig-Maximilians-University, 81377 Munich, Germany

Renukka Yaadav – Department of Chemistry and Center for NanoScience (CeNS), Ludwig-Maximilians-University, 81377 Munich, Germany

Tim Schröder – Department of Chemistry and Center for NanoScience (CeNS), Ludwig-Maximilians-University, 81377 Munich, Germany

ACKNOWLEDGMENT

The authors thank Thomas Bein (Ludwig-Maximilians-University, Department of Chemistry, Munich, Germany) for providing access to their facilities, especially to the dynamic light scattering. E.B. thanks Lorena Manzanares, and Viktorija Glembockytė for the fruitful discussions. This work was funded by the Deutsche Forschungsgemeinschaft (DFG, German Research Foundation) – Project-ID 201269156 – SFB 1032 (A13) and the Bavarian Ministry of Science and the Arts through the ONE MUNICH Project "Munich Multiscale Biofabrication".

REFERENCES

1. Seeman, N. C.; Belcher, A. M., Emulating biology: Building nanostructures from the bottom up. *Proceedings of the National Academy of Sciences* **2002,** *99* (suppl_2), 6451-6455.
2. Rothemund, P. W. K., Folding DNA to create nanoscale shapes and patterns. *Nature* **2006,** *440* (7082), 297-302.
3. Douglas, S. M.; Dietz, H.; Liedl, T.; Högberg, B.; Graf, F.; Shih, W. M., Self-assembly of DNA into nanoscale three-dimensional shapes. *Nature* **2009,** *459* (7245), 414-418.
4. Douglas, S. M.; Marblestone, A. H.; Teerapittayanon, S.; Vazquez, A.; Church, G. M.; Shih, W. M., Rapid prototyping of 3D DNA-origami shapes with caDNAno. *Nucleic Acids Research* **2009,** *37* (15), 5001-5006.
5. Castro, C. E.; Kilchherr, F.; Kim, D.-N.; Shiao, E. L.; Wauer, T.; Wortmann, P.; Bathe, M.; Dietz, H., A primer to scaffolded DNA origami. *Nature Methods* **2011,** *8* (3), 221-229.
6. Wagenbauer, K. F.; Engelhardt, F. A. S.; Stahl, E.; Hechtl, V. K.; Stömmer, P.; Seebacher, F.; Meregalli, L.; Ketterer, P.; Gerling, T.; Dietz, H., How We Make DNA Origami. *ChemBioChem* **2017,** *18* (19), 1873-1885.
7. Dey, S.; Fan, C.; Gothelf, K. V.; Li, J.; Lin, C.; Liu, L.; Liu, N.; Nijenhuis, M. A. D.; Saccà, B.; Simmel, F. C.; Yan, H.; Zhan, P., DNA origami. *Nature Reviews Methods Primers* **2021,** *1* (1).
8. Surana, S.; Shenoy, A. R.; Krishnan, Y., Designing DNA nanodevices for compatibility with the immune system of higher organisms. *Nature Nanotechnology* **2015,** *10* (9), 741-747.

9. Xiao, M.; Lai, W.; Man, T.; Chang, B.; Li, L.; Chandrasekaran, A. R.; Pei, H., Rationally Engineered Nucleic Acid Architectures for Biosensing Applications. *Chemical Reviews* **2019,** *119* (22), 11631-11717.
10. Wang, S.; Zhou, Z.; Ma, N.; Yang, S.; Li, K.; Teng, C.; Ke, Y.; Tian, Y., DNA Origami-Enabled Biosensors. *Sensors* **2020,** *20* (23), 6899.
11. Shen, L.; Wang, P.; Ke, Y., DNA Nanotechnology-Based Biosensors and Therapeutics. *Advanced Healthcare Materials* **2021**, 2002205.
12. Koirala, D.; Shrestha, P.; Emura, T.; Hidaka, K.; Mandal, S.; Endo, M.; Sugiyama, H.; Mao, H., Single-Molecule Mechanochemical Sensing Using DNA Origami Nanostructures. *Angewandte Chemie International Edition* **2014,** *53* (31), 8137-8141.
13. Zhang, H.; Chao, J.; Pan, D.; Liu, H.; Qiang, Y.; Liu, K.; Cui, C.; Chen, J.; Huang, Q.; Hu, J.; Wang, L.; Huang, W.; Shi, Y.; Fan, C., DNA origami-based shape IDs for single-molecule nanomechanical genotyping. *Nature Communications* **2017,** *8* (1), 14738.
14. Dutta, P. K.; Zhang, Y.; Blanchard, A. T.; Ge, C.; Rushdi, M.; Weiss, K.; Zhu, C.; Ke, Y.; Salaita, K., Programmable Multivalent DNA-Origami Tension Probes for Reporting Cellular Traction Forces. *Nano Lett* **2018,** *18* (8), 4803-4811.
15. Kosuri, P.; Altheimer, B. D.; Dai, M.; Yin, P.; Zhuang, X., Rotation tracking of genome-processing enzymes using DNA origami rotors. *Nature* **2019,** *572* (7767), 136-140.
16. Raveendran, M.; Lee, A. J.; Sharma, R.; Wälti, C.; Actis, P., Rational design of DNA nanostructures for single molecule biosensing. *Nature Communications* **2020,** *11* (1).
17. Pfeiffer, M.; Trofymchuk, K.; Ranallo, S.; Ricci, F.; Steiner, F.; Cole, F.; Glembockyte, V.; Tinnefeld, P., Single antibody detection in a DNA origami nanoantenna. *iScience* **2021,** *24* (9), 103072.
18. Liu, S.; Jiang, Q.; Zhao, X.; Zhao, R.; Wang, Y.; Wang, Y.; Liu, J.; Shang, Y.; Zhao, S.; Wu, T.; Zhang, Y.; Nie, G.; Ding, B., A DNA nanodevice-based vaccine for cancer immunotherapy. *Nature Materials* **2021,** *20* (3), 421-430.
19. Williamson, P.; Piskunen, P.; Ijäs, H.; Butterworth, A.; Linko, V.; Corrigan, D. K., Signal Amplification in Electrochemical DNA Biosensors Using Target-Capturing DNA Origami Tiles. *ACS Sensors* **2023,** *8* (4), 1471-1480.
20. Dimova, R., Giant Vesicles and Their Use in Assays for Assessing Membrane Phase State, Curvature, Mechanics, and Electrical Properties. *Annual Review of Biophysics* **2019,** *48* (1), 93-119.
21. Tenchov, R.; Bird, R.; Curtze, A. E.; Zhou, Q., Lipid Nanoparticles─From Liposomes to mRNA Vaccine Delivery, a Landscape of Research Diversity and Advancement. *ACS Nano* **2021,** *15* (11), 16982-17015.
22. Czogalla, A.; Kauert, D. J.; Franquelim, H. G.; Uzunova, V.; Zhang, Y.; Seidel, R.; Schwille, P., Amphipathic DNA Origami Nanoparticles to Scaffold and Deform Lipid Membrane Vesicles. *Angewandte Chemie International Edition* **2015,** *54* (22), 6501-6505.
23. Franquelim, H. G.; Khmelinskaia, A.; Sobczak, J.-P.; Dietz, H.; Schwille, P., Membrane sculpting by curved DNA origami scaffolds. *Nature Communications* **2018,** *9* (1).
24. Journot, C. M. A.; Ramakrishna, V.; Wallace, M. I.; Turberfield, A. J., Modifying Membrane Morphology and Interactions with DNA Origami Clathrin-Mimic Networks. *ACS Nano* **2019,** *13* (9), 9973-9979.
25. Liu, L.; Xiong, Q.; Xie, C.; Pincet, F.; Lin, C., Actuating tension-loaded DNA clamps drives membrane tubulation. *Science Advances* **2022,** *8* (41), eadd1830.

26. Hao, P.; Niu, L.; Luo, Y.; Wu, N.; Zhao, Y., Surface Engineering of Lipid Vesicles Based on DNA Nanotechnology. *ChemPlusChem* **2022,** *87* (5).
27. Büber, E.; Schröder, T.; Scheckenbach, M.; Dass, M.; Franquelim, H. G.; Tinnefeld, P., DNA Origami Curvature Sensors for Nanoparticle and Vesicle Size Determination with Single-Molecule FRET Readout. *ACS Nano* **2023,** *17* (3), 3088-3097.
28. Suzuki, Y.; Endo, M.; Sugiyama, H., Mimicking Membrane-Related Biological Events by DNA Origami Nanotechnology. *ACS Nano* **2015,** *9* (4), 3418-3420.
29. Shen, Q.; Grome, M. W.; Yang, Y.; Lin, C., Engineering Lipid Membranes with Programmable DNA Nanostructures. *Advanced Biosystems* **2020,** *4* (1), 1900215.
30. Rubio-Sánchez, R.; Fabrini, G.; Cicuta, P.; Di Michele, L., Amphiphilic DNA nanostructures for bottom-up synthetic biology. *Chemical Communications* **2021**.
31. Kong, Y.; Du, Q.; Li, J.; Xing, H., Engineering bacterial surface interactions using DNA as a programmable material. *Chemical Communications* **2022,** *58* (19), 3086-3100.
32. Douglas, S. M.; Bachelet, I.; Church, G. M., A Logic-Gated Nanorobot for Targeted Transport of Molecular Payloads. *Science* **2012,** *335* (6070), 831-834.
33. Thubagere, A. J.; Li, W.; Johnson, R. F.; Chen, Z.; Doroudi, S.; Lee, Y. L.; Izatt, G.; Wittman, S.; Srinivas, N.; Woods, D.; Winfree, E.; Qian, L., A cargo-sorting DNA robot. *Science* **2017,** *357* (6356), eaan6558.
34. Baumann, K. N.; Schröder, T.; Ciryam, P. S.; Morzy, D.; Tinnefeld, P.; Knowles, T. P. J.; Hernández-Ainsa, S., DNA–Liposome Hybrid Carriers for Triggered Cargo Release. *ACS Applied Bio Materials* **2022,** *5* (8), 3713-3721.
35. Schmied, J. J.; Gietl, A.; Holzmeister, P.; Forthmann, C.; Steinhauer, C.; Dammeyer, T.; Tinnefeld, P., Fluorescence and super-resolution standards based on DNA origami. *Nature Methods* **2012,** *9* (12), 1133-1134.
36. Zhang, Z.; Yomo, D.; Gradinaru, C., Choosing the right fluorophore for single-molecule fluorescence studies in a lipid environment. *Biochimica et Biophysica Acta (BBA) - Biomembranes* **2017,** *1859* (7), 1242-1253.
37. Mobarak, E.; Javanainen, M.; Kulig, W.; Honigmann, A.; Sezgin, E.; Aho, N.; Eggeling, C.; Rog, T.; Vattulainen, I., How to minimize dye-induced perturbations while studying biomembrane structure and dynamics: PEG linkers as a rational alternative. *Biochim Biophys Acta Biomembr* **2018,** *1860* (11), 2436-2445.
38. Ochmann, S. E.; Joshi, H.; Büber, E.; Franquelim, H. G.; Stegemann, P.; Saccà, B.; Keyser, U. F.; Aksimentiev, A.; Tinnefeld, P., DNA Origami Voltage Sensors for Transmembrane Potentials with Single-Molecule Sensitivity. *Nano Letters* **2021**.
39. Langecker, M.; Arnaut, V.; Martin, T. G.; List, J.; Renner, S.; Mayer, M.; Dietz, H.; Simmel, F. C., Synthetic Lipid Membrane Channels Formed by Designed DNA Nanostructures. *Science* **2012,** *338* (6109), 932-936.
40. List, J.; Weber, M.; Simmel, F. C., Hydrophobic Actuation of a DNA Origami Bilayer Structure. *Angewandte Chemie International Edition* **2014,** *53* (16), 4236-4239.
41. Kapanidis, A. N.; Laurence, T. A.; Lee, N. K.; Margeat, E.; Kong, X.; Weiss, S., Alternating-Laser Excitation of Single Molecules. *Accounts of Chemical Research* **2005,** *38* (7), 523-533.
42. Lee, N. K.; Kapanidis, A. N.; Wang, Y.; Michalet, X.; Mukhopadhyay, J.; Ebright, R. H.; Weiss, S., Accurate FRET Measurements within Single Diffusing Biomolecules Using Alternating-Laser Excitation. *Biophysical Journal* **2005,** *88* (4), 2939-2953.

43. Preus, S.; Noer, S. L.; Hildebrandt, L. L.; Gudnason, D.; Birkedal, V., iSMS: single-molecule FRET microscopy software. *Nature Methods* **2015,** *12* (7), 593-594.
44. Khmelinskaia, A.; Mücksch, J.; Petrov, E. P.; Franquelim, H. G.; Schwille, P., Control of Membrane Binding and Diffusion of Cholesteryl-Modified DNA Origami Nanostructures by DNA Spacers. *Langmuir* **2018,** *34* (49), 14921-14931.
45. Ohmann, A.; Göpfrich, K.; Joshi, H.; Thompson, R. F.; Sobota, D.; Ranson, N. A.; Aksimentiev, A.; Keyser, U. F., Controlling aggregation of cholesterol-modified DNA nanostructures. *Nucleic Acids Research* **2019,** *47* (21), 11441-11451.
46. Singh, J. K. D.; Darley, E.; Ridone, P.; Gaston, J. P.; Abbas, A.; Wickham, S. F. J.; Baker, M. A. B., Binding of DNA origami to lipids: maximizing yield and switching via strand displacement. *Nucleic Acids Res* **2021,** *49* (19), 10835-10850.
47. Pfeiffer, I.; Höök, F., Bivalent Cholesterol-Based Coupling of Oligonucletides to Lipid Membrane Assemblies. *Journal of the American Chemical Society* **2004,** *126* (33), 10224-10225.
48. Stengel, G.; Simonsson, L.; Campbell, R. A.; Höök, F., Determinants for Membrane Fusion Induced by Cholesterol-Modified DNA Zippers. *The Journal of Physical Chemistry B* **2008,** *112* (28), 8264-8274.
49. Dresser, L.; Graham, S. P.; Miller, L. M.; Schaefer, C.; Conteduca, D.; Johnson, S.; Leake, M. C.; Quinn, S. D., Tween-20 Induces the Structural Remodeling of Single Lipid Vesicles. *The Journal of Physical Chemistry Letters* **2022,** *13* (23), 5341-5350.

5. Conclusion and Outlook

This dissertation explored the integration of DNA origami technique with the principles of single-molecule fluorescence resonance energy transfer (sm-FRET) in order to develop biosensors specifically designed as particle curvature sensors and lipid vesicle sensors. The combination of the precision of DNA origami and the high sensitivity of sm-FRET has resulted in two key projects that can be potential platforms for particle characterization, cell membrane curvature detection, vesicle sensing and targeted cargo transport systems.

In Section 3, we exploited an alternative, non-destructive approach to particle characterization using DNA origami curvature sensors. Being an essential characterization parameter, particle size plays crucial roles in defining both inherent and operational features of materials. For example, as a compelling drug delivery platform and representative cell membrane models, lipid nanoparticles require precise size control. This need becomes even more critical considering the influence of curvature changes in cellular membranes on various biological functions. Existing techniques, such as dynamic light scattering (DLS) and electron microscopy, offer valuable insight into particle size, but they present several challenges. For example, laser diffraction methods are limited by their low sensitivity and resolution. As an ensemble method, DLS not only suffers from resolution problems, but is also significantly affected by the presence of large aggregates influencing the scattering intensities.[112-114] TEM or SEM techniques have the drawback of being performed in vacuum.[114] It is additionally important to measure the particle size on the nanoscale by developing cost-effective, rapid and sufficiently precise systems, since it is very difficult to track dynamic changes on submicron structures due to resolution limitations. With the influence of particle size in fields ranging from materials science to medicine, the need for accurate, reliable measurement systems is undeniable.

Addressing this we designed adaptable curvature sensors as precise particle size measurement tools utilizing DNA origami nanotechnology. These sensors featured two rigid blocks, a flexible hinge and specific binding sites at a set distance from the hinge. By combining this with sm-FRET, we introduced a novel approach to curvature sensing. Our

sensors were tested on various structures, including DNA origami templates of different shapes, solid silica particles and large unilamellar vesicles (LUVs). A variety of interaction methods, including DNA hybridization, biotin-NeutrAvidin bonding and cholesterol integration into lipid membranes demonstrated the versatility of the system. The performance of the sensors was further evaluated under varying salt conditions of NaCl and $MgCl_2$. In every test, the FRET values were in line with the expectations. An appealing aspect of the DNA origami curvature sensors was their modular design, which offered flexibility in tuning their dynamic range. Adjustments were made, for instance, in the location of the attachment chemistry or in the positioning of the FRET pair. Depending on the position of the FRET pair, the working principle of the sensors could even be reversed. Initially placing the dyes at a larger horizontal distance and moving them closer as the structure bends showed how the sensors can be tuned in a FRET ON or FRET OFF configuration. We could successfully measure nanoparticles within a size range of 50-300 nm and a bending angle range of 50-180° with the DNA origami curvature sensors.

In the follow-up experiments, we aimed to use the DNA origami curvature sensors in the detection of dynamic size changes of particles. The idea here was to utilize lipid vesicles and create osmotic imbalances in order to make them shrink or swell. The following agents were used in order to create osmotic pressure imbalances; salts, PEG or sucrose. While sucrose and PEG did not induce any change in in the sizes of LUVs, it was observed that salt concentration had a direct effect on DNA origami nanostructures. Probably due to the relative stiffness of LUVs due to their small size and the biotin modification, the osmotic shocks had no effect on the size of LUVs. Furthermore, because the natural behavior of LUVs can be affected by forces such as strong binding from the biotin-avidin interaction, electrical attraction and repulsion, and subtler forces such as van der Waals forces, performing these assays on the samples immobilized on the glass coverslips presented additional challenges. The switch from surface measurements to solution measurements was not helpful due to other issues that the sensors encountered in solution environment. In particular, the sensors had difficulty binding to the LUVs due to their preferred bent conformation while they were diffusing freely in solution.

Moving forward, the next goal was to explore the potential of the DNA origami curvature sensors in cellular biology research. The initial tests with HeLa cells highlighted both the

complexities and promising potential of this research direction. While it was possible to attach the curvature sensors to cell membranes via cholesterol anchors, they mostly appeared to be flat against the cell surfaces, which is probably beyond the range of the sensors. However, in areas where the curvature of the cells was particularly pronounced, our sensors did indicate possible variations in the fluorescence lifetime. The use of HeLa cells was a first step in exploring the ways to use DNA origami curvature sensors in biological applications.

We see the precision of DNA origami curvature sensors as a valuable tool for studying complex cellular structures such as neurons and important biological particles like exosomes. Given the medical importance of exosomes, our sensors may provide new ways to characterize them, leading to new treatments and diagnostic methods. Furthermore, attaching sensors inside endocytic vesicle membranes might help better understand how these internalized structures function. Additionally, the correlation of membrane curvatures with protein and receptor accumulations can provide a new perspective on membrane biophysics. Our current research presents an alternative method for nanoparticle analysis. Although there are challenges ahead, further development of the DNA origami curvature sensors has the potential to be impactful in nanotechnology and cellular biology.

In section 4, by combining the accuracy of DNA origami with the sensitivity of sm-FRET, we introduced DNA origami vesicle sensors using hydrophobic interactions for the detection of lipid vesicles. Cellular activities hinge on a complex web of precise molecular interactions, and biosensors have been engineered to detect and quantify these interactions. In that context, the detection of lipid vesicles is an important aspect because of their critical role in a variety of cellular activities, from endocytosis to intercellular communication. In another aspect, molecular cargo transport and drug delivery are central to many biological and therapeutic processes, ensuring the targeted movement of biomolecules and medicines within organisms. Biosensors play a crucial role in these areas, offering real-time insights into the transported materials. In light of the growing emphasis on lipid vesicle detection based on specific molecular interactions as well as cargo transport in medical applications, the goal in this study was to provide an alternative technology for lipid vesicle detection and molecular cargo transport.

The design of the vesicle sensors was based on a hydrophobic ATTO647N labeled ssDNA protrusion from a rectangular DNA origami and strategic placement of cholesterol anchors. Through a series of systematic experiments, we observed a critical conformational change in the ssDNA leash of the sensor in response to the presence or absence of vesicles which was quantified by pronounced shifts in FRET efficiencies. Notably, the control experiments using the hydrophilic AlexaF647 fluorophore showed no difference in FRET efficiency, confirming the findings regarding the unique interaction between the ATTO647N fluorophore and the LUVs. The system was further fine-tuned by adjusting the proximity of the cholesterol anchors, which revealed the sensitivity of the system to the size of the vesicles. An impressive component of the system was its ability to transport cargo: using a strand displacement reaction mechanism, the ATTO647N probe could be released and anchored to LUVs, demonstrating the potential of the system to go beyond vesicle detection. The incorporation of strand displacement reactions into DNA nanotechnology offers a dynamic method for applications in biosensing, information processing and therapeutic interventions. However, there are challenges to this potential. The kinetics of strand displacement, especially in complex designs, can be unpredictable, creating the risk of unintended or "leakage" reactions.[208-211] The need for careful DNA sequence design to avoid unwanted secondary structures or interactions while maintaining specificity adds further complications.

The vesicle sensors of this study provide a valuable insight into the design of precise and efficient molecular tools as molecular machines continue to dominate the focus of advanced research. It is conceivable that, with further refinement and optimization, these vesicle sensors could be designed for diverse applications ranging from targeted drug delivery to real-time monitoring of cellular processes or biological interactions. In addition, by diversifying the range of fluorophores and molecular anchors, this technology could contribute to the development of a variety of sensors that respond to a wide range of molecular cues. In the rapidly growing field of nanotechnology, the combination of DNA origami with molecular sensing and cargo transport, as presented in this study, is set to influence future nanoscale research.

Reviewing the research results, this dissertation has highlighted a wide array of potential applications. The developed systems show promise beyond their immediate

applications. These DNA origami systems could be employed for accurate drug delivery, especially targeting cancer cells or specific tissues. Moreover, the biosensors might become valuable diagnostic tools, aiding in early disease detection and treatment. As nanotechnology progresses, integrating our systems with new technologies will further extend their applicability. For instance, merging these sensors with microfluidic technologies might result in compact labs-on-a-chip, revolutionizing diagnostics and research methods. Another potential avenue is coupling the sensors with AI for real-time data analysis, facilitating better treatment choices.

Yet, key challenges include ensuring reproducibility and scalability without compromising functionality. The delicate nature of DNA origami makes it susceptible to environmental conditions such as temperature, pH, and ionic strength, demanding rigorous stability across physiological environments. Additionally, while the sensors have shown specificity in controlled settings, their performance in complex biological systems remains untested. Cost-effectiveness, biocompatibility, potential off-target effects and integration with other systems further add layers of complexity. Navigating this complex landscape requires a fusion of nanotechnology, molecular biology and engineering, promising a new era of molecular precision in areas such as personalized medicine and biotechnology. In addition, scaling these sensors for real-world applications, optimizing their stability in different physiological environments, and ensuring their biocompatibility are major challenges that remain to be solved.

This dissertation contributes to our understanding in nanobiotechnology, introducing platforms and methodologies that have the potential to impact different fields including materials science and diagnostics. As typical in research, new solutions lead to additional questions, prompting continuous investigation.

The merge of biology and technology is poised to significantly influence health. Utilizing DNA origami and the sensitivity of sm-FRET highlights potential advancements in biosensors. This work provides a base for future research to further exploit the power of these methods.

6. Appendix for Sections 3&4

6.1. Buffers, recipes and folding programs of the DNA Origami Nanostructures

Table 1. Buffers with corresponding recipes.

Buffer	Recipe
FOB17.5	10 mM Tris-HCl, 1 mM EDTA, 17.5 mM $MgCl_2$
FOB12.5	10 mM Tris-HCl, 1 mM EDTA, 12.5 mM $MgCl_2$
FOB20	5 mM Tris-HCl, 1 mM EDTA, 20 mM $MgCl_2$, pH 8.0
PEG Buffer	12% PEG-8000 (w/v), 10 mM Tris, 1 mM EDTA, 500 mM NaCl, 12 mM $MgCl_2$, pH 7.5
LUV Buffer	5 mM Tris-HCl, 1 mM EDTA, 0.5 mM Trolox and 650 mM NaCl, pH 7.0
AlexaF-Buffer	10 mM Tris-HCl, 1 mM EDTA,1 % (wt/v) D-(+)-glucose, 165 units/mL glucose oxidase, 2170 units/mL catalase, 1 mM Trolox, 12.5 mM $MgCl_2$
FRET Buffer	10 mM Tris-HCl, 1 mM EDTA,1 % (wt/v) D-(+)-glucose, 165 units/mL glucose oxidase, 2170 units/mL catalase, 1 mM Trolox, 12.5 mM $MgCl_2$
PCA/Trolox12	2 mM Trolox (6-hydroxy-2,5,7,8-tetramethylchroman-2-carboxylic acid) 25 mM PCA (protocatechuic acid) 2 M NaCl 40 mM Tris base 20 mM acetic acid 1 mM EDTA-$Na_2{\cdot}2H_2O$
50x PCD	2.8 mM PCD (protocatechuate 3,4-dioxygenase from pseudomonas sp.) 50% glycerol 50 mM KCl 100 mM Tris HCl 1 mM EDTA-$Na_2{\cdot}2H_2O$

Table 2. The list of scaffold strands, folding programs, folding buffers and purification techniques of the corresponding the DNA origami nanostructures.

DNA Origami Nanostructure	Scaffold	Folding Program	Folding buffer	Purification technique
Curvature sensor	p7560	1	FOB17.5	Gel electrophoresis
Half, Quarter, Linear	P7249	1	FOB20	PEG precipitation
NRO (Vesicle sensor)	P7249	2	FOB12.5	PEG precipitation
12HB	p8064	1	FOB12.5	Filtration

Table 3. Details of the DNA origami nanostructure folding programs.

Folding program (1) for curvature sensor, Half-Quarter-Linear and 12HB DNA origami nanostructures

Temperature (°C)	Time per °C (min)	Temperature (°C)	Time per °C (min)
65	2	44	75
64-61	3	43	60
60-59	15	42	45
58	30	41-39	30
57	45	38-37	15
56	60	36-30	8
55	75	29-25	2
54-45	90	4	Storage

Folding program (2) for NRO (vesicle sensor) DNA origami nanostructures

Temperature (°C)	Time per °C (min)
90	15
80-20	1
4	storage

Table 4. Reagents with the concentrations used in the folding mixture of DNA origami nanostructures.

DNA origami curvature sensors:

Reagent	Concentration (μM)
Scaffold	0.02
Core staples	0.2
Dye staples	0.6
PAINT docking staples	0.6
Biotin staples	2.0
Bridging staples	2.0

Half-Quarter-Linear DNA origami nanostructures:

Reagent	Concentration (μM)
Scaffold	0.02
Core staples	0.2
Side staples	0.2
Biotin staples	0.6
Binding staples	0.6

12HB DNA origami nanostructures:

Reagent	Concentration (μM)
Scaffold	0.02
Core staples	0.2
Biotin staples	0.4
Binding staples	0.4

NRO DNA origami nanostructures:

Reagent	Concentration (μM)
Scaffold	0.03
Core staples	0.3
Biotin staples	0.6
Binding staples	0.6

DNA origami vesicle sensors:

Reagent	Concentration (μM)
Scaffold	0.025
Core staples	0.25
Dye staples	0.75
Biotin staples	0.75

6.2. Materials and methods

6.2.1. Design, Synthesis and Purification of the DNA Origami Nanostructures

For all the DNA origami nanostructures used throughout this thesis, the detailed list of DNA staples can be found in the supplementary information of the related publications which are in Sections 8 and 9. For the details of all the buffers mentioned, please refer to Table 1 in Section 7.1.

The DNA origami curvature sensors of this thesis consisted of a 46-helix bundle with a hexagonal lattice structure. The design was based on the p7560 scaffold derived from M13mp18 bacteriophages and was created using caDNAno (version 2.2.0).[69] In order to design the nanostructures, initial 3D models were predicted using CanDo.[212, 213] The design incorporated positions for attaching fluorophores, anchoring moieties (biotins, ssDNA, or cholesterols), bridging staples and PAINT docking staples. The edges of each helical bundle were kept as single-stranded segments to avoid potential blunt-end interactions.

The necessary staples for origami preparation were supplied from IDT (Integrated DNA Technologies, Inc.), including the single-stranded M13mp18 scaffold plasmid (p7560) and high-purity salt-free (HPSF) purified unmodified staple oligonucleotides. Additionally, oligonucleotides labeled with ATTO647N and Cy3B (both HPLC-purified) for various positions, as well as 5'- and 3'-cholesterol-labeled and 5’ and 3’-biotin labeled oligonucleotides, were obtained from Eurofins Genomics.

The folding of all DNA origami structures was performed using a one-pot reaction mix. This involved mixing 20 nM scaffold DNA, a 10-fold excess of unmodified oligonucleotides, a 30-fold excess of fluorophore-labeled oligonucleotides, and a 100-fold excess of bridging and biotinylated oligonucleotides relative to the scaffold concentration. The folding was carried out in a folding buffer composed of 1xTE and 17.5 mM $MgCl_2$, following a multistep thermocycler protocol (refer to Table 3 for details).

In addition to the curvature sensors, other DNA origami nanostructures used as model testing platforms, including 12HB, Half-Quarter-Linear and NRO, were synthesized using

the corresponding scaffold strands and temperature programs indicated in Table 2. The modifications of the DNA nanostructures were arranged using caDNAno (version 2.2.0), and the modified staple strands were purchased from IDT. The folding of these DNA nanostructures followed specific multistep thermocycler protocols outlined in Table 3, with the scaffold strand and the staple strands mixed as specified in Table 4, using the corresponding folding buffer mentioned in Table 2.

The DNA origami vesicle sensors were based on a 7249 nt scaffold from the M12nm18 bacteriophage. It is crafted from a rectangular DNA origami nanostructure (NRO) with the dimensions of 70 x 100 nm. Further modifications for the experiments were designed using caDNAno.[69] Mainly, the structure has a 12 nucleotide (nt) single-stranded DNA (ssDNA) leash, modified with an ATTO647N fluorophore, which acts as the primary probe for vesicle detection. It further involves staples strands with fluorophore, biotin and cholesterol modifications for vesicle sensing. Staple strands with fluorophores ATTO647N and ATTO542 were supplied from Biomers GmbH. Unmodified staple oligonucleotides and those for strand displacement reaction were purchased from IDT. 3' Biotin, 5' Cholesterol-TEG labeled oligos and an AlexaF647 control probe were provided by Eurofins Genomics GmbH.

After folding, the DNA origami nanostructures were purified using different methods depending on the specific structure (Table 2). Gel electrophoresis purification involved adding 1x Blue Juice gel loading buffer (Thermo Fisher Scientific) to the folded DNA origami solution, followed by purification via agarose-gel electrophoresis using a 2.5% agarose gel containing ROTIGelStain (Roth) in the gel buffer. The gel was run at 60 V for 90 minutes while cooled in an ice bath. The bands containing the DNA origami nanostructures were then cut from the gel and collected by squeezing with a glass slide.

For PEG precipitation purification, the sample was mixed with a 1:1 ratio of PEG buffer and centrifuged for 30 minutes at 16.000 g at 4°C. The supernatant was discarded, and the pellet was dissolved in the corresponding folding buffer. This step was repeated three times. For DNA origami structures labeled with cholesterol moieties, the folded structures were incubated overnight with cholesterol-labeled oligonucleotides (10x excess per DNA origami nanostructure concentration) purchased from Eurofins Genomics GmbH. The resulting mixture was further purified using PEG precipitation.

Filter purification was carried out using Amicon Ultra filters (100 K, Merck, Germany). The samples were centrifuged at 10.000 g and 4°C for 5 minutes, with three washing steps. Afterward, the filter was inverted and placed into a new collection tube. The purified samples were collected by centrifugation at 1.000 g for 2 minutes.

The final concentration of all prepared DNA origami samples was determined using a Nanodrop 2000 spectrophotometer (Thermo Fisher Scientific), and the nanostructures were stored at -18°C until they were used.

6.2.2. Preparation of Silica Particles

Silica particles of the DNA origami curvature sensors project were purchased from Polysciences Europe GmbH in three different sizes (50 nm, 100 nm and 300 nm). Prior to use, the particles were subjected to a 10-minute sonication process using the Elmasonic P ultrasonic cleaner from Elma Schmidbauer GmbH. To facilitate functionalization, the particles were mixed with biotinylated-BSA from Thermo Fisher Scientific Inc. in a 1:1 ratio (10 mg/ml) and incubated at 4°C for 30 minutes. Excess, unbound biotinylated-BSA was removed by filtration using 100 K Amicon Ultra filters. The samples were then subjected to three washing steps, with each step involving centrifugation at 10.000 g and 4°C for 5 minutes. The resulting purified samples were collected by centrifugation at 1.000 g for 2 minutes.

6.2.3. Preparation of Lipid Vesicles

All lipids were purchased from Avanti Polar Lipids (Alabaster, AL, USA), unless otherwise stated. Large unilamellar vesicles (LUVs) of the DNA origami curvature sensors project composed of DOPC (1,2-dioleoyl-sn-glycero-3-phosphocholine) containing Biotinyl-cap-PE (1,2-dioleoyl-sn-glycero-3-hosphoethanolamine-N-(cap biotinyl)) in 99:1 percent ratio. For the experiments with DNA origami vesicle sensors, the LUVs were produced using 100% DOPC.

Briefly, the corresponding lipids dissolved in chloroform were dried under a nitrogen stream, and the remaining chloroform was evaporated under vacuum application for ~3 hours in a desiccator. The produced lipid film was rehydrated in LUV buffer resulting in a lipid concentration of 0.5 mM. After seven freeze-and-thaw cycles using liquid nitrogen and a 70°C water bath, the solution was extruded with a LiposoFast Basic extruder (Avestin, INC.) using Nucleopore PC membranes with different pore sizes ranging from 50 nm to 200 nm (Whatman, Cytiva Ltd.).

6.2.4. Surface Preparation

The microscope coverslips used in these studies were obtained from Carl Roth GmbH in Germany, with dimensions of 24 mm × 60 mm and a thickness of 170 µm. Prior to use, these coverslips were subjected to a cleaning process using a UV-Ozone cleaner (PSD-UV4, Novascan Technologies, USA). The cleaning was performed at a temperature of 100 °C for a duration of 30 minutes. Subsequently, the cleaned glass coverslips were affixed with self-adhesive 150 µl SecureSeal Hybridization Chambers obtained from Grace Bio-Labs.

For passivation of the glass coverslips, biotinylated-BSA from Thermo Fisher Scientific Inc. (1.0 mg/ml) was added and allowed to incubate for 15 minutes. This was followed by further functionalization using NeutrAvidin from Thermo Fisher Scientific Inc. (1.0 mg/ml), with an additional incubation period of 15 minutes. After each incubation step, the coverslips were washed three times using 1× PBS buffer.

The preparation of various surfaces was carried out according to the methods described in the subsequent sections.

6.2.4.1. Surfaces for DNA Origami Curvature Sensors

Flat surface:

For the preparation of flat surfaces, the curvature sensors with a concentration of approximately 50 pM were immobilized directly onto NeutrAvidin-functionalized glass coverslips using biotin modifications. This immobilization process was carried out in a buffer consisting of 1x TE, 17.5 mM $MgCl_2$ and 750 mM NaCl.

Surface with DNA Nanostructures:

To prepare the surface with alternative DNA origami nanostructures, the nanostructures were diluted to approximately 100 pM using the corresponding folding buffer. Subsequently, these DNA origami nanostructures were immobilized on NeutrAvidin-functionalized glass coverslips. After immobilization, the coverslips were washed three times using the corresponding folding buffer. Following the washing steps, curvature sensors with a concentration of approximately 50 pM were immobilized onto the surface through DNA hybridization. This was done in a buffer containing 1x TE, 17.5 mM $MgCl_2$ and 750 mM NaCl.

Surface with Silica Particles:

To prepare the curved surface with silica particles, the filtered Biotinylated-BSA coated silica particles were diluted 10x times using 1x PBS buffer. These diluted silica particles were then immobilized on NeutrAvidin-functionalized glass coverslips for a duration of 30 minutes. Following a washing step using 1x PBS buffer, a NeutrAvidin incubation step was carried out for 15 minutes, using a concentration of 1 mg/ml, in order to bind to the biotin molecules on the silica particles and ensure complete coverage. Subsequently, the coverslips were exposed to another washing step using 1x PBS buffer. Finally, curvature sensors with a concentration of approximately 50 pM were immobilized onto the surface through biotin modifications in a buffer containing 1x TE, 17.5 mM $MgCl_2$ and 750 mM NaCl.

Surface with Lipid Vesicles:

To prepare the surface with lipid vesicles, the biotinylated vesicles of corresponding size were diluted to a vesicle concentration of 100 pM using the LUV buffer. These diluted vesicles were then immobilized on NeutrAvidin-functionalized glass coverslips for approximately 2 minutes. Following the immobilization step, the coverslips were washed three times using the LUV buffer. Subsequently, a NeutrAvidin incubation was carried out for 15 minutes, using a concentration of 1.0 mg/ml. This incubation allowed the NeutrAvidin to bind to the biotin molecules on the vesicles, effectively covering them. Afterwards, the coverslips were subjected to another washing step using the LUV buffer. Finally, curvature sensors with a concentration of approximately 50 pM were immobilized onto the surface using biotin/cholesterol modifications in the LUV buffer.

Surface with HeLa cells:

HeLa cells (ATCC) were cultured in DMEM (Gibco, No. 11965084) medium supplemented with 10% Fetal Bovine Serum (FBS, Gibco, No. 10500064) and 1% Pencillin Streptomycin (Gibco, No. 15140122). Cells were passaged biweekly using 0.05% Trypsin EDTA (Gibco, No. 25300054). For the fluorescence lifetime imaging microscopy (FLIM) experiments with DNA origami curvature sensors, HeLa cells were seeded on ibidi eight-well glass-bottom chambers (No. 80827) at a density of 25000 cells per cm^2 and allowed to adhere for 1 hour. Prior to imaging, cells were fixed using Methanol (4°C) for 10 min, followed by three times of washing with PBS.

DNA origami curvature sensors modified with cholesterol anchors at 6 nm distance to the hinge position were used to be anchored to HeLa cells. In order to minimize nonspecific adherence of the sensors, cell surfaces were passivated using a 4 mg/mL BSA solution, followed by three times washing with PBS. DNA origami curvature sensors were then immobilized onto the prepared cell surfaces at a concentration of 1 nM in LUV buffer. The surface density of the sensors was verified under the confocal microscope, followed by three additional washes with LUV buffer to remove any unbound sensors.

6.2.4.2. Surfaces for DNA Origami Vesicle Sensors

Similar to the flat surface preparation of the curvature sensors, the vesicle sensor surfaces were prepared by immobilizing approximately 50 pM of the DNA origami nanostructures directly onto NeutrAvidin-functionalized glass coverslips using biotin modifications. This immobilization process was carried out in the LUV buffer.

For the experiments with lipid vesicles, the vesicles of corresponding size were diluted to a vesicle concentration of 1 nM using the LUV buffer. These diluted vesicles were then immobilized on vesicle sensor covered glass coverslips for approximately 30 minutes. Following the immobilization step, the coverslips were washed three times using the LUV buffer.

6.3. Imaging and Data Analysis

6.3.1. Single-Molecule FRET Imaging and Data Analysis

To conduct fluorescence measurements for DNA origami curvature sensors and vesicle sensors, different buffer conditions were used.

For the experiments of DNA origami curvature sensors with flat surfaces, with silica particles and with DNA origami platforms, the buffer was exchanged to the FRET buffer. This FRET buffer was designed to enhance the photostability of the fluorophores and included a reducing and oxidizing system (ROXS)[214] as well as oxygen scavenging agents all sourced from Sigma Aldrich. It utilized a reducing and oxidizing system consisting of trolox (Sigma Aldrich) and troloxquinone[215], with approximately 12% of the trolox being converted to troloxquinone under UV light. For the fluorescence measurements involving lipid vesicles, the LUV buffer was used instead of the FRET buffer.

For the fluorescence measurements of the DNA origami vesicle sensors, all the experiments (without and with lipid vesicles) were performed using the LUV buffer.

All the sm-FRET measurements were performed using a commercial Nanoimager S from ONI Ltd. in the UK, utilizing Total Internal Reflection Fluorescence (TIRF)

illumination. Red excitation was employed at a wavelength of 638 nm, while green excitation was set at 532 nm. To begin, the objective was initially focused on the sample plane, and the auto-focus function was activated. The light program was configured for alternating laser excitation, utilizing green and red lasers with the corresponding power outputs listed in Table 5. For each sample, approximately 10 videos were recorded within a large field of view measuring 50 µm × 80 µm. Each video had an exposure time of 100 ms per frame, with a total length of 500 frames (equivalent to 50 seconds).

Table 5. The laser power outputs for the corresponding experiments.

Experiment	Green Laser Power	Red Laser Power
Curvature sensor	15 mW	20 mW
Vesicle sensor	5 mW	8 mW

For the FRET data analysis, the iSMS[216] software was utilized, running on MATLAB. The analysis involved superimposing the individual green and red emission channels. The peakfinder algorithm was applied to locate donor and acceptor peaks, enabling the identification of FRET-pairs. From the recorded movies, intensity-time transients of individual immobilized molecules were extracted. These single-molecule transients were further analyzed to identify DNA origami structures exhibiting FRET. The FRET correlation between different channels, such as I_{DD} (donor excitation-donor emission), I_{DA} (donor excitation-acceptor emission) and I_{AA} (acceptor excitation-acceptor emission), was investigated. When observing a simultaneous intensity increase in the I_{DD} channel and a decrease in the I_{DA} channel coinciding with a spontaneous drop in the I_{AA} channel, the corresponding transient was selected for further analysis. The mean FRET efficiency for each sensor was quantified as in the following equation by using the intensity information from the I_{DD} and I_{DA} channels for each molecule throughout the entire energy transfer period:

$$FRET\ efficiency = \frac{I_{DA}}{\gamma \cdot I_{DD} + I_{DA}}$$

The I_{DA} signal is further corrected to account for the contribution of direct acceptor

excitation at the donor excitation wavelength and the leakage of donor emission into the acceptor emission channel. This corrected I_{DA} is calculated as follows:

$$I_{DA} = I_{DA,raw} - D_{leakage} \cdot I_{DD} - A_{direct} \cdot I_{AA}$$

where $I_{DA,\,raw}$ is the total intensity measured in the acceptor emission channel, I_{AA} is the direct acceptor excitation.

When applicable, the correction factors $\boldsymbol{\gamma}$, $\mathbf{D_{leakage}}$ and $\mathbf{A_{direct}}$, are calculated as follows:

$D_{leakage}$ accounts for the amount of leakage of the donor emission into the acceptor emission channel upon donor excitation. It is calculated by taking the average ratio of the intensity in the acceptor emission channel ($\mathbf{I_{DA}(t)}$) to the intensity in the donor emission channel ($\mathbf{I_{DD}(t)}$) during the time interval after the acceptor was bleached and before the donor was bleached, representing a donor-only signal. It can be expressed as:

$$D_{leakage} = avg\left(\frac{I_{DA}(t)}{I_{DD}(t)}\right)$$

A_{direct} accounts for the direct excitation of the acceptor at the donor wavelength. It is calculated by taking the average ratio of the intensity in the acceptor emission channel ($\mathbf{I_{DA}(t)}$) to the intensity in the acceptor emission channel under direct acceptor excitation ($\mathbf{I_{AA}(t)}$) during the time interval after the donor was bleached and before the acceptor was bleached. This time interval captures the signal corresponding to direct excitation of the acceptor. The calculation of $\mathbf{A_{direct}}$ is:

$$A_{direct} = avg\left(\frac{I_{DA}(t)}{I_{AA}(t)}\right)$$

The $\boldsymbol{\gamma}$ correction factor quantifies the relative difference in the number of photons measured between the acceptor and the donor for the same number of excited states. It takes into account the varying quantum yields of the dyes and the wavelength-dependent detection efficiencies of the detector. In the iSMS software, $\boldsymbol{\gamma}$ was calculated for all molecules where the acceptor bleached prior to the donor as the following:

$$\gamma = \frac{I_{DA,1} - I_{DA,2}}{I_{DD,2} - I_{DD,1}}$$

Mean values for all the correction factors were determined by averaging the values obtained from individual transients. These average correction factors were then used in the calculations of FRET efficiency.

6.3.2. Fluorescence Lifetime Imaging Microscopy of Curvature Sensors with HeLa cells

FLIM experiments on HeLa cells are performed on a home-built confocal microscope based on an Olympus IX71 inverted microscope. DNA-origami structures are excited by pulsed lasers (636 nm, LDHD-C-640; 532 nm, LDH-P- FA-530B; both PicoQuant GmbH) in a pulsed interleaved excitation (PIE)[217] pattern with a repetition rate of 20 MHz and a laser pulse offset of 25 ns. The lasers are coupled into a single mode fiber (P3-488PM-FC, Thorlabs GmbH) to obtain a Gaussian beam profile and to perfectly overlay the two excitation beams. Circular polarized light is obtained by combining a linear polarizer (LPVISE100-A, Thorlabs GmbH) and a consecutive quarter-wave plate (AQWP05M- 600, Thorlabs GmbH). The light is focused onto the sample using an oil-immersion objective (UPLSAPO100XO, NA 1.40, Olympus Deutschland GmbH). The position of the sample is adjusted using a piezo stage (P-517.3CD, Physik Instrumente (PI) GmbH & Co. KG) and controller (E-727.3CDA, Physik Instrumente (PI) GmbH & Co. KG). The emission light is separated from the excitation beam by a dichroic beamsplitter (zt532/640rpc, Chroma) and focused onto a 50 µm diameter pinhole (Thorlabs GmbH). After the pinhole, the donor and acceptor signals are separated by a dichroic beamsplitter (640 LPXR, Chroma) into a green (Brightline HC582/75, AHF; RazorEdge LP 532, Semrock) and red (SP 750, AHF; RazorEdge LP 647, Semrock) detection channel. Emission is focused onto avalanche photodiodes (SPCMAQRH-14-TR, Excelitas) and the signals are registered by a time-correlated single photon counting (TCSPC) unit (HydraHarp400, PicoQuant). The setup is controlled by a commercial software package (SymPhoTime64, Picoquant GmbH).

7. Appendix for Section 3

7.1. Supplementary Information

Supporting Information for

DNA origami curvature sensors for nanoparticle and vesicle size determination with single-molecule FRET readout

Ece Büber[a], Tim Schröder[a], Michael Scheckenbach[a], Mihir Dass[b], Henri G. Franquelim[c,d,], and Philip Tinnefeld[a,*]*

[a]Department of Chemistry and Center for NanoScience, Ludwig-Maximilians-University, Butenandtstraße 5−13, 81377, Munich, Germany

[b]Faculty of Physics and Center for NanoScience, Ludwig-Maximilians-University, 80539 Munich, Germany

[c]Max Planck Institute of Biochemistry, Am Klopferspitz 18, 82152, Martinsried, Germany

[d]Interfaculty Centre for Bioactive Matter, Leipzig University, % Deutscher Platz 5 (BBZ), 04109 Leipzig, Germany

Correspondence to henri.franquelim@uni-leipzig.de or philip.tinnefeld@cup.lmu.de

Table of Contents

1. Materials and methods

1.1. Design, production and characterization of the DNA origami nanostructures

The curvature sensing DNA origami nanostructures of this work consist of a 46-helix bundle with hexagonal lattice. The structures utilized the p7560 scaffold derived from M13mp18 bacteriophages and were designed using caDNAno (version 2.2.0) (Figure S2).[1] The initial 3D models were predicted using CanDo.[2, 3] The design includes labeled positions for attaching fluorophores, anchoring moieties (biotins, ssDNA or cholesterols), bridging staples and PAINT docking staples. The edges of each of the helical bundles were kept as single-stranded segments to avoid possible blunt-end interactions. Single stranded M13mp18 scaffold plasmid (p7560) as well as high purity salt free (HPSF) purified unmodified staple oligonucleotides and 5'- and 3'-Biotin-functionalized oligonucleotides were supplied from IDT (Integrated DNA Technologies, Inc.). Further for origami preparation, oligonucleotides labeled with ATTO647N and Cy3B (all HLPC-purified) for several different positions and 5'- and 3' Cholesterol-labeled oligonucleotides were purchased from Eurofins Genomics. Folding of all the DNA origami structures was performed in a one-pot reaction mix. In brief, 20 nM scaffold DNA, a 10-fold excess of unmodified oligonucleotides, 30-fold excess of fluorophore attached oligonucleotides and a 100-fold excess of bridging and biotinylated oligonucleotides in comparison to the scaffold concentration were mixed in the folding buffer (1xTE, 17.5 mM $MgCl_2$) and were subjected to a multistep thermocycler protocol. The details of the folding program can be found in Table S3.

Besides curvature sensors, all the DNA origami nanostructures that were used as model testing platforms (12HB, Half-Quarter-Linear, NRO) were synthesized using the corresponding scaffold strands and temperature programs given in Table S2. Modifications of the DNA nanostructures were arranged using caDNAno (version 2.2.0) and the modified staple strands (Table S8) were purchased from IDT. For the folding of the DNA origami nanostructures, the scaffold strand and the staple strands were mixed as given in Table S4 in the corresponding folding buffer as listed in Table S2 and were subjected to the multistep thermocycler protocols depicted in Table S3.

The folded DNA origami nanostructures were purified either by gel electrophoresis, PEG precipitation or by filter purification (Table S2). For gel electrophoresis, 1x Blue Juice gel loading buffer (Thermo Fischer Scientific) was added to the folded DNA origami solution which was then purified via agarose-gel electrophoresis with 2.5% agarose gel (Biozym LE agarose) containing ROTIGelStain (Roth) in 50 mL of 1xTAE, 12.5 mM $MgCl_2$ buffer. The gel was run at 60 V for 90 minutes cooled in an ice bath. After electrophoresis, the bands in the gel containing the DNA origami nanostructures were cut out and squeezed with a glass slide to extract the purified structures. For PEG precipitation, the sample was mixed in a 1:1 ratio with the PEG buffer (12% PEG-8000 (w/v), 10 mM Tris, 1 mM EDTA, 500 mM NaCl, 12 mM $MgCl_2$, pH 7.5) and centrifuged for 30 min at 16000 g at 4°C. The supernatant was discarded and the pellet was dissolved in the folding buffer which was further mixed with the same amount of PEG buffer. This step was repeated three times. In order to label the curvature sensing DNA origami with cholesterol moieties, the folded structures were incubated with () the cholesterol-labeled oligonucleotides (20x excess per binding site, purchased from Eurofins Genomics GmbH) over night at room temperature and further purified by PEG precipitation. Filter purification was performed using Amicon Ultra filters (100 K, Merck, Germany). The samples were centrifuged for 5 minutes at 10000 g, 4°C with 3 washing steps. After that the filter was inverted and placed into a new collection tube. The purified samples could then be collected by centrifugation for 2 minutes at 1000 g. For all of the prepared DNA origami

samples, the final concentration was determined on a Nanodrop 2000 spectrophotometer (Thermo Fisher Scientific) and the nanostructures were stored at -18°C until usage.

1.2. Preparation of silica particles

The unmodified silica particles of 50 nm, 100 nm and 300 nm size were purchased from Polysciences Europe GmbH. Before use, the particles were sonicated for 10 minutes using Elmasonic P ultrasonic cleaner (Elma Schmidbauer GmbH). Forfunctionalization, they were mixed in a 1:1 ratio with biotinylated-BSA (10 mg/mL Thermo Fisher Scientific Inc.) and incubated for 30 minutes at 4°C. Filtration of the particles was performed using 100 K Amicon Ultra filters in order to get rid of the excess, unbound biotinylated-BSA. The samples were centrifuged for 5 minutes at 10000 g, 4°C with 3 washing steps. The purified samples were collected by centrifugation for 2 minutes at 1000 g.

1.3. Preparation of lipid vesicles

All lipids were purchased from Avanti Polar Lipids (Alabaster, AL, USA), unless otherwise stated. Large unilamellar vesicles (LUVs) composed of DOPC (1,2-dioleoyl-sn-glycero-3-phosphocholine) containing Biotinyl-cap-PE (1,2-dioleoyl-sn-glycero-3-hosphoethanolamine-N-(cap biotinyl)) in 99:1 percent ratio. Lipids dissolved in chloroform were dried under a nitrogen stream, and the remaining chloroform was evaporated under vacuum application for ~3 hours in a desiccator. The produced lipid film was rehydrated in LUV buffer containing 5 mM Tris, 1 mM EDTA, 0.5 mM Trolox and 650 mM NaCl at pH 7.0 resulting in a lipid concentration of 0.5 mM. After seven freeze-and-thaw cycles using liquid nitrogen and a 70°C water bath, the solution was extruded with a LiposoFast Basic extruder (Avestin, INC.) using Nucleopore PC membranes with different pore sizes ranging from 50 nm to 200 nm (Whatman, Cytiva Ltd.).

1.4. Surface preparation

For surface immobilization, glass coverslips were cleaned in 100% Hellmanex® III solution (Hellma GmbH & Co. KG) by ultrasonication for 30 minutes. They were then rinsed with Milli-Q water and dried under nitrogen stream. The 150 µL SecureSeal Hybridization Chambers (Grace Bio-Labs) were fixed on the cleaned glass coverslips with the help of the adhesive side of the chambers.

The glass coverslips were passivated with biotinylated-BSA (1.0 mg/mL, Thermo Fisher Scientific Inc) and further functionalized with NeutrAvidin (1.0 mg/mL, Thermo Fisher Scientific Inc.), both incubated for 15 min and washed three times with 1× PBS buffer after incubation.

Surfaces with different testing platforms are depicted in Figure S1 which were prepared as described in the next sections.

1.4.1. Flat surface

For the flat surface preparation, the curvature sensors (~50 pM) were directly immobilized on NeutrAvidin functionalized glass coverslips via biotin modifications in a buffer containing 1xTE, 17.5mM $MgCl_2$, 750mM NaCl.

1.4.2. Surface with DNA origami nanostructures

For the surface with the alternative DNA origami nanostructures, after diluting to ~100 pM with the corresponding folding buffer, the DNA origami nanostructures were immobilized on NeutrAvidin functionalized glass coverslips. After washing three times with the corresponding folding buffer, ~50 pM curvature sensors were immobilized via DNA hybridization in a buffer containing 1xTE, 17.5 mM $MgCl_2$, 750mM NaCl.

1.4.3. Surface with silica particles

For the curved surface with the silica particles, the filtered Biotinylated-BSA coated silica particles were diluted 10x times with 1xPBS buffer and immobilized on NeutrAvidin functionalized glass coverslips for 30 minutes. After washing with 1xPBS, NeutrAvidin (1 mg/mL) incubation was performed for 15 minutes in order to cover the biotin molecules on the silica particles. The last washing step with 1xPBS was followed by the immobilization of ~50 pM curvature sensors via biotin modifications in a buffer containing 1xTE, 17.5 mM $MgCl_2$, 750 mM NaCl.

1.4.4. Surface with lipid vesicles

For the surface with vesicles, the biotinylated vesicles of corresponding size were diluted to 100 pM with the LUV buffer and immobilized on NeutrAvidin functionalized glass coverslips for ~2 minutes. After washing three times with the LUV buffer, NeutrAvidin (1.0 mg/mL) incubation was performed for 15 minutes in order to cover the biotin molecules on the vesicles. The last washing step with the LUV buffer was followed by the immobilization of ~50 pM curvature sensors via biotin/cholesterol modifications in LUV buffer.

2. Characterization methods

2.1. Transmission electron microscopy (TEM)

The correct folding of the DNA origami nanostructures and the size distribution of silica particles were characterized with transmission electron microscopy (TEM). 5 µL of a sample was incubated for 30 s – 5 min, depending on concentration, on glow discharged TEM grids (formvar/carbon, 300 mesh Cu; Ted Pella) at room temperature. After incubation on the grids, the sample was wicked off by bringing the grid into contact with a filter paper strip. For the DNA nanostructures, a 5 µL drop of uranyl formate staining solution (2% uranyl formate aqueous solution containing 25 mM sodium hydroxide) was applied to the grid, immediately wicked off, followed by applying another 5 µL drop of uranyl formate staining solution. This drop was allowed to incubate on the grid for 10 seconds and then wicked off. The grid was dried for 5 minutes before imaging. Imaging was performed with a JEM1011 transmission electron microscope (JEOL) operated at 80 kV.

The size of the silica particles was analyzed by manual selection of particles using ImageJ (FIJI).[4]

2.2. Dynamic light scattering (DLS)

Size and dispersity of extruded LUV suspensions (at a total lipid concentration of 200 µM in LUV buffer) were determined by dynamic light scattering (DLS). For each sample, 10

cumulative measurements were performed after an incubation time 90 s in disposable polystyrene cuvettes using a Zetaszier Nano ZSP (Malvern Instruments, Worcestershire, United Kingdom) with an incident wavelength of 633 nm and a backscattering detection at 173°. The intensity- and number-normalized size distributions of the various LUV samples were calculated from the correlation functions using the Malvern General Purpose Non-Negative Least Squares (NNLS) algorithm provided on the manufacturer's software (Malvern Zetasizer Software 7.13).

3. Imaging and data analysis

For the fluorescence measurements on a flat surface with silica particles and on the DNA origami platforms, the buffer was exchanged to the FRET buffer containing a reducing and oxidizing system (ROXS)[5] as well as oxygen scavenging agents in order to increase the photostability of the fluorophores. In particular, we used trolox/troloxquinone[6] as the reducing and oxidizing system in a 10mM Tris-HCl, 1 mM EDTA buffer with 1 % (wt/v) D-(+)-glucose (Sigma Aldrich, USA), 165 units/mL glucose oxidase (G2133, Sigma Aldrich, USA), 2170 units/mL catalase (C3155, Sigma Aldrich, USA), 1 mM Trolox (~12% was converted to Troloxquinone under UV light) and 12.5 mM $MgCl_2$. LUV buffer was used for the fluorescence measurements with lipid vesicles.

The single-molecule Fluorescence Resonance Energy Transfer (smFRET) measurements of the curvature sensor were performed on a commercial Nanoimager S (ONI Ltd., UK) with TIRF illumination. Red excitation was applied at 638 nm and green excitation at 532 nm. The objective was first focused into the sample plane and the auto focus was activated. The light program was set to alternating laser excitation of green (15 mW) and red (20 mW) lasers. For each sample, ~15 videos were acquired in a large field of view (50 µm × 80 µm) with 100 ms exposure time per frame with a length of 500 frames (50 seconds).

For the FRET data analysis, the iSMS software that is run on Matlab[7] was used. The individual green and red emission channels were superimposed and with the peakfinder algorithm donor and acceptor peaks were localized and FRET-pairs were defined. Intensity-time transients of individual immobilized molecules were derived from each of the movies. These single-molecule transients were analyzed in order to identify individual DNA origami structures showing FRET. Typical FRET correlation between the channels of I_{DD} (donor excitation-donor emission), I_{DA} (donor excitation-acceptor emission) and I_{AA} (acceptor excitation-acceptor emission) was examined. When an intensity increase in the I_{DD} channel and a decrease in the I_{DA} channel upon spontaneous drop in the I_{AA} channel were observed, the transient was picked and the mean FRET efficiency for each sensor was quantified from the intensity information of data channels I_{DD} and I_{DA} for each molecule over the whole period of the energy transfer as

$$FRET\ efficiency = \frac{I_{DA}}{\gamma \cdot I_{DD} + I_{DA}}$$

The I_{DA} is corrected for direct acceptor excitation at the donor excitation wavelength and leakage of donor emission into the acceptor emission channel. The corrected I_{DA} is calculated as

$$I_{DA} = I_{DA,raw} - D_{leakage} \cdot I_{DD} - A_{direct} \cdot I_{AA}$$

where $I_{DA,\,raw}$ is the total intensity measured in the acceptor emission channel, I_{AA} is the direct acceptor excitation.

Wherever applicable, the correction factors γ, $D_{leakage}$ and A_{direct}, are calculated as in the following:

The $D_{leakage}$ accounts for the amount of leakage of the donor emission into the acceptor emission channel upon donor excitation and is calculated as

$$D_{leakage} = avg\left(\frac{I_{DA}(t)}{I_{DD}(t)}\right)$$

in the time interval after the acceptor was bleached and before the donor was bleached, corresponding to a donor-only signal.

The A_{direct} accounts for the direct excitation of the acceptor at the donor wavelength and is calculated as

$$A_{direct} = avg\left(\frac{I_{DA}(t)}{I_{AA}(t)}\right)$$

in the time interval after the donor was bleached and before the acceptor was bleached.

From individual transients, we calculated average values for all the correction factors and used them for FRET efficiency calculations.

The γ correction factor describes the relative difference in the number of photons measured of the acceptor and the donor for the same number of excited states. It accounts for the different quantum yields of the dyes and the wavelength dependent detection efficiencies of the detector. In iSMS γ was calculated for all molecules in which the acceptor bleached before the acceptor:

$$\gamma = \frac{I_{DA,1} - I_{DA,2}}{I_{DD,2} - I_{DD,1}}$$

From individual transients, we calculated average values for all the correction factors and used them for FRET efficiency calculations.

4. Figures

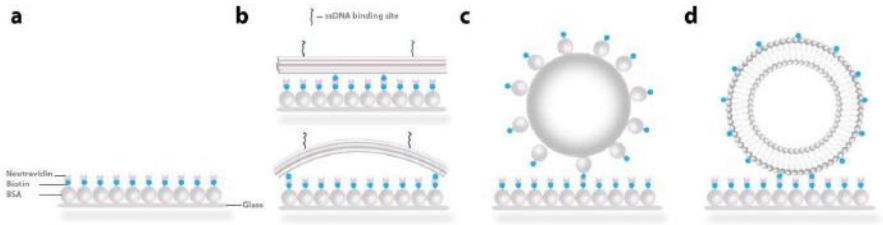

Figure S1. Sketches of surfaces as different testing platforms. **(a)** Flat surface passivated with BSA-Biotin-NeutrAvidin **(b)** Surfaces with flat and curved DNA origami nanostructures **(c)** Surface with silica particles **(d)** Surface with lipid vesicles. All the testing platforms were attached to the passivated glass coverslips via biotin anchoring moieties.

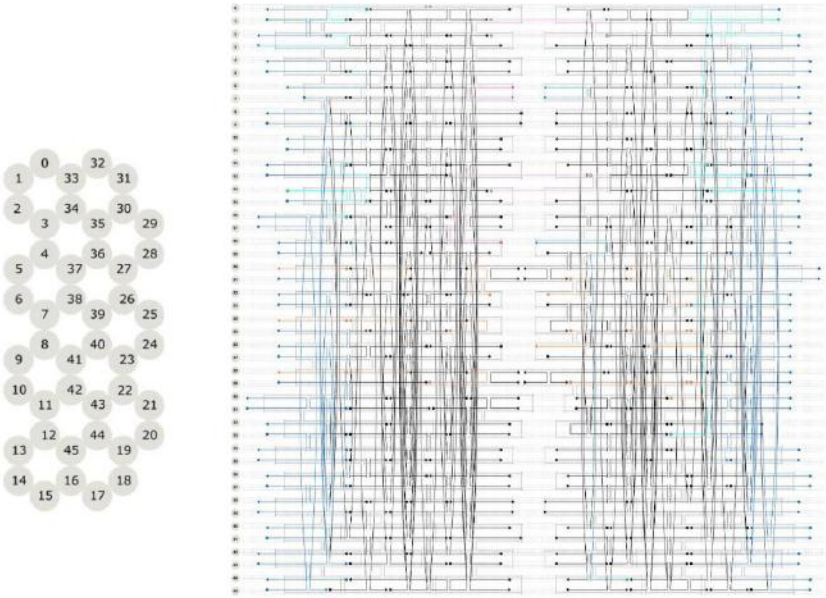

Figure S2. CaDNAno design of the curvature sensor. Zoom in to see details. Donor positions are colored in teal, while acceptor positions are in magenta. Positions of the anchoring moieties are colored in orange, bridging staples are in pink and PAINT docking cites are in cyan. Edge positions and core staples are colored in blue and black respectively, and M13 p7560 scaffold is colored in gray. List of all the unmodified and modified DNA staples that are incorporated in the DNA origami design are found in Table S5 and Table S6.

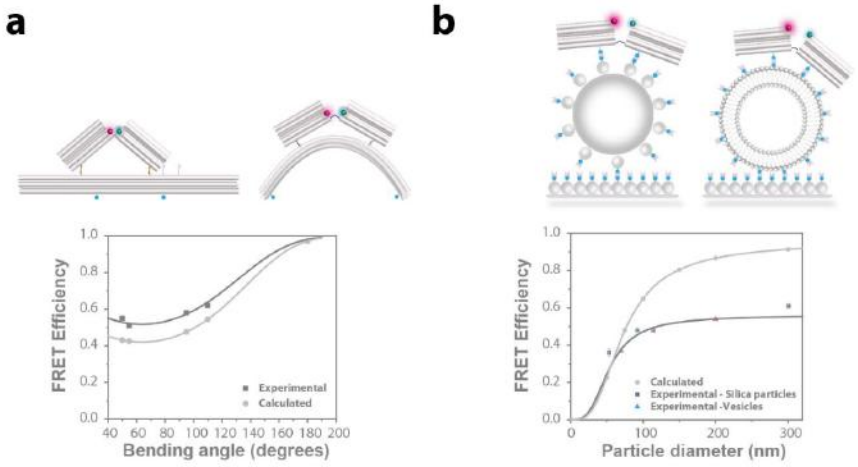

Figure S3. Calibration curves of **(a)** FRET efficiency vs bending angle from the experiments performed with DNA nanostructures **(b)** FRET efficiency vs measured particle diameter from the experiments performed with Silica particles and lipid vesicles. Experimental particle size values are plotted from the TEM data of the silica particles and the DLS data of the lipid vesicles. The error refers to the standard error (SE). The data point for 200 nm particle diameter is masked as we could not obtain a reasonable mean number-normalized diameter.

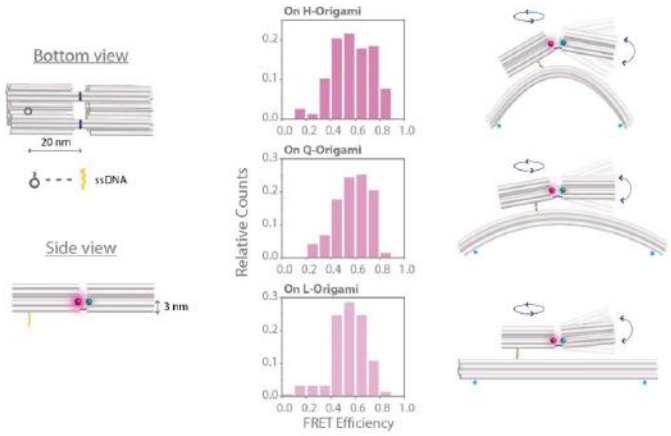

Figure S4. FRET efficiency distributions of the curvature sensor on Half, Quarter and Linear DNA nanostructures with only one anchoring moiety on one of the blocks. The illustrations on the right side show the possible movements of the curvature sensor on the testing platforms when one of the blocks is free. Number of molecules used in data analysis is 157 for Half, 147 for Quarter and 158 for Linear DNA nanostructures.

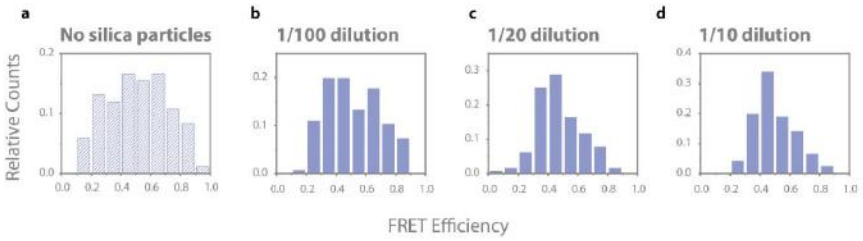

Figure S5. FRET efficiency distributions of the curvature sensor on **(a)** BSA-Biotin-NeutrAvidin coated glass coverslips **(b)** surface covered with 1/100, **(c)** 1/20, and **(d)** 1/10 diluted silica particles. Number of molecules used in data analysis is 84 for the sensor on functionalized glass coverslips, 136 for 1/100, 128 for 1/20, and 121 for 1/10 diluted silica particles.

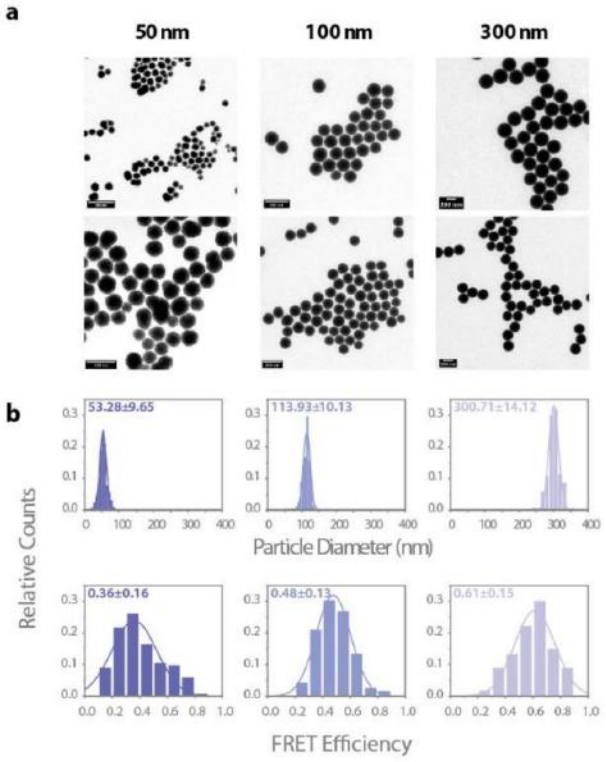

Figure S6. Characterization of Silica particles. **(a)** Corresponding negative-stain TEM images of the silica particles. **(b)** Size distributions of 50 nm, 100 nm and 300 nm Silica particles (from left to right) and FRET efficiency distributions of the curvature sensor on silica particles of corresponding sizes. The error refers to the standard deviation (SD).

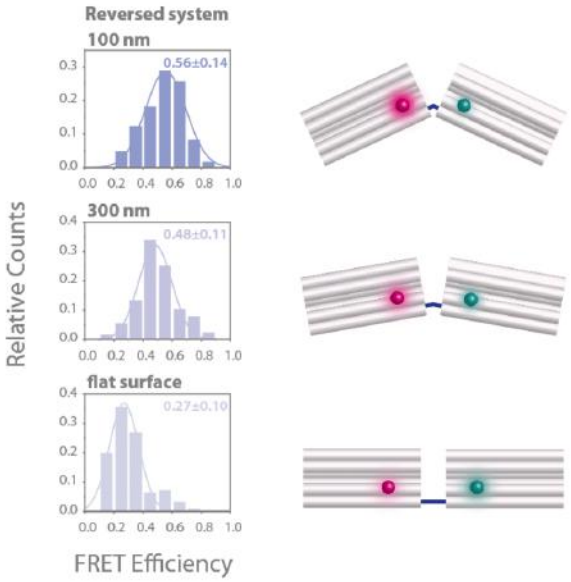

Figure S7. Curvature sensor in the reversed design with the FRET pair positioned on the sides of the sensor blocks. FRET efficiency distributions of the curvature sensor on 100 nm, and 300 nm silica particles, and on a flat surface of a passivated glass coverslip together with the illustrations of the sensor in different conformations on these platforms. The error refers to the standard deviation (SD).

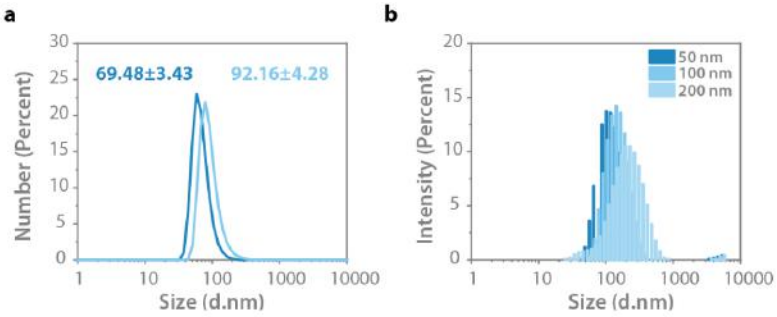

Figure S8. DLS data of the lipid vesicles. **(a)** Number distributions of 50 nm and 100 nm, and **(b)** intensity distributions of 50 nm, 100 nm and 200 nm vesicles. The error refers to the standard error (SE of the mean).

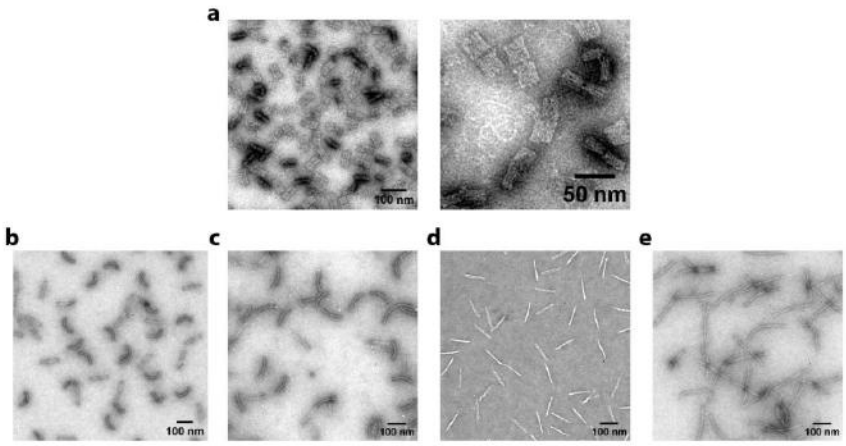

Figure S9. TEM images of the **(a)** curvature sensor, **(b)** Half, **(c)** Quarter, **(d)** Linear, and **(e)** 12HB DNA origami nanostructures.

5. Tables

Table S1. The list of buffers with recipes.

Buffer	Recipe
FOB17.5	10 mM Tris-HCl, 1 mM EDTA, 17.5 mM $MgCl_2$
FOB12.5	10 mM Tris-HCl, 1 mM EDTA, 12.5 mM $MgCl_2$
FOB20	5 mM Tris-HCl, 1 mM EDTA, 20 mM $MgCl_2$, pH 8.0
Gel Buffer	40 mM Tris, 20 mM Acetic acid, 1 mM EDTA, pH 8.4
PEG Buffer	12% PEG-8000 (w/v), 10 mM Tris, 1 mM EDTA, 500 mM NaCl, 12 mM $MgCl_2$, pH 7.5
LUV Buffer	5 mM Tris-HCl, 1 mM EDTA, 0.5 mM Trolox and 650 mM NaCl, pH 7.0
FRET Buffer	10 mM Tris-HCl, 1 mM EDTA,1 % (wt/v) D-(+)-glucose, 165 units/mL glucose oxidase, 2170 units/mL catalase, 1 mM Trolox, 12.5 mM $MgCl_2$
PCA/Trolox1 2	2 mM Trolox (6-hydroxy-2,5,7,8-tetramethylchroman-2-carboxylic acid) 25 mM PCA (protocatechuic acid) 2 M NaCl 40 mM Tris base 20 mM acetic acid 1 mM EDTA-Na2·2H2O
50x PCD	2.8 mM PCD (protocatechuate 3,4-dioxygenase from pseudomonas sp.) 50% glycerol 50 mM KCl 100 mM Tris HCl 1 mM EDTA-Na2·2H2O

Table S2. Scaffold strands, folding programs, folding buffers and purification techniques used for the folding of the DNA origami nanostructures (curvature sensor, Half-Quarter-Linear, 12HB, and NRO).

DNA Origami Nanostructure	Scaffold	Folding Program	Folding buffer	Purification technique
Curvature sensor	p7560	1	FOB17.5	Gel electrophoresis
Half, Quarter, Linear	P7249	1	FOB20	PEG precipitation
NRO	P7249	2	FOB12.5	PEG precipitation
12HB	p8064	1	FOB12.5	Filtration

Table S3. Folding programs used for the folding of the DNA origami nanostructures.

Folding program (1) for curvature sensor, Half-Quarter-Linear and 12HB DNA origami nanostructures

Temperature (°C)	Time per °C (min)	Temperature (°C)	Time per °C (min)
65	2	44	75
64-61	3	43	60
60-59	15	42	45
58	30	41-39	30
57	45	38-37	15
56	60	36-30	8
55	75	29-25	2
54-45	90	4	Storage

Folding program (2) for NRO DNA origami nanostructures

Temperature (°C)	Time per °C (min)
90	15
80-20	1
4	storage

Table S4. Folding reagents with final concentrations for different DNA origami nanostructures.

Curvature sensor

Reagent	Concentration (μM)
Scaffold	0.02
Core staples	0.2
Dye staples	0.6
PAINT docking staples	0.6
Biotin staples	2
Bridging staples	2

Half-Quarter-Linear DNA origami nanostructures

Reagent	Concentration (μM)
Scaffold	0.02
Core staples	0.2
Side staples	0.2
Biotin staples	0.6
Binding staples	0.6

12HB DNA origami nanostructures

Reagent	Concentration (μM)
Scaffold	0.02
Core staples	0.2
Biotin staples	0.4
Binding staples	0.4

NRO DNA origami nanostructures

Reagent	Concentration (μM)
Scaffold	0.03
Core staples	0.3
Biotin staples	0.6
Binding staples	0.6

Table S5. The list of unmodified staples for the curvature sensor.

Name	Sequence (5' to 3' end)
C000	AGAAAAGAGATAACCCACAAAATAAGAA
C001	CGTTTTTCCGCACTTCTATCAGCGATGGAAATACCTTTCTGACATCTTA

C002	GAAAAAGATATATTTTAATGGTTTTTAG
C003	CAAAATATTCAACATGTAATTTAGCGTA
C004	TGAATATTTTTGAAAGTATTA
C005	GGAGTTATTTTCATACTTTGCCCCTCAGATTATTCAAGTATTGACTCCT
C006	CAACCAATCATAGGTCTGAAAATAGTGATTTAAC
C007	AGCAAGGCCGAGAGCTAATAGACGTAATC
C008	CCAGCGCCAAGTGGGAAAATTCAT
C009	AGTAGAGTAAGCAGATCCATTTGGGA
C010	TGACCTGGCTGGCAAGAAGG
C011	GACTTCTTGATGGCTCGCTATTCGAACC
C012	GCCAGTCACACTCACCAGCGATTACCAG
C013	TGAGATGAACTTTAAATCTTGACAATCGTGCGGAAGAACCGG
C014	CAGCAAAATCTCTTACCGAAGGAATCAGCAAGC
C015	GAGACTCCAGGGTGGTTTT
C016	GAGCTAACTGCGTTGCCATGTA
C017	AAGCCCCGTTGGGTAAAATTACAAAGCGGTAAAACTACATAACGCCAAA
C018	AAATTGGTTTTGCAATTATCGAGCCAGC
C019	TTTGCGTATTGGCAACGCGCGGGG
C020	CGATTTCGTTTAATAAAAACCGAGGCTTTTAGAAC
C021	AACGCATCCAATTGAGAATCG
C022	GTCACAATCAATATGGTCGTGCC
C023	TTCTCCGAACCGCTTAAGGCTCGCTCGCTTTCGGTTAAGCTACGTGGT
C024	CACCGCCTGGCCCTTACACCACGGAATAAG
C025	TATCAAACGTAAAATTAGATT
C026	AATGAATGGATTTTTTTCAACAGACAACAAACTTTGCCACCAG
C027	AAACAAACATCAAGAAAGGCGAAATAAA
C028	GACGGAAATTATTCGAACGGAAGGTAAATATT
C029	TTTACCGCTGAATAGAAAGGAGAATTGCGAATAAG
C030	CAGCTTGTTGACCCTCTTTGCACAACAAAGTAAGCGCTTTTG
C031	ACCACCAGAGCCGCACATGGTCATCGCGCTGAA
C032	AATGCTAGAGGCTTGCAACGGGTAATTGAGCTTAAAATACGT
C033	TATTACGTTTTAGCGAACCTTTTCTAAGAACGCGATAGAAGG
C034	CAATAAAAATTTGACTCCTGGGCAAAAT
C035	GGCAGGCCCATTGAGAAGCAAGCCCGAA
C036	TTTTCAACCACTGAACACCCTAGAGGGTAATTGAC
C037	CCAATACTCATAAATAGACGA
C038	TTGAATCGGCTGACCGTCAGGGATGCATTTCACA
C039	CGGTCCACGCAGTTTGAGAGAGTT
C040	GCATTAAAACGGTAATCGTTA
C041	AGTGCGTTCATGATGAAATTCATAATCAAAAT
C042	GCTGTAGTTTAAATATGCATT
C043	AAGGGAGCGATAGCCATGAGG
C044	GTACCAAAACGGGCCGGTGACATCAGAA
C045	GGCTTAGCTGAATACGTTATGTTACCTT
C046	CAGTTGGGTTGAAAGGAATGAAATAAAG
C047	GCATTGCCCCCTTGCCATCGCCCTGCC

15

C048	GCATAATTTTTTCACGTTAATTCACATTTGGCCTTG
C049	CAAAATTAATTACATTAAAATCATTATA
C050	ATTCAGGACCAGAGTAAGAGCAACACTGGAGAATCGAGAGGC
C051	AGACTAAACAAAAGATTAAGACCCACATAATACCG
C052	ACTTGCGGGTGGTTTGCCCCAGCAGG
C053	GAGTAGTAAATTCTCAGCTTTCAGAGGCGAAAGACCGAGGGTATACCGAC
C054	CTAAAGTTTTGTCGTCTTTCCAGACGTATTTCGGATA
C055	CCGATTGAGGGAGTGGCCACCAC
C056	ACCAGTACGCCTGTAGACAGCC
C057	AACCGAATTGGAACAACATTAAAAGATTCCATGTTATTGTGT
C058	GAAGATGATGAAAAGCAATTACCTGAGCAAAATAAACAGCGC
C059	CAGACAATCTGTAAATGTAAGAAAGCCGAAGGATTTTTGATT
C060	GATAGCAGCACAACGTCACCAA
C061	TATAGAGAGGATAAAGTTGAGAACGGAGATTTGTCTAGCGCGACCAAAA
C062	AAACAAATAAATCCTCAGCTTGGGAGCCT
C063	CTTATCCTAGCAAGCAAATCAGAATAAATCAAAAGA
C064	CGAAATCTATATCATCGCCTGATTCAAA
C065	GAGCCACCACCCTCAGAGATAAGTTTTAACTCTAGTA
C066	CGCGCCTAACAACAATAAATCAAGTAATTGAGAAGGTGCATTCAGAGTA
C067	TAAATGAGCTTCAAAGCGAATAAACAAAGTTTAATTCCGGTT
C068	GTTGATAATTATGACTTTTGC
C069	CAGTGAATAAGGGGGGTAACCGTTCTAGAAAAGTTTTGCCAG
C070	TCATATCAAAAGGAAACGCAGCGGATTGCATCATTTTATAGT
C071	CCATATAACAGTCATAGCTATAGGTCAT
C072	TTAATTGCGAAAAATCCAACGACCTGCTCAAATGG
C073	TAACATTGGGTTATCGAACAAACCAGAAGGTATTAACTCGAG
C074	ATGATAGAAAAATCAAACGAACTAACCCCCTACAC
C075	ACATAAAATGTTAGGTTGCTAGTTTTGAAGCCTTAGTTCCCG
C076	CTGATCTAAACAGTGTGAATTGAGGCGCGCATACC
C077	AATAGGAACCGCTCACTG
C078	TTAATTTCCTAAATTGTCTTT
C079	CCCAATTCTGCGAATAGTTTGTCGCCCTGGAGTGAACGAGAA
C080	AGGCAGGTCAGACCAGCATTGACA
C081	AGATACCTTAGAAAATAACGG
C082	TGCCTATCAATCTACAAAGGCTAAAAAG
C083	CAATAATAAACCAGAAGTTCT
C084	GTCTTTCCAGAGGCTTACCAACGCTAACGGAATTT
C085	TCCCTGATTTCTTACCAGTATAACTATATGTTGCTTAACCTA
C086	TTAGTACCGCCACCCTCAGCAAAAGAGGAAACG
C087	GCAGATTCGAGTTAGAGGAAGTTTCATT
C088	AACGTCAAAGGGCGATAACCAGTAGCACCA
C089	GAGTTAAGCCCAAAAGAAACAATGACCGTGTGATTTAGAATT
C090	CGAAAATCCTGTTTGATCGCAAGACAAAAGGGCGACAT
C091	GCCGCCACCCGTAACCTTGATCAGAACCGCCACCCTCA
C092	TAAACCTGTTAGTAAGTTATATTGGAAC
C093	AGTGCCGTCGAGAGGGTTGAGTAGCGC

16

C094	CGTCAGACTTATAAGTAT
C095	TGTCTGGTTGTGAACGATTTTTCATTATACGTTGGTGAAAGAACAAGGG
C096	ACAAGTCGAACACGCCGAACAAAGGAAACCGCGCC
C097	CGCCCACTACACTACGAAGGCACCAACCGAGGCAAAAGAAAT
C098	TCCATATATCATCTCGAAACCCAAAGGCTTGAATTACAGCCC
C099	GCTTGTTACCTCGAACCGAGCATATAAAGACGGAGGAT
C100	TTCATGTCTCAATCCATTAAG
C101	CTAATGCAGATAGCTATGTACGGCTTTA
C102	AATTATGTACAGGGAAAAATG
C103	CCGCTTTCCAGGATAGCAAGCC
C104	AAATCAATATATACAAAGAACCAATAATAATTTAC
C105	CTTCTGATAGATTAGAGCCGTCTTCTGA
C106	GACGACATGTTCAGCTCCTGAATAATAATGCAGAA
C107	CAATAGCAAAACCGCATCGAGAACTATT
C108	CCTTATTAACCAATGCGAGAAAAAATCC
C109	CGTTTGCATCATGGTATTAAACCAAGTAATTCATTCCAAGAA
C110	TACCATCATACTAAAGTACGG
C111	GCCCGGAATAGGTTTGCCTTTA
C112	CTACCTTTTAATTTTAATTTA
C113	AATAGGCAAGAGAGTCTATCATAACCCTTAATCAAGTGGCAT
C114	ACAATTTCATTTAATGGTTTGCCCACTACGTGAAC
C115	AGTAATATACGTGAATTACTGCACGGAT
C116	ACCTCCGATAGATAAGTCAGAGATTATCAGGTGAG
C117	TTTGCCAAGAGAAAATAAATCAATACAT
C118	ACAGTAGGGCTTAAATAAGAAGTTTAAC
C119	AAGTTACAATATCATTTAGAATCGCGCAATTACTA
C120	ATTCGACCTTACATCCTTTCA
C121	AAAACAAAGCTGCTACGGGCT
C122	TCAGTGCAGTGCCCTTAATGCTTTCGGACAGATTAAGAAGTT
C123	ACCCAATTTATCCTGCAACATCGCAAAGGCACCCA
C124	AATCGCACTGAACATATCCCA
C125	TGGTACCTCAGCGGAGTGAGACCAACTTGAACAGGAGTGTAC
C126	ACCGGAAACAGGTCAGTACCT
C127	GTCCACAATTGTTGTTCCA
C128	AATGCTGATGCACGGTTATATAAAATAGATGAAAGC
C129	CAATAGATCATCGTAGCCCTTGAAATAG
C130	TAAAGTGTAAAACTACATACGAGC
C131	AAGACGCTCTGTCCAAGTACCGACAAAAGAGTAATAAGAGAA
C132	ACCGAGCTCGAATTCAATGGCCGACGTAATCATG
C133	TTAATTGTAAGAGGTCCGAAATAAAAATTTTTGTC
C134	AATGAACAGATGAACGGTGTACAACAACGCTAAGA
C135	AGCTTGCCCGCTGAAAGAGTGCTCTATGAGCAACG
C136	GCTACTAAAGATTACAAACGTTTCTCCT
C137	CCAGAGCCACCACCGCCTACCCCTGGAACCGCCT
C138	GTCAAAACAGCCTTATAACATAAGCGCA
C139	CATCATATTCGGAGGGATTAGCGGGG

C140	ATTCCACACATTCGAGGTGAATTTCTGGTTTATCATTAAA
C141	TATAATACCCTGTCGCGTTACATTTAGGTCGGTAGTTACAAA
C142	GAGCATGGGAATAAAGAAATAATCAACAGCTTAGGAGAGAGA
C143	ATATTCACAAGAGTATAACAGGTATACAACTAAAGGAGGAAG
C144	GATTTTCTCAGATGAATATATAATTTATCAATCCTTGAAAAC
C145	CAAGAGATACAGGAGCATGATTAAGAGGGAATACCACGGGAG
C146	ATAACAAGAGCATTAGGTAAAGATTCTTCATGCCTTGCAAGAAAACGAG
C147	AGATAGGGTTGAGTACCATTAAAGGTGAAT
C148	TCACCGACTTGAGAGTACTCAGG
E000	AATCAAAAATATTTTAGACAGACGACAAGAGTAATGTCTGCCAGTTTTTT
E001	TTGAAACTGCCGTCTAAAAATTTATCGCACTCCAGCCAGCTTTTTT
E002	ATTCTCCGTGGGAAAAATTCTGATCATCAATATGCGGCCGAGAAAGT
E003	TTTTTTGGGAAGGGCGATCTCTTCGCTATTTTTTT
E004	TTTTTTCGCCATTCGTGCGCAACTGTTTTTTT
E005	TTTTTTTTAGACAGGAACGGTGAGACACGCTACGTGGCA
E006	TTTTTTTTTGAGGGGTATCGGCCTTTTTTT
E007	TTTTTTTAATGGGAAAACATTAAATGTTTTTT
E008	TTTTTTGCTGGTAATATATTACCGCCATTTTTT
E009	TTTTTTTTTGTTAAATCAGCTC
E010	TTTTTTTCCTGTAGCCAGCTTTAATTCGCGTCTGGCCTTTTTTT
E011	AACTAAAAAGCAAAAGTTTTTTGGGGTCGATTTTTT
E012	TTTTTTTGGATTATTTACTCACCAGTCTTTTTT
E013	TTTTTTGAATCAGAGCGGGATGAACCTTGCGCCCAACAG
E014	CATCAATTTGTCAATAGATAATAGGCGCTGTTTTTT
E015	TTTTTTACACGACCAGTACTATGGTTGTTTTTT
E016	TTTTTTTAATCAGTGAGGCCGTGAGCAGAGACGCGCGAA
E017	TTTTTTTACCTACATTTTGATGAAAACGCTCATGGAAATTTTTTT
E018	TTTTTTGAGCGAGTAACAAATTGTCAACCTTTTTTT
E019	TTTTTTGCAAGTGAACCCGCTCAATCGTCTGAAATTTTTT
E020	TTTTTTAAGCCGGCGAACGTCAAAGAGCTTGACGGGGATTTTTT
E021	TTTTTTCGCGTAACCACCACGACTTAGCGGTCACGCTGTTTTTT
E022	AAATTCGTCAGGAGAAACGACGGCCAGTGCTTTTTT
E023	TTTTTTCTTTGACGAGCACGCAACACAAATTATAACGTTTTTT
E024	TTTTTTCTTAAGTGTCCTTAGTGAATTCATGCGCACGATTTTTT
E025	TTTTTTGCCATTGCAACAGGAAATACGCCAGAATCCTTTTTTT
E026	TTTTTTCGATTAAAAATCTAAAGCA
E027	TTTTTTTAACCCCGCTTCTAATCTACCGGAGATTAGCGAAAAATTT
E028	TTTTTTGGAGCGGGCGCTAGCATAGGAAGAAAGCGAAATTTTTT
E029	GGGGGATGTGCTGCAATTTTTT
E030	TTTTTTCCTGAGTAGAAGAACTCATCGAGTAACACCAGCAGAAGAT
E031	GGGGGCGTAGATTGGAGACAGTCATAGGTCTTTTTT
E032	TTTTTTCGCAAATTAACCGTACAAGAGTCTGTCCATCATTTTTT
E033	ATACATTCTCAGATATTGGGGTAAACAGGAGGCTTTTTT
E034	TTTTTTTTTCCGGCACCGCTTCTGGCAGGCAAAGTTTTTT
E035	AAGGAAGGATGGAACAATCCAGCTAAAACTATCGGCCTTTTTTT
E036	CGGAATTTCTACAAACAATTCGAGGCGAGATTTTTT

E037	TTTTTTGGTGCCGTATCGGAACCCTAATTTTTT
E038	TTTTTTGAACGCCATCAACAGGGTGGATGTTTTTT
E039	TTTTTTCAGGAAGTTTTAAATTGTAAATTTTTT
E040	TTTTTTCGTGCATGTTTTAACCAATAGTTTTTT
E041	TTTTTTCGTTAATATTTTCCAGGGTTTTCCTTTTT
E042	TTTTTTAAGATTGTATAAGCAAATAATCAATGTCATAGAACCC
E043	TTTTTTGCGCTTAATAGGGCGCGTAATAA
E044	GAGAGTCATCACCAAACGGCGGATTGACCGTTTTTT
E045	TTTTTTACGTTGGTGCATCGTAACTTTTTT
E046	TTTTTTGGCGATTAAAAAAACAGGTTTTTT
E047	TTTTTTCAAGCTTTCCATTAAATTTTTTT
E048	TAAAACATCAGTAATGATTGCACCGAACGATGTAGCATTTTTT
E049	TCATTTGGGGCGGTGCCTGTTATAACTGACGCTATGGGTACCGTCGG
E050	TTTTTTGAGAAGTCCGCCTGCAACAACGTCTTTATTAAT
E051	TTTTTTATACTTCTTTAACATCACTTGTTTTTT
E052	TTTTTTTCTTCTAAGTGGTTCGAGCTGAAAAGTTCTACT
E053	TTTTTTTGCTTTCTCAATCAATATCTGTAACGAGGTTGT
E054	TTTTTTCAGTCACGACGTTGCAGGCTCATATAAATAGTA

Table S6. The list of modified staples for the curvature sensor. Donor positions are colored in teal, while acceptor positions are in magenta. Positions of the anchoring moieties are colored in orange, bridging staples are in pink and PAINT docking cites are in cyan.

Name	Sequence (5' to 3' end)	Replace
	Cy3B-labeled donor dye staples	
G01-mod	ATGAGTAAACAGGTGACCTCCTGGTTGGT-Cy3B	G01
G02-mod	AAAGCGCAGTCTATGAAAATCAGGCTCCAAAGCCTGGGG[Cy3B]TGCCTAAT	G02
	ATTO647N-labeled acceptor dye staples	
R01-mod	ATTO647N-CGGCAAAATCCCTTTAGGGGTGGTTCCGA	R01
R02-mod	GCAT[ATTO647N]TAATGAATCGCCATAAACAGGCGCCCTAA	R02
	Bridging staples	
B01-mod	GTGATAGATACCGTGAAATTGTTATCCGCTGGGGAGGGAGGTTCACCAGT	B01
B02-mod	AAAGAACGTGGAGGGGAGGGAGGGTAAGCAACTCGTCCGGAA	B02
B03-mod	TATCCTGAAGGGCAACAGCTGATTGCGGGGAGGGAGGTAGCTGTTTCCT	B03
B04-mod	AGCATGGTGGGCACGAATATAGGGGGGAGGGAGCGGAACAAGA	B04
	Anchor staples	
A01-mod	TCCTCTACCACCTACATCACCGGAATCATAATTCATTTCGG	A01
A02-mod	TCCTCTACCACCTACATCACCTGTATGTTTCTCATAGTTAGC	A02
A03-mod	TCCTCTACCACCTACATCACGTTTTTGCTCAGTACCAGGAC	A03
A04-mod	TCCTCTACCACCTACATCACCTGGATAGATATTCAATAGTA	A04
A05-mod	TCCTCTACCACCTACATCACTCAGTATTAACAGTTTTTATTTTTT	A05
A06-mod	TCCTCTACCACCTACATCACCCTAAAGACAACGTAACACTGA	A06
A07-mod	TCCTCTACCACCTACATCACACGGTCAATCATTAAGCCGGAACGAGGC	A07
A08-mod	TCCTCTACCACCTACATCACGCAGCAAATGAAAGGGATTTTTTTT	A08

A09-mod	TCCTCTACCACCTACATCACCCACAGTAACAGTACGGGAGAAAGCTCA	A09
A10-mod	TCCTCTACCACCTACATCACAATATCAAACCCCTCGTTATTTTTT	A10
A11-mod	TTAGAACCGCCACCCCACCCTTTATGAGAAGTTAGGAATGTTA	A11
A12-mod	TCCTCTACCACCTACATCACCGTTATACAAATGCTTTGACA	A12
A13-mod	TCCTCTACCACCTACATCACCCAAATCAACGTATGTTTAGA	A13
A14-mod	TCCTCTACCACCTACATCACCCAGGCGCATAGAATGCTTTA	A14
A15-mod	TCATTTTTACGATGGTCGGGAATTATGAGAAGTTAGGAATGTTA	A15
A16-mod	TCCTCTACCACCTACATCACCAGAAGCAGGTCTTTACCCTGGGCCATA	A16
A17-mod	TAATATCAGCGACAGAATCAAGTGTATCTTATGAGAAGTTAGGAATGTTA	A17
A18-mod	TCCTCTACCACCTACATCACAACAGTTCATTGAATCCCCCTCAGCTGGC	A18
	PAINT docking site staples	
P01-mod	CATCACCCAAATCAGTTTGAGAATGCCCG	P01
P02-mod	TTTTTTACGCCAGCTGGCGAAGAGCGCCTCAAGGGGGATAATGCCCG	P02
P03-mod	ATAACAAGCACTAATGGAAGGACTAAAATTATCCAAATGCCCG	P03
P04-mod	TACTCCAGCAAAAGCAATAAAATAAAAATGCCCG	P04
P05-mod	AAGCTACGCGCCGGTATCTTTAGACCCGCCTTTTTTAATGCCCG	P05
P06-mod	TTTTTTTATGACAATGTCCCAAATGTTCGCGCCAAAATTTTTTAATGCCCG	P06
P07-mod	ACACCGCAAAAGTGTTTACGCACCATTAGATACATGTTGATTAATGCCCG	P07
P08-mod	TTTTTTAGGGAGCCCCCGATTTATCCTTTGCCTAATTTTAATGCCCG	P08

Table S7. The list of modified staples for the external labeling of the curvature sensor.

Name	Sequence (5' to 3' end)	Modification
8 nt aptamer imager	CGGGCATT-Cy3B	Cy3B on 3' end
Bridge complementary	CCTCCCTCCCC	
Biotin-5'	Bio-GTGATGTAGGTGGTAGAGGA	Biotin on 5' end
Biotin-3'	TAACATTCCTAACTTCTCATAA-Bio	Biotin on 3' end
Cholesterol-5'	Chol-GTGATGTAGGTGGTAGAGGA	Cholesterol on 5' end
Cholesterol-3'	TAACATTCCTAACTTCTCATAA-Chol	Cholesterol on 3' end

Table S8. The list of modified staples for the application of curvature sensor on the other DNA origami nanostructures (Half-Quarter-Linear, 12HB and NRO).

Name	Sequence (5' to 3' end)
12HB-fixed	AATAACGCGCGGGGAGAGGGTGATGTAGGTGGTAGAGGA
12HB-18nm	ACTACCTTTAAACGGGTAACAGGGAGACGGGCAGTGATGTAGGTGGTAGAGGA
12HB-29nm	TCGTTCACCGCCTGGCCCTGTGATGTAGGTGGTAGAGGA
12HB-42nm	TACCTGGTTTGCCCCAGCAGTGATGTAGGTGGTAGAGGA
12HB-Biotin-1	GTACATCGACATCGTTAACGGCA-Bio
12HB-Biotin-2	AACGCCAAAAGGCGGATGGCTTA-Bio
12HB-Biotin-3	AAGAAACAATGACCGGAAACGTC-Bio
12HB-Biotin-4	ATACCACCATCAGTGAGGCCAAACCGTTGTAGCAA-Bio

Half-T3	CAGCCGTCGAAGCGCAGTCTCTGGTGATGTAGGTGGTAGAGGA
Half-T6	ACAAAGCCCCTGCCTGAGTAATGGTGATGTAGGTGGTAGAGGA
Half-Biotin-1	TTATCAGATGATCGGGACT-Bio
Half-Biotin-2	AGGGTGAGAAAATGTCAAG-Bio
Quarter-T3	ACCCGTCGAGAGCGCAGTCTCTGTGATGTAGGTGGTAGAGGA
Quarter-T6	AACCCAAAAATGAGTAATGTGTGTGATGTAGGTGGTAGAGGA
Quarter-Biotin-1	ATTCCTGATTACTTTTACCT-Bio
Quarter-Biotin-2	GTGAGAAAGGCCAATCATCA-Bio
Linear-T3	AAGTGCCGTGGAAAGCGCAGTGTGATGTAGGTGGTAGAGGA
Linear-T6	AGACAGGAAATGTGTAGGTAAGTGATGTAGGTGGTAGAGGA
Linear-Biotin-1	ATTATCATCATAAACAGTATG-Bio
Linear-Biotin-2	AAGGCCGGAGACATGTACCTC-Bio
NRO-fixed	ACACTCATCCATGTTACTTAGCCGAAAGCTGCGTGATGTAGGTGGTAGAGGA
NRO-42nm	GCTTTCCGATTACGCCAGCTGGCGGCTGTTTCGTGATGTAGGTGGTAGAGGA
NRO-Biotin-1	Bio-CGGATTCTGACGACAGTATCGGCCGCAAGGCGATTAAGTT
NRO-Biotin-2	Bio-AGCCACCACTGTAGCGCGTTTTCAAGGGAGGGAAGGTAAA
NRO-Biotin-3	Bio-ATAAGGGAACCGGATATTCATTACGTCAGGACGTTGGGAA
NRO-Biotin-4	Bio-GAGAAGAGATAACCTTGCTTCTGTTCGGGAGAAACAATAA
NRO-Biotin-5	Bio-TAGAGAGTTATTTTCATTTGGGGATAGTAGTAGCATTA
NRO-Biotin-6	Bio-GAAACGATAGAAGGCTTATCCGGTCTCATCGAGAACAAGC

6. Appendix A - Calculations

In order to estimate the working range of our curvature sensor, we performed multiple calculations. First of all, the expected FRET efficiencies for different sizes of curved platforms were investigated. We performed calculations for different positions of the anchoring moieties as well as different heights of the FRET pair using the following parameters and equations;

a=height of the FRET pair (3 nm or 10 nm)

b=length of the dsDNA linker between the two blocks (3.74 nm)

d=distance to the anchoring moieties, 4 nm, 11 nm and 18 nm

r=radius of the particle

α=central angle

β=angle of the linker

x=distance between the FRET pair

$\mathbf{R_0}$=Förster Radius of the FRET pair (6.7 nm for ATTO647N and Cy3B)

E=FRET efficiency

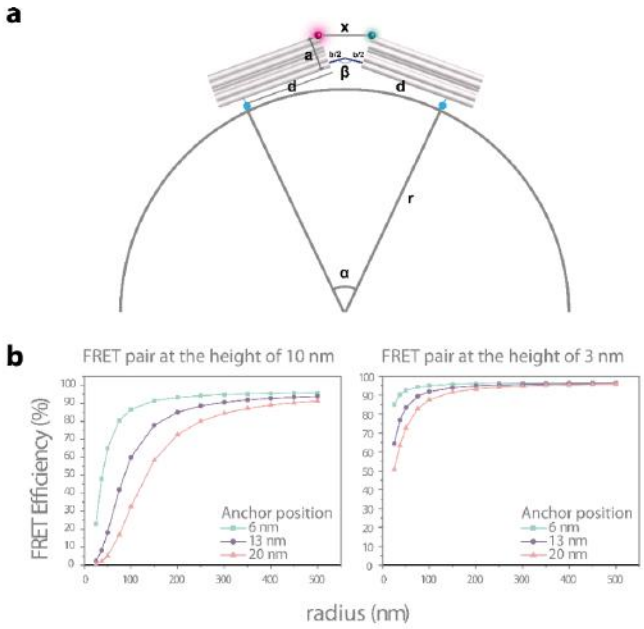

Figure S-A1. (a) Sketch of the curvature sensor on a particle labeled with the parameters. (**b**) Calculated FRET efficiency vs particle radius plots for different anchor positions of 6 nm, 13 nm and 20 nm. Left plot displays the relation for the dye pair at 10 nm position and the right one displays it for 3 nm.

$$x = 2 \cdot a \cdot \sin\left[\arctan\left(\frac{\frac{b}{2}+d}{r}\right)\right] + \sqrt{\left[2 \cdot \left(\frac{b}{2}\right)^2 - 2 \cdot \left(\frac{b}{2}\right)^2 \cdot \cos\left(2 \cdot \arctan\left(\frac{r}{\frac{b}{2}+d}\right)\right)\right]}$$

$$E = \frac{1}{1+\left(\frac{x}{R_0}\right)^6}$$

Further, for the application of our sensor on DNA nanostructures, we made calculations to describe the relation between binding site distances and bending angle, and eventually FRET efficiencies. We utilized the single-stranded extensions of the curvature sensor at 18 nm distance in order to enlarge the suitable range of binding site distances. According to the FRET efficiencies against the bending angle plot for different dye positions (Figure S-A2), we had to shift the FRET pair from its initial position of 10 nm height to 3 nm in order to be sensitive within the bending range of our interest. The calculations were made using the following parameters and equations;

a=height of the FRET pair

b=length of the dsDNA linker between the two blocks (3.74 nm)

d=distance to the anchoring moieties (18 nm)

β=angle of the linker

x=distance between the FRET pair

y=distance between the binding sites on a surface

R_0=Förster Radius of the FRET pair (6.7 nm for ATTO647N and Cy3B)

E=FRET efficiency

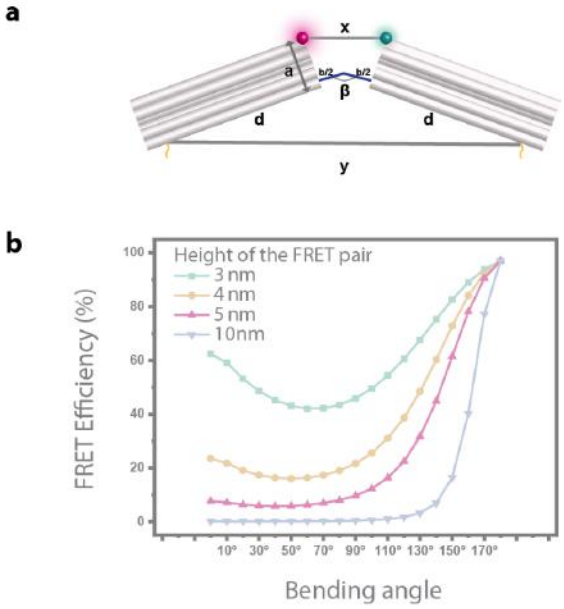

Figure S-A2. (a) Sketch of the curvature sensor attached on a platform via anchors on 18 nm distance, labels show the calculation parameters. **(b)** Calculated FRET efficiency vs bending angle calculations for the dyes at different height positions.

$$x = \sqrt{[2 \cdot \left(\frac{b}{2}\right)^2 - 2 \cdot \left(\frac{b}{2}\right)^2 \cdot \cos\beta + (2 \cdot a \cdot cos\frac{\beta}{2})}$$

$$E = \frac{1}{1 + \left(\frac{x}{R_0}\right)^6}$$

7. Appendix B - Sensor in flat conformation

We investigated the linear behavior of the curvature sensor on a flat surface where it is attached to a BSA-biotin-NeutrAvidin coated glass coverslip via biotin anchors at 6 nm distance (Figure S-B1-a). As the dyes had the shortest distance, the highest FRET efficiency of ~0.9 was anticipated. The single molecule FRET analysis of the flat conformation of the curvature sensor on glass resulted in a very broad distribution of the mean FRET efficiencies (Figure S-B1-b, dashed histogram). This outcome suggested that the sensor was attached in a variety of conformations inducing different distances between the dyes. Such conformations were easy to adapt on a flat surface that is full of anchoring points. The flexible sensor could get fixed in distorted conformations due to torsional as well as up-and-down or back-and-forth vibrational movements during immobilization. Furthermore, a lot of single-molecule transients showed fluorescence quenching in the acceptor signal which was the indication of the dyes being in contact.[8] Fluorophore quenching helped us to understand the reason of the lower FRET efficiencies covering a large population of the histogram. This result was in line with previous studies stating that ATTO647N dye can exhibit contact quenching with other fluorophores like Cy3B.[9] Further, dye contacts can yield spectral fluctuations which reduce the precision of smFRET experiments.[10] It is conceivable that these photophysical effects were more dominant as the dyes are in a closer contact, explaining increased visibility of such effects mostly in flat conformation of the curvature sensor.

In order to prevent the high flexibility on a flat surface and achieve the expected high FRET scenario, the two blocks of the curvature sensor were further connected via dsDNA linkers, called the bridge, at the top of the structure (Figure S-B1-a, fixed structure). Subsequently, the single-molecule FRET analysis of the fixed curvature sensor resulted in a FRET efficiency histogram shifted to a higher FRET range with a mean value of 0.72±0.10 (Figure S-B1-b, filled histogram). This indicates that up-and-down vibrational movements as well as the torsional movements of the sensor were fairly prevented with the additional bridging linkers also avoiding dye-dye contact. Further support of this model comes from single molecule transients of the two structures. Whereas the flexible structure mostly exhibited fluctuations in the I_{DD}, I_{DA}, and I_{AA} channels, the fixed structure had moderately stable signals (Figure S-B1-c). In addition, the number of transients showing fluorophore quenching was significantly reduced.

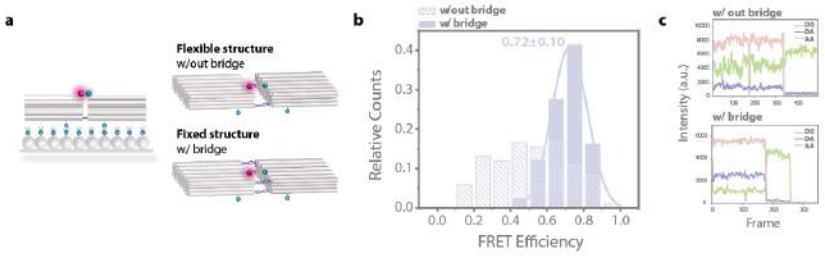

Figure S-B1. Curvature sensor in the flat conformation. **(a)** Sketch of the sensor on BSA-biotin-NeutrAvidin coated glass surface together with the design of the two sensor constructs; the flexible sensor without the bridge, and the fixed sensor with the bridge. **(b)** FRET efficiency distributions for the curvature sensors without (dashed) and with (filled) the bridge. Number of molecules is 84 for the flexible structure and 123 for the fixed structure. **(c)** Exemplary single-molecule FRET transients for the sensors without and with the bridge. The fluorescence intensity over time is shown for I_{DD} (green), I_{DA} (purple), and I_{AA} (rose) channels.

7.1. DNA-PAINT experiments

In order to confirm the linearity and the improved rigidity of the curvature sensor when it was linked with the bridge, a DNA-PAINT (DNA point accumulation in nanoscale topography)[11] experiment was designed. In line with this objective, the curvature sensor was modified with eight protruding single-stranded DNA extensions (called docking sites) at the four corners for the hybridization of the complementary dye-labeled strands (imager strands). The designed distances were ~25 nm and ~45 nm between the docking sites (Figure S-B2-a). The goal was to quantify these distances for the flexible and the fixed structures. Since the flexible structure can take a variety of different conformations, the expected case was to observe shorter mean distance between the docking sites with a broader distribution compared to the fixed structure.

Super-resolution measurements using the DNA-PAINT technique were performed on a custom-built total internal reflection fluorescence (TIRF) microscope with a 560 nm fiber laser (1 W, MPB Communications). The excitation beam is cleaned up with a filter (560 nm: Brightline HC 561/4, Semrock) and is lead through a dichroic mirror (T612lpxr, Chroma). The beam profile is expanded by passing through lenses (Bi-convex f50, Thorlabs; AC f120, Linos). The laser beam is coupled into the microscope body (IX 71, Olympus) with a triple-color beam splitter (Chroma z476-488/568/647, AHF Analysentechnik) and focused on the backfocal plane of an oil-immersion objective (100 ×, NA = 1.4, UPlanSApo, Olympus) aligned for TIRF illumination. To avoid drift, the objective is mounted on a nose piece (IX-2NPS, Olympus). The emitted light is collected by the same objective, magnified by a 1.6× optical lens and cleaned by an emission filter (Brightline HC 561/4, Chroma). Images and movies are recorded by an EMCCD (electron multiplying charge-coupled device) camera (iXon+ 3384, Andor), which is controlled by the ImageJ plugin Micro-Manager 1.4.[11]

The DNA origami stock solution was diluted to a concentration of 200 pM with 1xTE+17.5 mM $MgCl_2$+750 mM NaCl and immobilized onto a passivated glass surface. DNA-PAINT imaging was performed with the 8 nM Cy3B imager strand. In order to provide photostabilization, a combination of ROXS and oxygen scavenging system was used. The photostabilization buffer was a combined aqueous solution of aged Trolox (6-hydroxy-2,5,7,8-tetramethylchroman-2-carboxylic acid) with PCA (protocatechuic acid) (PCA/Trolox12) and a 50x PCD (protocatechuate 3,4-dioxygenase from pseudomonas sp.). For measurements, both solutions were diluted in a 1:50 ratio (50x PCD:Trolox/PCA12).[6, 12] Typically, a frame time of 200 ms over an experiment time of 30 min was used with 560 nm laser excitation at 100 mW measured before the objective.

Acquired DNA PAINT raw data were analyzed using the Picasso software package.[13] The obtained TIF-movies were first analyzed with the "localize" software from Picasso. For fitting the centroid position information of single point spread functions (PSF) of individual imager strands, the MLE (maximum likelihood estimation) analysis was used with a minimal net gradient of 20000 and a box size of 5 px. The fitted localizations were further analyzed with the "render" software from Picasso. x-y-drift correction of the localizations was corrected with the RCC drift correction.[14] For quantitative distance analysis, the super-resolution image information was exported as a hd5f file. Individual DNA origami nanostructures were picked and their distances analyzed with a self-written Python script.

Analysis of the DNA PAINT data revealed that the flexible sensor showed deviations in designed distances with the values of 21.62 ± 4.48 nm and 42.01 ± 6.42 nm indicating that the structure was not attached linearly on a flat surface (Figure S-B2-b). On the other hand, the bridged sensor presented narrower distributions with the distances of 22.80 ± 3.94 nm and 44.04 ± 3.99 nm matching coherently with the designed distances of ~25 nm and ~45 nm proving the flat conformation of the fixed sensor (Figure S-B2-c).

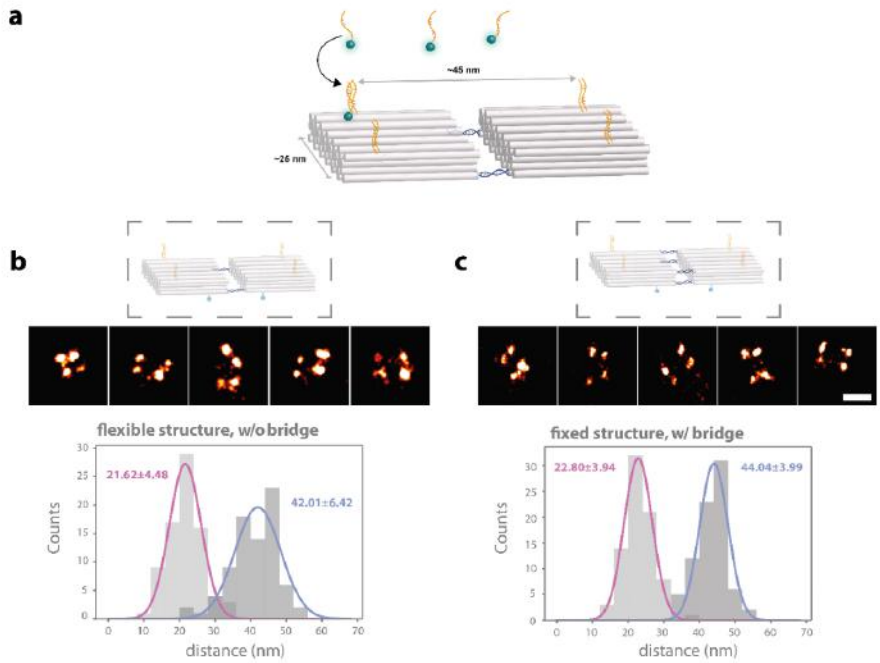

Figure S-B2. DNA-PAINT experiment on the flat conformation. **(a)** Sketch of the DNA-PAINT design and the working principle. Examples of the resolved structures with the distance distributions of **(b)** the flexible sensor without the bridge **(c)** the fixed sensor with the bridge. The sketches in the dashed squares illustrates the flexible and fixed sensors. The error refers to the standard deviation (SD) and the number of molecules is 79 for both of the samples.

7.2. Linear Dichroism experiment

Although the DNA-PAINT experiment revealed reasonable dimensions for the designed curvature sensors, only a maximum mean FRET efficiency of 0.72 could be obtained (Figure S-B1-b, dashed histogram) which was still lower than the anticipated FRET efficiency of 0.9. It is well-known that the photophysics of the dyes and their interaction with each other as well as with the environment can affect the FRET efficiency.[8, 15-17] Additionally, the dyes may stick to the blunt end of the DNA origami structure which may result in intensity and FRET efficiency fluctuations due to temporally fixed transition dipole orientations.[18]

Organic dyes host a conjugated pi-system which is the chromophore. The position of the dyes at the blunt-end of the dsDNA helix can lead to sticking of the organic dye to the exposed hydrophobic bases. Sticking of the organic dyes affects the average transition dipole moment (TDM) orientation of the dyes to each other (κ^2) which is a crucial parameter for FRET. Different sticking positions will affect the FRET efficiency due to a change in the expected R_0 value and depending on the average orientation. In order to monitor the sticking of the dyes on the curvature sensor, we performed confocal measurements with a polarizing beam splitter in the detection path. Although the dyes were excited with circular polarized light, the emission can have preferred polarization if the dye sticks in a certain conformation. We used the linear dichroism (LD) to monitor the TDM orientations. The LD is the difference-sum-ratio between two polarization components.

$$LD = \frac{I_1 - I_2}{I_1 + I_2}$$

I_1 and I_2 are the detected fluorescence intensities which detect P or S polarized light respectively due to the polarizing beam splitter. The LD can attain values between -1 and 1. A LD of -1 indicates parallel orientation of the dye's TDM to detector 2 and a value of 1 indicates a parallel orientation of the TDM to detector 1. A value of 0 corresponds either to a freely rotating dye or to a dye which emits to both channels equally from a fixed position.

A home-built confocal microscope based on an Olympus IX-71 inverted microscope was used for these confocal measurements. The samples were excited by a pulsed laser (639 nm, ~80 ps full width at half-maximum, LDH-D-C-640; PicoQuant GmbH) operated at 40 MHz repetition rate. The laser light was focused to a diffraction-limited spot, with power adjusted to either 1.1 kW/cm^2 or 4.3 kW/cm^2 by means of a neutral-density filter (ND06A, Thorlabs GmbH) assuming the confocal diameter of 300 nm. Circularly polarized light was obtained by combining a linear polarizer (LPVISE100-A, Thorlabs GmbH) and a quarter-wave plate (AQWP05M-600, Thorlabs GmbH). The light was focused onto the sample by an oil-immersion objective (UPLSAPO100XO, NA 1.40, Olympus Deutschland GmbH). The sample was moved by a piezo stage (P-517.3CD, Physik Instrumente (PI) GmbH & Co. KG) controlled by a piezo controller (E-727.3CDA, Physik Instrumente (PI) GmbH & Co. KG). The emission was separated from the excitation beam by a dichroic beam splitter (zt532/640rpc, Chroma) and focused onto a 50 µm diameter pinhole (Thorlabs GmbH). The emission light was separated from scattered excitation light by a 647 nm long-pass filter (RazorEdge LP 647, Semrock Inc.). The filtered emission was split into two detection channels by a polarizing beam splitter (CCM1-PBS251/M. In each detection channel, a 750 nm short-pass filter (FES0750, Thorlabs GmbH) blocked the afterglow luminescence of the avalanche photodiode. Emission was focused onto avalanche photodiodes (SPCM-AQRH-14-TR, Excelitas Technologies GmbH & Co. KG), and the signals were registered by a multichannel picosecond event timer (HydraHarp 400, PicoQuant GmbH). The setup was controlled by a commercial software package (SymPhoTime64, PicoQuant GmbH).

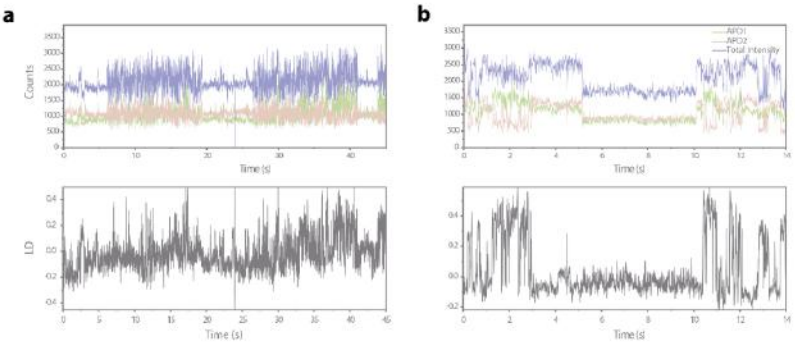

Figure S-B3. Example trajectories of the ATTO647N dye with the corresponding LD plots.

Dye sticking was confirmed by linear dichroism experiments which showed changes of the emitted light polarization with dynamics in the millisecond to second regime. When the transients of the donor and acceptor dyes of the curvature sensor were analyzed, a pronounced sticking of the dyes was observed, with the acceptor dye showing this behavior being more prominent. Example trajectories of ATTO647N acceptor together with the corresponding LD plots were shown in Figure S-B3. The first trajectory in Figure S-B3-a displays very fast temporal fluctuations and the other one in Figure S-B3-b shows anticorrelated behavior between the channels on longer timescales. The dye shows different preferred sticking orientations which is indicated by the change of the LD from 0.4 to -0.2. The result

of fixed transition dipole orientations both effects the photon collection efficiency as well as the FRET efficiency. Both effects result in a broadening of the FRET histogram as well as shifts in the FRET efficiency value. Although it limits the working range by lowering the sensitivity of the system, the sticking of the dyes does not affect the bending of the curvature sensor. On that account, it is not an obstacle for the functionality of our sensor.

Additionally, we performed steady state anisotropy measurements on the spectrofluorometer FS5 (Edinburgh Instruments) to further support our statements regarding the photophysical issues of the fluorophores on our sensor. We found out the anisotropy values of 0.30 and 0.26 for Cy3B and ATTO647N fluorophores on our sensor, respectively. This relatively high anisotropy values support that the fluorophores are not freely rotating in our system which explains the deviations from the theoretical values.

7.3. Comparison of the curvature sensor on different linear surfaces

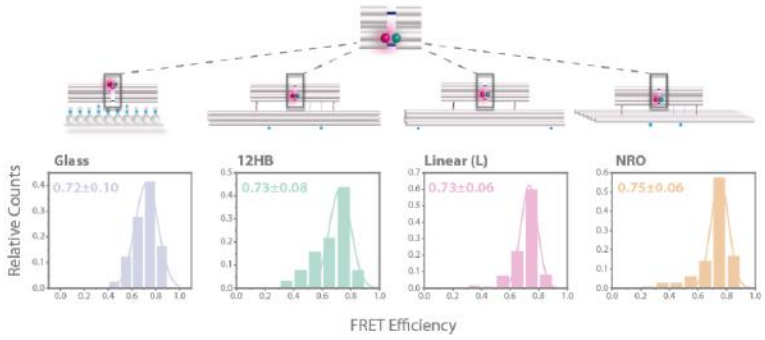

Figure S-B4. Comparison of curvature sensor in flat conformation. PR distributions of the fixed structure on different platforms; passivated glass surface, 12HB-Linear and NRO DNA origami nanostructures. The mean values with the corresponding width (standard deviation (SD)) of the Gaussian fit are given.

In order to study the influence of the immobilization schemes on the FRET efficiencies, we compared the data of the bridged sensor on different linear platforms (glass, 12HB, Linear and NRO nanostructures with 180° bending angle). Correspondingly, the fixed sensor exhibited the mean FRET efficiencies of 0.72±0.10, 0.73±0.08, 0.73±0.06 and 0.75±0.06 on glass, 12HB, Linear, and NRO nanostructures, respectively (Figure S-B4). The fact that it exhibited the same mean FRET efficiency of ~0.73 on all different linear surfaces shows that the FRET efficiencies were not influenced by the specific immobilization.

Additionally, when the FRET efficiency histograms of the flexible sensor on different linear platforms were compared, it is quite noticeable that the flexible sensor worked more robustly on DNA nanostructures than it did on glass. This is predictable because the DNA nanostructures were modified with only two binding sites that the curvature sensor could be attached to, whereas on glass surface there were plenty of NeutrAvidin anchors inducing a variety of conformations.

8. References

1. Douglas, S. M.; Marblestone, A. H.; Teerapittayanon, S.; Vazquez, A.; Church, G. M.; Shih, W. M., Rapid prototyping of 3D DNA-origami shapes with caDNAno. *Nucleic Acids Research* **2009,** *37* (15), 5001-5006.

2. Castro, C. E.; Kilchherr, F.; Kim, D.-N.; Shiao, E. L.; Wauer, T.; Wortmann, P.; Bathe, M.; Dietz, H., A primer to scaffolded DNA origami. *Nature Methods* **2011,** *8* (3), 221-229.

3. Kim, D.-N.; Kilchherr, F.; Dietz, H.; Bathe, M., Quantitative prediction of 3D solution shape and flexibility of nucleic acid nanostructures. *Nucleic Acids Research* **2012,** *40* (7), 2862-2868.

4. Schindelin, J.; Arganda-Carreras, I.; Frise, E.; Kaynig, V.; Longair, M.; Pietzsch, T.; Preibisch, S.; Rueden, C.; Saalfeld, S.; Schmid, B.; Tinevez, J.-Y.; White, D. J.; Hartenstein, V.; Eliceiri, K.; Tomancak, P.; Cardona, A., Fiji: an open-source platform for biological-image analysis. *Nature Methods* **2012,** *9* (7), 676-682.

5. Vogelsang, J.; Kasper, R.; Steinhauer, C.; Person, B.; Heilemann, M.; Sauer, M.; Tinnefeld, P., A Reducing and Oxidizing System Minimizes Photobleaching and Blinking of Fluorescent Dyes. *Angewandte Chemie International Edition* **2008,** *47* (29), 5465-5469.

6. Cordes, T.; Vogelsang, J.; Tinnefeld, P., On the Mechanism of Trolox as Antiblinking and Antibleaching Reagent. *Journal of the American Chemical Society* **2009,** *131* (14), 5018-5019.

7. Preus, S.; Noer, S. L.; Hildebrandt, L. L.; Gudnason, D.; Birkedal, V., iSMS: single-molecule FRET microscopy software. *Nature Methods* **2015,** *12* (7), 593-594.

8. Schröder, T.; Scheible, M. B.; Steiner, F.; Vogelsang, J.; Tinnefeld, P., Interchromophoric Interactions Determine the Maximum Brightness Density in DNA Origami Structures. *Nano Letters* **2019,** *19* (2), 1275-1281.

9. Cordes, T.; Santoso, Y.; Tomescu, A. I.; Gryte, K.; Hwang, L. C.; Camará, B.; Wigneshweraraj, S.; Kapanidis, A. N., Sensing DNA Opening in Transcription Using Quenchable Förster Resonance Energy Transfer. *Biochemistry* **2010,** *49* (43), 9171-9180.

10. Di Fiori, N.; Meller, A., The Effect of Dye-Dye Interactions on the Spatial Resolution of Single-Molecule FRET Measurements in Nucleic Acids. *Biophysical Journal* **2010,** *98* (10), 2265-2272.

11. Jungmann, R.; Steinhauer, C.; Scheible, M.; Kuzyk, A.; Tinnefeld, P.; Simmel, F. C., Single-Molecule Kinetics and Super-Resolution Microscopy by Fluorescence Imaging of Transient Binding on DNA Origami. *Nano Letters* **2010,** *10* (11), 4756-4761.

12. Aitken, C. E.; Marshall, R. A.; Puglisi, J. D., An Oxygen Scavenging System for Improvement of Dye Stability in Single-Molecule Fluorescence Experiments. *Biophysical Journal* **2008,** *94* (5), 1826-1835.

13. Schnitzbauer, J.; Strauss, M. T.; Schlichthaerle, T.; Schueder, F.; Jungmann, R., Super-resolution microscopy with DNA-PAINT. *Nature Protocols* **2017,** *12* (6), 1198-1228.

14. Wang, Y.; Schnitzbauer, J.; Hu, Z.; Li, X.; Cheng, Y.; Huang, Z.-L.; Huang, B., Localization events-based sample drift correction for localization microscopy with redundant cross-correlation algorithm. *Opt. Express* **2014,** *22* (13), 15982-15991.

15. Lerner, E.; Ploetz, E.; Hohlbein, J.; Cordes, T.; Weiss, S., A Quantitative Theoretical Framework For Protein-Induced Fluorescence Enhancement–Förster-Type Resonance Energy Transfer (PIFE-FRET). *The Journal of Physical Chemistry B* **2016,** *120* (26), 6401-6410.

16. Iqbal, A.; Arslan, S.; Okumus, B.; Wilson, T. J.; Giraud, G.; Norman, D. G.; Ha, T.; Lilley, D. M. J., Orientation dependence in fluorescent energy transfer between Cy3 and Cy5 terminally attached to double-stranded nucleic acids. *Proceedings of the National Academy of Sciences* **2008,** *105* (32), 11176-11181.

17. Holden, S. J.; Uphoff, S.; Hohlbein, J.; Yadin, D.; Le Reste, L.; Britton, O. J.; Kapanidis, A. N., Defining the Limits of Single-Molecule FRET Resolution in TIRF Microscopy. *Biophysical Journal* **2010,** *99* (9), 3102-3111.

18. Hübner, K.; Joshi, H.; Aksimentiev, A.; Stefani, F. D.; Tinnefeld, P.; Acuna, G. P., Determining the In-Plane Orientation and Binding Mode of Single Fluorescent Dyes in DNA Origami Structures. *ACS Nano* **2021,** *15* (3), 5109-5117.

8. Appendix for Section 4

8.1. Supplementary Information

Supplementary Information for

DNA Origami Vesicle Sensors with Triggered Cargo Transfer

Ece Büber[a], Renukka Yaadav[a], Tim Schröder[a], Henri G. Franquelim[b,], and Philip Tinnefeld[a,*]*

[a]Department of Chemistry and Center for NanoScience, Ludwig-Maximilians-University, Butenandtstraße 5−13, 81377, Munich, Germany

[b]Interfaculty Centre for Bioactive Matter, Leipzig University, % Deutscher Platz 5 (BBZ), 04109 Leipzig, Germany

Correspondence to henri.franquelim@uni-leipzig.de or philip.tinnefeld@cup.lmu.de

Contents

1. List of Buffers

Buffer	Recipe
FOB12.5	10 mM Tris-HCl, 1 mM EDTA, 12.5 mM $MgCl_2$
PEG Buffer	12% PEG-8000 (w/v), 10 mM Tris, 1 mM EDTA, 500 mM NaCl, 12 mM $MgCl_2$, pH 7.5
LUV Buffer	5 mM Tris-HCl, 1 mM EDTA, 0.5 mM Trolox and 650 mM NaCl, pH 7.0
AlexaF-Buffer	10 mM Tris-HCl, 1 mM EDTA,1 % (wt/v) D-(+)-glucose, 165 units/mL glucose oxidase, 2170 units/mL catalase, 1 mM Trolox, 12.5 mM $MgCl_2$

2. List of DNA Oligonucleotides

5' position	Oligonucleotide Sequence	Comments
	Sensing Unit Staples	
12[79]	AAATTAAGTTGACCATTAGATACTTTTGCGAAAAAAAAAAAA-ATTO647N	Sensing probe – ATTO647N
12[79]	AAATTAAGTTGACCATTAGATACTTTTGCGAAAAAAAAAAAA-Alexa647	Control probe – AlexaF647
10[79]	ATTO542-GATGGCTTATCAAAAAGATTAAGAGCGTCC	Donor dye – ATTO542
	Anchoring Staples – for Cholesterol labeling	
11[96]	TCCTCTACCACCTACATCACAATGGTCAACAGGCAAGGCAAAGAGTAATGTG	5nm chol-1
13[96]	TCCTCTACCACCTACATCACTAGGTAAACTATTTTTGAGAGATCAAACGTTA	5nm chol-2
9[96]	TCCTCTACCACCTACATCACCGAAAGACTTTGATAAGAGGTCATATTTCGCA	5nm chol-3
7[96]	TCCTCTACCACCTACATCACTAAGAGCAAATGTTTAGACTGGATAGGAAGCC	5nm chol-4
10[111]	TCCTCTACCACCTACATCACTTGCTCCTTTCAAATATCGCGTTTGAGGGGGT	10nm chol-1
12[111]	TCCTCTACCACCTACATCACTAAATCATATAACCTGTTTAGCTAACCTTTAA	10nm chol-2
14[111]	TCCTCTACCACCTACATCACGAGGGTAGGATTCAAAAGGGTGAGACATCCAA	10nm chol-3
8[111]	TCCTCTACCACCTACATCACAATAGTAAACACTATCATAACCCTCATTGTGA	10nm chol-4

13[128]	TCCTCTACCACCTACATCACGAGACAGCTAGCTGATAAATTAATTTTTGT	15nm chol-1
7[128]	TCCTCTACCACCTACATCACAGACGACAAAGAAGTTTTGCCATAATTCGA	15nm chol-2
11[128]	TCCTCTACCACCTACATCACTTTGGGGATAGTAGTAGCATTAAAAGGCCG	15nm chol-3
9[128]	TCCTCTACCACCTACATCACGCTTCAATCAGGATTAGAGAGTTATTTTCA	15nm chol-4
10[143]	TCCTCTACCACCTACATCACCCAACAGGAGCGAACCAGACCGGAGCCTTTAC	20nm chol-1
12[143]	TCCTCTACCACCTACATCACTTCTACTACGCGAGCTGAAAAGGTTACCGCGC	20nm chol-2
14[143]	TCCTCTACCACCTACATCACCAACCGTTTCAAATCACCATCAATTCGAGCCA	20nm chol-3
8[143]	TCCTCTACCACCTACATCACCTTTTGCAGATAAAAACCAAAATAAAGACTCC	20nm chol-4
	Chol-GTGATGTAGGTGGTAGAGGA	Cholesterol label on 5' end
	Surface Binding Staples – for Biotin labeling	
4[63]	ATAAGGGAACCGGATATTCATTACGTCAGGACGTTGGGAAGAGGCAATGGCTTGACTCGA	Biotin-1
4[255]	AGCCACCACTGTAGCGCGTTTTCAAGGGAGGGAAGGTAAAGAGGCAATGGCTTGACTCGA	Biotin-2
16[63]	CGGATTCTGACGACAGTATCGGCCGCAAGGCGATTAAGTTGAGGCAATGGCTTGACTCGA	Biotin-3
16[255]	GAGAAGAGATAACCTTGCTTCTGTTCGGGAGAAACAATAAGAGGCAATGGCTTGACTCGA	Biotin-4
	TCGAGTCAAGCCATTGCCTC-Bio	Biotin label on 3' end
	Strand Displacement System Staples	
12[79]	AAATTAAGTTGACCATTAGATACTTTTGCGGGGAAGTTCCAGCAGGG	17nt protrusion at the probe position
	GTTCCAGCAGGGATTCA-Chol	Cholesterol label on 3' end
	ATTO647N-TGAATCCCTGCTGGAAC	Sensing probe for the strand displacement system, 5' ATTO647N label
	Unmodified Staples	
20[207]	GCGGAACATCTGAATAATGGAAGGTACAAAAT	
23[192]	ACCCTTCTGACCTGAAAGCGTAAGACGCTGAG	
0[175]	TCCACAGACAGCCCTCATAGTTAGCGTAACGA	
1[256]	CAGGAGGTGGGGTCAGTGCCTTGAGTCTCTGAATTTACCG	
21[64]	GCCCTTCAGAGTCCACTATTAAAGGGTGCCGT	
16[207]	ACCTTTTTATTTTAGTTAATTTCATAGGGCTT	

21[128]	GCGAAAAATCCCTTATAAATCAAGCCGGCG	
18[271]	CTTTTACAAAATCGTCGCTATTAGCGATAG	
8[239]	AAGTAAGCAGACACCACGGAATAATATTGACG	
1[192]	GCGGATAACCTATTATTCTGAAACAGACGATT	
2[239]	GCCCGTATCCGGAATAGGTGTATCAGCCCAAT	
14[271]	TTAGTATCACAATAGATAAGTCCACGAGCA	
0[239]	AGGAACCCATGTACCGTAACACTTGATATAA	
9[224]	AAAGTCACAAAATAAACAGCCAGCGTTTTA	
20[175]	ATTATCATTCAATATAATCCTGACAATTAC	
6[175]	CAGCAAAAGGAAACGTCACCAATGAGCCGC	
12[239]	CTTATCATTCCCGACTTGCGGGAGCCTAATTT	
3[96]	ACACTCATCCATGTTACTTAGCCGAAAGCTGC	
18[79]	GATGTGCTTCAGGAAGATCGCACAATGTGA	
6[271]	ACCGATTGTCGGCATTTTCGGTCATAATCA	
21[224]	CTTTAGGGCCTGCAACAGTGCCAATACGTG	
1[96]	AAACAGCTTTTTGCGGGATCGTCAACACTAAA	
19[224]	CTACCATAGTTTGAGTAACATTTAAAATAT	
21[192]	TGAAAGGAGCAAATGAAAAATCTAGAGATAGA	
18[207]	CGCGCAGATTACCTTTTTTAATGGGAGAGACT	
4[47]	GACCAACTAATGCCACTACGAAGGGGGTAGCA	
13[32]	AACGCAAAATCGATGAACGGTACCGGTTGA	
1[160]	TTAGGATTGGCTGAGACTCCTCAATAACCGAT	
22[271]	CAGAAGATTAGATAATACATTTGTCGACAA	
1[32]	AGGCTCCAGAGGCTTTGAGGACACGGGTAA	
16[79]	GCGAGTAAAAATATTTAAATTGTTACAAAG	
4[239]	GCCTCCCTCAGAATGGAAAGCGCAGTAACAGT	
16[143]	GCCATCAAGCTCATTTTTTAACCACAAATCCA	
4[207]	CCACCCTCTATTCACAAACAAATACCTGCCTA	
19[96]	CTGTGTGATTGCGTTGCGCTCACTAGAGTTGC	
22[47]	CTCCAACGCAGTGAGACGGGCAACCAGCTGCA	
12[47]	TAAATCGGGATTCCCAATTCTGCGATATAATG	
8[271]	AATAGCTATCAATAGAAAATTCAACATTCA	
7[56]	ATGCAGATACATAACGGGAATCGTCATAAATAAAGCAAAG	
18[143]	CAACTGTTGCGCCATTCGCCATTCAAACATCA	
14[47]	AACAAGAGGGATAAAAATTTTTAGCATAAAGC	
14[207]	AATTGAGAATTCTGTCCAGACGACTAAACCAA	
0[271]	CCACCCTCATTTTCAGGGATAGCAACCGTACT	
23[32]	CAAATCAAGTTTTTTGGGGTCGAAACGTGGA	

10[271]	ACGCTAACACCCACAAGAATTGAAAATAGC	
3[128]	AGCGCGATGATAAATTGTGTCGTGACGAGA	
10[239]	GCCAGTTAGAGGGTAATTGAGCGCTTTAAGAA	
5[128]	AACACCAAATTTCAACTTTAATCGTTTACC	
0[207]	TCACCAGTACAAACTACAACGCCTAGTACCAG	
19[56]	TACCGAGCTCGAATTCGGGAAACCTGTCGTGCAGCTGATT	
17[192]	CATTTGAAGGCGAATTATTCATTTTTGTTTGG	
4[79]	GCGCAGACAAGAGGCAAAAGAATCCCTCAG	
20[239]	ATTTTAAAATCAAAATTATTTGCACGGATTCG	
19[160]	GCAATTCACATATTCCTGATTATCAAAGTGTA	
15[128]	TAAATCAAAATAATTCGCGTCTCGGAAACC	
0[143]	TCTAAAGTTTTGTCGTCTTTCCAGCCGACAA	
10[47]	CTGTAGCTTGACTATTATAGTCAGTTCATTGA	
17[128]	AGGCAAAGGGAAGGGCGATCGGCAATTCCA	
21[96]	AGCAAGCGTAGGGTTGAGTGTTGTAGGGAGCC	
2[207]	TTTCGGAAGTGCCGTCGAGAGGGTGAGTTTCG	
22[239]	TTAACACCAGCACTAACAACTAATCGTTATTA	
19[32]	GTCGACTTCGGCCAACGCGCGGGGTTTTTC	
11[64]	GATTTAGTCAATAAAGCCTCAGAGAACCCTCA	
6[239]	GAAATTATTGCCTTTAGCGTCAGACCGGAACC	
18[47]	CCAGGGTTGCCAGTTTGAGGGGACCCGTGGGA	
10[191]	GAAACGATAGAAGGCTTATCCGGTCTCATCGAGAACAAGC	
3[160]	TTGACAGGCCACCACCAGAGCCGCGATTTGTA	
8[47]	ATCCCCCTATACCACATTCAACTAGAAAAATC	
13[64]	TATATTTTGTCATTGCCTGAGAGTGGAAGATTGTATAAGC	
5[160]	GCAAGGCCTCACCAGTAGCACCATGGGCTTGA	
5[32]	CATCAAGTAAAACGAACTAACGAGTTGAGA	
11[224]	GCGAACCTCCAAGAACGGGTATGACAATAA	
17[160]	AGAAAACAAAGAAGATGATGAAACAGGCTGCG	
4[271]	AAATCACCTTCCAGTAAGCGTCAGTAATAA	
15[32]	TAATCAGCGGATTGACCGTAATCGTAACCG	
13[184]	GACAAAAGGTAAAGTAATCGCCATATTTAACAAAACTTTT	
20[143]	AAGCCTGGTACGAGCCGGAAGCATAGATGATG	
14[79]	GCTATCAGAAATGCAATGCCTGAATTAGCA	
6[207]	TCACCGACGCACCGTAATCAGTAGCAGAACCG	
3[192]	GGCCTTGAAGAGCCACCACCCTCAGAAACCAT	
23[256]	CTTTAATGCGCGAACTGATAGCCCCACCAG	
2[47]	ACGGCTACAAAAGGAGCCTTTAATGTGAGAAT	

13[224]	ACAACATGCCAACGCTCAACAGTCTTCTGA	
20[79]	TTCCAGTCGTAATCATGGTCATAAAAGGGG	
9[64]	CGGATTGCAGAGCTTAATTGCTGAAACGAGTA	
22[175]	ACCTTGCTTGGTCAGTTGGCAAAGAGCGGA	
23[160]	TAAAAGGGACATTCTGGCCAACAAAGCATC	
16[239]	GAATTTATTTAATGGTTTGAAATATTCTTACC	
3[32]	AATACGTTTGAAAGAGGACAGACTGACCTT	
23[224]	GCACAGACAATATTTTTGAATGGGGTCAGTA	
15[192]	TCAAATATAACCTCCGGCTTAGGTAACAATTT	
7[192]	ATACATACCGAGGAAACGCAATAAGAAGCGCATTAGACGG	
12[271]	TGTAGAAATCAAGATTAGTTGCTCTTACCA	
4[111]	GACCTGCTCTTTGACCCCCAGCGAGGGAGTTA	
17[96]	GCTTTCCGATTACGCCAGCTGGCGGCTGTTTC	
23[96]	CCCGATTTAGAGCTTGACGGGGAAAAAGAATA	
16[111]	TGTAGCCATTAAAATTCGCATTAAATGCCGGA	
0[79]	ACAACTTTCAACAGTTTCAGCGGATGTATCGG	
1[128]	TGACAACTCGCTGAGGCTTGCATTATACCA	
6[111]	ATTACCTTTGAATAAGGCTTGCCCAAATCCGC	
20[271]	CTCGTATTAGAAATTGCGTAGATACAGTAC	
22[79]	TGGAACAACCGCCTGGCCCTGAGGCCCGCT	
18[239]	CCTGATTGCAATATATGTGAGTGATCAATAGT	
9[256]	GAGAGATAGAGCGTCTTTCCAGAGGTTTTGAA	
22[143]	TCGGCAAATCCTGTTTGATGGTGGACCCTCAA	
10[207]	ATCCCAATGAGAATTAACTGAACAGTTACCAG	
21[32]	TTTTCACTCAAAGGGCGAAAAACCATCACC	
5[192]	CGATAGCATTGAGCCATTTGGGAACGTAGAAA	
8[79]	AATACTGCCCAAAAGGAATTACGTGGCTCA	
15[224]	CCTAAATCAAAATCATAGGTCTAAACAGTA	
0[111]	TAAATGAATTTTCTGTATGGGATTAATTTCTT	
6[143]	GATGGTTTGAACGAGTAGTAAATTTACCATTA	
13[256]	GTTTATCAATATGCGTTATACAAACCGACCGTGTGATAAA	
14[239]	AGTATAAAGTTCAGCTAATGCAGATGTCTTTC	
22[111]	GCCCGAGAGTCCACGCTGGTTTGCAGCTAACT	
3[224]	TTAAAGCCAGAGCCGCCACCCTCGACAGAA	
1[224]	GTATAGCAAACAGTTAATGCCCAATCCTCA	
19[128]	CACAACAGGTGCCTAATGAGTGCCCAGCAG	

2[79]	CAGCGAAACTTGCTTTCGAGGTGTTGCTAA	
2[271]	GTTTTAACTTAGTACCGCCACCCAGAGCCA	
7[224]	AACGCAAAGATAGCCGAACAAACCCTGAAC	
19[248]	CGTAAAACAGAAATAAAAATCCTTTGCCCGAAAGATTAGA	
15[160]	ATCGCAAGTATGTAAATGCTGATGATAGGAAC	
6[47]	TACGTTAAAGTAATCTTGACAAGAACCGAACT	
18[111]	TCTTCGCTGCACCGCTTCTGGTGCGGCCTTCC	
16[271]	CTTAGATTTAAGGCGTTAAATAAAGCCTGT	
1[64]	TTTATCAGGACAGCATCGGAACGACACCAACCTAAAACGA	
2[143]	ATATTCGGAACCATCGCCCACGCAGAGAAGGA	
16[47]	ACAAACGGAAAAGCCCCAAAAACACTGGAGCA	
7[32]	TTTAGGACAAATGCTTTAAACAATCAGGTC	
15[96]	ATATTTTGGCTTTCATCAACATTATCCAGCCA	
20[111]	CACATTAAAATTGTTATCCGCTCATGCGGGCC	
2[111]	AAGGCCGCTGATACCGATAGTTGCGACGTTAG	
19[192]	ATTATACTAAGAAACCACCAGAAGTCAACAGT	
17[224]	CATAAATCTTTGAATACCAAGTGTTAGAAC	
21[256]	GCCGTCAAAAAACAGAGGTGAGGCCTATTAGT	
0[47]	AGAAAGGAACAACTAAAGGAATTCAAAAAAA	
7[248]	GTTTATTTTGTCACAATCTTACCGAAGCCCTTTAATATCA	
4[143]	TCATCGCCAACAAAGTACAACGGACGCCAGCA	
18[175]	CTGAGCAAAAATTAATTACATTTTGGGTTA	
11[256]	GCCTTAAACCAATCAATAATCGGCACGCGCCT	
6[79]	TTATACCACCAAATCAACGTAACGAACGAG	
22[207]	AGCCAGCAATTGAGGAAGGTTATCATCATTTT	
12[207]	GTACCGCAATTCTAAGAACGCGAGTATTATTT	
8[207]	AAGGAAACATAAAGGTGGCAACATTATCACCG	
5[96]	TCATTCAGATGCGATTTTAAGAACAGGCATAG	
21[160]	TCAATATCGAACCTCAAATATCAATTCCGAAA	
4[175]	CACCAGAAAGGTTGAGGCAGGTCATGAAAG	
23[128]	AACGTGGCGAGAAAGGAAGGGAAACCAGTAA	
23[64]	AAAGCACTAAATCGGAACCCTAATCCAGTT	
5[224]	TCAAGTTTCATTAAAGGTGAATATAAAAGA	
9[32]	TTTACCCCAACATGTTTTAAATTTCCATAT	
20[47]	TTAATGAACTAGAGGATCCCCGGGGGGTAACG	
11[32]	AACAGTTTTGTACCAAAAACATTTTATTTC	
2[175]	TATTAAGAAGCGGGGTTTTGCTCGTAGCAT	

16[175]	TATAACTAACAAAGAACGCGAGAACGCCAA	
17[32]	TGCATCTTTCCCAGTCACGACGGCCTGCAG	

3. Methods

3.1. Design and production of the vesicle sensors

As the base of the vesicle sensors, a rectangular DNA origami based on a 7249 nt long scaffold derived from the M13mp18 bacteriophage was designed in the software CaDNAno[1] with several modifications indicated in Figure S1. All staple strand sequences and modifications are given in the list of DNA oligonucleotides in Section 2.

The design includes positions for the sensing unit involving fluorophore labelled staples, surface binding staples with biotin modifications, and vesicle anchoring staples with cholesterol modifications. High performance liquid chromatograph (HPLC) purified sensing unit oligonucleotides labeled with ATTO647N and ATTO 542 were obtained from Biomers GmbH. High purity salt free (HPSF) purified unmodified staple oligonucleotides and staples for the strand displacement reaction system were supplied from IDT (Integrated DNA Technologies, Inc.). 3' Biotin and 5' Cholesterol-TEG labeled oligonucleotides as well as the control probe carrying AlexaF647 fluorophore were purchased from Eurofins Genomics GmbH.

The DNA origami nanostructures were folded using a one-pot reaction mix in a thermocycler (primus 25, peqlab). Briefly, 25 nM of scaffold DNA, unmodified oligonucleotides at a concentration 10-times, fluorophore-labeled and biotinylated oligonucleotides, both at a concentration 30-times that of the scaffold were mixed in FOB12.5 buffer and subjected to a multistep thermocycling procedure. The folding began by heating the mixture to 70°C, allowing it to equilibrate for 5 minutes, and then gradually cooling it to 20°C at a rate of 1°C per minute.

Once folded, the DNA origami nanostructures were purified using PEG precipitation. To achieve this, the sample was mixed with the PEG buffer in equal parts and then centrifuged for 30 min at 16,000 g in a 4°C environment. The resulting supernatant was removed, leaving the pellet which was further dissolved in FOB12 buffer and an equal amount of PEG buffer was added in the solution. Two times of the PEG purification were performed for each sample. For the purpose of labeling the vesicle sensors with cholesterol anchors, the neatly folded

nanostructures were mixed with cholesterol-labeled oligonucleotides (at a 20-fold excess for each labeling position) and left for overnight incubation at room temperature. A subsequent PEG precipitation step was performed for further purification.

3.2. Preparation and characterization of lipid vesicles

All lipids used in the study were obtained from Avanti Polar Lipids, located in Alabaster, AL, USA, unless stated otherwise. In order to prepare large unilamellar vesicles (LUVs) of 100% DOPC (1,2-dioleoyl-sn-glycero-3-phosphocholine), the lipid solutions in chloroform were dried using a nitrogen stream, and the remaining chloroform was evaporated under vacuum for approximately 3 hours in a desiccator. The resulting lipid film was rehydrated in the LUV buffer, resulting in a final lipid concentration of 2.5 mM. To ensure uniform vesicle size, the solution underwent seven freeze-and-thaw cycles alternating between liquid nitrogen and a water bath at 70°C. Subsequently, the vesicles were extruded using a LiposoFast Basic extruder (Avestin, INC.), employing Nucleopore PC membranes (Whatman, Cytiva Ltd.) with the desired pore size.

The size and distribution of the extruded LUV suspensions were evaluated using dynamic light scattering (DLS). These measurements were taken at dilutions that produced attenuation values between 7 and 8. Every sample underwent 10 consecutive measurements after they were allowed to incubate for 60 seconds. These measurements were conducted in disposable polystyrene cuvettes utilizing a Zetasizer Nano ZSP (Malvern Instruments, Worcestershire, UK). The device operated with a 633 nm incident wavelength and detected backscattering at an angle of 173°. Both intensity and number-normalized size distributions for the LUV samples were deduced from the correlation functions. These calculations employed the General Purpose Non-Negative Least Squares (NNLS) algorithm available in the Malvern Zetasizer Software version 7.13.

3.3. Surface preparation

24 x 60 mm microscope coverslips with a thickness of 170 µm utilized in the experiments (Carl Roth GmbH, Germany). Prior to use, they were cleaned with a UV-Ozone cleaner (PSD-UV4,

Novascan Technologies, USA) operating at 100°C for 30 minutes. Once cleaned, they were fitted with self-adhesive 150 µL SecureSeal Hybridization Chambers from Grace Bio-Labs. For the passivation process, the coverslips were treated with biotinylated-BSA (1.0 mg/mL, Thermo Fisher Scientific Inc.), allowing it to incubate for 15 minutes. This was succeeded by an additional functionalization step using NeutrAvidin (1.0 mg/mL, Thermo Fischer Scientific Inc.), with another 15-minute incubation. After each of these steps, the coverslips underwent a triple wash with 1× PBS buffer.

When the glass coverslips are ready for incorporating the sensors, roughly 50 pM of vesicle sensors (diluted in the LUV buffer) were immobilized onto NeutrAvidin-treated glass coverslips using biotin modifications on the sensors.

For tests involving lipid vesicles, vesicles were diluted to a 1 nM concentration using LUV buffer. The sensor-coated coverslips were incubated with the diluted vesicles for around an hour to capture the vesicles via cholesterol modifications. Post this anchoring phase, the coverslips were rinsed thrice with the LUV buffer.

3.4. Imaging and data analysis

The smFRET experiments were executed with a Nanoimager S (ONI Ltd. UK), under Total Internal Reflection Fluorescence (TIRF) illumination. A red excitation wavelength of 638 nm was used, while the green excitation was set at 532 nm. Initially, the objective was adjusted to focus on the sample plane, followed by activating the auto-focus function. The alternating laser excitation setting employed both green and red lasers[2-4], with power outputs of 5 mW and 8 mW, respectively. For each sample, around 10 videos were captured over a field of view spanning 50 µm × 80 µm. Videos consisted of 500 frames, each with an exposure time of 100 ms, leading to a total video duration of 50 seconds.

In all the experiments utilizing the sensing probe with ATTO647N, a standard LUV buffer (5 mM Tris-HCl, 1 mM EDTA, 0.5 mM Trolox and 650 mM NaCl, pH 7.0) was utilized. However, for the experiments involving the control probe with AlexaF647, the buffer composition was specifically altered to enhance the photostability of this fast bleaching fluorophore. The modified AlexaF-buffer incorporated a reducing and oxidizing system (ROXS)[5] along with oxygen scavenging agents. In detail, the imaging buffer for the AlexaF647

experiments consisted of 10 mM Tris-HCl and 1 mM EDTA with 1 % (wt/v) D-(+)-glucose (Sigma Aldrich, USA), 165 units/mL glucose oxidase (G2133, Sigma Aldrich, USA), 2170 units/mL catalase (C3155, Sigma Aldrich, USA), 1 mM Trolox (~12% was converted to Troloxquinone under UV light)[6] and 650 mM NaCl.

Analysis of the FRET data was performed using the iSMS software on MATLAB.[7] The process integrated individual green and red emission channels. The peakfinder algorithm was used to distinguish donor and acceptor peaks, facilitating the detection of FRET pairs. From the captured sequences, intensity-time trajectories of specific immobilized molecules were extracted. These single-molecule data sets were then further examined to detect DNA origami structures manifesting FRET. Interrelations of FRET across different channels, including I_{DD} (donor excitation-donor emission), I_{DA} (donor excitation-acceptor emission), and I_{AA} (acceptor excitation-acceptor emission), were analyzed. Instances where an increase in the I_{DD} channel intensity and a decrease in the I_{DA} channel occurred concurrently with a sudden drop in the I_{AA} channel led to that specific data set being chosen for extended evaluation. Using the intensity data of these channels for each molecule, the average FRET efficiency of every sensor was calculated over the entire energy transfer duration.

$$FRET\ efficiency = \frac{I_{DA}}{\gamma \cdot I_{DD} + I_{DA}}$$

The I_{DA} is corrected for direct acceptor excitation at the donor excitation wavelength and leakage of donor emission into the acceptor emission channel. The corrected I_{DA} is determined as

$$I_{DA} = I_{A,raw} - D_{leakage} * I_{DD} - A_{direct} * I_{AA}$$

where $I_{A,raw}$ represents the total intensity detected in the acceptor emission channel, and I_{AA} signifies the direct excitation of the acceptor.

Wherever applicable, the correction factors γ, $D_{leakage}$ and A_{direct}, are calculated as in the following:

The γ correction factor describes the relative difference in the number of photons measured of the acceptor and the donor for the same number of excited states. In iSMS γ is calculated for all molecules in which the acceptor bleaches before the acceptor:

$$\gamma = \frac{I_{DA,1} - I_{DA,2}}{I_{DD,2} - I_{DD,1}}$$

The $D_{leakage}$ accounts for the amount of leakage of the donor emission into the acceptor emission channel upon donor excitation and is calculated as

$$D_{leakage} = avg(\frac{I_{DA}(t)}{I_{DD}(t)})$$

in the time interval after the acceptor has bleached and before the donor has bleached, corresponding to a donor-only signal.

The A_{direct} accounts for the direct excitation of the acceptor at the donor wavelength and is calculated as

$$A_{direct} = avg(\frac{I_{DA}(t)}{I_{AA}(t)})$$

in the time interval after the donor has bleached and before the acceptor has bleached. From individual transients, we calculated average values for all the correction factors and used them for FRET efficiency calculations.

4. Figures

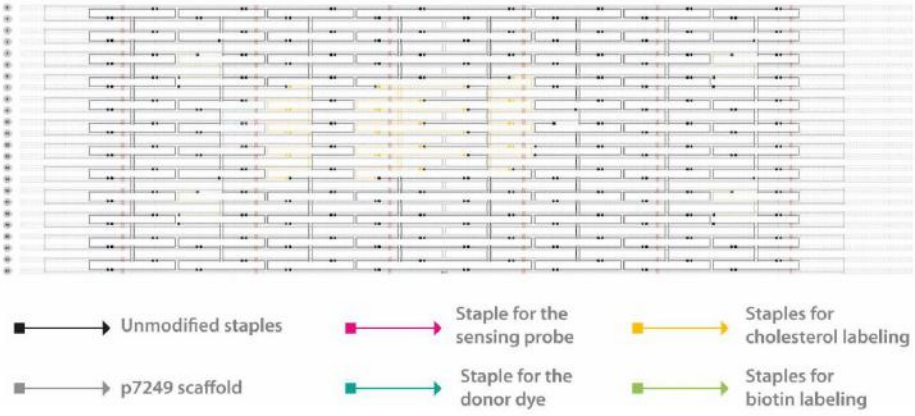

Figure S1. CaDNAno design of the vesicle sensor. Zoom in to see details. Sensing probe position is colored in magenta, and the donor dye position is in cyan. Positions of the staples for cholesterol modification are colored in orange, and for biotin modification are in green.

Unmodified staples are colored in black, and M13 p7249 scaffold is colored in gray. The sequences and details of all the staples incorporated in the DNA origami design are listed in Section 2.

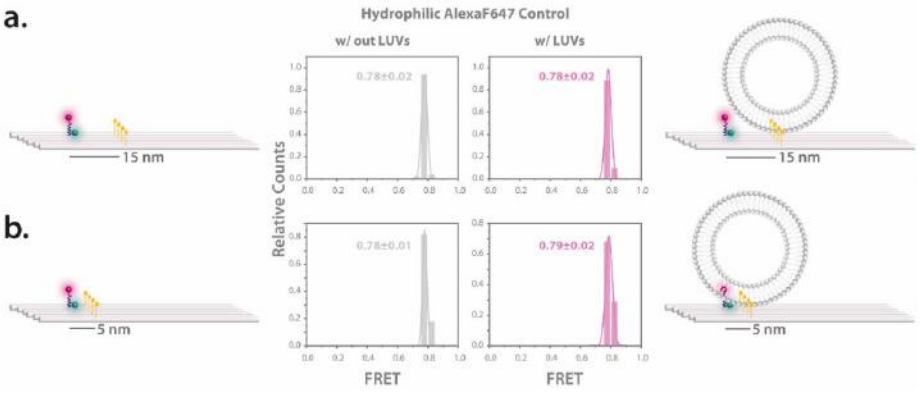

Figure S2. Sensor with the control probe AlexaF647. Effect of different cholesterol anchoring distances both in the absence and presence of lipid vesicles. The distribution of FRET efficiency for the vesicle sensors, both without and with lipid vesicles, is depicted for **(a)** 15 nm, and **(b)** 5 nm cholesterol configurations. Illustrations accompanying the data highlight the positions of the cholesterol anchors and potential movement patterns of the sensing probe. The error refers to the standard deviation (SD).

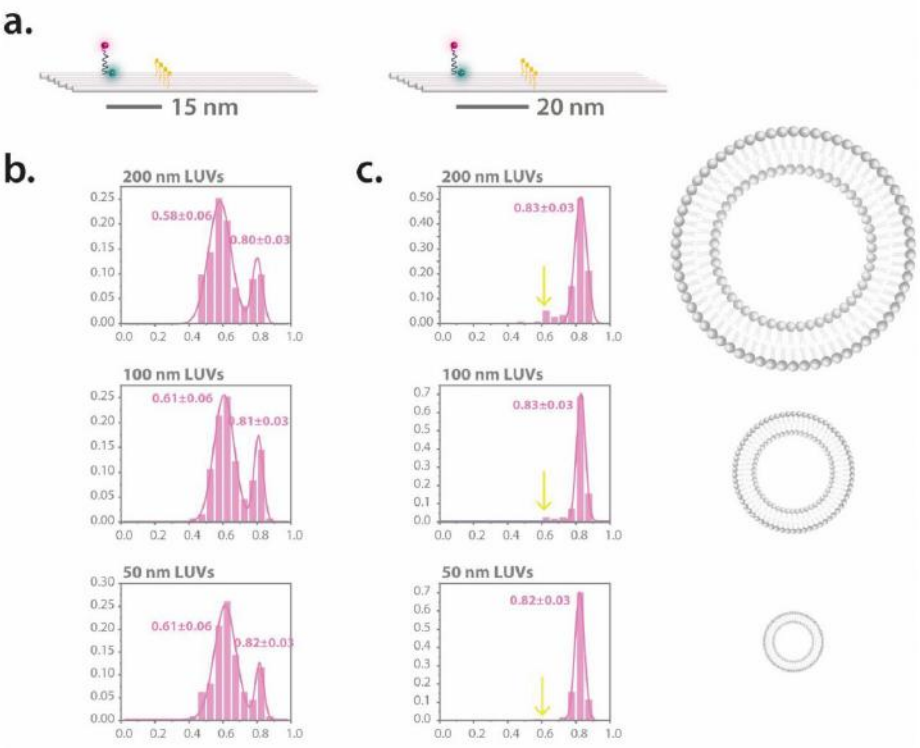

Figure S3. Sensor with different sizes of vesicles. **(a)** The sketches of the utilized sensors showing the position of the anchors. FRET efficiency distributions of the vesicle sensors **(b)** with 15 nm and **(c)** with 20 nm cholesterol configurations tested with lipid vesicles of 200 nm, 100 nm and 50 nm (from top to bottom). The yellow arrows highlight the slight increase in the lower FRET population for larger vesicles. The error refers to the standard deviation (SD).

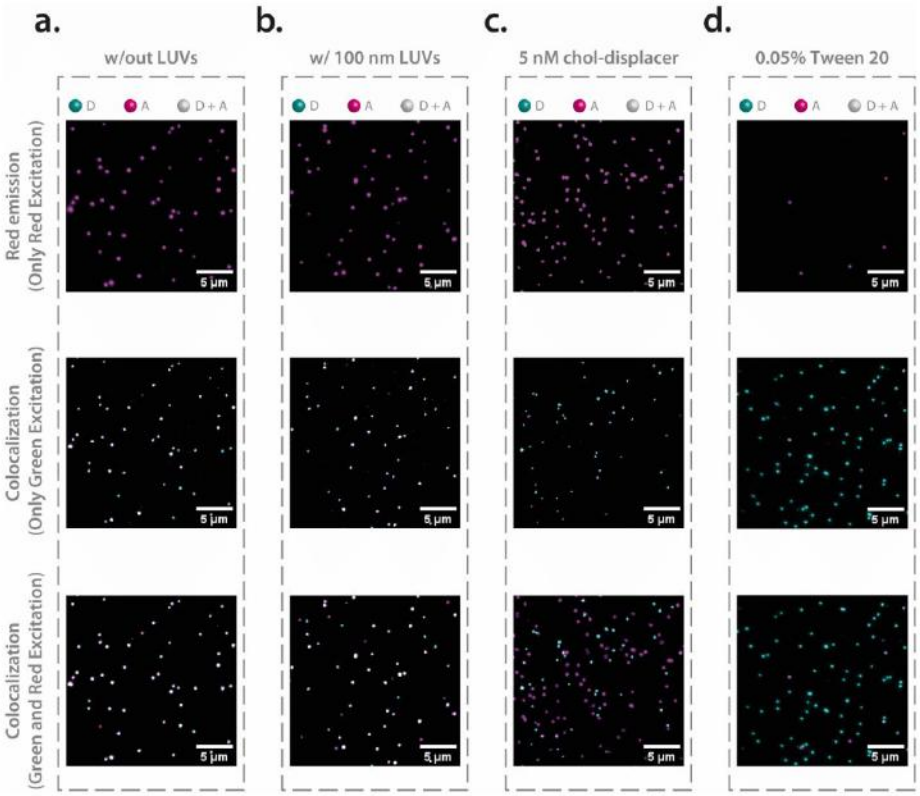

Figure S4. Validation of specific vesicle-probe interaction via the introduction of 0.05% Tween20. Each row presents distinct imaging modalities for different experimental stages: red emission after red excitation (top), superimposed TIRF images following green excitation (middle), and superimposed TIRF images after both green and red excitation (bottom). **(a)** Control system without lipid vesicles, serving as a baseline for fluorescence emission and colocalization. **(b)** System containing 100 nm lipid vesicles, demonstrating the initial state before displacement. **(c)** Post-incubation with a 5 nM cholesterol-labeled displacer strand, revealing the successful translocation of the ATTO647N-labeled probe to the vesicles. **(d)** Post-washing with a buffer containing 0.05% Tween20, showing a near-complete disappearance of red emission spots, which affirms the specificity of vesicle-probe interaction.

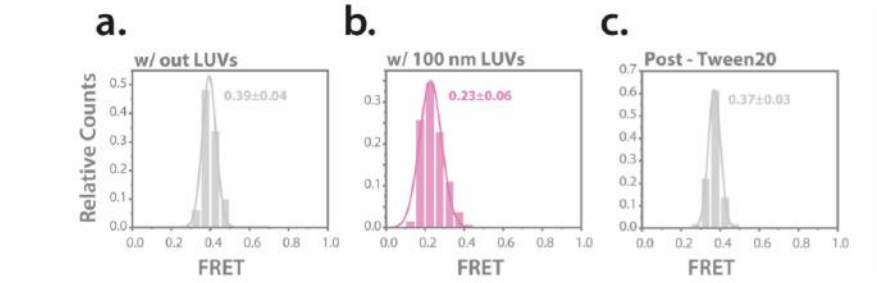

Figure S5. Examination of the impact of Tween20 on Sensor Behavior. The figure displays FRET histograms to evaluate the effect of 0.05% Tween20 on the system, specifically focusing on its ability to disrupt lipid vesicles without affecting sensor behavior. **(a)** FRET histogram of the system without lipid vesicles, serving as a control to establish baseline FRET values. **(b)** FRET histogram after the introduction of 100 nm lipid vesicles, demonstrating the change in FRET values upon vesicle binding. **(c)** FRET histogram following washing with a buffer containing 0.05% Tween20, but without prior incubation with the cholesterol-labeled displacer strand. The similarity between this histogram and the control (a) confirms that Tween20 exclusively disrupts the lipid vesicles without altering the FRET efficiency of the sensor. The error refers to the standard deviation (SD).

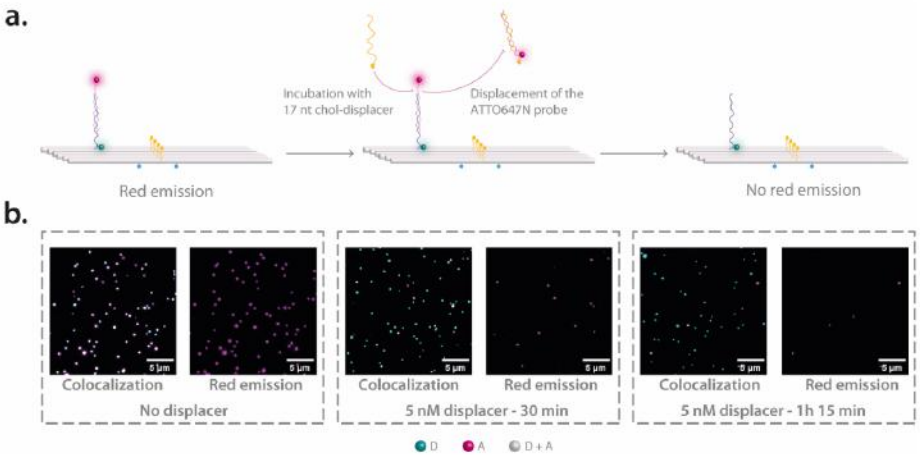

Figure S6. Experimental evidence illustrating the absence of non-specific probe adherence in a system devoid of lipid vesicles and the effectiveness of cholesterol-labeled displacer strand. **(a)** Schematic representation of the DNA origami-based sensor at various stages of the control experiment. The left panel shows the initial system with the ATTO647N-labeled sensing probe bound to the DNA origami, emitting red fluorescence. The middle panel illustrates the sensor after incubation with the 17 nt cholesterol-labeled displacer strand, depicting how the probe is displaced into solution due to the absence of lipid vesicles for anchoring. The right panel shows the sensor solely with the ATTO542 fluorophore, representing the disappearance of the red emission signal. **(b)** Superimposed TIRF images corroborating the above sequence of events. The left images show both colocalized and isolated red emission spots before the introduction of the cholesterol displacer strand. The middle images show reduced numbers of colocalized and red spots after 30 minutes of incubation with the displacer strand. The right images, taken after 1 hour and 15 minutes of incubation followed by washing, reveal a near-complete disappearance of red emission spots, confirming that the displacer efficiently translocates the sensing probe without unspecific sticking.

5. References

1. Douglas, S. M.; Marblestone, A. H.; Teerapittayanon, S.; Vazquez, A.; Church, G. M.; Shih, W. M., Rapid prototyping of 3D DNA-origami shapes with caDNAno. *Nucleic Acids Research* **2009,** *37* (15), 5001-5006.
2. Kapanidis, A. N.; Laurence, T. A.; Lee, N. K.; Margeat, E.; Kong, X.; Weiss, S., Alternating-Laser Excitation of Single Molecules. *Accounts of Chemical Research* **2005,** *38* (7), 523-533.
3. Lee, N. K.; Kapanidis, A. N.; Wang, Y.; Michalet, X.; Mukhopadhyay, J.; Ebright, R. H.; Weiss, S., Accurate FRET Measurements within Single Diffusing Biomolecules Using Alternating-Laser Excitation. *Biophysical Journal* **2005,** *88* (4), 2939-2953.
4. Margeat, E.; Kapanidis, A. N.; Tinnefeld, P.; Wang, Y.; Mukhopadhyay, J.; Ebright, R. H.; Weiss, S., Direct Observation of Abortive Initiation and Promoter Escape within Single Immobilized Transcription Complexes. *Biophysical Journal* **2006,** *90* (4), 1419-1431.

5. Vogelsang, J.; Kasper, R.; Steinhauer, C.; Person, B.; Heilemann, M.; Sauer, M.; Tinnefeld, P., A Reducing and Oxidizing System Minimizes Photobleaching and Blinking of Fluorescent Dyes. *Angewandte Chemie International Edition* **2008,** *47* (29), 5465-5469.
6. Cordes, T.; Vogelsang, J.; Tinnefeld, P., On the Mechanism of Trolox as Antiblinking and Antibleaching Reagent. *Journal of the American Chemical Society* **2009,** *131* (14), 5018-5019.
7. Preus, S.; Noer, S. L.; Hildebrandt, L. L.; Gudnason, D.; Birkedal, V., iSMS: single-molecule FRET microscopy software. *Nature Methods* **2015,** *12* (7), 593-594.

9. Bibliography

1. Turner, A. P. F.; Karube, I.; Wilson, G. S., *Biosensors: Fundamentals and Applications*. Oxford University Press: 1987.
2. Ramesh, M.; Janani, R.; Deepa, C.; Rajeshkumar, L., Nanotechnology-Enabled Biosensors: A Review of Fundamentals, Design Principles, Materials, and Applications. *Biosensors* 2022, *13* (1), 40.
3. Naresh, V.; Lee, N., A Review on Biosensors and Recent Development of Nanostructured Materials-Enabled Biosensors. *Sensors* 2021, *21* (4), 1109.
4. Saha, K.; Agasti, S. S.; Kim, C.; Li, X.; Rotello, V. M., Gold Nanoparticles in Chemical and Biological Sensing. *Chemical Reviews* 2012, *112* (5), 2739-2779.
5. Gulati, S.; Singh, P.; Diwan, A.; Mongia, A.; Kumar, S., Functionalized gold nanoparticles: promising and efficient diagnostic and therapeutic tools for HIV/AIDS. *RSC Med Chem* 2020, *11* (11), 1252-1266.
6. Seeman, N. C., Nucleic acid junctions and lattices. *Journal of Theoretical Biology* 1982, *99* (2), 237-247.
7. Rothemund, P. W. K., Folding DNA to create nanoscale shapes and patterns. *Nature* 2006, *440* (7082), 297-302.
8. Wang, P.; Meyer, T. A.; Pan, V.; Dutta, P. K.; Ke, Y., The Beauty and Utility of DNA Origami. *Chem* 2017, *2* (3), 359-382.
9. Dey, S.; Fan, C.; Gothelf, K. V.; Li, J.; Lin, C.; Liu, L.; Liu, N.; Nijenhuis, M. A. D.; Saccà, B.; Simmel, F. C.; Yan, H.; Zhan, P., DNA origami. *Nature Reviews Methods Primers* 2021, *1* (1).
10. Rothemund, P. W. K.; Andersen, E. S., The importance of being modular. *Nature* 2012, *485* (7400), 584-585.
11. Lee, C.; Lee, J. Y.; Kim, D.-N., Polymorphic design of DNA origami structures through mechanical control of modular components. *Nature Communications* 2017, *8* (1), 2067.
12. Rubio-Sánchez, R.; Barker, S. E.; Walczak, M.; Cicuta, P.; Michele, L. D., A Modular, Dynamic, DNA-Based Platform for Regulating Cargo Distribution and Transport between Lipid Domains. *Nano Letters* 2021, *21* (7), 2800-2808.
13. Mao, M.; Lin, Z.; Chen, L.; Zou, Z.; Zhang, J.; Dou, Q.; Wu, J.; Chen, J.; Wu, M.; Niu, L.; Fan, C.; Zhang, Y., Modular DNA-Origami-Based Nanoarrays Enhance Cell Binding Affinity through the "Lock-and-Key" Interaction. *Journal of the American Chemical Society* 2023, *145* (9), 5447-5455.
14. Andersen, E. S.; Dong, M.; Nielsen, M. M.; Jahn, K.; Subramani, R.; Mamdouh, W.; Golas, M. M.; Sander, B.; Stark, H.; Oliveira, C. L. P.; Pedersen, J. S.; Birkedal, V.; Besenbacher, F.; Gothelf, K. V.; Kjems, J., Self-assembly of a nanoscale DNA box with a controllable lid. *Nature* 2009, *459* (7243), 73-76.
15. Acuna, G. P.; Möller, F. M.; Holzmeister, P.; Beater, S.; Lalkens, B.; Tinnefeld, P., Fluorescence Enhancement at Docking Sites of DNA-Directed Self-Assembled Nanoantennas. *Science* 2012, *338* (6106), 506-510.

16. Marras, A. E.; Shi, Z.; Lindell, M. G.; Patton, R. A.; Huang, C.-M.; Zhou, L.; Su, H.-J.; Arya, G.; Castro, C. E., Cation-Activated Avidity for Rapid Reconfiguration of DNA Nanodevices. *ACS Nano* 2018, *12* (9), 9484-9494.

17. Wang, S.; Zhou, Z.; Ma, N.; Yang, S.; Li, K.; Teng, C.; Ke, Y.; Tian, Y., DNA Origami-Enabled Biosensors. *Sensors* 2020, *20* (23), 6899.

18. Shen, L.; Wang, P.; Ke, Y., DNA Nanotechnology-Based Biosensors and Therapeutics. *Advanced Healthcare Materials* 2021, 2002205.

19. Ha, T., Single-Molecule Fluorescence Resonance Energy Transfer. *Methods* 2001, *25* (1), 78-86.

20. Roy, R.; Hohng, S.; Ha, T., A practical guide to single-molecule FRET. *Nature Methods* 2008, *5* (6), 507-516.

21. Hirata, E.; Kiyokawa, E., Future Perspective of Single-Molecule FRET Biosensors and Intravital FRET Microscopy. *Biophysical Journal* 2016, *111* (6), 1103-1111.

22. Hellenkamp, B.; Schmid, S.; Doroshenko, O.; Opanasyuk, O.; Kühnemuth, R.; Rezaei Adariani, S.; Ambrose, B.; Aznauryan, M.; Barth, A.; Birkedal, V.; Bowen, M. E.; Chen, H.; Cordes, T.; Eilert, T.; Fijen, C.; Gebhardt, C.; Götz, M.; Gouridis, G.; Gratton, E.; Ha, T.; Hao, P.; Hanke, C. A.; Hartmann, A.; Hendrix, J.; Hildebrandt, L. L.; Hirschfeld, V.; Hohlbein, J.; Hua, B.; Hübner, C. G.; Kallis, E.; Kapanidis, A. N.; Kim, J.-Y.; Krainer, G.; Lamb, D. C.; Lee, N. K.; Lemke, E. A.; Levesque, B.; Levitus, M.; McCann, J. J.; Naredi-Rainer, N.; Nettels, D.; Ngo, T.; Qiu, R.; Robb, N. C.; Röcker, C.; Sanabria, H.; Schlierf, M.; Schröder, T.; Schuler, B.; Seidel, H.; Streit, L.; Thurn, J.; Tinnefeld, P.; Tyagi, S.; Vandenberk, N.; Vera, A. M.; Weninger, K. R.; Wünsch, B.; Yanez-Orozco, I. S.; Michaelis, J.; Seidel, C. A. M.; Craggs, T. D.; Hugel, T., Precision and accuracy of single-molecule FRET measurements—a multi-laboratory benchmark study. *Nature Methods* 2018, *15* (9), 669-676.

23. Agam, G.; Gebhardt, C.; Popara, M.; Mächtel, R.; Folz, J.; Ambrose, B.; Chamachi, N.; Chung, S. Y.; Craggs, T. D.; de Boer, M.; Grohmann, D.; Ha, T.; Hartmann, A.; Hendrix, J.; Hirschfeld, V.; Hübner, C. G.; Hugel, T.; Kammerer, D.; Kang, H.-S.; Kapanidis, A. N.; Krainer, G.; Kramm, K.; Lemke, E. A.; Lerner, E.; Margeat, E.; Martens, K.; Michaelis, J.; Mitra, J.; Moya Muñoz, G. G.; Quast, R. B.; Robb, N. C.; Sattler, M.; Schlierf, M.; Schneider, J.; Schröder, T.; Sefer, A.; Tan, P. S.; Thurn, J.; Tinnefeld, P.; van Noort, J.; Weiss, S.; Wendler, N.; Zijlstra, N.; Barth, A.; Seidel, C. A. M.; Lamb, D. C.; Cordes, T., Reliability and accuracy of single-molecule FRET studies for characterization of structural dynamics and distances in proteins. *Nature Methods* 2023, *20* (4), 523-535.

24. Verma, A. K.; Noumani, A.; Yadav, A. K.; Solanki, P. R., FRET Based Biosensor: Principle Applications Recent Advances and Challenges. *Diagnostics* 2023, *13* (8), 1375.

25. Li, C.-c.; Li, Y.; Zhang, Y.; Zhang, C.-y., Single-molecule fluorescence resonance energy transfer and its biomedical applications. *TrAC Trends in Analytical Chemistry* 2020, *122*, 115753.

26. Albanese, A.; Tang, P. S.; Chan, W. C. W., The Effect of Nanoparticle Size, Shape, and Surface Chemistry on Biological Systems. *Annual Review of Biomedical Engineering* 2012, *14* (1), 1-16.

27. Mosquera, J.; García, I.; Liz-Marzán, L. M., Cellular Uptake of Nanoparticles versus Small Molecules: A Matter of Size. *Accounts of Chemical Research* 2018, *51* (9), 2305-2313.

28. Mitchell, M. J.; Billingsley, M. M.; Haley, R. M.; Wechsler, M. E.; Peppas, N. A.; Langer, R., Engineering precision nanoparticles for drug delivery. *Nature Reviews Drug Discovery* 2021, *20* (2), 101-124.

29. Clark, L. C., Jr.; Lyons, C., Electrode systems for continuous monitoring in cardiovascular surgery. *Ann N Y Acad Sci* 1962, *102*, 29-45.

30. Chen, C.; Wang, J., Optical biosensors: an exhaustive and comprehensive review. *The Analyst* 2020, *145* (5), 1605-1628.

31. Borisov, S. M.; Wolfbeis, O. S., Optical Biosensors. *Chemical Reviews* 2008, *108* (2), 423-461.

32. Dove, A., Quenching biosensor. *Nature Biotechnology* 1999, *17* (12), 1149-1149.

33. Fritz, R. D.; Letzelter, M.; Reimann, A.; Martin, K.; Fusco, L.; Ritsma, L.; Ponsioen, B.; Fluri, E.; Schulte-Merker, S.; van Rheenen, J.; Pertz, O., A Versatile Toolkit to Produce Sensitive FRET Biosensors to Visualize Signaling in Time and Space. *Science Signaling* 2013, *6* (285), rs12-rs12.

34. Zhang, X.; Hu, Y.; Yang, X.; Tang, Y.; Han, S.; Kang, A.; Deng, H.; Chi, Y.; Zhu, D.; Lu, Y., FÖrster resonance energy transfer (FRET)-based biosensors for biological applications. *Biosensors and Bioelectronics* 2019, *138*, 111314.

35. Wu, L.; Huang, C.; Emery, B. P.; Sedgwick, A. C.; Bull, S. D.; He, X.-P.; Tian, H.; Yoon, J.; Sessler, J. L.; James, T. D., Förster resonance energy transfer (FRET)-based small-molecule sensors and imaging agents. *Chemical Society Reviews* 2020, *49* (15), 5110-5139.

36. Megalathan, A.; Wijesinghe, K. M.; Dhakal, S., Single-Molecule FRET-Based Dynamic DNA Sensor. *ACS Sensors* 2021, *6* (3), 1367-1374.

37. Lai, W.-Q.; Chang, Y.-F.; Chou, F.-N.; Yang, D.-M., Portable FRET-Based Biosensor Device for On-Site Lead Detection. *Biosensors* 2022, *12* (3), 157.

38. Disha; Kumari, P.; Patel, M. K.; Kumar, P.; Nayak, M. K., Carbon Dots Conjugated Antibody as an Effective FRET-Based Biosensor for Progesterone Hormone Screening. *Biosensors* 2022, *12* (11), 993.

39. Wang, Q.; Wang, J.; Huang, Y.; Du, Y.; Zhang, Y.; Cui, Y.; Kong, D.-m., Development of the DNA-based biosensors for high performance in detection of molecular biomarkers: More rapid, sensitive, and universal. *Biosensors and Bioelectronics* 2022, *197*, 113739.

40. Stangherlin, S.; Liu, J., Nanomaterials enabled and enhanced DNA-based biosensors. *Journal of Materials Chemistry B* 2023, *11* (30), 6994-7003.

41. Song, J.; Li, Z.; Wang, P.; Meyer, T.; Mao, C.; Ke, Y., Reconfiguration of DNA molecular arrays driven by information relay. *Science* 2017, *357* (6349), eaan3377.

42. Liu, Y.; Cheng, J.; Fan, S.; Ge, H.; Luo, T.; Tang, L.; Ji, B.; Zhang, C.; Cui, D.; Ke, Y.; Song, J., Modular Reconfigurable DNA Origami: From Two-Dimensional to Three-Dimensional Structures. *Angewandte Chemie International Edition* 2020, *59* (51), 23277-23282.

43. Wang, D.; Yu, L.; Huang, C.-M.; Arya, G.; Chang, S.; Ke, Y., Programmable Transformations of DNA Origami Made of Small Modular Dynamic Units. *Journal of the American Chemical Society* 2021, *143* (5), 2256-2263.

44. Sarraf, N.; Rodriguez, K. R.; Qian, L., Modular reconfiguration of DNA origami assemblies using tile displacement. *Science Robotics* 2023, *8* (77), eadf1511.

45. Watson, J. D.; Crick, F. H. C., Molecular Structure of Nucleic Acids: A Structure for Deoxyribose Nucleic Acid. *Nature* 1953, *171* (4356), 737-738.

46. Dickerson, R. E.; Drew, H. R.; Conner, B. N.; Wing, R. M.; Fratini, A. V.; Kopka, M. L., The Anatomy of A-, B-, and Z-DNA. *Science* 1982, *216* (4545), 475-485.

47. Ghosh, A.; Bansal, M., A glossary of DNA structures from A to Z. *Acta Crystallogr D Biol Crystallogr* 2003, *59* (Pt 4), 620-6.

48. Wing, R.; Drew, H.; Takano, T.; Broka, C.; Tanaka, S.; Itakura, K.; Dickerson, R. E., Crystal structure analysis of a complete turn of B-DNA. *Nature* 1980, *287* (5784), 755-758.

49. Saran, R.; Wang, Y.; Li, I. T. S., Mechanical Flexibility of DNA: A Quintessential Tool for DNA Nanotechnology. *Sensors* 2020, *20* (24), 7019.

50. Kratky, O.; Porod, G., Röntgenuntersuchung gelöster Fadenmoleküle. *Recueil des Travaux Chimiques des Pays-Bas* 1949, *68* (12), 1106-1122.

51. Shimada, J.; Yamakawa, H., Ring-closure probabilities for twisted wormlike chains. Application to DNA. *Macromolecules* 1984, *17* (4), 689-698.

52. Smith, S. B.; Cui, Y.; Bustamante, C., Overstretching B-DNA: The Elastic Response of Individual Double-Stranded and Single-Stranded DNA Molecules. *Science* 1996, *271* (5250), 795-799.

53. Rippe, K., Making contacts on a nucleic acid polymer. *Trends Biochem Sci* 2001, *26* (12), 733-40.

54. Douglas, S. M.; Dietz, H.; Liedl, T.; Högberg, B.; Graf, F.; Shih, W. M., Self-assembly of DNA into nanoscale three-dimensional shapes. *Nature* 2009, *459* (7245), 414-418.

55. Sun, W.; Boulais, E.; Hakobyan, Y.; Wang, W. L.; Guan, A.; Bathe, M.; Yin, P., Casting inorganic structures with DNA molds. *Science* 2014, *346* (6210), 1258361.

56. Dietz, H.; Douglas, S. M.; Shih, W. M., Folding DNA into Twisted and Curved Nanoscale Shapes. *Science* 2009, *325* (5941), 725-730.

57. Han, D.; Pal, S.; Nangreave, J.; Deng, Z.; Liu, Y.; Yan, H., DNA Origami with Complex Curvatures in Three-Dimensional Space. *Science* 2011, *332* (6027), 342-346.

58. Wang, D.; Yu, L.; Ji, B.; Chang, S.; Song, J.; Ke, Y., Programming the Curvatures in Reconfigurable DNA Domino Origami by Using Asymmetric Units. *Nano Letters* 2020, *20* (11), 8236-8241.

59. Wagenbauer, K. F.; Sigl, C.; Dietz, H., Gigadalton-scale shape-programmable DNA assemblies. *Nature* 2017, *552* (7683), 78-83.

60. Yao, G.; Zhang, F.; Wang, F.; Peng, T.; Liu, H.; Poppleton, E.; Šulc, P.; Jiang, S.; Liu, L.; Gong, C.; Jing, X.; Liu, X.; Wang, L.; Liu, Y.; Fan, C.; Yan, H., Meta-DNA structures. *Nat Chem* 2020, *12* (11), 1067-1075.

61. Sigl, C.; Willner, E. M.; Engelen, W.; Kretzmann, J. A.; Sachenbacher, K.; Liedl, A.; Kolbe, F.; Wilsch, F.; Aghvami, S. A.; Protzer, U.; Hagan, M. F.; Fraden, S.; Dietz, H., Programmable icosahedral shell system for virus trapping. *Nature Materials* 2021.

62. Wintersinger, C. M.; Minev, D.; Ershova, A.; Sasaki, H. M.; Gowri, G.; Berengut, J. F.; Corea-Dilbert, F. E.; Yin, P.; Shih, W. M., Multi-micron crisscross structures from combinatorially assembled DNA-origami slats. Cold Spring Harbor Laboratory: 2022.

63. Geary, C.; Rothemund, P. W.; Andersen, E. S., A single-stranded architecture for cotranscriptional folding of RNA nanostructures. *Science* 2014, *345* (6198), 799-804.
64. Han, D.; Qi, X.; Myhrvold, C.; Wang, B.; Dai, M.; Jiang, S.; Bates, M.; Liu, Y.; An, B.; Zhang, F.; Yan, H.; Yin, P., Single-stranded DNA and RNA origami. *Science* 2017, *358* (6369).
65. Gerling, T.; Wagenbauer, K. F.; Neuner, A. M.; Dietz, H., Dynamic DNA devices and assemblies formed by shape-complementary, non-base pairing 3D components. *Science* 2015, *347* (6229), 1446-52.
66. Zhang, Y.; Pan, V.; Li, X.; Yang, X.; Li, H.; Wang, P.; Ke, Y., Dynamic DNA Structures. *Small* 2019, *15* (26), 1900228.
67. Deluca, M.; Shi, Z.; Castro, C. E.; Arya, G., Dynamic DNA nanotechnology: toward functional nanoscale devices. *Nanoscale Horizons* 2020, *5* (2), 182-201.
68. Vogt, M.; Langecker, M.; Gouder, M.; Kopperger, E.; Rothfischer, F.; Simmel, F. C.; List, J., Storage of mechanical energy in DNA nanorobotics using molecular torsion springs. *Nature Physics* 2023, *19* (5), 741-751.
69. Douglas, S. M.; Marblestone, A. H.; Teerapittayanon, S.; Vazquez, A.; Church, G. M.; Shih, W. M., Rapid prototyping of 3D DNA-origami shapes with caDNAno. *Nucleic Acids Research* 2009, *37* (15), 5001-5006.
70. Edwardson, T. G. W.; Carneiro, K. M. M.; McLaughlin, C. K.; Serpell, C. J.; Sleiman, H. F., Site-specific positioning of dendritic alkyl chains on DNA cages enables their geometry-dependent self-assembly. *Nature Chemistry* 2013, *5* (10), 868-875.
71. Chandrasekaran, A. R., Reconfigurable DNA Nanoswitches for Graphical Readout of Molecular Signals. *ChemBioChem* 2018, *19* (10), 1018-1021.
72. Trinh, T.; Liao, C.; Toader, V.; Barłóg, M.; Bazzi, H. S.; Li, J.; Sleiman, H. F., DNA-imprinted polymer nanoparticles with monodispersity and prescribed DNA-strand patterns. *Nature Chemistry* 2018, *10* (2), 184-192.
73. Xiao, M.; Lai, W.; Man, T.; Chang, B.; Li, L.; Chandrasekaran, A. R.; Pei, H., Rationally Engineered Nucleic Acid Architectures for Biosensing Applications. *Chemical Reviews* 2019, *119* (22), 11631-11717.
74. Patino, T.; Porchetta, A.; Jannasch, A.; Lladó, A.; Stumpp, T.; Schäffer, E.; Ricci, F.; Sánchez, S., Self-Sensing Enzyme-Powered Micromotors Equipped with pH-Responsive DNA Nanoswitches. *Nano Letters* 2019, *19* (6), 3440-3447.
75. Stokes, G. G., On the Change of Refrangibility of Light. *Philosophical Transactions of the Royal Society of London* 1852, *142*, 463-562.
76. Lakowicz, *Principles of Fluorescence Microscopy*.
77. Jabłoński, A., Über den Mechanismus der Photolumineszenz von Farbstoffphosphoren. *Zeitschrift für Physik* 1935, *94* (1-2), 38-46.
78. Kasha, M., Characterization of electronic transitions in complex molecules. *Discussions of the Faraday Society* 1950, *9*, 14.
79. Franck, J.; Dymond, E. G., Elementary processes of photochemical reactions. *Transactions of the Faraday Society* 1926, *21* (February), 536.

80. Condon, E., A Theory of Intensity Distribution in Band Systems. *Physical Review* 1926, *28* (6), 1182-1201.
81. Stryer, L.; Haugland, R. P., Energy transfer: a spectroscopic ruler. *Proc Natl Acad Sci U S A* 1967, *58* (2), 719-26.
82. Förster, T., Ein Beitrag zur Theorie der Photosynthese. *Zeitschrift für Naturforschung B* 1947, *2* (5-6), 174-182.
83. Förster, T., Zwischenmolekulare Energiewanderung und Fluoreszenz. *Annalen der Physik* 1948, *437* (1-2), 55-75.
84. Weiss, S., Fluorescence Spectroscopy of Single Biomolecules. *Science* 1999, *283* (5408), 1676-1683.
85. Moerner, W. E.; Orrit, M., Illuminating Single Molecules in Condensed Matter. *Science* 1999, *283* (5408), 1670-1676.
86. Tinnefeld, P.; Sauer, M., Branching out of single-molecule fluorescence spectroscopy: challenges for chemistry and influence on biology. *Angew Chem Int Ed Engl* 2005, *44* (18), 2642-2671.
87. Bavishi, K.; Hatzakis, N. S., Shedding light on protein folding, structural and functional dynamics by single molecule studies. *Molecules* 2014, *19* (12), 19407-34.
88. Orrit, M., Dynamic Heterogeneity in the Optical Signals from Single Nano-Objects. *The Journal of Physical Chemistry B* 2023, *127* (18), 3982-3989.
89. Lavis, L. D.; Raines, R. T., Bright Ideas for Chemical Biology. *ACS Chemical Biology* 2008, *3* (3), 142-155.
90. Holzmeister, P.; Acuna, G. P.; Grohmann, D.; Tinnefeld, P., Breaking the concentration limit of optical single-molecule detection. *Chemical Society Reviews* 2014, *43* (4), 1014-1028.
91. Hänselmann, S.; Herten, D. P., Single-Molecule Spectroscopy. In *Encyclopedia of Spectroscopy and Spectrometry (Third Edition)*, Lindon, J. C.; Tranter, G. E.; Koppenaal, D. W., Eds. Academic Press: Oxford, 2017; pp 84-88.
92. Morshed, A.; Karawdeniya, B. I.; Bandara, Y.; Kim, M. J.; Dutta, P., Mechanical characterization of vesicles and cells: A review. *Electrophoresis* 2020, *41* (7-8), 449-470.
93. Davide Zocco; Pietro Ferruzzi; Francesco Cappello; Winston Patrick Kuo; Fais, S., Extracellular vesicles as shuttles of tumor biomarkers and anti-tumor drugs. *Frontiers in Oncology* 2014, *4*.
94. Skotland, T.; Sagini, K.; Sandvig, K.; Llorente, A., An emerging focus on lipids in extracellular vesicles. *Advanced Drug Delivery Reviews* 2020, *159*, 308-321.
95. Akbarzadeh, A.; Rezaei-Sadabady, R.; Davaran, S.; Joo, S. W.; Zarghami, N.; Hanifehpour, Y.; Samiei, M.; Kouhi, M.; Nejati-Koshki, K., Liposome: classification, preparation, and applications. *Nanoscale Research Letters* 2013, *8* (1), 102.
96. Dimova, R., Giant Vesicles and Their Use in Assays for Assessing Membrane Phase State, Curvature, Mechanics, and Electrical Properties. *Annual Review of Biophysics* 2019, *48* (1), 93-119.
97. Pick, H.; Alves, A. C.; Vogel, H., Single-Vesicle Assays Using Liposomes and Cell-Derived Vesicles: From Modeling Complex Membrane Processes to Synthetic Biology and Biomedical Applications. *Chemical Reviews* 2018, *118* (18), 8598-8654.

98. Novick, P.; Schekman, R., Secretion and cell-surface growth are blocked in a temperature-sensitive mutant of Saccharomyces cerevisiae. *Proceedings of the National Academy of Sciences* 1979, *76* (4), 1858-1862.

99. Balch, W. E.; Dunphy, W. G.; Braell, W. A.; Rothman, J. E., Reconstitution of the transport of protein between successive compartments of the Golgi measured by the coupled incorporation of N-acetylglucosamine. *Cell* 1984, *39* (2 Pt 1), 405-16.

100. Kaiser, C. A.; Schekman, R., Distinct sets of SEC genes govern transport vesicle formation and fusion early in the secretory pathway. *Cell* 1990, *61* (4), 723-33.

101. Perin, M. S.; Fried, V. A.; Mignery, G. A.; Jahn, R.; Südhof, T. C., Phospholipid binding by a synaptic vesicle protein homologous to the regulatory region of protein kinase C. *Nature* 1990, *345* (6272), 260-3.

102. Söllner, T.; Whiteheart, S. W.; Brunner, M.; Erdjument-Bromage, H.; Geromanos, S.; Tempst, P.; Rothman, J. E., SNAP receptors implicated in vesicle targeting and fusion. *Nature* 1993, *362* (6418), 318-324.

103. Hata, Y.; Slaughter, C. A.; Südhof, T. C., Synaptic vesicle fusion complex contains unc-18 homologue bound to syntaxin. *Nature* 1993, *366* (6453), 347-351.

104. Danaei, M.; Dehghankhold, M.; Ataei, S.; Hasanzadeh Davarani, F.; Javanmard, R.; Dokhani, A.; Khorasani, S.; Mozafari, M., Impact of Particle Size and Polydispersity Index on the Clinical Applications of Lipidic Nanocarrier Systems. *Pharmaceutics* 2018, *10* (2), 57.

105. Pfeiffer, I.; Höök, F., Bivalent cholesterol-based coupling of oligonucletides to lipid membrane assemblies. *J Am Chem Soc* 2004, *126* (33), 10224-5.

106. Banchelli, M.; Gambinossi, F.; Durand, A.; Caminati, G.; Brown, T.; Berti, D.; Baglioni, P., Modulation of density and orientation of amphiphilic DNA on phospholipid membranes. II. Vesicles. *J Phys Chem B* 2010, *114* (21), 7348-58.

107. Langecker, M.; Arnaut, V.; List, J.; Simmel, F. C., DNA Nanostructures Interacting with Lipid Bilayer Membranes. *Accounts of Chemical Research* 2014, *47* (6), 1807-1815.

108. Khmelinskaia, A.; Franquelim, H. G.; Petrov, E. P.; Schwille, P., Effect of anchor positioning on binding and diffusion of elongated 3D DNA nanostructures on lipid membranes. *Journal of Physics D: Applied Physics* 2016, *49* (19), 194001.

109. Khmelinskaia, A.; Mücksch, J.; Petrov, E. P.; Franquelim, H. G.; Schwille, P., Control of Membrane Binding and Diffusion of Cholesteryl-Modified DNA Origami Nanostructures by DNA Spacers. *Langmuir* 2018, *34* (49), 14921-14931.

110. Cho, E. J.; Holback, H.; Liu, K. C.; Abouelmagd, S. A.; Park, J.; Yeo, Y., Nanoparticle Characterization: State of the Art, Challenges, and Emerging Technologies. *Molecular Pharmaceutics* 2013, *10* (6), 2093-2110.

111. Mourdikoudis, S.; Pallares, R. M.; Thanh, N. T. K., Characterization techniques for nanoparticles: comparison and complementarity upon studying nanoparticle properties. *Nanoscale* 2018, *10* (27), 12871-12934.

112. Bruce J. Berne; Pecora, R., *Dynamic Light Scattering*. Dover Publications: 2000; p 376.

113. Stetefeld, J.; McKenna, S. A.; Patel, T. R., Dynamic light scattering: a practical guide and applications in biomedical sciences. *Biophysical Reviews* 2016, *8* (4), 409-427.
114. Merkus, H. G., *Particle Size Measurements: Fundamentals, Practice, Quality*. Springer Netherlands: 2009.
115. McMahon, H. T.; Gallop, J. L., Membrane curvature and mechanisms of dynamic cell membrane remodelling. *Nature* 2005, *438* (7068), 590-596.
116. Kabbani, A. M.; Woodward, X.; Kelly, C. V., Revealing the Effects of Nanoscale Membrane Curvature on Lipid Mobility. *Membranes* 2017, *7* (4), 60.
117. Herlo, R.; Lund, V. K.; Lycas, M. D.; Jansen, A. M.; Khelashvili, G.; Andersen, R. C.; Bhatia, V.; Pedersen, T. S.; Albornoz, P. B. C.; Johner, N.; Ammendrup-Johnsen, I.; Christensen, N. R.; Erlendsson, S.; Stoklund, M.; Larsen, J. B.; Weinstein, H.; Kjærulff, O.; Stamou, D.; Gether, U.; Madsen, K. L., An Amphipathic Helix Directs Cellular Membrane Curvature Sensing and Function of the BAR Domain Protein PICK1. *Cell Reports* 2018, *23* (7), 2056-2069.
118. Zeno, W. F.; Thatte, A. S.; Wang, L.; Snead, W. T.; Lafer, E. M.; Stachowiak, J. C., Molecular Mechanisms of Membrane Curvature Sensing by a Disordered Protein. *Journal of the American Chemical Society* 2019, *141* (26), 10361-10371.
119. Sitarska, E.; Almeida, S. D.; Beckwith, M. S.; Stopp, J.; Czuchnowski, J.; Siggel, M.; Roessner, R.; Tschanz, A.; Ejsing, C.; Schwab, Y.; Kosinski, J.; Sixt, M.; Kreshuk, A.; Erzberger, A.; Diz-Muñoz, A., Sensing their plasma membrane curvature allows migrating cells to circumvent obstacles. *Nature Communications* 2023, *14* (1), 5644.
120. Kabbani, A. M.; Kelly, C. V., The Detection of Nanoscale Membrane Bending with Polarized Localization Microscopy. *Biophys J* 2017, *113* (8), 1782-1794.
121. Sorre, B.; Callan-Jones, A.; Manzi, J.; Goud, B.; Prost, J.; Bassereau, P.; Roux, A., Nature of curvature coupling of amphiphysin with membranes depends on its bound density. *Proceedings of the National Academy of Sciences* 2012, *109* (1), 173-178.
122. Shi, Z.; Baumgart, T., Membrane tension and peripheral protein density mediate membrane shape transitions. *Nature Communications* 2015, *6* (1), 5974.
123. Czogalla, A.; Henri; Schwille, P., DNA Nanostructures on Membranes as Tools for Synthetic Biology. *Biophysical Journal* 2016, *110* (8), 1698-1707.
124. Franquelim, H. G.; Khmelinskaia, A.; Sobczak, J.-P.; Dietz, H.; Schwille, P., Membrane sculpting by curved DNA origami scaffolds. *Nature Communications* 2018, *9* (1).
125. Ramezani, H.; Dietz, H., Building machines with DNA molecules. *Nature Reviews Genetics* 2020, *21* (1), 5-26.
126. Rubio-Sánchez, R.; Fabrini, G.; Cicuta, P.; Di Michele, L., Amphiphilic DNA nanostructures for bottom-up synthetic biology. *Chemical Communications* 2021.
127. Qutbuddin, Y.; Krohn, J.-H.; Brüggenthies, G. A.; Stein, J.; Gavrilovic, S.; Stehr, F.; Schwille, P., Design Features to Accelerate the Higher-Order Assembly of DNA Origami on Membranes. *The Journal of Physical Chemistry B* 2021.

128. Eto, H.; Franquelim, H. G.; Heymann, M.; Schwille, P., Membrane-coated 3D architectures for bottom-up synthetic biology. *Soft Matter* 2021, *17* (22), 5456-5466.
129. Shen, Q.; Grome, M. W.; Yang, Y.; Lin, C., Engineering Lipid Membranes with Programmable DNA Nanostructures. *Advanced Biosystems* 2020, *4* (1), 1900215.
130. Xu, W.; Nathwani, B.; Lin, C.; Wang, J.; Karatekin, E.; Pincet, F.; Shih, W.; Rothman, J. E., A Programmable DNA Origami Platform to Organize SNAREs for Membrane Fusion. *Journal of the American Chemical Society* 2016, *138* (13), 4439-4447.
131. Grome, M. W.; Zhang, Z.; Pincet, F.; Lin, C., Vesicle Tubulation with Self-Assembling DNA Nanosprings. *Angewandte Chemie* 2018, *130* (19), 5428-5432.
132. Grome, M. W.; Zhang, Z.; Lin, C., Stiffness and Membrane Anchor Density Modulate DNA-Nanospring-Induced Vesicle Tubulation. *ACS Applied Materials & Interfaces* 2019, *11* (26), 22987-22992.
133. Madsen, K. L.; Bhatia, V. K.; Gether, U.; Stamou, D., BAR domains, amphipathic helices and membrane-anchored proteins use the same mechanism to sense membrane curvature. *FEBS Letters* 2010, *584* (9), 1848-1855.
134. McMurray, M. A., The long and short of membrane curvature sensing by septins. *Journal of Cell Biology* 2019, *218* (4), 1083-1085.
135. Sayed; Ghatak, C.; Mohammad; Moniruzzaman, M.; Yamazaki, M., Experimental Estimation of Membrane Tension Induced by Osmotic Pressure. *Biophysical Journal* 2016, *111* (10), 2190-2201.
136. Malinin, V. S.; Frederik, P.; Lentz, B. R., Osmotic and Curvature Stress Affect PEG-Induced Fusion of Lipid Vesicles but Not Mixing of Their Lipids. *Biophysical Journal* 2002, *82* (4), 2090-2100.
137. Logisz, C. C.; Hovis, J. S., Effect of salt concentration on membrane lysis pressure. *Biochimica et Biophysica Acta (BBA) - Biomembranes* 2005, *1717* (2), 104-108.
138. Saha, S. K.; Alam Shibly, S. U.; Yamazaki, M., Membrane Tension in Negatively Charged Lipid Bilayers in a Buffer under Osmotic Pressure. *The Journal of Physical Chemistry B* 2020, *124* (27), 5588-5599.
139. Liu, X.; Stenhammar, J.; Wennerström, H.; Sparr, E., Vesicles Balance Osmotic Stress with Bending Energy That Can Be Released to Form Daughter Vesicles. *The Journal of Physical Chemistry Letters* 2022, *13* (2), 498-507.
140. Zong, W.; Li, Q.; Zhang, X.; Han, X., Deformation of giant unilamellar vesicles under osmotic stress. *Colloids and Surfaces B: Biointerfaces* 2018, *172*, 459-463.
141. Daljit Singh, J. K.; Luu, M. T.; Abbas, A.; Wickham, S. F. J., Switchable DNA-origami nanostructures that respond to their environment and their applications. *Biophysical Reviews* 2018, *10* (5), 1283-1293.
142. Naskar, S.; Gosika, M.; Joshi, H.; Maiti, P. K., Tuning the Stability of DNA Nanotubes with Salt. *The Journal of Physical Chemistry C* 2019, *123* (14), 9461-9470.
143. Jepsen, M. D. E.; Sørensen, R. S.; Maffeo, C.; Aksimentiev, A.; Kjems, J.; Birkedal, V., Single molecule analysis of structural fluctuations in DNA nanostructures. *Nanoscale* 2019, *11* (39), 18475-18482.
144. Shi, Z.; Arya, G., Free energy landscape of salt-actuated reconfigurable DNA nanodevices. *Nucleic Acids Research* 2020, *48* (2), 548-560.

145. Hübner, K.; Raab, M.; Bohlen, J.; Bauer, J.; Tinnefeld, P., Salt-induced conformational switching of a flat rectangular DNA origami structure. *Nanoscale* 2022, *14* (21), 7898-7905.
146. Bhatia, T.; Husen, P.; Brewer, J.; Bagatolli, L. A.; Hansen, P. L.; Ipsen, J. H.; Mouritsen, O. G., Preparing giant unilamellar vesicles (GUVs) of complex lipid mixtures on demand: Mixing small unilamellar vesicles of compositionally heterogeneous mixtures. *Biochimica et Biophysica Acta (BBA) - Biomembranes* 2015, *1848* (12), 3175-3180.
147. Tripepi, M.; Ferrauto, G.; Bennardi, P. O.; Aime, S.; Delli Castelli, D., Multilamellar LipoCEST Agents Obtained from Osmotic Shrinkage of Paramagnetically Loaded Giant Unilamellar Vescicles (GUVs). *Angewandte Chemie International Edition* 2020, *59* (6), 2279-2283.
148. Vadlapudi, A. D.; Vadlapatla, R. K.; Earla, R.; Sirimulla, S.; Bailey, J. B.; Pal, D.; Mitra, A. K., Novel Biotinylated Lipid Prodrugs of Acyclovir for the Treatment of Herpetic Keratitis (HK): Transporter Recognition, Tissue Stability and Antiviral Activity. *Pharmaceutical Research* 2013, *30* (8), 2063-2076.
149. Gey, G. O.; Coffman, W. D.; Kubicek, M. T., Tissue culture studies of the proliferative capacity of cervical carcinoma and normal epithelium. *Cancer research* 1952, *12*, 264-265.
150. Landry, J. J.; Pyl, P. T.; Rausch, T.; Zichner, T.; Tekkedil, M. M.; Stütz, A. M.; Jauch, A.; Aiyar, R. S.; Pau, G.; Delhomme, N.; Gagneur, J.; Korbel, J. O.; Huber, W.; Steinmetz, L. M., The genomic and transcriptomic landscape of a HeLa cell line. *G3 (Bethesda)* 2013, *3* (8), 1213-24.
151. HeLa Cells: A Lasting Contribution to Biomedical Research. https://osp.od.nih.gov/hela-cells/.
152. Théry, C.; Zitvogel, L.; Amigorena, S., Exosomes: composition, biogenesis and function. *Nat Rev Immunol* 2002, *2* (8), 569-79.
153. Pegtel, D. M.; Gould, S. J., Exosomes. *Annual Review of Biochemistry* 2019, *88* (1), 487-514.
154. Kalluri, R.; LeBleu, V. S., The biology, function, and biomedical applications of exosomes. *Science* 2020, *367* (6478), eaau6977.
155. Tenchov, R.; Sasso, J. M.; Wang, X.; Liaw, W. S.; Chen, C. A.; Zhou, Q. A., ExosomesNature's Lipid Nanoparticles, a Rising Star in Drug Delivery and Diagnostics. *ACS Nano* 2022, *16* (11), 17802-17846.
156. Martín-Gracia, B.; Martín-Barreiro, A.; Cuestas-Ayllón, C.; Grazú, V.; Line, A.; Llorente, A.; M. De La Fuente, J.; Moros, M., Nanoparticle-based biosensors for detection of extracellular vesicles in liquid biopsies. *Journal of Materials Chemistry B* 2020, *8* (31), 6710-6738.
157. Guo, P.; Busatto, S.; Huang, J.; Morad, G.; Moses, M. A., A Facile Magnetic Extrusion Method for Preparing Endosome-Derived Vesicles for Cancer Drug Delivery. *Advanced Functional Materials* 2021, *31* (44), 2008326.
158. Kwok, Z. H.; Ni, K.; Jin, Y., Extracellular Vesicle Associated Non-Coding RNAs in Lung Infections and Injury. *Cells* 2021, *10* (5), 965.
159. García-Manrique, P.; Gutiérrez, G.; Blanco-López, M. C., Fully Artificial Exosomes: Towards New Theranostic Biomaterials. *Trends in Biotechnology* 2018, *36* (1), 10-14.
160. Man, K.; Brunet, M. Y.; Jones, M.-C.; Cox, S. C., Engineered Extracellular Vesicles: Tailored-Made Nanomaterials for Medical Applications. *Nanomaterials* 2020, *10* (9), 1838.
161. Li, Y.-J.; Wu, J.-Y.; Liu, J.; Xu, W.; Qiu, X.; Huang, S.; Hu, X.-B.; Xiang, D.-X., Artificial exosomes for translational nanomedicine. *Journal of Nanobiotechnology* 2021, *19* (1).

162. De Jong, O. G.; Kooijmans, S. A. A.; Murphy, D. E.; Jiang, L.; Evers, M. J. W.; Sluijter, J. P. G.; Vader, P.; Schiffelers, R. M., Drug Delivery with Extracellular Vesicles: From Imagination to Innovation. *Accounts of Chemical Research* 2019, *52* (7), 1761-1770.

163. Dang, X. T. T.; Kavishka, J. M.; Zhang, D. X.; Pirisinu, M.; Le, M. T. N., Extracellular Vesicles as an Efficient and Versatile System for Drug Delivery. *Cells* 2020, *9* (10), 2191.

164. Zhao, L.; Gu, C.; Gan, Y.; Shao, L.; Chen, H.; Zhu, H., Exosome-mediated siRNA delivery to suppress postoperative breast cancer metastasis. *Journal of Controlled Release* 2020, *318*, 1-15.

165. Nicolini, A.; Ferrari, P.; Biava, P. M., Exosomes and Cell Communication: From Tumour-Derived Exosomes and Their Role in Tumour Progression to the Use of Exosomal Cargo for Cancer Treatment. *Cancers* 2021, *13* (4), 822.

166. Valadi, H.; Ekström, K.; Bossios, A.; Sjöstrand, M.; Lee, J. J.; Lötvall, J. O., Exosome-mediated transfer of mRNAs and microRNAs is a novel mechanism of genetic exchange between cells. *Nature Cell Biology* 2007, *9* (6), 654-659.

167. Skog, J.; Würdinger, T.; Van Rijn, S.; Meijer, D. H.; Gainche, L.; Curry, W. T.; Carter, B. S.; Krichevsky, A. M.; Breakefield, X. O., Glioblastoma microvesicles transport RNA and proteins that promote tumour growth and provide diagnostic biomarkers. *Nature Cell Biology* 2008, *10* (12), 1470-1476.

168. Alvarez-Erviti, L.; Seow, Y.; Yin, H.; Betts, C.; Lakhal, S.; Wood, M. J. A., Delivery of siRNA to the mouse brain by systemic injection of targeted exosomes. *Nature Biotechnology* 2011, *29* (4), 341-345.

169. Haney, M. J.; Klyachko, N. L.; Zhao, Y.; Gupta, R.; Plotnikova, E. G.; He, Z.; Patel, T.; Piroyan, A.; Sokolsky, M.; Kabanov, A. V.; Batrakova, E. V., Exosomes as drug delivery vehicles for Parkinson's disease therapy. *Journal of Controlled Release* 2015, *207*, 18-30.

170. Yim, N.; Ryu, S. W.; Choi, K.; Lee, K. R.; Lee, S.; Choi, H.; Kim, J.; Shaker, M. R.; Sun, W.; Park, J. H.; Kim, D.; Heo, W. D.; Choi, C., Exosome engineering for efficient intracellular delivery of soluble proteins using optically reversible protein-protein interaction module. *Nat Commun* 2016, *7*, 12277.

171. Hong, Y.; Nam, G.-H.; Koh, E.; Jeon, S.; Kim, G. B.; Jeong, C.; Kim, D.-H.; Yang, Y.; Kim, I.-S., Exosome as a Vehicle for Delivery of Membrane Protein Therapeutics, PH20, for Enhanced Tumor Penetration and Antitumor Efficacy. *Advanced Functional Materials* 2018, *28* (5), 1703074.

172. Reiser, A.; Woschée, D.; Mehrotra, N.; Krzysztoń, R.; Strey, H. H.; Rädler, J. O., Correlation of mRNA delivery timing and protein expression in lipid-based transfection. *Integrative Biology* 2019, *11* (9), 362-371.

173. Grava, M.; Ibrahim, M.; Sudarsan, A.; Pusterla, J.; Philipp, J.; Rädler, J. O.; Schwierz, N.; Schneck, E., Combining molecular dynamics simulations and x-ray scattering techniques for the accurate treatment of protonation degree and packing of ionizable lipids in monolayers. *The Journal of Chemical Physics* 2023, *159* (15).

174. Gabizon, A.; Catane, R.; Uziely, B.; Kaufman, B.; Safra, T.; Cohen, R.; Martin, F.; Huang, A.; Barenholz, Y., Prolonged circulation time and enhanced accumulation in malignant exudates of doxorubicin encapsulated in polyethylene-glycol coated liposomes. *Cancer Res* 1994, *54* (4), 987-92.

175. Working, P. K.; Newman, M. S.; Huang, S. K.; Mayhew, E.; Vaage, J.; Lasic, D. D., Pharmacokinetics, Biodistribution and Therapeutic Efficacy of Doxorubicin Encapsulated in Stealth® Liposomes (Doxil®). *Journal of Liposome Research* 1994, *4* (1), 667-687.

176. Working, P. K.; Dayan, A. D., Pharmacological-toxicological expert report. CAELYX. (Stealth liposomal doxorubicin HCl). *Hum Exp Toxicol* 1996, *15* (9), 751-85.

177. Barenholz, Y., Doxil® — The first FDA-approved nano-drug: Lessons learned. *Journal of Controlled Release* 2012, *160* (2), 117-134.

178. Sahin, U.; Muik, A.; Derhovanessian, E.; Vogler, I.; Kranz, L. M.; Vormehr, M.; Baum, A.; Pascal, K.; Quandt, J.; Maurus, D.; Brachtendorf, S.; Lörks, V.; Sikorski, J.; Hilker, R.; Becker, D.; Eller, A.-K.; Grützner, J.; Boesler, C.; Rosenbaum, C.; Kühnle, M.-C.; Luxemburger, U.; Kemmer-Brück, A.; Langer, D.; Bexon, M.; Bolte, S.; Karikó, K.; Palanche, T.; Fischer, B.; Schultz, A.; Shi, P.-Y.; Fontes-Garfias, C.; Perez, J. L.; Swanson, K. A.; Loschko, J.; Scully, I. L.; Cutler, M.; Kalina, W.; Kyratsous, C. A.; Cooper, D.; Dormitzer, P. R.; Jansen, K. U.; Türeci, Ö., COVID-19 vaccine BNT162b1 elicits human antibody and TH1 T cell responses. *Nature* 2020, *586* (7830), 594-599.

179. Mulligan, M. J.; Lyke, K. E.; Kitchin, N.; Absalon, J.; Gurtman, A.; Lockhart, S.; Neuzil, K.; Raabe, V.; Bailey, R.; Swanson, K. A.; Li, P.; Koury, K.; Kalina, W.; Cooper, D.; Fontes-Garfias, C.; Shi, P.-Y.; Türeci, Ö.; Tompkins, K. R.; Walsh, E. E.; Frenck, R.; Falsey, A. R.; Dormitzer, P. R.; Gruber, W. C.; Şahin, U.; Jansen, K. U., Phase I/II study of COVID-19 RNA vaccine BNT162b1 in adults. *Nature* 2020, *586* (7830), 589-593.

180. Corbett, K. S.; Edwards, D. K.; Leist, S. R.; Abiona, O. M.; Boyoglu-Barnum, S.; Gillespie, R. A.; Himansu, S.; Schäfer, A.; Ziwawo, C. T.; Dipiazza, A. T.; Dinnon, K. H.; Elbashir, S. M.; Shaw, C. A.; Woods, A.; Fritch, E. J.; Martinez, D. R.; Bock, K. W.; Minai, M.; Nagata, B. M.; Hutchinson, G. B.; Wu, K.; Henry, C.; Bahl, K.; Garcia-Dominguez, D.; Ma, L.; Renzi, I.; Kong, W.-P.; Schmidt, S. D.; Wang, L.; Zhang, Y.; Phung, E.; Chang, L. A.; Loomis, R. J.; Altaras, N. E.; Narayanan, E.; Metkar, M.; Presnyak, V.; Liu, C.; Louder, M. K.; Shi, W.; Leung, K.; Yang, E. S.; West, A.; Gully, K. L.; Stevens, L. J.; Wang, N.; Wrapp, D.; Doria-Rose, N. A.; Stewart-Jones, G.; Bennett, H.; Alvarado, G. S.; Nason, M. C.; Ruckwardt, T. J.; McLellan, J. S.; Denison, M. R.; Chappell, J. D.; Moore, I. N.; Morabito, K. M.; Mascola, J. R.; Baric, R. S.; Carfi, A.; Graham, B. S., SARS-CoV-2 mRNA vaccine design enabled by prototype pathogen preparedness. *Nature* 2020, *586* (7830), 567-571.

181. Patel, R.; Kaki, M.; Potluri, V. S.; Kahar, P.; Khanna, D., A comprehensive review of SARS-CoV-2 vaccines: Pfizer, Moderna & Johnson & Johnson. *Human Vaccines & Immunotherapeutics* 2022, *18* (1), 1-12.

182. Altmann, D. M.; Boyton, R. J., COVID-19 vaccination: The road ahead. *Science* 2022, *375* (6585), 1127-1132.

183. Fang, E.; Liu, X.; Li, M.; Zhang, Z.; Song, L.; Zhu, B.; Wu, X.; Liu, J.; Zhao, D.; Li, Y., Advances in COVID-19 mRNA vaccine development. *Signal Transduction and Targeted Therapy* 2022, *7* (1).

184. Xu, L.; Wang, X.; Liu, Y.; Yang, G.; Falconer, R. J.; Zhao, C.-X., Lipid Nanoparticles for Drug Delivery. *Advanced NanoBiomed Research* 2022, *2* (2), 2100109.

185. Tenchov, R.; Bird, R.; Curtze, A. E.; Zhou, Q., Lipid Nanoparticles─From Liposomes to mRNA Vaccine Delivery, a Landscape of Research Diversity and Advancement. *ACS Nano* 2021, *15* (11), 16982-17015.

186. Manzari, M. T.; Shamay, Y.; Kiguchi, H.; Rosen, N.; Scaltriti, M.; Heller, D. A., Targeted drug delivery strategies for precision medicines. *Nature Reviews Materials* 2021, *6* (4), 351-370.

187. Douglas, S. M.; Bachelet, I.; Church, G. M., A Logic-Gated Nanorobot for Targeted Transport of Molecular Payloads. *Science* 2012, *335* (6070), 831-834.
188. Kopperger, E.; List, J.; Madhira, S.; Rothfischer, F.; Lamb, D. C.; Simmel, F. C., A self-assembled nanoscale robotic arm controlled by electric fields. *Science* 2018, *359* (6373), 296-301.
189. Pumm, A.-K.; Engelen, W.; Kopperger, E.; Isensee, J.; Vogt, M.; Kozina, V.; Kube, M.; Honemann, M. N.; Bertosin, E.; Langecker, M.; Golestanian, R.; Simmel, F. C.; Dietz, H., A DNA origami rotary ratchet motor. *Nature* 2022, *607* (7919), 492-498.
190. Linko, V.; Ora, A.; Kostiainen, M. A., DNA Nanostructures as Smart Drug-Delivery Vehicles and Molecular Devices. *Trends in Biotechnology* 2015, *33* (10), 586-594.
191. Pitikultham, P.; Wang, Z.; Wang, Y.; Shang, Y.; Jiang, Q.; Ding, B., Stimuli-Responsive DNA Origami Nanodevices and Their Biological Applications. *ChemMedChem* 2022, *17* (1), e202100635.
192. Zhan, P.; Peil, A.; Jiang, Q.; Wang, D.; Mousavi, S.; Xiong, Q.; Shen, Q.; Shang, Y.; Ding, B.; Lin, C.; Ke, Y.; Liu, N., Recent Advances in DNA Origami-Engineered Nanomaterials and Applications. *Chemical Reviews* 2023, *123* (7), 3976-4050.
193. Ghosal, S.; Bag, S.; Bhowmik, S., Unravelling the Drug Encapsulation Ability of Functional DNA Origami Nanostructures: Current Understanding and Future Prospects on Targeted Drug Delivery. *Polymers* 2023, *15* (8), 1850.
194. Gu, H.; Chao, J.; Xiao, S.-J.; Seeman, N. C., A proximity-based programmable DNA nanoscale assembly line. *Nature* 2010, *465* (7295), 202-205.
195. Banerjee, A.; Bhatia, D.; Saminathan, A.; Chakraborty, S.; Kar, S.; Krishnan, Y., Controlled Release of Encapsulated Cargo from a DNA Icosahedron using a Chemical Trigger. *Angewandte Chemie International Edition* 2013, *52* (27), 6854-6857.
196. Kopperger, E.; Pirzer, T.; Simmel, F. C., Diffusive Transport of Molecular Cargo Tethered to a DNA Origami Platform. *Nano Letters* 2015, *15* (4), 2693-2699.
197. Thubagere, A. J.; Li, W.; Johnson, R. F.; Chen, Z.; Doroudi, S.; Lee, Y. L.; Izatt, G.; Wittman, S.; Srinivas, N.; Woods, D.; Winfree, E.; Qian, L., A cargo-sorting DNA robot. *Science* 2017, *357* (6356), eaan6558.
198. Stömmer, P.; Kiefer, H.; Kopperger, E.; Honemann, M. N.; Kube, M.; Simmel, F. C.; Netz, R. R.; Dietz, H., A synthetic tubular molecular transport system. *Nature Communications* 2021, *12* (1).
199. Ramm, B.; Goychuk, A.; Khmelinskaia, A.; Blumhardt, P.; Eto, H.; Ganzinger, K. A.; Frey, E.; Schwille, P., A diffusiophoretic mechanism for ATP-driven transport without motor proteins. *Nature Physics* 2021, *17* (7), 850-858.
200. Zhao, Y.-X.; Shaw, A.; Zeng, X.; Benson, E.; Nyström, A. M.; Högberg, B., DNA Origami Delivery System for Cancer Therapy with Tunable Release Properties. *ACS Nano* 2012, *6* (10), 8684-8691.
201. Li, S.; Jiang, Q.; Liu, S.; Zhang, Y.; Tian, Y.; Song, C.; Wang, J.; Zou, Y.; Anderson, G. J.; Han, J.-Y.; Chang, Y.; Liu, Y.; Zhang, C.; Chen, L.; Zhou, G.; Nie, G.; Yan, H.; Ding, B.; Zhao, Y., A DNA nanorobot functions as a cancer therapeutic in response to a molecular trigger in vivo. *Nature Biotechnology* 2018, *36* (3), 258-264.

202. Ora, A.; Järvihaavisto, E.; Zhang, H.; Auvinen, H.; Santos, H. A.; Kostiainen, M. A.; Linko, V., Cellular delivery of enzyme-loaded DNA origami. *Chemical Communications* 2016, *52* (98), 14161-14164.

203. Brown, J. W. P.; Alford, R. G.; Walsh, J. C.; Spinney, R. E.; Xu, S. Y.; Hertel, S.; Berengut, J. F.; Spenkelink, L. M.; Van Oijen, A. M.; Böcking, T.; Morris, R. G.; Lee, L. K., Rapid Exchange of Stably Bound Protein and DNA Cargo on a DNA Origami Receptor. *ACS Nano* 2022, *16* (4), 6455-6467.

204. Ijäs, H.; Hakaste, I.; Shen, B.; Kostiainen, M. A.; Linko, V., Reconfigurable DNA Origami Nanocapsule for pH-Controlled Encapsulation and Display of Cargo. *ACS Nano* 2019, *13* (5), 5959-5967.

205. Mobarak, E.; Javanainen, M.; Kulig, W.; Honigmann, A.; Sezgin, E.; Aho, N.; Eggeling, C.; Rog, T.; Vattulainen, I., How to minimize dye-induced perturbations while studying biomembrane structure and dynamics: PEG linkers as a rational alternative. *Biochimica et Biophysica Acta (BBA) - Biomembranes* 2018, *1860* (11), 2436-2445.

206. Ochmann, S. E.; Joshi, H.; Büber, E.; Franquelim, H. G.; Stegemann, P.; Saccà, B.; Keyser, U. F.; Aksimentiev, A.; Tinnefeld, P., DNA Origami Voltage Sensors for Transmembrane Potentials with Single-Molecule Sensitivity. *Nano Letters* 2021, *21* (20), 8634-8641.

207. Zhang, Z.; Yomo, D.; Gradinaru, C., Choosing the right fluorophore for single-molecule fluorescence studies in a lipid environment. *Biochimica et Biophysica Acta (BBA) - Biomembranes* 2017, *1859* (7), 1242-1253.

208. Zhang, D. Y.; Winfree, E., Control of DNA Strand Displacement Kinetics Using Toehold Exchange. *Journal of the American Chemical Society* 2009, *131* (47), 17303-17314.

209. Srinivas, N.; Ouldridge, T. E.; Sulc, P.; Schaeffer, J. M.; Yurke, B.; Louis, A. A.; Doye, J. P.; Winfree, E., On the biophysics and kinetics of toehold-mediated DNA strand displacement. *Nucleic Acids Res* 2013, *41* (22), 10641-58.

210. Olson, X.; Kotani, S.; Padilla, J. E.; Hallstrom, N.; Goltry, S.; Lee, J.; Yurke, B.; Hughes, W. L.; Graugnard, E., Availability: A Metric for Nucleic Acid Strand Displacement Systems. *ACS Synthetic Biology* 2017, *6* (1), 84-93.

211. Wang, B.; Thachuk, C.; Ellington, A. D.; Winfree, E.; Soloveichik, D., Effective design principles for leakless strand displacement systems. *Proceedings of the National Academy of Sciences* 2018, *115* (52), E12182-E12191.

212. Castro, C. E.; Kilchherr, F.; Kim, D.-N.; Shiao, E. L.; Wauer, T.; Wortmann, P.; Bathe, M.; Dietz, H., A primer to scaffolded DNA origami. *Nature Methods* 2011, *8* (3), 221-229.

213. Kim, D.-N.; Kilchherr, F.; Dietz, H.; Bathe, M., Quantitative prediction of 3D solution shape and flexibility of nucleic acid nanostructures. *Nucleic Acids Research* 2012, *40* (7), 2862-2868.

214. Vogelsang, J.; Kasper, R.; Steinhauer, C.; Person, B.; Heilemann, M.; Sauer, M.; Tinnefeld, P., A reducing and oxidizing system minimizes photobleaching and blinking of fluorescent dyes. *Angew Chem Int Ed Engl* 2008, *47* (29), 5465-9.

215. Cordes, T.; Vogelsang, J.; Tinnefeld, P., On the Mechanism of Trolox as Antiblinking and Antibleaching Reagent. *Journal of the American Chemical Society* 2009, *131* (14), 5018-5019.

216. Preus, S.; Noer, S. L.; Hildebrandt, L. L.; Gudnason, D.; Birkedal, V., iSMS: single-molecule FRET microscopy software. *Nature Methods* 2015, *12* (7), 593-594.

217. Müller, B. K.; Zaychikov, E.; Bräuchle, C.; Lamb, D. C., Pulsed interleaved excitation. *Biophys J* 2005, *89* (5), 3508-22.

10. Publications and Presentations

List of publications

- S.E. Ochmann, H. Joshi, **E. Büber**, H. Franquelim, P. Stegemann, B. Saccà, U.F. Keyser, A. Aksimentiev, P. Tinnefeld, *Nano Letters* 21(20) (2021) 8634.

- **E. Büber**, T. Schröder, M. Scheckenbach, M. Dass, H.G. Franquelim, P. Tinnefeld, DNA Origami Curvature Sensors for Nanoparticle and Vesicle Size Determination with Single-Molecule FRET Readout, *ACS Nano* 17(3) (2023) 3088.

- **E. Buber**, R. Yaadav, T. Schröder, H.G. Franquelim, P. Tinnefeld, DNA Origami Vesicle Sensors with Triggered Cargo Transfer, *bioRxiv* 2023.11.03.565475.

List of presentations

- S.E. Ochmann, **E. Büber**, H.G. Franquelim, U.F. Keyser, P. Tinnefeld, DNA Nanotechnology for Membrane Sensing, International Physics of Living Systems Network, Munich, Germany, July 2019.

- **E. Büber**, T. Schröder, S.E. Ochmann, H.G. Franquelim, P. Tinnefeld, A Curvature Ruler: Sensing by DNA Nanotech, 4th Functional DNA Nanotechnology Workshop, Rome, October 2020.

- **E. Büber**, T. Schröder, S.E. Ochmann, H.G. Franquelim, P. Tinnefeld, A Curvature Ruler Enabled by DNA Nanotech, FNANO2021 18th Annual Conference Foundations of Nanoscience, Online Event, April 2021.

- **E. Büber**, T. Schröder, M. Scheckenbach, M. Dass, H.G. Franquelim, P. Tinnefeld, A FRET based DNA origami tool for particle curvature sensing, Center for Nanoscience Retreat, Kleinwalsertal, May 2022.

- **E. Büber**, T. Schröder, M. Scheckenbach, M. Dass, H.G. Franquelim, P. Tinnefeld, A FRET based DNA origami tool for particle curvature sensing, Methods and Applications of Fluorescence 2022 Conference (MAF 2022), Gothenburg, September 2022.

- **E. Büber**, T. Schröder, M. Scheckenbach, M. Dass, H.G. Franquelim, P. Tinnefeld, A FRET based DNA origami tool for particle curvature sensing, SFB1032 Annual Workshop 2022, Munich, October 2022.

- **E. Büber**, T. Schröder, M. Scheckenbach, M. Dass, H.G. Franquelim, P. Tinnefeld, Unveiling Particle Shape with FRET-Enabled DNA Origami Curvature Sensors,

20th Annual Conference on Foundations of Nanoscience, Snowbird-Utah, April 2023.

List of awards

- Best Poster Award - CeNS Retreat Kleinwalsertal May 2022

- CeNS Travel Award January 2023 - The Center for NanoScience announces a limited number of Travel Awards for LMU CeNS associates. The travel awards can be used for active participation (talk or poster) in a scientific conference or workshop.

11. Acknowledgements

Embarking on this Ph.D. journey was more than just an academic decision; it was a life-changing move that involved adaptability and commitment. The enormity of moving from Turkey to Germany cannot be understated—a shift not just in place but in culture, especially within the academic environment, bringing its own set of challenges.

I am genuinely grateful to my advisor, Philip Tinnefeld, who shattered all my apprehensions about hierarchies and academic formalities from day one. Your open-door policy, easy-going nature, and deep respect and belief for your group made it not just comfortable but enriching to engage with you.

My deepest gratitude goes to my co-advisor, Henri G. Franquelim, who has been the cornerstone of my journey here. During my initial, challenging six months, the emotional burden and the weight of isolation had nearly convinced me to return to Turkey, and your guidance was my lifeline. Your support extended beyond academia, touching the very core of my well-being and helping me integrate my emotional and intellectual self. Thank you for being more than just a supervisor; you have been an irreplaceable pillar of support.

I owe a special debt of gratitude to my committee members. Your invaluable advice and keen review have been instrumental in refining both my research and my character.

I am grateful to Moritz Ehrl, for his countless helps regarding all formal stuff and providing tips to track through the German bureaucracy.

I would like to extend heartfelt thanks to the entire Tinnefeld group. Each one of you contributed to an atmosphere where ideas flourish and debates ignite curiosity. Special thanks to Viki for the invaluable guidance and consistent encouragement. Thank you for believing in me.

A huge shout-out to Tim, whose brainpower is so immense it probably has its own gravitational pull. You have always made time to guide me without making me feel like a complete novice. Thanks for your patience, infinite support and countless help.

To my friends beyond colleagues, Michi, Alan, Luciano, Giovanni, thank you for the environment you created, particularly when homesickness and cultural disorientation threatened to overshadow my focus.

A big, warm thank you to Lorena. When you joined the group and brought your expertise in biosensors, it was like finding a missing puzzle piece in my own academic journey. Beyond that, you have been a steadfast colleague and a true friend. Our conversations—about work and life—helped me trust my own skills in a way that nothing else has. I am and will always be so grateful for that, and for you.

Now comes someone exceptional, my dearest Renukka. When I first moved here, I felt like a fish out of water, constantly questioning my place here both culturally and academically. Then you arrived from India, and suddenly, my struggles felt less isolating. Our shared challenges and laughs, not to mention our unforgettable trips, have turned this journey into something irreplaceable. You are not just a colleague or a travel buddy; your presence has turned what felt like an ordeal into an adventure. Words cannot express how grateful I am for your friendship and the perspective it has brought to my life.

Here, a gigantic thank goes to Negin, who has been my touchstone of normalcy in an often chaotic life journey. Your arrival here felt like you brought the beauty of our earlier university life with you. This place is where our bond really grew. Now, you make me feel like my thoughts and feelings are not just okay, but totally normal—even when life feels anything but. Our almost 'telepathic' understanding has turned into something deeper and I am loving it.

A unique thank to Dilara, our friendship had an unconventional start, but what has unfolded since is something beyond my expectations and something I hold very dear. Your imaginative spirit not only makes you a colorful friend but also a source of inspiration. You have been an anchor in this swirling sea of new experiences, and you played matchmaker in the most monumental way. It is hard to sum up what your friendship means to me, but let's just say, it has always been a power in turning challenges into milestones and uncertainties into joys.

An everlasting thank-you to Eda, the other half of “the Bolber team” and my lifetime tea-drinking partner. We have navigated the ups and downs of life and covered countless miles of distance, yet our friendship has not missed a beat. In a world where relationships just come and go, your consistent support has been a solid and comforting presence in my life. That consistency is something I do not take for granted, and I am incredibly thankful for it.

I would be remiss not to acknowledge Elif, my sister in every sense. Our friendship has stood the test of time, different cities and countless life changes. The universe graciously brought us together again here in Germany, and having you close has been nothing short of a lifeline. Our growth together will keep unfolding, now enriched by the presence of your wonderful Ada. Also together with the pure joy we have – Rikki.

To Cem, my rock and my refuge — the first time we met felt like perfect timing, as if all the pieces suddenly clicked into place. From our first conversation, I have been captivated by your complex character, your decisiveness and your openness for new adventures. You impress me in ways words fall short of expressing. Your infectiously cheerful spirit is like a burst of sunlight on a cloudy day, always brightening up my life. Whenever I am down, just seeing you there lifts me up, giving me a reason to smile and believe. Our complementary characters make everything seem not just possible, but probable. For all the love, endless support and inspiration you provide, know that my gratitude is boundless and everlasting.

To my beautiful family, who has always created a warm and cheerful environment that felt like a sanctuary of happiness and support—thank you. This nurturing atmosphere has been a constant source of strength throughout my journey, and it is a testament to the love and unity that defines us as a family.

Finally, to my late grandmother and my incredible mother, the guiding stars of my life — firstly, to my granny, a woman of incomparable grace and resilience, whose wisdom and love touched not only me but everyone fortunate enough to know her. Your influence is indelibly imprinted on my life and your spirit continues to inspire me. To my mother, the embodiment of strength and unconditional love. As life unfolds its lessons, my admiration for you only deepens, making me realize the enormity of the sacrifices you have made and the tremendous job you have done raising me. Your presence in my life is not just

pivotal; it is foundational. You are the cornerstone on which I have built my dreams, the unwavering support that makes any achievement possible. In every step of this journey, you have been my unspoken reassurance and my greatest inspiration. For your love, for your sacrifice and for being the extraordinary woman you are, my gratitude is endless.